EVALUATION OF INNOVATIVE CONCEPTS FOR SEMI-ACTIVE AND ACTIVE ROTORCRAFT CONTROL

A Thesis
Presented to
The Academic Faculty

by

Yannick Van Weddingen

In Partial Fulfillment
of the Requirements for the Degree
Doctor of Philosophy in the
School of Aerospace Engineering

Georgia Institute of Technology
December 2011

EVALUATION OF INNOVATIVE CONCEPTS FOR SEMI-ACTIVE AND ACTIVE ROTORCRAFT CONTROL

Approved by:

Olivier A. Bauchau
Mechanical Engineering Department
UM-SJTU Joint Institute

Massimo Ruzzene
School of Aerospace Engineering
Georgia Institute of Technology

Dewey H. Hodges
School of Aerospace Engineering
Georgia Institute of Technology

Serkan Ozbay
Senior Research Engineer
Materials Technologies Corporation

Mark Costello
School of Aerospace Engineering
Georgia Institute of Technology

Date Approved: September 2, 2011

To my parents

ACKNOWLEDGEMENTS

I would like to express my deepest gratitude to my advisor, Prof. Olivier Bauchau, for his guidance and support. I sincerely appreciate the patience with which he answered all my questions and the unique wisdom he was always able to provide.

I would like to give special thanks to Prof. Massimo Ruzzene for his involvement in my latest project and for accepting to become my co-advisor. His insight and encouragement are greatly appreciated.

I am indebted to Dr. Serkan Ozbay for his invaluable help on several projects. This work would not have been possible otherwise. My sincere thanks go to him for his kind participation in generating some of the results contained in this thesis.

I would also like to thank the other members of my thesis committee, Profs. Dewey Hodges and Mark Costello, for their time and suggestions.

I am grateful to Prof. Jeff Jagoda as well for his advice and support.

This work was completed with support from Dr. Yogesh Mehrotra (Materials Technologies Corporation), through a Phase II Army SBIR program (Program Manager: Dr. Thomas Maier) and a Phase I NASA SBIR program (Technical Lead: Dr. Sesi Kottapalli), as well as funding from the NRTC/CRI. Their support is gratefully acknowledged.

I would like to thank all those who have helped me in my research, and in particular Drs. Sandeep Agarwal, Jielong Wang, Haiying Liu, and Alessandro Spadoni.

Finally, I would like to acknowledge the close friends I have made, many in the School of Aerospace Engineering themselves, and others around campus. Your friendship sincerely means the world to me.

But most importantly, I cannot overstate how grateful I am for the love, unlimited support and endless encouragement of my parents Brigitta and Marc, my sisters Catherine and Isabelle, and my girlfriend Callie. Their unwavering belief in me throughout my academic career pushed me to surpass my own expectations.

TABLE OF CONTENTS

LIST OF TABLES

LIST OF FIGURES

SUMMARY

Lead-lag dampers are present in most rotor systems to provide the desired level of damping for all flight conditions. These dampers are critical components of the rotor system, and the performance of semi-active Coulomb friction-based lead-lag dampers is examined for the UH-60 aircraft. The concept of adaptive damping, or "damping on demand," is discussed for both ground resonance and forward flight. The concept of selective damping is also assessed, and shown to face many challenges.

In rotorcraft flight dynamics, optimized warping twist change is a potentially enabling technology to improve overall rotorcraft performance. Research efforts in recent years have led to the application of active materials for rotorcraft blade actuation. An innovative concept is proposed wherein the typically closed section blade is cut open to create a torsionally compliant structure that acts as its own amplification device; deformation of the blade is dynamically controlled by out-of-plane warping. Full-blade warping is shown to have the potential for great design flexibility.

Recent advances in rotorcraft blade design have also focused on variable-camber airfoils, particularly concepts involving "truss-core" configurations. One promising concept is the use of hexagonal chiral lattice structures in continuously deformable helicopter blades. The static behavior of passive and active chiral networks using piezoelectric actuation strategies is investigated, including under typical aerodynamic load levels. The analysis is then extended to the dynamic response of active chiral networks in unsteady aerodynamic environments.

CHAPTER I

INTRODUCTION

1.1 Background and literature review

1.1.1 Helicopter lead-lag dampers

Many rotor systems include complex and costly lead-lag dampers designed to provide sufficient damping for all flight conditions, in particular to alleviate ground and air resonance. Hydraulic dampers, such as those used on the UH-60, present major issues associated with the presence of hydraulic fluids in the rotating system. They are complex mechanical devices that are prone to oil leaks and internal seal failures that can drastically reduce their performance. Elastomeric dampers also present several shortcomings, such as the dependence of their damping characteristics on temperature and stress cycling, or the impact of their stiffness on the rotor dynamics. In both cases, damping degradation can occur without external signs of failure, which leads to higher maintenance costs.

The hydraulic and elastomeric lead-lag dampers described in the previous paragraph are usually passive devices. Dampers are generally designed to provide sufficient damping for the most critical flight conditions, typically ground resonance and violent maneuvers. For passive devices, this damping level and the associated damping forces will then be present at all flight conditions, whether required or not. In many cases, the required level of damping in forward flight might be significantly lower than that required in ground resonance, yet, when a passive device is used, the same damping level will be present throughout the flight envelope. In forward flight, dampers will experience large 1P motions due to Coriolis and drag forces, resulting in large damper forces; since 1P motions will not lead to an instability, these large damping

forces might not be necessary, although they contribute to fatigue of the damper and connected components. This problem was recognized in the design of hydraulic lead-lag dampers. The hydraulic damper of the UH-60 helicopter, for instance, features a pressure relief valve that limits the damper force to a preset level for high stroking velocity. While such a hydraulic damper remains a passive device, it clearly features an attempt to achieve "damping on demand," *i.e.*, the tailoring of the amount of damping provided by the device to the required damping level.

The concept of "adaptive damping" or "damping on demand" takes on new dimensions when semi-active devices are used as rotorcraft lead-lag dampers. In semi-active devices, actuation is used to modify the physical characteristics of a passive element. This is to be contrasted with active devices, for which controlled actuation forces are directly applied to the system. For instance, the use of semi-active, magnetorheological fluid dampers was explored by Gandhi *et al.* (Refs. 39, 59) and Zhao *et al.* (Ref. 98). In this concept, the lead-lag damper is a hydraulic device featuring a magnetic particle laden fluid. A magnetic field is used to change the rheological properties of the fluid, thereby adjusting damping levels to meet the requirement for a specific flight condition. Further investigations, such as in Ref. 50, have included magnetorheological fluid devices in more advanced damper designs.

In this work, a different concept is investigated: Coulomb friction forces will be used to provide the required damping force. Using Coulomb friction forces in a passive device presents numerous difficulties. If the normal force acting on the frictional interface is low, sliding takes place, but according to Coulomb's law the frictional force remains small, as does the resulting energy dissipation. On the other hand, for high values of the normal force, high static frictional forces are obtained and the interface remains locked; no energy is dissipated since no relative motion is taking place. Clearly, the ability to control the normal contact force is crucial.

Friction damping is extensively used in engineering applications. Automotive

and aircraft brakes operate based on Coulomb friction forces: the kinetic energy of the vehicle is transformed into heat through the frictional process. Furthermore, semi-active brakes are in service for both aircraft and automotive applications: the anti-lock brake concept uses modulation of the normal contact force at the frictional interface to control the frictional force level, thereby preventing locking the wheels and losing control of the vehicle. Jet engine turbine blade vibrations are often damped by Coulomb friction forces (Refs. 94,95). A wedge contacting two neighboring blades creates frictional interfaces, and the centrifugal force provides the constant normal force at the interface.

Semi-active friction dampers have also been used for structural vibration control. Gaul *et al.* (Refs. 41,42,44) have developed and tested instrumented joints for optimal vibration control of space truss structures. In their concept, a piezoelectric element is used to modulate the normal force at the frictional interface of a bolted joint. A controller measures the relative motion at the joint and varies the normal force level to achieve maximum energy dissipation. Various control algorithms have been developed to perform this task, as detailed in Refs. 36,37,43. The effectiveness of this approach was experimentally validated for a large space truss structure (Ref. 40).

The proposed semi-active friction lead-lag dampers are similar to the semi-active devices discussed in the previous paragraphs, although important differences exist. The most important difference is that structural vibration control devices are designed to dissipate as much energy as possible, whereas the role of lead-lag dampers is far more complex. On the ground, the role of lead-lag dampers is to control ground resonance, a well understood mechanical instability (Ref. 32). It is critical for the device to provide enough damping to control the instability. However, if this condition is met, little vibratory energy will build up and hence, little energy dissipation capacity is required. In forward flight, lead-lag motions are driven by the blade's coupled

flap/lag/torsion dynamics and hence, dampers presenting large damping characteristics will generate undesirably high loads in the hub and blade. Lowering damping capacity and resulting loads might be desirable in this flight regime. Finally, in maneuvering flight, larger damping capacity might once more be required. The study in Ref. 1 will form the basis for the investigation of friction-based lead-lag dampers.

1.1.2 Variable twist and camber rotor blades

The development of rotor blades with controllable twist or camber through distributed actuation has been a major area of research in recent years. This concept would provide the ability to modify the airfoil twist and camber around the azimuth and along the span of the blade. Such actuation would operate without hinges and bearings, reducing the number of mechanical parts in rotor blades. The complexity of rotor hub designs could be reduced by simplifying or completely eliminating the swashplate. Additional possible advantages include performance improvement, vibration reduction, or noise control. In particular, extensive research efforts have been devoted to the application of active materials, such as piezoceramics, piezoelectric polymers and shape memory alloys (SMA), for the controlled actuation of rotorcraft blades.

Many proposed designs represent an attempt at controllable morphing through a mechanical system. Recent investigations have focused on the improvement of their design, in particular through the use of smart and active materials. Actuation systems designed to deflect elevons and trailing edge flaps, often using piezoelectric actuators, have been widely investigated (Refs. 18, 38, 53, 61, 82, 89). Other systems discussed in Refs. 19, 74 use similar smart materials to deflect leading edge control surfaces or active blade tip sections. Piezoelectric materials are preferred candidates for high-frequency on-blade actuation due to the flexibility in control provided by their rapid response to applied electric fields. In such applications, piezoelectric actuators would typically be expected to induce significant changes in the shape of the blade, with the

aim of inducing large changes in airloads. However, current piezoelectric materials are inherently constrained by limited authority because of their very small linear actuation strain/displacement capability. Therefore, amplification of the actuator output is required to achieve larger strains, and hence, the desired dynamic airfoil twist/camber deformation.

Mechanical amplification devices have been used to amplify the available piezoelectric actuation (Refs. 46,57,58,71,81). While this approach has met with some success, the performance of such actuation methods in a demanding, long-term, fielded, full-scale rotor blade environment is deemed inadequate. Their performance may be degraded by friction, free play, and aerodynamic and inertial loads. The additional complexity of the required amplification mechanisms, which involve "rigid" bodies and joints subjected to wear and clearance issues, goes against the reason for using active material actuation, *i.e.*, the development of a simple reliable actuation scheme with no moving components. Moreover, many full-scale configurations tested thus far are limited to actuating a discrete trailing or leading edge deflection system with limited authority, and thus are subject to the aerodynamic inefficiencies of a limited span application. Finally, the reduced number of degrees-of-freedom in these mechanisms only allow moderate levels of adaptibility.

In one alternative approach implementing continuous rotor blade deformation, the strain induced by embedded actuators was used to cause overall twisting of the complete rotor blade (Refs. 28, 30, 31, 69, 73, 76, 77). Again, success was limited in terms of the magnitude of the resulting blade deformation. This embedded actuator approach has the inherent limitation that relatively weak actuators are used in an attempt to deform a nominally stiff structure. Additionally, this approach requires that the actuators be structurally integrated into the blade spar thus making the in-service repair of any failed actuators very difficult.

A different approach for continuous deformation of lifting surfaces has sought to

introduce conformable airfoils in rotorcraft and fixed wing aircraft to achieve better efficiency, performance, handling qualities, as well as reduced vibrations (Refs. 54,55, 60,90,93). These studies aim at replacing slats, variable droop leading edges or flaps actuated by structural mechanisms by continuously deformable airfoils with actuation capabilities integrated into the compliant system. Some of these new concepts can be biologically inspired (Ref. 60). Methodologies for the design of compliant mechanisms have been investigated in Refs. 85,86. These methods consider the concurrent design of all aspects of a compliant mechanism: actuators and sensors are directly embedded in the system made of flexible members, and the numbers, locations and geometry of these three classes of elements are optimized simultaneously, while satisfying additional constraints such as weight, energy efficiency or performance requirements.

The concept of tensegrity has been proposed as a way to morph wings using truss-like structures which combine compressed elements with tensioned cables (Ref. 62). Such a structure integrates actuators and sensors directly into its members. Other approaches include the use of piezoelectric materials to actuate a flap-like trailing edge, through a piezoelectric plate embedded in the aft part of a foam-filled wind turbine blade (Ref. 4). Another solution involves the combined use of a truss-like Kagome active back-plane and a solid face whose deformation constitutes the desired output (Refs. 34,35). Similarly to some of the previous cases, actuators replace some of the members of the back-plane to morph the face. However, this last concept has not specifically been applied to aerospace applications.

A promising concept for the continuous deformation of an airfoil is the design of "truss-core" configurations, in which the cambering of the airfoil section is achieved by replacing typical stiffening structures such as ribs or honeycomb cores by truss-type compliant mechanisms inside the airfoil. The "Belt-Rib" concept proposed by DLR in Ref. 24 is a type of truss-core system, in which deformation is obtained by actuating a closed belt connected to a network of compliant members hosted inside

the airfoil. Other truss-core designs have been investigated in Refs. 21, 63, where discrete compliant elements are located in the aft part of an airfoil in conjunction with embedded actuators. Finally, a novel truss-core airfoil configuration as been proposed in Refs. 22, 78–80. It is based on the hexagonal chiral lattice first described in Ref. 70. In this strategy, the replication of a unit cell in a periodic fashion generates the global truss-core structure which can be used to fill the aft part of an airfoil. Since the properties of the chiral network are inherited from those of the elementary unit cell, only a small number of design variables needs to be taken into account, considerably simplifying the design and optimization processes. These novel types of structures and the study in Ref. 78 will form the basis for the development of active chiral cores for helicopter rotor blades.

1.2 Objectives

The discussion in the introductory paragraphs points out some desirable features of semi-active lead-lag dampers. First, they should be *adaptive*, in the sense that the available damping level should be adjusted as a function of flight regime. For example, high damping levels are required at take-off or landing, while lower levels would be adequate in hover or forward flight. Second, a *selective* design could enhance device performance: damping could target specific rotor modes, in contrast with passive designs that are unable to distinguish among the various modes contained in the blade response. To be more precise, it would be ideal if the damper could dissipate energy of the rotor regressive lag mode when operating in forward flight, while minimally affecting the other modes. Selectivity requires control algorithms that are aware of the level of excitation of rotor modes to target energy dissipation to the desired modes. This research effort has studied the feasibility of both control strategies.

In contrast to the current approaches for variable twist and camber rotor blades, this work will present a novel three-dimensional concept, in which the blade section

is cut open to create a torsionally compliant structure that acts as its own amplification device, and in which out-of-plane warping controls the blade deformation. This innovative concept would provide a means for dynamically changing the twist of a rotor blade, without requiring the actuator to deliver excessively high forces. This concept could be applied to trailing edge flaps, the aft section of a rotor blade behind the D-spar, or even to the full chord length of the blade. The objective of the work is to determine the feasibility of such a structure as well as some general guidelines on its design. Furthermore, this research aims at expanding currently existing analysis tools to include the effect of warping actuation on rotor blades.

Finally, an alternative innovative approach for the continuous camber deformation of rotor blades will be investigated. Chiral networks have been shown to allow large global deformations while staying within the elastic range of the material, and to provide interesting load carrying capabilities as well. Embedded actuation options will be investigated, in order to determine whether an active chiral structure can reproduce such large deflections while carrying externally applied loads such as the aerodynamic pressure on a rotor blade. Design guidelines will be determined based on some important parameters defining the geometry of the chiral structure. Various actuation strategies will be considered to optimize the output deflection. Then, the structural behavior of the active chiral network will be coupled to an unsteady aerodynamic environment to study possible aeroelastic effects, and to determine the applicability of these concepts to rotor blades evolving in complex aerodynamic environments. The ability to control the camber distribution along the span of a rotor blade using active chiral networks, through 1-per-rev and/or higher harmonic actuation strategies, may provide the solution to the practical implementation of a conformable airfoil concept.

1.3 Overview

Chapters 2 and 3 focus on the study of semi-active friction-based lead-lag dampers for improved stability of helicopters. In Chapter 2, the behavior of adaptive friction dampers is simulated in both ground resonance and forward flight for the UH-60 aircraft and compared with that of present hydraulic dampers. The simulations rely on a finite element based multibody dynamics code and the approach used for modeling the frictional process is presented in detail. The assessment of the energy dissipation characteristics of the various designs is based on an autoregressive signal analysis procedure. Results will be presented for various normal force levels to demonstrate the ability of the proposed friction devices to provide damping on demand. Next, in Chapter 3, the concept of selective damping is explored using a simplified analytical rotor model. The selective damping algorithm is shown, as well as the signal identification algorithm needed to compute the targeted regressive mode. Results are provided to show the power of this approach. However, practical implementation of this concept is shown to face many challenges.

In Chapter 4, a general description of an early 3D warping concept is first presented, highlighting the design flexibility provided by the 3D concept. Second, the theoretical background behind this concept is summarized, including the necessary modifications to the classical Vlasov beam theory to ensure the applicability of its results. Static finite element analyses were validated against the theory, and were used to investigate concentrated and distributed warping actuation schemes. Dynamic analyses were also performed to determine the effect of inertial loads, and to estimate the effect of unsteady aerodynamic loads. These studies led to a final proposed 3D warping concept based on the design guidelines that were identified earlier. Next, in Chapter 5, the finite element based codes SECTIONBUILDER and DYMORE are introduced, and the theoretical foundation is laid for extending them to include the study of beams undergoing warping actuation. The implementation of

the warping function and sectional coefficients in SECTIONBUILDER is then discussed and validated against analytical results and ABAQUS simulations. Finally, the implementation of warping degrees of freedom into the comprehensive analysis code DYMORE is presented and static and dynamic results are shown.

In Chapters 6 and 7, research efforts concerning the application of actuated chiral networks to rotor blade morphing are presented. Chapter 6 provides details on this concept, introduces chiral lattices and their properties, and mentions some basic elements on piezoelectric materials. Next, simple static analyses are presented. First, passive configurations are considered, in an attempt to increase understanding of the deformation mechanisms at work, and to determine equivalent mechanical properties. Then, simple actuation strategies are considered and compared. To finish the presentation on the static behavior of these novel designs, a rough estimate of the static aeroelastic response will be obtained based on approximate values of aerodynamic loads found on a typical UH-60 in forward flight. Chapter 7 then details the development of an aeroelastic analysis code used to study the dynamic behavior of such designs in unsteady aerodynamic environments. The theoretical foundation for static and dynamic analyses of active chiral networks is presented, as well as the unsteady aerodynamic models which are used. Details are provided on the modeling of applied piezoelectric actuation using bonded piezobenders. Validation cases are mentioned and the study of static actuation is broadened. This chapter then ends with dynamic simulations aiming at determining whether the performance of the concept can be enhanced compared to the static case. Finally, concluding remarks are offered in Chapter 8.

CHAPTER II

ADAPTIVE FRICTION-BASED LEAD-LAG DAMPERS

In this chapter, the concept of adaptive friction-based lead-lag dampers will be investigated. The feasibility of adaptive damping will be studied using a comprehensive model of the UH-60 in DYMORE, a finite-element-based multibody dynamics analysis tool. Specifically, it will be determined whether damping-on-demand can be achieved, and whether a friction-based damper could produce the loads necessary to match current damping levels from the UH-60 hydraulic dampers. Answers to these questions will be obtained in both ground resonance and forward flight conditions.

It should be noted that these studies are all conceptual in nature and do not aim to provide detailed designs. In all cases, simple friction models will be used to represent the effect of the lead-lag dampers, without much attention to the practical engineering solutions that would provide this damping. Several possibilities are detailed in Refs. 1, 14. Such semi-active dampers would require a relatively low amount of power for operation. Indeed, the actuators do not directly apply force to the structure; rather, they modulate the normal force at the frictional interface, indirectly affecting the damper's energy dissipation characteristics.

2.1 Numerical model for adaptive friction damping analysis

2.1.1 Rotor, fuselage and landing gear model

Sikorsky's UH-60 four-bladed helicopter will be used as a test bed for this analysis. The description of the physical properties of the rotor can be found in Ref. 23. The structural model involves four blades connected to the hub through blade root retention structures and lead-lag dampers. Figure 1 shows the configuration of a typical

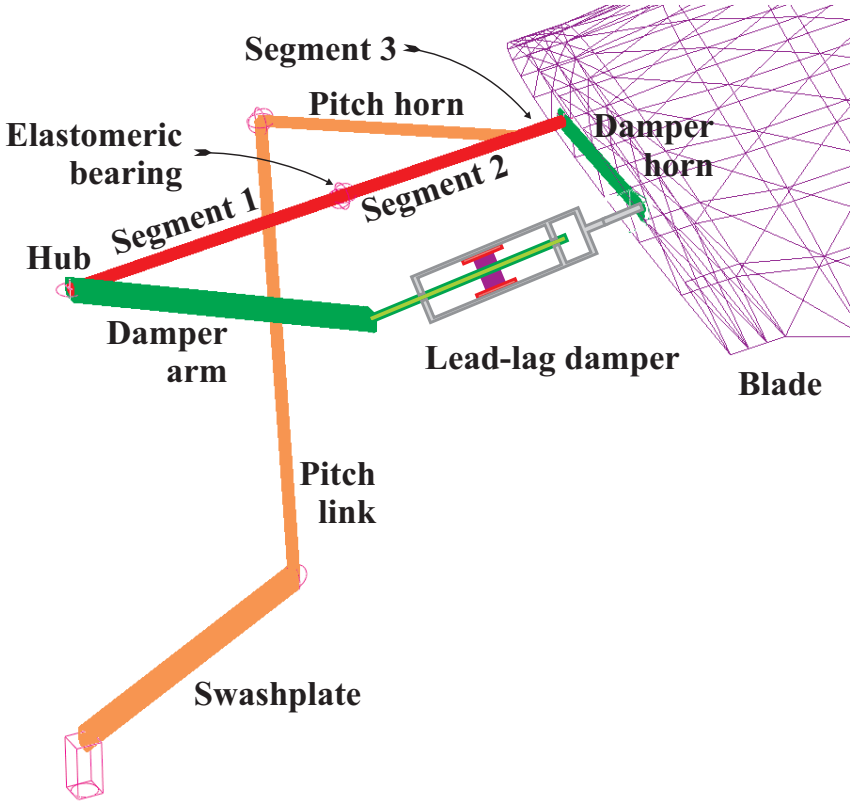

Figure 1: UH-60 rotor system with the proposed semi-active Coulomb friction lead-lag damper

blade, which was discretized by means of thirteen cubic beam finite elements using the finite element based multibody dynamics code described in Ref. 8. The root retention structure, connecting the hub to the blade, was separated into three segments labeled segment 1, 2 and 3, respectively, in Fig. 1. The first segment, modeled by one beam element, was attached to the hub. The flap, lead-lag and pitch hinges of the blade were modeled by three revolute joints connecting the first two segments of the root retention structure. The physical characteristics of the elastomeric bearing were represented by springs and dampers in the joints to model the stiffness and energy dissipation characteristics of the elastomeric material. The outer two segments, each modeled by two beam elements, were rigidly connected to each other and to the pitch horn. Finally, the outermost segment was rigidly connected to the blade and damper horn. The pitch angle of the blade was set by the following control linkages: the swashplate, pitch link, and pitch horn. The pitch link, modeled by three cubic beam elements, was attached to the rigid swashplate by means of a universal joint and to the rigid pitch horn by a spherical joint. The damper arm and damper horn were modeled as rigid bodies. The lead-lag damper was modeled as a prismatic joint; its end points were connected to the damper arm and horn. Since the kinematics of the damper are accurately modeled, all kinematic couplings between blade and damper motions are taken into account.

For forward flight simulations, the hub of the rotor model described in the previous paragraph was connected to the ground; fuselage dynamics was therefore ignored in this case. For ground resonance simulations, the same rotor model was connected to the fuselage, represented by a rigid body with appropriate mass and moment of inertia characteristics. The landing gear consists of three supporting structures: the left, right and tail gears, respectively. Each gear includes an oleo strut and tire. The oleo struts were modeled as prismatic joints connected to the fuselage center of mass and to the tires. The axis of each prismatic joint was properly aligned with the axis

of the corresponding strut, and a combination including springs and a linear dashpot was added to each prismatic joint to model the characteristics of the two-stage oleo device. The tires were modeled by a set of linear springs and dashpots connected to the ground. Each tire features three spring stiffness constants: one constant for motion in the direction perpendicular to the ground plane and two constants for motions in the ground plane. Additional information and data about the fixed system model can be found in Refs. 91, 92.

2.1.2 Friction modeling

An important aspect of the present work is the modeling of the friction dampers. From a kinematics standpoint, the damper is modeled as a prismatic joint, which allows the relative displacement, Δ, of the two sides of the joint along a prescribed direction in the material frame, $\bar{n}$. The normal force at the frictional interface is denoted f^n, a time dependent user input. The friction model described below then evaluates the magnitude of the frictional force, which is applied as equal and opposite forces on the two sides of the joint, providing full coupling between the frictional process and the system dynamic response.

According to Coulomb's law, the friction force $F^f = -\mu_k(v)\ f^n\ \text{sign}(v)$ is proportional to the magnitude of the normal force f^n, with $\mu_k(v)$ the coefficient of kinetic friction and $v = \dot{\Delta}$ the relative velocity at the prismatic joint. Both friction force and relative displacement are positive in the direction of $\bar{n}$. Sticking occurs when the relative velocity vanishes, and the friction force then satisfies $|F^f| \leq \mu_s\ f^n$, where μ_s is the static friction coefficient.

Discrete transitions between sticking and sliding cause numerical difficulties, and many authors (Refs. 26, 64, 75) have advocated the use of regularized friction laws describing both sliding and sticking behaviors such as

$$F^f = -\mu_k(v)\ f^n\ \text{sign}(v)\ (1 - e^{-|v|/v_0}), \tag{1}$$

where v_0 is a characteristic velocity usually chosen to be small compared to the maximum relative velocity encountered during the simulation. Ref. 3 compares various models with different regularization factors. However, beyond their obvious inability to treat systems with $\mu_s \neq \mu_k$, additional issues arise (Refs. 6, 12). In particular, the physical behavior of the system is altered, and the numerical computation may require very small time step sizes.

More accurate friction models have been proposed, such as the Valanis model (Ref. 87), the exponential decay model (Ref. 49), Dahl's model (Ref. 33), or the bristle model and reset integrator model of Ref. 45. In Ref. 25, Canudas de Wit *et al.* introduced the LuGre model

$$\mu = \sigma_0 z + \sigma_1 \frac{\mathrm{d}z}{\mathrm{d}t} + \sigma_2 v, \tag{2}$$

$$\frac{\mathrm{d}z}{\mathrm{d}t} = v - \frac{\sigma_0 |v|}{\mu_k + (\mu_s - \mu_k) e^{-|v/v_s|^\gamma}} \; z, \tag{3}$$

which predicts the instantaneous friction coefficient μ such that $F^f = \mu f^n$ in terms of v and the average bristle deflection z. The additional coefficients σ_0, σ_1, and σ_2 are experimentally determined parameters, v_s is the Stribeck velocity, and γ is often set equal to 2. The LuGre model has further been refined by Swevers *et al.* (Ref. 83) and Lampaert *et al.* (Ref. 56). The LuGre model has been used in conjunction with finite element based multibody formulations to solve a number of aerospace applications (Refs. 10, 13), and further details may be found in Ref. 52.

In all the simulations presented here, the dynamic friction coefficient was set to $\mu_k = 0.3$, while the static friction coefficient was chosen to be $\mu_s = 0.35$. An initial study was conducted to compare the efficacy of the LuGre model with a regularized Coulomb model in which $F^f = -\mu_k \; f^n \; \mathrm{sign}(v) \; \tanh(v/v_0)$, where the characteristic velocity was selected as $v_0 = 5 \times 10^{-6}$ ft/sec. The regularized Coulomb model was found to yield similar results, with reduced computational costs. Therefore, all further simulations discussed here use the regularized Coulomb model. To avoid numerical

difficulties during the simulations, the normal force was slowly increased from zero to its nominal value. As explained in Refs. 10, 13, time adaptivity must be used for the integration of the equations when frictional processes are present in the model. This allows time step sizes to be selected more judiciously: smaller time step sizes are used in the vicinity of the singularities stemming from the highly nonlinear friction model.

2.1.3 Stability analysis

To compare the proposed friction based dampers with present hydraulic dampers, a performance index must be defined that characterizes the energy dissipation capability of the devices. For a linear dashpot, the dashpot constant fully defines the device and its energy dissipation characteristics. However, in view of the strongly nonlinear characteristics of both hydraulic and friction devices, it is unlikely that a single number can be used to rank their respective performances. Furthermore, because the response of the rotor system is fully coupled with that of the damper, the performance of the complete system must be assessed, rather than that of the damping device *per se*. Hence, the rotor damping rate in the lead-lag mode seems to be a good measure of performance.

Typically, rotor damping rates are assessed by means of the following stability analysis procedure: first, the equations of motion of the system are linearized, second, rotor frequencies and damping rates are evaluated as the eigenvalues of the system's characteristic matrix. Such an approach is not possible here, because a phenomenon such as friction cannot be linearized. Bauchau and Wang (Refs. 15–17) have proposed a different approach to stability analysis: comprehensive rotorcraft models are used as virtual prototypes of the actual dynamical system, and the analyst runs a set of "experiments" to determine the stability characteristics of the system by means of methods that are typically used in an experimental setting. Two approaches were proposed based on closely related autoregressive and partial Floquet

formulations, respectively; the autoregressive formulation will be used in this work. Since this approach assumes the system to be linear, any nonlinearity in its response is interpreted as noise. In fact, the autoregressive method synthesizes a best fit linear approximation of the observed nonlinear response of the system. To deal with noise, the autoregressive procedure makes systematic use of the singular value decomposition. By selecting the rank of the autoregressive matrix, the user automatically eliminates from the data set the unwanted noise. Of course, selecting different rank numbers will lead to slightly different predictions of the system stability characteristics. Finally, it must be noted that it is difficult to identify the heavily damped modes of the system with this approach: indeed, the amplitudes of such modes rapidly decay, making it difficult to distinguish them from noise. More details can be found in Refs. 15–17.

2.2 Assessment of adaptive damping

2.2.1 Ground resonance analysis

The rotor/fuselage model described earlier will now be used to assess the performance of the proposed friction dampers in ground resonance. Simulations were run for rotor speeds within the range of 0 to 300 RPM. In this simplified analysis, the effects of aerodynamic forces were ignored, and all blades were set at zero pitch angle at the 3/4 radius. The structural equations were integrated using at least 256 time steps per rotor revolution; when modeling friction dampers, time adaptivity was used resulting in higher numbers of time steps. A number of revolutions were simulated until a periodic solution was obtained or an instability observed. To extract the rotor stability characteristics, a perturbation was applied to the system in the form of a lateral impulsive force of triangular shape acting at the fuselage center of mass for a duration of 0.4 sec and with a peak amplitude of 2,000 lb. This provides a suitable perturbation to excite any unstable behavior. The signals used for the

stability analysis are the vertical displacements of the left and right landing gears. A positive damping ratio, or decay rate, associated with an identified mode indicates that this mode is stable, whereas negative decay rates correspond to unstable modes.

Three cases will be contrasted. At first, simulations were run with the lead-lag dampers removed from the model; in that case, the system does present the ground resonance instability, as expected. Figure 2 shows the decay rates of the least damped mode extracted from the simulations using the autoregressive stability analysis procedure. While the rotor/fuselage system is stable without lead-lag dampers for the lowest rotor speeds, it goes into ground resonance for speeds at and above about 75 RPM. The most unstable range is for rotor speeds of 100 to 150 RPM. For each simulation, the stability analysis procedure was run for rank numbers of the autoregressive matrix r = 6, 12, 18, 24, 30, 36, 42, 48 and 54. The minimum and maximum decay rates are reported in the figure as error bars, together with the average decay rate for all rank numbers. All other figures in this section will present decay rate predictions in a similar manner. The stability analysis procedure also extracted the pitch mode of the fuselage, which is well damped at all rotor speeds. In Fig. 2, the decay rates for the regressive lag mode are indicated by circles, whereas the corresponding predictions for the fuselage pitch mode are indicated by triangles; a similar convention will be used in subsequent figures. At low rotor speeds, it is difficult to identify the regressive lag mode because it is heavily damped; hence, the corresponding data do not appear in the figure. At 100 RPM, the estimated stability characteristics exhibit a large amount of scatter. This stems from the fact that at this rotor speed, the rotor lag regressive and fuselage pitch mode frequencies are nearly coincident. In fact, in all subsequent cases, the two frequencies will be matching at around 100 RPM. Hence, it is difficult for the autoregressive algorithm to estimate the characteristics of these two modes, one stable, the other unstable. The frequencies of unstable modes extracted from the landing gear motion, *i.e.*, in the fixed system, were found to be at 7 and

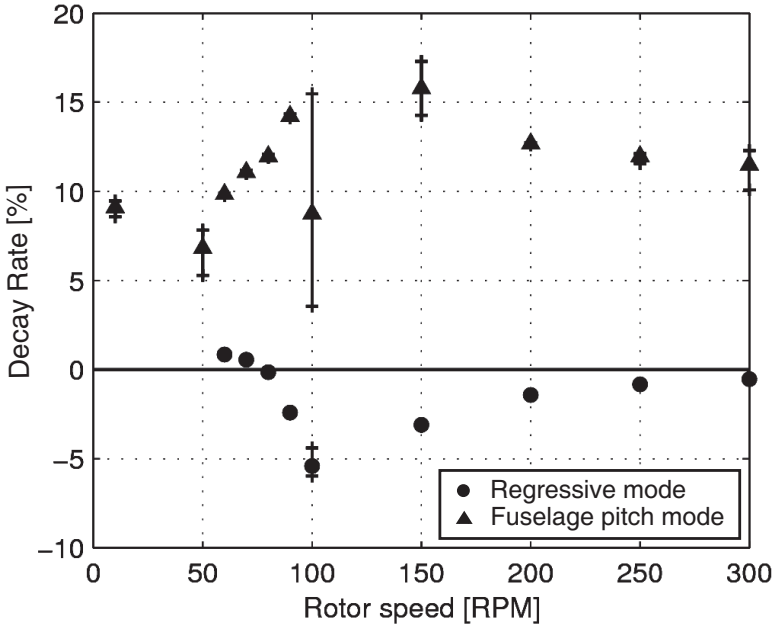

Figure 2: Decay rate for several rotor speeds, for a helicopter in ground resonance without lead-lag damper

10.8 rad/s, for rotor speeds of 100 and 150 RPM, respectively, corresponding to 10.5 and 15.7 rad/s, respectively. The corresponding frequencies extracted from the blade lag motion or the damper displacement, *i.e.*, in the rotating system, were found to be at 3.1 and 4.7 rad/s, respectively. These results are consistent since at 100 RPM, $|3.1 - 10.5| = 7.4 \approx 7$ rad/s, and at 150 RPM, $|4.7 - 15.7| = 11 \approx 10.8$ rad/s.

Next, a set of simulations was run with the hydraulic dampers in place. The actual hydraulic dampers mounted on the UH-60 helicopter were simulated using the physics based modeling approach developed by Bauchau and Liu (Ref. 11). Figure 3 shows the decay rates of the least damped mode extracted from these simulations; clearly, the hydraulic damper stabilizes the system at all rotor speeds, always providing about 12% critical decay rates. Here again, it was difficult to extract the regressive lag mode decay rate because the hydraulic damper provides ample damping to the system, thereby stabilizing the regressive lag mode. In general, it was only possible to identify the regressive lag mode when it was unstable or lightly damped.

Finally, a set of simulations was run with the proposed friction dampers in place.

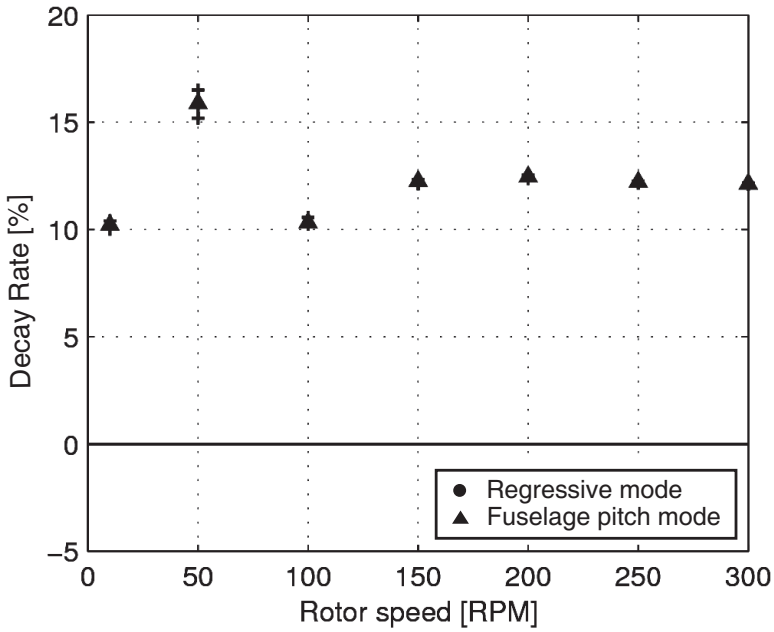

Figure 3: Decay rate for several rotor speeds, for a helicopter in ground resonance with a hydraulic lead-lag damper

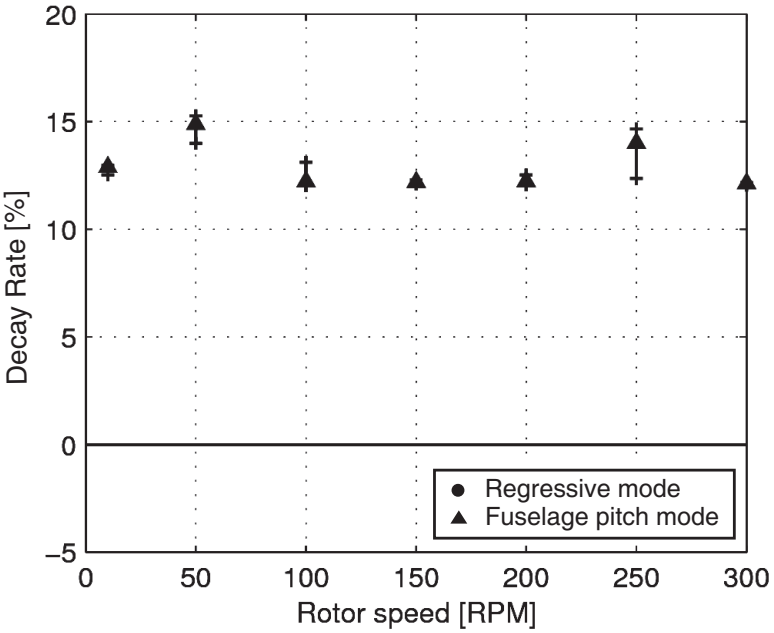

Figure 4: Decay rate for several rotor speeds, for a helicopter in ground resonance with a friction damper under a 6,000 lb normal force

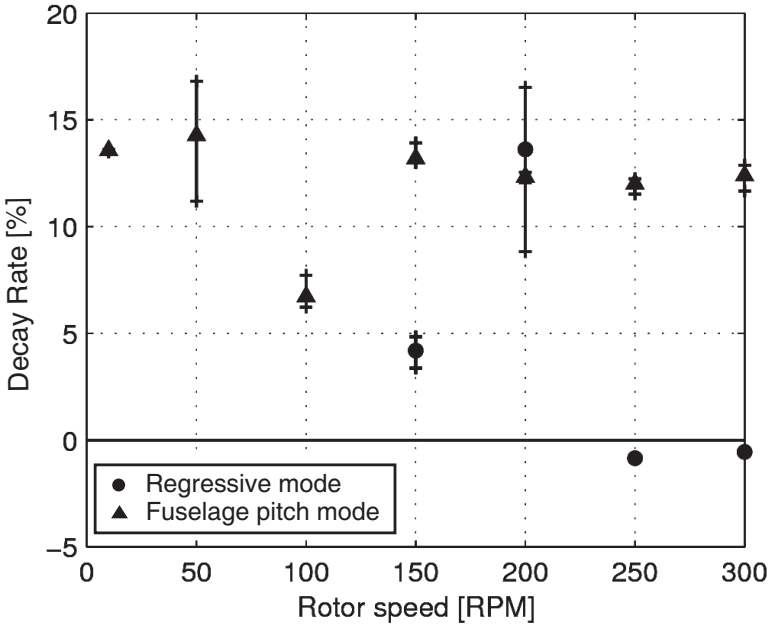

Figure 5: Decay rate for several rotor speeds, for a helicopter in ground resonance with a friction damper under a 500 lb normal force

Figures 4 and 5 show the predicted decay rates for two levels of the normal force at the frictional interface, 6,000 and 500 lb, respectively. At the 6,000 lb normal force level, the decay rate of the least damped mode is about 13%. This level of normal force totally eliminates the ground resonance instability. Hence, the friction damper provides decay rates that are comparable or better than those provided by the hydraulic device. In the case of the 500 lb normal force, the decay rates for the fuselage pitch mode are similar to those observed with the hydraulic device, but the regressive lag mode is stable only for rotor speeds up to about 200 RPM. Clearly, under a 500 lb normal force, the performance of the friction device is not sufficient to control the ground resonance.

To complete this study, a set of simulations was run at a constant rotor speed of 150 RPM, but varying the magnitude of the normal force at the frictional interface from 0 to 6,000 lb; the decay rates extracted from these simulations are shown in Fig. 6. For very low normal force levels, the friction damper controls the ground resonance instability, but stability margins are clearly insufficient. As the normal

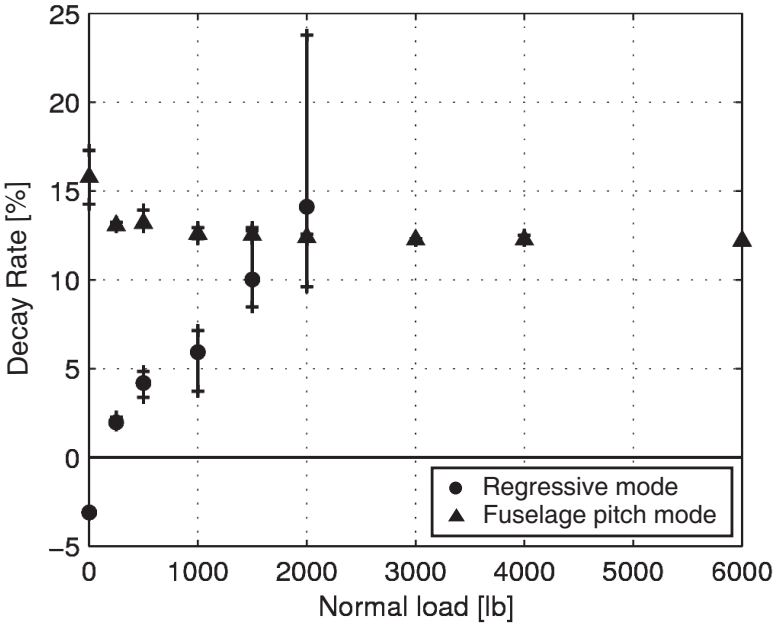

Figure 6: Decay rate for several normal force levels, for a helicopter in ground resonance with a rotor speed of 150 RPM

force level increases, the magnitude of the decay rate rapidly increases. For normal force levels larger than about 2,000 lb, the fuselage pitch mode is the least damped mode of the system. Note that the lead-lag damper has little effect on the fuselage pitch mode damping, and hence, the least damped mode of the system, the fuselage pitch mode, retains a nearly constant decay rate for all normal force levels greater than about 2,000 lb.

2.2.2 Forward flight analysis

Next, the performance of the proposed friction damper will be assessed in the forward flight regime. The model described in the above sections will be used here again, but the rotor hub is now connected to an inertial point; the rotor speed is set to its nominal speed of 258 RPM and the forward speed is 154.8 knots, corresponding to an advance ratio of $\mu = 0.36$. The aerodynamic model combines thin airfoil theory with a three-dimensional dynamic inflow model. The inflow velocities at each span-wise location were computed using the finite state induced flow model developed by

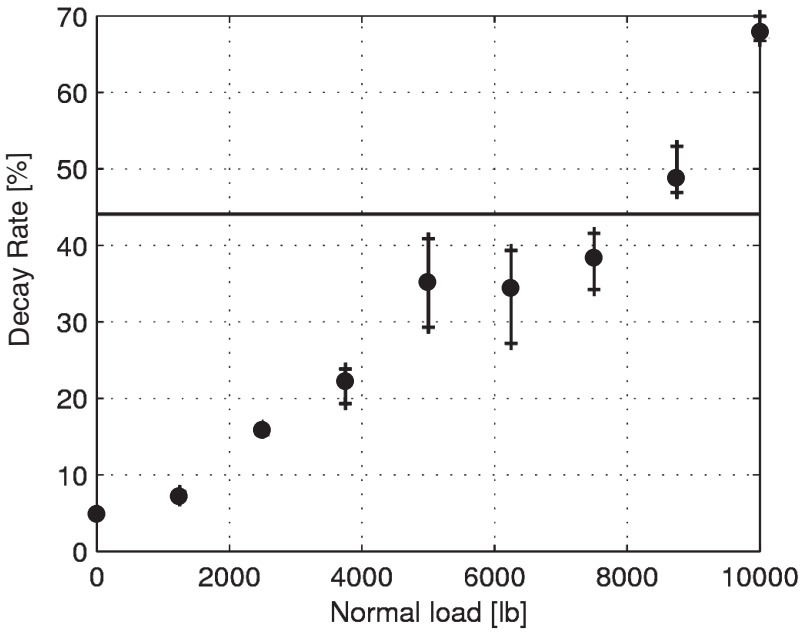

Figure 7: Evolution of the regressive decay rate with the normal load, in forward flight at 154 kt. The horizontal line indicates the decay rate obtained with the hydraulic damper

Peters *et al.* (Refs. 66, 68). The airfoil has a constant lift curve slope, $a_0 = 5.73$, drag coefficient, $c_d = 0.018$, and a vanishing moment coefficient about the quarter-chord. The number of inflow harmonics was selected as $m = 10$, corresponding to 66 aerodynamic inflow states for this problem.

Simulations were run with various normal load levels to assess the effect of the normal force on the decay rate for the undesirable regressive lag mode. In each case, the stability analysis procedure was run for rank numbers of the autoregressive matrix r = 12, 24, 36, 48, 60, 72, 84, 96, 108 and 120. For each load level, the decay rates for these different rank numbers were averaged and the minimal and maximal values were computed. Figure 7 shows that increasing the normal load level increases the regressive lag mode decay rate, as expected. Furthermore, in the range of normal loads investigated in this study, the relationship between these two quantities seems roughly linear. As in the case of the ground resonance analysis, the damping capacity of the proposed friction device can exceed that of the currently installed hydraulic

damper, for high enough levels of the normal force.

This finding is visually confirmed by observing Fig. 8, which shows the response of the lead-lag angle to an initial excitation for the hydraulic and friction dampers with three different normal load levels: 2,500, 5,000, and 10,000 lb. It is clear that the hydraulic device provides higher levels of damping than the friction device for normal force levels of 2,500 and 5,000 lb, but at the 10,000 lb level, the situation is reversed. Clearly, the proposed friction device is able to provide damping on demand by varying the normal force level. In forward flight at 154.8 knots, the rotor is stable without lead-lag dampers, although the decay rate is undesirably low. With a semi-active device, the damping level in the various flight regimes can be selected independently; in forward flight, once a desired damping level has been determined, Fig. 7 can be used to estimate the required normal force level. For passive devices, the damping level is a consequence of the physical characteristics of the damper, which have been selected to provide adequate energy dissipation characteristics in ground resonance and maneuver flights.

As shown in Fig. 8, the asymptotic average lead-lag angles as well as their wave forms are different for the hydraulic and friction dampers with various normal load levels. This underlines the fully coupled nature of the problem: damper performance is not solely a consequence of the device's physical characteristics, but also of its interaction with the dynamical system. This is also observed in the top plot of Fig. 9, which represents the damper stroke in the hydraulic damper and in the friction damper with a 5,000 lb normal force, over one period of the rotor. The other plots show the damper velocity and the damper force in both cases. It can be seen that the two responses share some similarities. In fact, comparing the force outputs of both dampers, it seems quite natural that the hydraulic damper has a slightly better decay rate than the friction damper under a 5,000 lb normal force, although they are apparently close. Also note the square waves characteristics of friction behavior. It

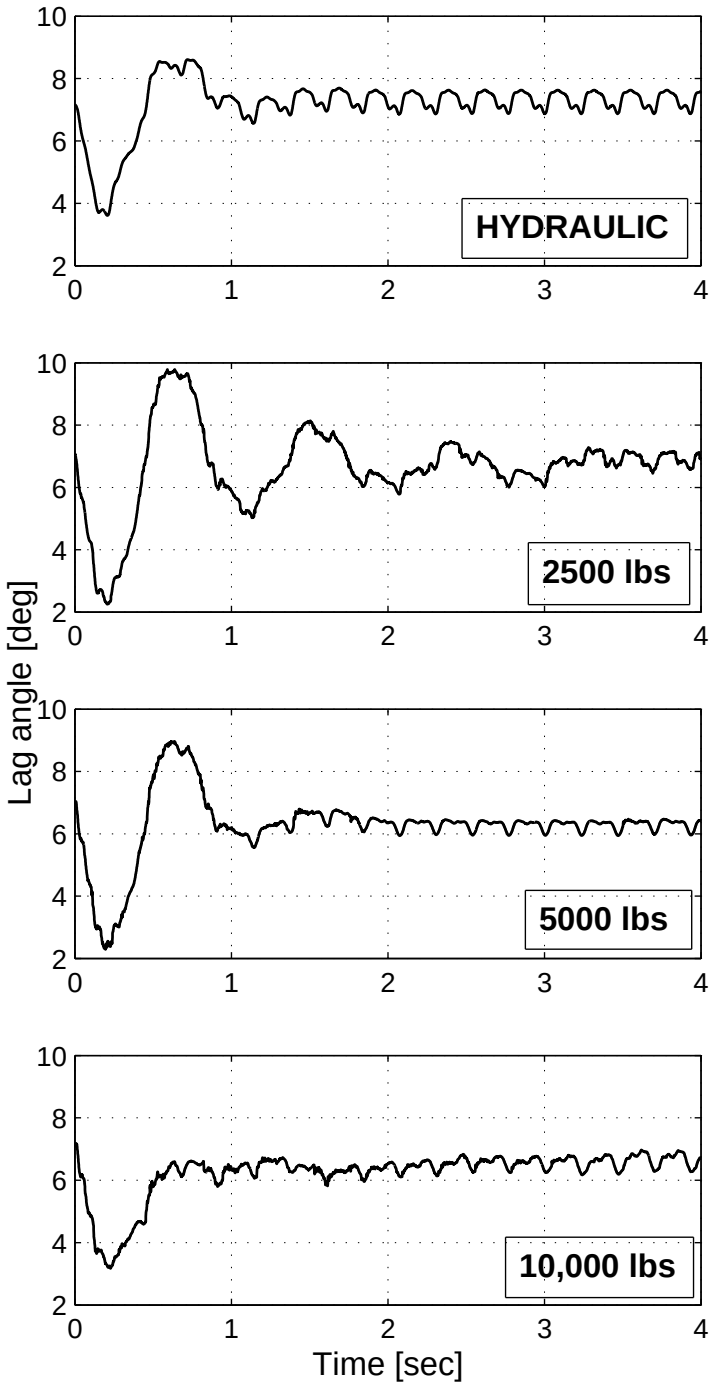

Figure 8: Time histories of the blade lag angle for several normal force levels in forward flight at 154 kt

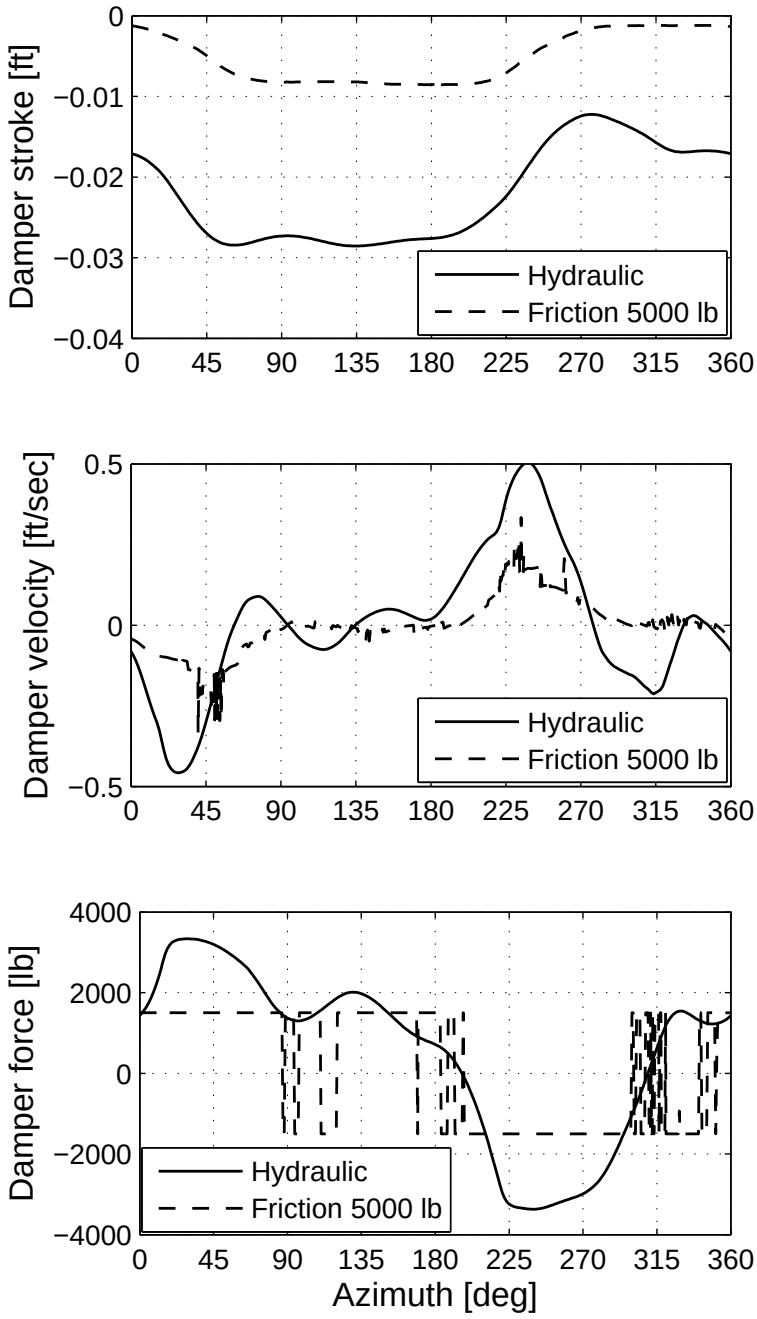

Figure 9: Comparison of the time histories of the damper stroke, the damper velocity and the damper force over one period in forward flight at 154 kt

also shows that the peak damper forces are about ±1500 lb in the friction damper, whereas those observed in the hydraulic damper are about ±3200 lb. Clearly, the friction damper reduces blade in-plane loads.

2.3 Summary

It has been shown that the proposed friction-based lead-lag damper is able to match or exceed the damping levels of the presently installed hydraulic dampers on the UH-60 aircraft, both in ground resonance and forward flight. Through identification of modal decay rates, the ability to adapt the damping level of the device was demonstrated. Damping forces can thus be lowered, in particular for flight conditions requiring lower energy dissipation levels. Blade and hub force levels are decreased, resulting in lower stress levels and potential weight savings.

CHAPTER III

APPLICATION OF SELECTIVE DAMPING TO ROTORCRAFT

Chapter 2 has focused on adaptive damping or "damping on demand." With semi-active dampers, it is possible to proceed one step further and selectively damp the component of damper stroke at a specific frequency, while minimally affecting other components. The concept of selective damping will be investigated by modifying the Coleman and Feingold model of Ref. 32 to include blade flapping at 1P. This simplified ground resonance model will be used to evaluate whether simple selective control laws are possible and practical.

3.1 Selective damping concept

3.1.1 Introduction

The stroking of a rotorcraft lead-lag damper consists of the superposition of motions at the first lag frequency, ω_ζ, and the response at all other frequencies. The former contains motions due to the stable progressive mode, the collective and differential in-plane modes, and the potentially unstable regressive in-plane mode that is targeted here, while the latter contains, in particular, the contributions at 1P, and at nP in general. The relative velocity of the damper, $v(t)$, is written as $v(t) = v_r(t) + v_o(t)$, where v_r is the relative velocity at the regressive lag frequency, whereas v_o represents all other components. Included in this latter category, is the large damper stroke rate at 1P, generated by the Coriolis forces associated with the flapping of the blade; in forward flight, this 1P component dominates the damper stroke rate. The reason for making a distinction between lag regressive and other components is clear: the

purpose of the damper is to control the potentially unstable regressive lag mode. Passive dampers will generate damping forces that depend, in general, on the device's stroke and stroke rate across the entire frequency spectrum, and consequently, they apply large damping forces in response to large 1P stroke rates. These large forces are not necessary since the inherently stable 1P motion does not need damping, and yet, are applied to the blade and hub, in turn creating large stresses and potential fatigue problems. The concept of selective damping can now be defined more precisely for rotorcraft problems: can a semi-active damper be used to selectively damp the regressive lag mode of the blade while minimally affecting the other modes?

3.1.2 Selective damping algorithm

To assess the concept of selectivity, a semi-active friction damper will be considered. It is assumed that a controller adjusts the normal force at the friction interface to be proportional to the relative velocity, *i.e.*, $f^n = (f^n_{\text{ref}}/v_{\text{ref}})\,|v|$, where f^n_{ref} and v_{ref} are reference values of the normal force and relative velocity, respectively. The friction force becomes $F^f = -c_{\text{ref}} v$, where $c_{\text{ref}} = \mu(f^n_{\text{ref}}/v_{\text{ref}})$. If the maximum normal force can be modulated in time, the friction force becomes $F^f = -c(t)v$, where $0 \leq c(t) \leq c_{\max}$: the friction damper behaves like a viscous damper with an adjustable dashpot constant. Note that a similar effect could be obtained with magnetorheological dampers (Ref. 98), or with hydraulic dampers featuring controllable flow valves, although in both cases, some level of nonlinearity would be typically observed. The present controller makes the damper behave like a viscous damper, but other strategies are possible, such as a full normal force strategy (bang-bang controller). However, this strategy creates undesirable impulsive forces and simulations also showed selective damping to be ineffective in this case. In view of the exploratory nature of this study, the simple model described above will be used. Note that if the device is passive, *i.e.*, if $c(t) = c$, the damper becomes a simple, linear viscous damper.

The work done by the damper force between two arbitrary times, t_i and $t_f > t_i$, is

$$W^{t_i \to t_f} = \int_{t_i}^{t_f} F^f v \, \mathrm{d}t = -\int_{t_i}^{t_f} c(t) v^2 \, \mathrm{d}t \leq 0. \tag{4}$$

This work is necessarily negative, as expected in view of the dissipative nature of the device. Next, the work done by the damper force on the regressive lag component of the relative velocity during the same period is

$$W_r^{t_i \to t_f} = \int_{t_i}^{t_f} F^f v_r \, \mathrm{d}t = -\int_{t_i}^{t_f} c(t) v v_r \, \mathrm{d}t \lessgtr 0. \tag{5}$$

It is important to note that the instantaneous work done by the friction force on the regressive lag component can be negative, positive, or even zero, because the product vv_r can be negative, positive, or zero. Even a passive device, for which $c(t) = c$, could instantaneously add energy to the regressive lag mode, although the device is instantaneously dissipative, as implied by Eq. (4). This observation clearly underlines the fact that passive devices are not ideally suited to the targeted damping of a specific component of the stroke rate. On the other hand, the same observation suggests a strategy for selective damping, when a semi-active device is available. If $vv_r > 0$, the damper extracts energy from the regressive lag mode, whereas if $vv_r < 0$, the damper adds energy to the same mode. The following selective strategy is proposed: if $vv_r > 0$, select $c = c_{\max}$ to maximize energy dissipation of the regressive lag mode, while possible, whereas if $vv_r < 0$, select $c = 0$ to avoid adding any energy to the targeted mode. This approach will maximize energy dissipation of the targeted mode.

3.2 Assessment of selectivity

3.2.1 Model problem

The concept of selectivity will be tested within the framework of the ground resonance analysis developed by Coleman and Feingold (Ref. 32). Their model was modified to include the blades' flapping motion in addition to the lead-lag motion, as shown in

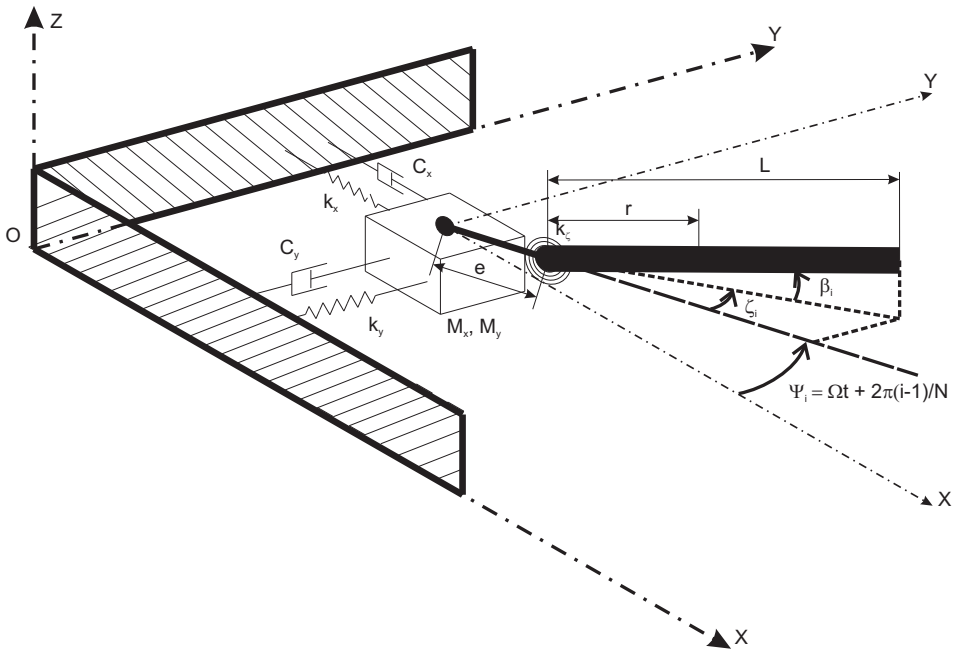

Figure 10: Model problem for ground resonance analysis (only one blade is included in this figure for clarity)

Fig. 10. Only one blade is included in the figure for clarity. The flapping degrees-of-freedom β_i influence the lead-lag degrees-of-freedom ζ_i through the Coriolis coupling term. The presence of a flapping motion is representative of slope landing for example. The rotor of radius R consists of $N = 4$ identical rigid blades of mass m and length L connected to the hub by means of offset lag hinges a distance e away from the hub. Ω is the rotor angular speed, and ψ_i denotes the azimuthal position of the i^{th} blade. q_x and q_y represent the hub deflections in the x- and y-directions. A semi-active friction damper is located in each hinge; Q_i denotes the friction moment applied to the i^{th} blade. The hub is represented by a concentrated mass, of effective masses M_x and M_y for deflections in the x- and y-directions as detailed in Ref. 32, and is connected to the ground by springs k_x and k_y, and linear dashpots c_x and c_y, along two orthogonal directions. All the model parameters can be found in Table 1.

Table 1: System parameters for the ground resonance analysis, from Ref. 98

Number of blades	4
Rotor radius	18.5 ft
Rotor speed	240 RPM
Blade mass	6.5 slug
Blade mass moment	65 slug·ft
Blade mass moment of inertia	800 slug·ft^2
Lag hinge offset	1 ft
Lag spring constant	0 ft·lb/rad
Hub mass in x-direction	550 slug
Hub mass in y-direction	225 slug
Hub spring constant in x-direction	85000 lb/ft
Hub spring constant in y-direction	85000 lb/ft
Hub damping constant in x-direction	2100 lb/ft·s
Hub damping constant in y-direction	1050 lb/ft·s

The i^{th} blade flap angle is decomposed into constant and time-varying components $\beta_i = \beta_0 + \beta_{1,i}$. Assuming small angles and neglecting higher-order terms, the non-dimensional, linearized equations describing the motion of the hub are

$$\bar{q}_x^{**} + \bar{c}_x \bar{q}_x^{*} + \bar{\omega}_x^2 \bar{q}_x - \bar{S}_x \sum_{i=1}^{N} (\zeta_i \sin\psi_i)^{**} = \bar{S}_x \beta_0 \sum_{i=1}^{N} (\beta_{1,i} \cos\psi_i)^{**}, \tag{6}$$

$$\bar{q}_y^{**} + \bar{c}_y \bar{q}_y^{*} + \bar{\omega}_y^2 \bar{q}_y + \bar{S}_y \sum_{i=1}^{N} (\zeta_i \cos\psi_i)^{**} = \bar{S}_y \beta_0 \sum_{i=1}^{N} (\beta_{1,i} \sin\psi_i)^{**}, \tag{7}$$

while the motion of each of the $N = 4$ blades is described by

$$\zeta_i^{**} + \bar{\nu}_\zeta^2 \zeta_i - \bar{S} \bar{q}_x^{**} \sin\psi_i + \bar{S} \bar{q}_y^{**} \cos\psi_i = 2\beta_0 \beta_{1,i}^{*} + \bar{Q}_i, \tag{8}$$

where the notation $(\cdot)^*$ indicates a derivative with respect to the non-dimensional time $\Psi = \Omega t$, $\bar{q}_x = q_x/R$ and $\bar{q}_y = q_y/R$ are non-dimensional hub deflections, $\bar{\omega}_x = \sqrt{k_x/(M_x + Nm)\Omega^2}$, $\bar{\omega}_y = \sqrt{k_y/(M_y + Nm)\Omega^2}$ and $\bar{\nu}_\zeta = \sqrt{Se/I}$ are non-dimensional frequency parameters, $\bar{c}_x = c_x/(M_x + Nm)\Omega$ and $\bar{c}_y = c_y/(M_y + Nm)\Omega$ are non-dimensional damping parameters, $\bar{S}_x = S/R(M_x + Nm)$, $\bar{S}_y = S/R(M_y + Nm)$ and $\bar{S} = SR/I$ are non-dimensional coupling parameters for which $I = \int_0^L r^2 \mathrm{d}m$ and $S = \int_0^L r \mathrm{d}m$, and finally $\bar{Q}_i = Q_i/I\Omega^2$ is the non-dimensional lead-lag damper moment applied to the i^{th} blade. Details of this derivation can be found in Appendix A.

To introduce a 1P component into the lag motion, a sinusoidal flap motion of the blade was prescribed at the 1P frequency, $\beta_i = \beta_0 + \beta_1 \sin\psi_i$, where $\beta_0 = 15°$ and $\beta_1 = 7°$, finally leading to the following equations of motion

$$\bar{q}_x^{**} + \bar{c}_x \bar{q}_x^{*} + \bar{\omega}_x^2 \bar{q}_x - \bar{S}_x \sum_{i=1}^{N} (\zeta_i \sin\psi_i)^{**} = 0, \tag{9}$$

$$\bar{q}_y^{**} + \bar{c}_y \bar{q}_y^{*} + \bar{\omega}_y^2 \bar{q}_y + \bar{S}_y \sum_{i=1}^{N} (\zeta_i \cos\psi_i)^{**} = 0, \tag{10}$$

$$\zeta_i^{**} + \bar{\nu}_\zeta^2 \zeta_i - \bar{S}\bar{q}_x^{**} \sin\psi_i + \bar{S}\bar{q}_y^{**} \cos\psi_i = 2\beta_0\beta_1 \cos\psi_i + \bar{Q}_i. \tag{11}$$

Hence, the total lead-lag response contains a 1P contribution, a regressive component, and several other modes. A relatively high value of the coning angle β_0 was chosen to ensure the presence of a large enough 1P contribution, so as to better exhibit the identification and stabilization of the lag regressive component that might potentially be small compared to the dominant (but stable) 1P component. The smaller the amplitude of the 1P motion, the easier one would expect the identification of the lag regressive part to be; hence, a more demanding case is being considered here.

Using the multi-blade coordinate transformation, the lead-lag angle, ζ_i, $i = 1$, 2, 3, 4, of each blade can be written as

$$\zeta_i = \zeta_0 + \zeta_s \sin\psi_i + \zeta_c \cos\psi_i + (-1)^i \zeta_d, \tag{12}$$

where ζ_0, ζ_s, ζ_c, ζ_d are functions of the non-dimensional time $\Psi = \Omega t$. It will be convenient to introduce the following notation for the cyclic component of the lead-lag angle, $\zeta_{y,i} = \zeta_s \sin\psi_i + \zeta_c \cos\psi_i$, and the non-dimensional time derivative of the blade lead-lag angle becomes

$$\zeta_i^{*} = \zeta_0^{*} + \zeta_{y,i}^{*} + (-1)^i \zeta_d^{*}. \tag{13}$$

It is now possible to describe the proposed selective damping algorithm for the model problem at hand. The damper friction moment for the i^{th} blade has the

following form $M_i^f = -p(t)\zeta_i^*(t)$, where $p(t) = c(t)d^2\Omega$ and d is the distance from the center of the lag hinge to the lead-lag damper axis. The selective damping control algorithm now becomes

$$p(t) = \begin{cases} p_{\max}, & \text{if} \quad \zeta_i^*\zeta_{i,r}^* > 0, \\ 0, & \text{if} \quad \zeta_i^*\zeta_{i,r}^* < 0, \end{cases} \tag{14}$$

where $\zeta_{i,r}^*$ is the regressive lag component of the velocity signal for the i^{th} blade.

3.2.2 Identification algorithm

To implement the proposed selective damping algorithm, it is necessary to accurately estimate the regressive velocity, $\zeta_{i,r}^*$, since the sign of this quantity dictates the switching strategy, see Eq. (14). At first, the cyclic components of the angular velocities are obtained from Eq. (13) as

$$\zeta_{y,1}^* = \frac{\zeta_1^* - \zeta_3^*}{2}, \quad \zeta_{y,2}^* = \frac{\zeta_2^* - \zeta_4^*}{2}, \quad \zeta_{y,3}^* = -\frac{\zeta_1^* - \zeta_3^*}{2}, \quad \zeta_{y,4}^* = -\frac{\zeta_2^* - \zeta_4^*}{2}. \tag{15}$$

Next, for a given azimuth angle Ψ, estimates of the Fourier components of the regressive velocity are found as follows

$$\bar{A}_{c,i}(\Psi) = \frac{\hat{\omega}_\zeta}{\pi} \int_{\Psi - 2\pi/\hat{\omega}_\zeta}^{\Psi} \zeta_{y,i}^* \cos \hat{\omega}_\zeta \psi \, \mathrm{d}\psi, \tag{16a}$$

$$\bar{A}_{s,i}(\Psi) = \frac{\hat{\omega}_\zeta}{\pi} \int_{\Psi - 2\pi/\hat{\omega}_\zeta}^{\Psi} \zeta_{y,i}^* \sin \hat{\omega}_\zeta \psi \, \mathrm{d}\psi, \tag{16b}$$

where $\hat{\omega}_\zeta = \omega_\zeta/\Omega$ is an estimate of the regressive lag frequency identified by Fourier analysis. Finally, the estimated regressive velocity for the i^{th} blade becomes

$$\bar{\zeta}_{i,r}^*(\Psi) = \bar{A}_{c,i}(\Psi) \cos \hat{\omega}_\zeta \Psi + \bar{A}_{s,i}(\Psi) \sin \hat{\omega}_\zeta \Psi. \tag{17}$$

This estimate will be used in the proposed selective damping algorithm, Eq. (14), instead of the unknown, actual regressive velocity of the i^{th} blade, $\zeta_{i,r}^*$.

3.2.3 Simulations and results

At first, consider the case of a passive damper characterized by a friction moment $M_i^f = -p\zeta_i^*(t)$, where p is a constant. It is well known that if too little damping is available, the system becomes unstable due to the ground resonance phenomenon. Let $p_{\rm cr}$ be the minimum constant required to stabilize the system. The non-dimensional damping constant, $\eta = p/p_{\rm cr}$, is introduced: for $\eta = 1$, the system is neutrally stable, for $\eta < 1$, the system is unstable, and for $\eta > 1$, it is stable.

Next, simulations were performed with the semi-active friction damper controlled by the proposed selective damping algorithm, Eq. (14), using the estimated regressive velocity, Eq. (17). Simulations were run for non-dimensional damping constants $\eta =$ 0.75, 0.85, 1.15 and 2.0; in each case, the performance of passive and semi-active dampers was contrasted. For the passive dampers, $\eta = p/p_{\rm cr}$, where p is the dashpot constant of the device, whereas for semi-active dampers, $\eta = p_{\rm max}/p_{\rm cr}$, where $p_{\rm max}$ is defined in Eq. (14). Figure 11 shows the results of the simulations for the four η values: the lateral displacement q_y of the hub, non-dimensionalized by the rotor radius R, is shown as a function of the non-dimensional time Ψ for both passive and semi-active devices. When $\eta = 0.75$, the system is unstable with the passive damper, as expected; the system is also unstable with the semi-active device, although with a lower growth rate. For $\eta = 0.85$, the system is still unstable with the passive damper, as expected; however, the selective damping approach is able to stabilize the system. This simulation clearly demonstrates the advantage of selective damping: the system can be stabilized by targeting the damping to the unstable mode. By trial and error, it was determined that the selective damping algorithm is able to stabilize the system for non-dimensional damping constants $\eta \gtrsim 0.76$.

Next, Fig. 11 shows the simulation results for the case of $\eta = 1.15$. In this case, the passive damper is able to stabilize the system, although the selective damper shows better performance. Finally, the last plot of Fig. 11 compares the two dampers

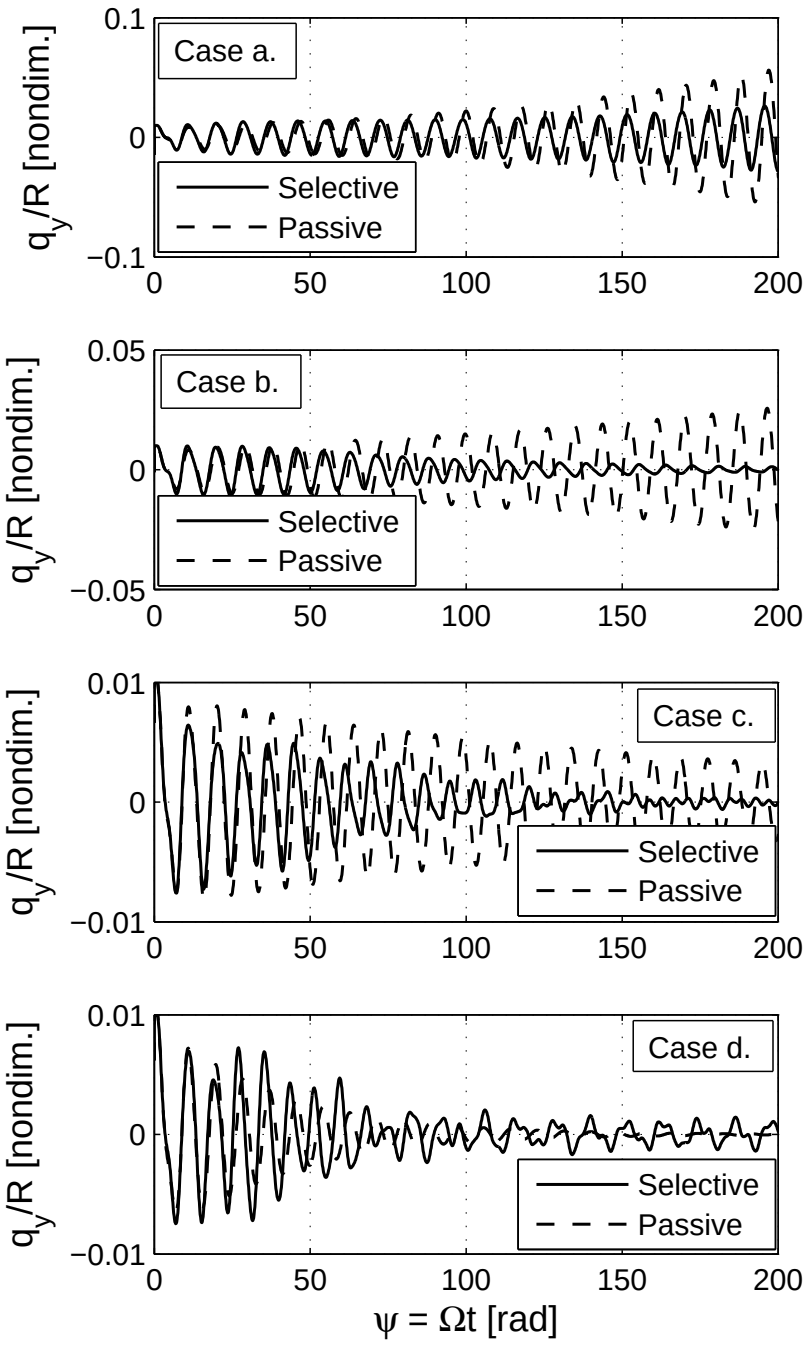

Figure 11: Lateral motion of the fuselage as a function of time in ground resonance. Four values of the damping ratio are presented: (a) $\eta = 0.75$; (b) $\eta = 0.85$; (c) $\eta = 1.15$; (d) $\eta = 2$

for $\eta = 2.0$: here again, the two devices are able to stabilize the system and feature similar decay rates. Unfortunately, these two last plots also reveal a disturbing trend associated with the selective damper: while system response rapidly decays, residual oscillations of small amplitude, akin to a limit cycle oscillation, cannot be eliminated. This phenomenon is not observed for the passive damper. The presence of residual oscillations is easily explained: as the selective algorithm quickly controls the instability, the amplitude of the regressive lag mode rapidly decays and becomes much smaller than the 1P component of the lead-lag signal. In effect, the regressive lag component becomes noise compared to the 1P signal, and the estimated regressive velocity, Eq. (17), becomes increasingly inaccurate. In the presence of this inaccurate estimate of the regressive velocity, the selective algorithm, Eq. (14), is no longer capable of properly targeting the regressive lag mode and loses its effectiveness. These observations are consistent with the fact that the selective control law is only meaningful when a significant regressive lag component is present.

A logical solution to this problem is to transition from selective to passive damping strategies once the average regressive lag vibration amplitude falls below a given threshold. Figure 12 compares the performance of the selective damper without and with thresholds: clearly, the latter approach eliminates unwanted residual vibrations.

Figure 13 compares the passive and selective devices in terms of the energy dissipation of the damper, for $\eta = 1.30$. In both cases, the total work done by the damper is monotonically decreasing, which is consistent with the property that a damper can only extract energy from the system. However, the total work done over a given time interval is larger in the passive case. Indeed, the system response is larger in that case, as the plots in the bottom part of Fig. 13 show, and moreover, the damper is always on. The work done on the regressive lag component in both cases can also be compared. It should be stressed that this quantity is computed using the identified regressive lag component. The advantage of using selectivity becomes apparent here:

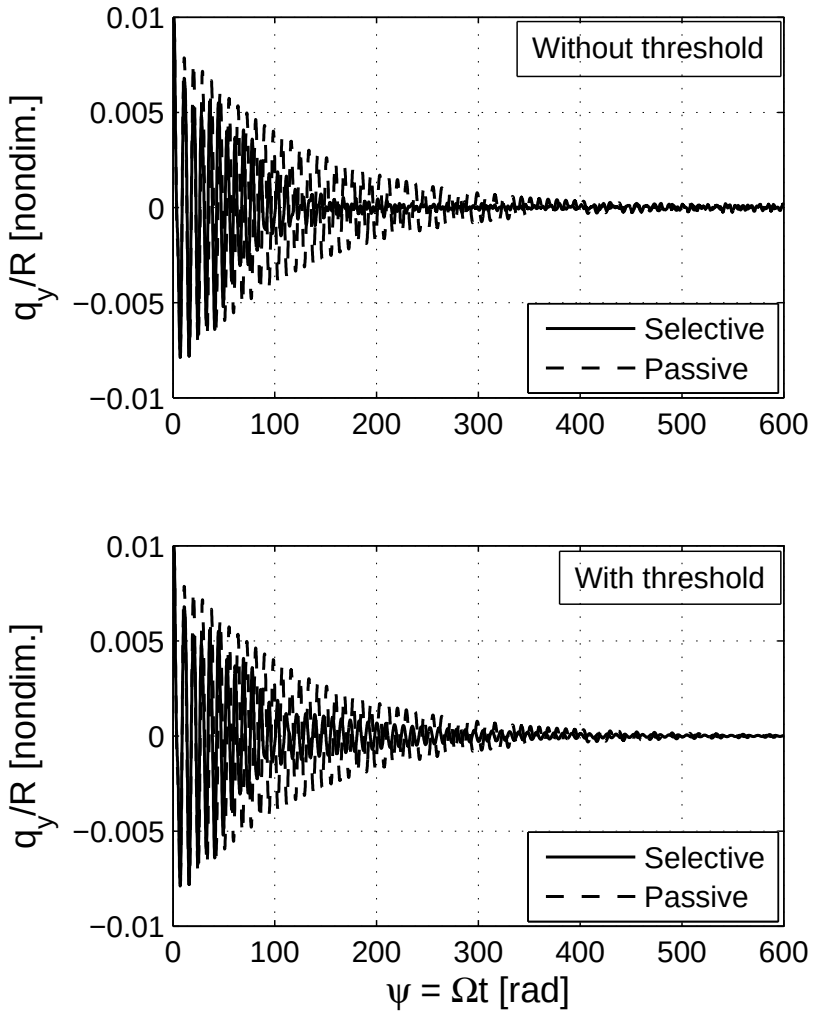

Figure 12: Lateral motion of the fuselage as a function of time in ground resonance, with and without threshold, for a damping ratio $\eta = 1.25$

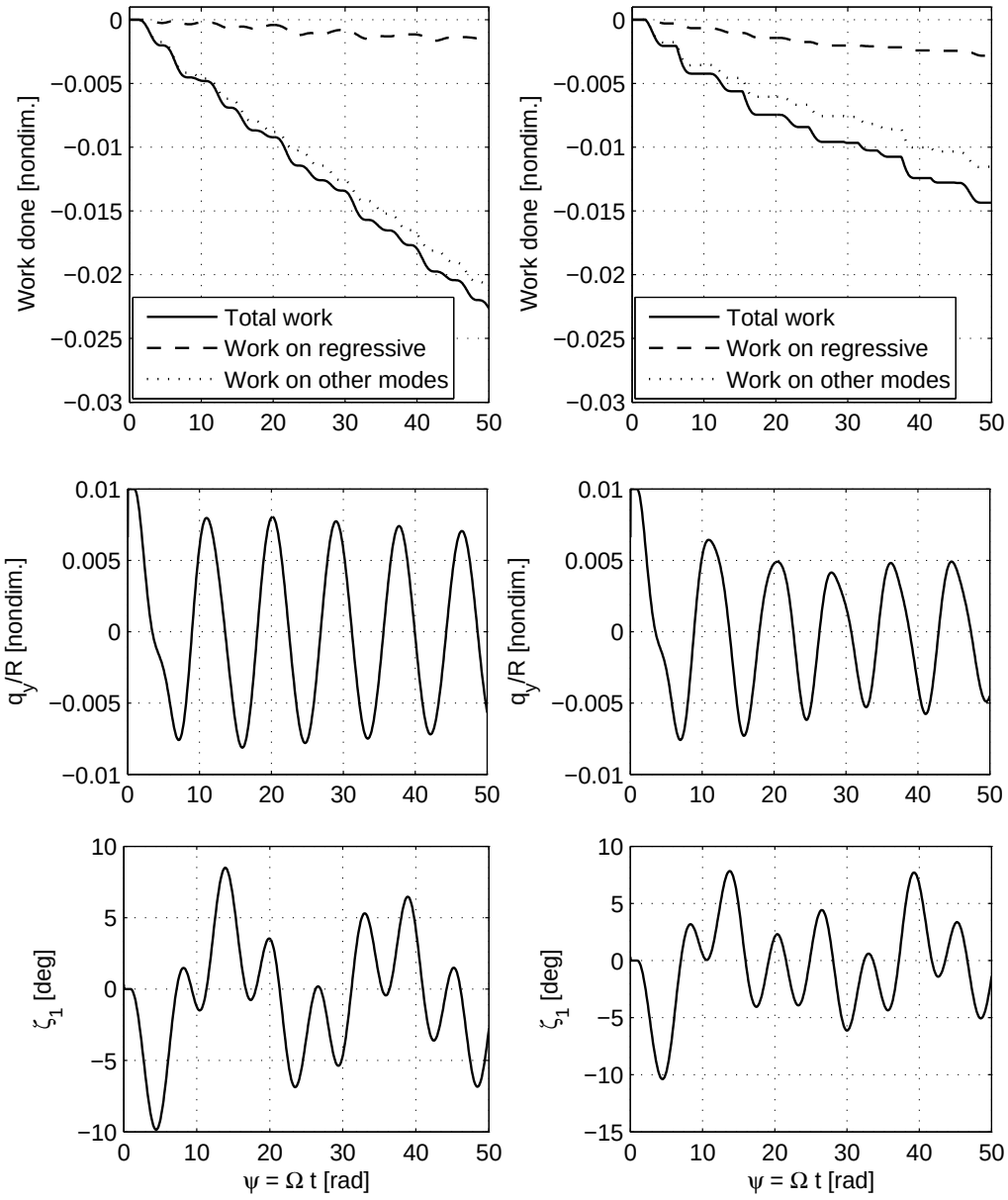

Figure 13: Total work done by the damper, work done on the regressive component and work done on the other components in ground resonance, as well as lateral displacement and first blade's lead-lag angle, for $\eta = 1.30$. Passive case: left part; selective case: right part. See next figure for a more detailed view of the work done by the regressive lag component

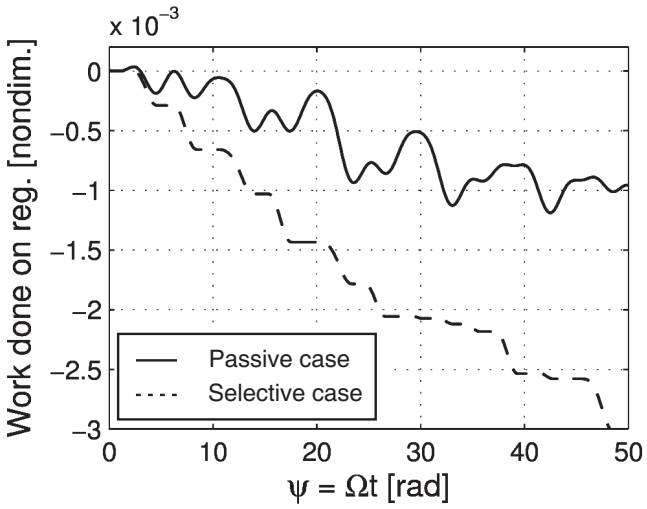

Figure 14: Work done on the regressive component in ground resonance

in the semi-active case, the work done on the regressive lag component decreases monotonically, whereas in the passive device, the instantaneous power on the regressive lag component can be positive, implying that energy is in fact transferred to the regressive lag component. Consequently, it can be observed that the work done on the regressive lag component over a given period of time is larger in the selective case, leading to a better damping out of the instability. This is clearly shown in Fig. 14, which represents the work done on the regressive lag component in more detail.

Finally, simulations have been run that reveal some of the drawbacks to the use of selectivity: indeed, for the selective law to work correctly, the regressive lag component used in the control law needs to be properly identified. This is visually demonstrated in Fig. 15, which shows the lateral motion of the fuselage in the passive and selective cases, the latter being this time performed with an error introduced intentionally in the frequency identification: the identified regressive lag frequency used in the control law was set to a value lower than that obtained through Fourier analysis by 2.5%, to simulate the unavoidable error inherent to any identification algorithm. It clearly shows that the passively stable system can be destabilized through an inappropriate control schedule.

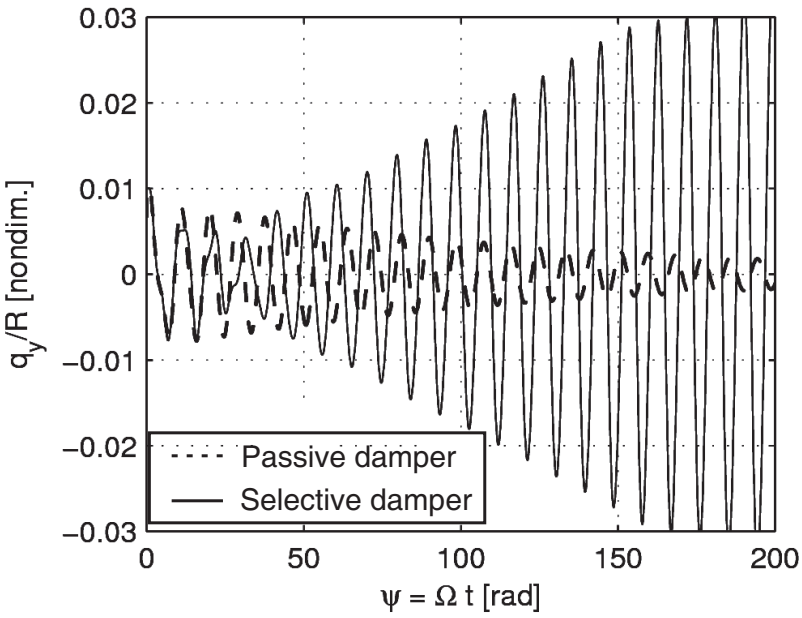

Figure 15: Lateral motion of the fuselage as a function of time in ground resonance. An erroneous value of the estimated regressive frequency was used

3.3 Summary

It has been demonstrated that a simple algorithm for selective damping can be very effective. In fact, when using selectivity, it is possible to stabilize a system that would be unstable when using a passive damper of identical dashpot constant. On the other hand, selective damping also presents serious drawbacks. First, as the available damping of the device increases, the advantage of selectivity decreases. For fail safe design considerations, semi-active devices are likely to be built with $\eta > 1.0$ to ensure system stability in the case of controller or actuator failure. Hence, it is unlikely that selective damping will lead to dramatic performance improvements. Second, because the aperiodic regressive lag mode is targeted for damping, the selective damper actuation is itself aperiodic; this will result in unwanted 1P fixed system vibrations. Third, the accurate identification of the regressive lag component is indispensable. Finally, the actuation associated with selective damping is more complex than that required for adaptive damping. Whereas adaptive damping calls for slow actuation, typically

varying with flight condition only, selective damping requires a more complex, faster actuation schedule.

CHAPTER IV

WARPING-BASED VARIABLE-TWIST HELICOPTER BLADES

In a radical departure from the current approaches for camber control, a unique concept is proposed in which the typically closed rotor blade section is cut open to create a torsionally compliant structure. The deformation of the blade is controlled by out-of-plane warping resulting in three-dimensional morphing. The integration, along the length of such a slender beam, of a moderate twist rate created through warping actuation translates into a sizeable rotation of the tip cross-section. In other words, the rotor blade acts as its own amplification device.

To illustrate this innovative concept, Fig. 16 depicts a modified rotor blade in which the front D-spar is kept essentially intact, compared to current blade designs, while the aft part is converted into a torsionally compliant open section susceptible to out-of-plane cross-sectional warping. The aft section is cut to allow for relative axial displacement. By actuating one side of the cut relative to the other, out-of-plane warping is induced in the section, resulting in significant twisting; this is the reciprocal effect of out-of-plane warping in a beam under torsional loading. In view of the low torsional stiffness of open sections, little actuation effort is required to warp the section.

As shown in Fig. 17, the aft section essentially becomes a flap spanning up to about 75% of the chord length, and extending over the entire length of the blade. Other design options include shorter flap lengths, as well as limited span flaps along the length of the blade. However, the 75% of chord flap design extending over the full span of the blade, as illustrated in Fig. 17, will be the main focus of this chapter. The larger

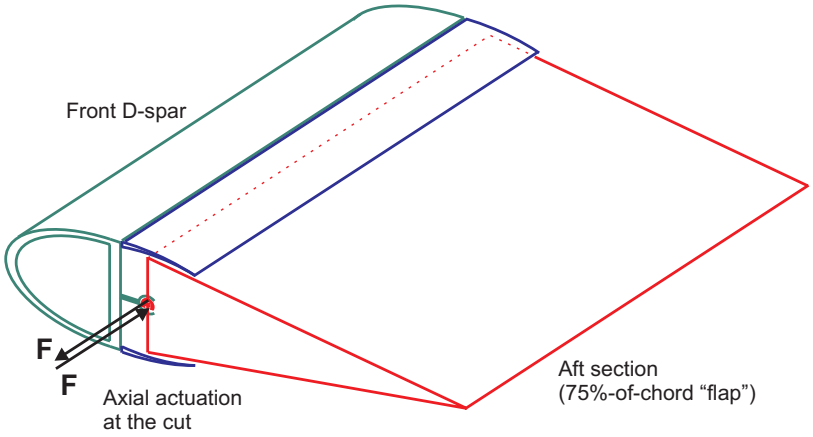

Figure 16: Warping actuation concept

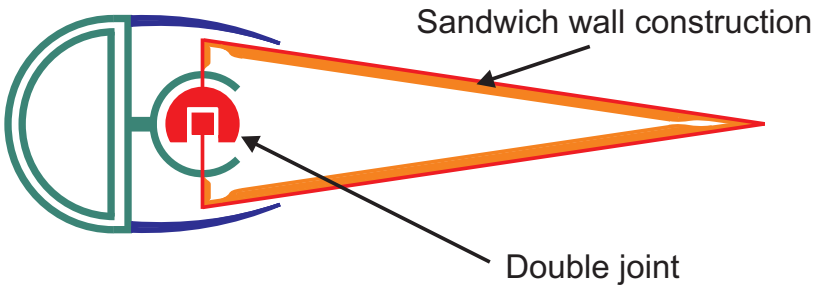

Figure 17: Cross-section of morphing blade

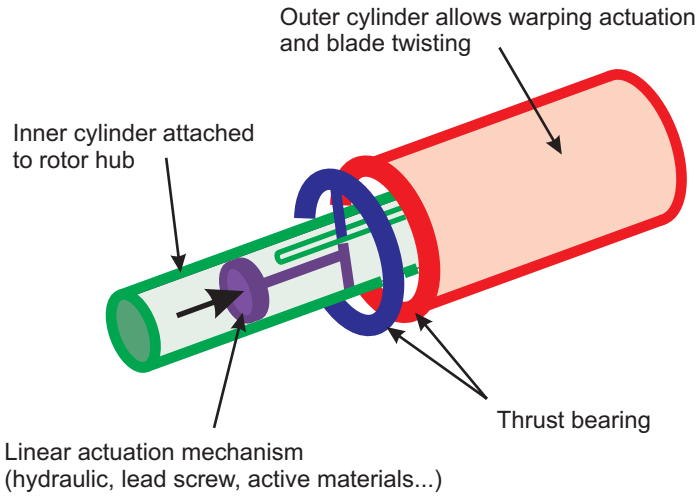

Figure 18: Double joint design

flap size results in larger camber deformation for a given cross-section, while extending the deformable section over the full rotor blade generates large tip rotation. Cyclic control could be provided through warping actuation of such a structure, thereby eliminating the need for swashplates. Additionally, aerodynamic losses related to end effects on a limited span flap would be reduced.

To allow for relative motion between the upper and lower skin, the typical honeycomb core found in rotor blades must be redesigned. As shown in Fig. 17, a sandwich wall construction could replace the honeycomb core by providing similar stiffening effects.

For this concept to work, the aft portion of the blade must be able to rotate as a rigid body. Indeed, in-plane warping of the cross-section due to shell bending deformations in the blade's walls should be avoided for a successful design. Therefore, the axis of rotation of the aft section must be collocated with the line of action of axial actuation. Such a double joint design is graphically illustrated in Fig. 17, and Fig. 18 provides a possible practical implementation of such a joint. This joint simultaneously allows blade twisting about its axis, and axial warping actuation along its axis.

Depending on the points of application of the actuation, two main configurations can be realized: distributed actuation or concentrated actuation. Figure 19 illustrates the difference between these two options. Concentrated actuation would be achieved using a single, relatively large actuator placed close to the rotor hub. Distributed actuation would be obtained by placing several relatively small actuators along the blade span.

4.1 Theoretical background

4.1.1 Classical Vlasov beam theory

This section will summarize the classical theory for warping of thin-walled beams with open cross-sections. As described in Ref. 9, such a beam under torsion undergoes two

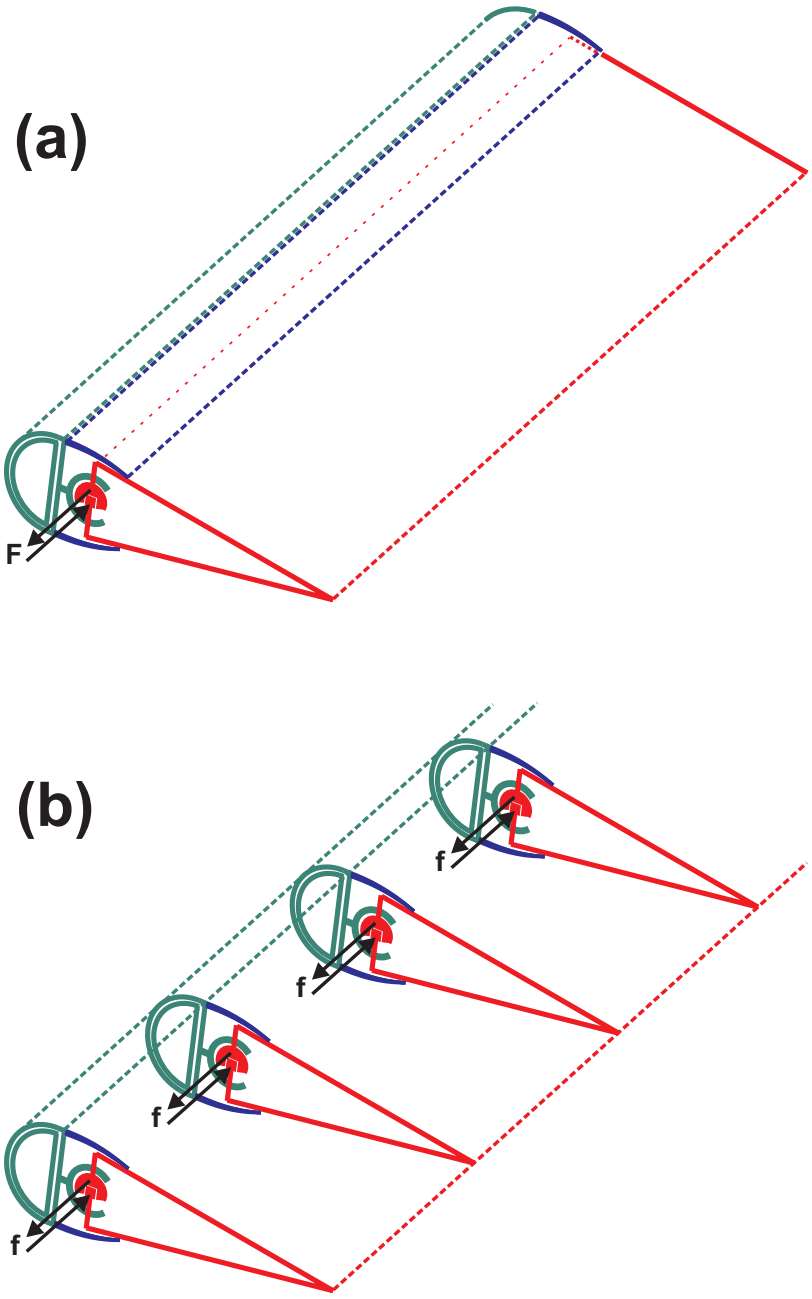

Figure 19: (a) Concentrated actuation vs. (b) distributed actuation

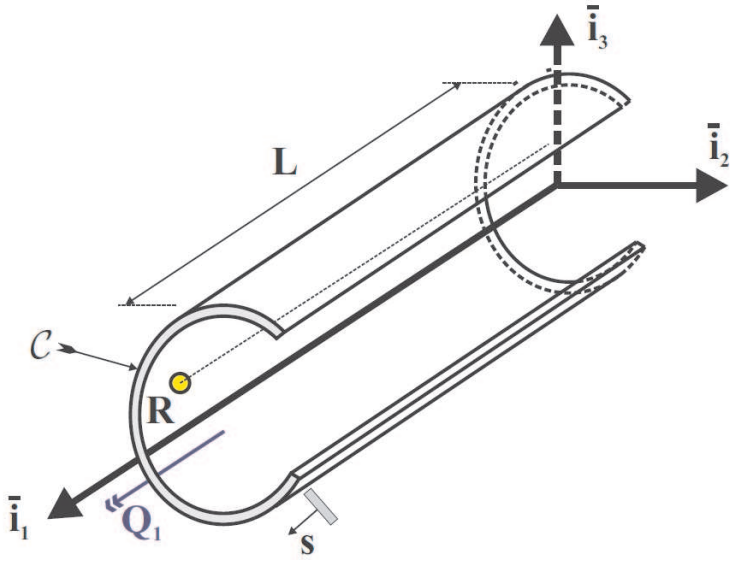

Figure 20: A thin-walled beam subject to torsion

forms of out-of-plane warping: one found from Saint-Venant's solution under the assumption of uniform torsion, according to which the twist rate is constant along the length of the beam, *i.e.*, $\frac{\mathrm{d}\kappa_1}{\mathrm{d}x_1} = 0$; and the other being a much larger global warping of the overall cross-section, obtained by considering non-uniform torsion, *i.e.*, $\frac{\mathrm{d}\kappa_1}{\mathrm{d}x_1} \neq 0$. For thin-walled open sections, the first contribution to out-of-plane warping is very small, and will be neglected in this work. Clearly, actuation inducing the second form of warping results in the large deformations needed for the proposed blade morphing concept.

Consider an arbitrary thin-walled beam with open section, as shown in Fig. 20. The axis of the beam is along $\bar{\imath}_1$ while $\bar{\imath}_2$ and $\bar{\imath}_3$ define the plane of the cross-section. The origin of the axes and the orientation of the cross-sectional axes are chosen arbitrarily at first. $\mathcal{C}$ denotes the contour line defining the cross-sectional geometry, and s the associated curvilinear coordinate. Point R, of cross-sectional coordinates x_{2r} and x_{3r}, corresponds to the as of yet unknown center of rotation about which the beam twists.

First, assume the following displacement field

$$u_1(x_1, s) = \Psi(s)\,\kappa_1(x_1), \tag{18a}$$

$$u_2(x_1, s) = -\,(x_3 - x_{3r})\,\phi_1(x_1), \tag{18b}$$

$$u_3(x_1, s) = \quad (x_2 - x_{2r})\,\phi_1(x_1). \tag{18c}$$

The axial displacement field u_1 is proportional to the twist rate $\kappa_1 = \frac{\mathrm{d}\phi_1}{\mathrm{d}x_1}$ and is characterized by an unknown cross-sectional warping function $\Psi(s)$. The displacement components u_2 and u_3 describe the rotation of the cross-section by an angle ϕ_1 about $\bar{\imath}_1$. The associated strain field is computed using the linear strain displacement relationships

$$\varepsilon_1 = \Psi(s)\,\frac{\mathrm{d}\kappa_1}{\mathrm{d}x_1}, \tag{19a}$$

$$\gamma_{12} = \left[\frac{\partial\Psi}{\partial x_2} - (x_3 - x_{3r})\right]\kappa_1, \tag{19b}$$

$$\gamma_{13} = \left[\frac{\partial\Psi}{\partial x_3} + (x_2 - x_{2r})\right]\kappa_1, \tag{19c}$$

and the remaining strain components vanish: $\varepsilon_2 = \varepsilon_3 = \gamma_{23} = 0$. With the assumption of non-uniform torsion, the axial strain does not vanish. The stress components are obtained from the constitutive laws for a linearly elastic, isotropic material

$$\sigma_1 = E\,\Psi(s)\,\frac{\mathrm{d}\kappa_1}{\mathrm{d}x_1}, \tag{20a}$$

$$\tau_{12} = G\left[\frac{\partial\Psi}{\partial x_2} - (x_3 - x_{3r})\right]\kappa_1, \tag{20b}$$

$$\tau_{13} = G\left[\frac{\partial\Psi}{\partial x_3} + (x_2 - x_{2r})\right]\kappa_1. \tag{20c}$$

The shear stress component normal to $\mathcal{C}$ must vanish at the wall edges based on equilibrium considerations, and no appreciable shear strain can develop through the thin wall. Hence, $\tau_n \approx 0$, and the tangential shear stress τ_s is the only remaining component

$$\tau_s = \tau_{12}\frac{\mathrm{d}x_2}{\mathrm{d}s} + \tau_{13}\frac{\mathrm{d}x_3}{\mathrm{d}s} = G\left(\frac{\mathrm{d}\Psi}{\mathrm{d}s} + r_o - x_{2r}\frac{\mathrm{d}x_3}{\mathrm{d}s} + x_{3r}\frac{\mathrm{d}x_2}{\mathrm{d}s}\right)\kappa_1, \tag{21}$$

where $r_o = x_2 \frac{\mathrm{d}x_3}{\mathrm{d}s} - x_3 \frac{\mathrm{d}x_2}{\mathrm{d}s}$ is the distance from the origin O to the tangent to $\mathcal{C}$. In Ref. 9, it is shown that the tangential shear stress distribution is linearly distributed through the thickness of the open section's thin wall, and vanishes along the midline defined by curve $\mathcal{C}$. Hence, the following differential equation holds along this curve

$$\frac{\mathrm{d}\Psi}{\mathrm{d}s} = -r_o + x_{2r}\frac{\mathrm{d}x_3}{\mathrm{d}s} - x_{3r}\frac{\mathrm{d}x_2}{\mathrm{d}s}. \tag{22}$$

Integration of this equation then yields

$$\Psi(s) = \Gamma(s) + x_{2r}x_3 - x_{3r}x_2 + a, \tag{23}$$

where $\Gamma(s)$ satisfies $\frac{\mathrm{d}\Gamma}{\mathrm{d}s} = -r_o$, and a is a constant of integration. In the classical theory, x_{2r}, x_{3r} and a are determined by imposing the vanishing of the axial force, $N_1 = \int_{\mathcal{C}} \sigma_1 t \,\mathrm{d}s = 0$, and of the bending moments, $M_2 = \int_{\mathcal{C}} \sigma_1 x_3 t \,\mathrm{d}s = 0$ and $M_3 = -\int_{\mathcal{C}} \sigma_1 x_2 t \,\mathrm{d}s = 0$. Introducing Eq. (23) into Eq. (20a), substituting σ_1 in these three sectional load expressions and casting them in matrix form, one finds

$$\begin{bmatrix} S & Sx_{3c} & -Sx_{2c} \\ Sx_{3c} & H^o_{22} & -H^o_{23} \\ -Sx_{2c} & -H^o_{23} & H^o_{33} \end{bmatrix} \begin{Bmatrix} a \\ x_{2r} \\ x_{3r} \end{Bmatrix} = \begin{Bmatrix} -\int_{\mathcal{C}} E\Gamma t \,\mathrm{d}s \\ -\int_{\mathcal{C}} E\Gamma x_3 t \,\mathrm{d}s \\ \int_{\mathcal{C}} E\Gamma x_2 t \,\mathrm{d}s \end{Bmatrix}, \tag{24}$$

where x_{2c} and x_{3c} represent the location of the centroid with respect to the chosen origin, S is the axial stiffness, and H^o_{22}, H^o_{33} and H^o_{23} are the bending stiffnesses. This linear system of equations can then be solved for a, x_{2r} and x_{3r}. Alternatively, if the principal centroidal axes are chosen with the origin at the centroid C, then $x_{2c} = x_{3c} = 0$ and $H^c_{23} = 0$, and the solution is readily obtained as

$$a = -\frac{1}{S}\int_{\mathcal{C}} E\Gamma t \,\mathrm{d}s, \tag{25}$$

and

$$x_{2r} = -\frac{1}{H^c_{22}}\int_{\mathcal{C}} E\Gamma x_3 t \,\mathrm{d}s, \tag{26a}$$

$$x_{3r} = \frac{1}{H^c_{33}}\int_{\mathcal{C}} E\Gamma x_2 t \,\mathrm{d}s. \tag{26b}$$

It can be shown that the center of twist R, of coordinates x_{2r} and x_{3r}, is at the shear center K of the cross-section, *i.e.*, $x_{2r} = x_{2k}$ and $x_{3r} = x_{3k}$ (see Ref. 9). The warping function $\Psi(s)$ is now fully determined, and can be used to identify all the displacement, strain and stress components using Eqs. (18), (19), and (20). A relevant example of the application of this theory is included in Appendix B.

As a final note, it can be observed that the terms $x_{2r}x_3 - x_{3r}x_2 + a$ correspond to the equation of a plane in three dimensions. In other words, applying conditions on the axial force as well as the bending moments determines the x_{2r}, x_{3r} and a coefficients defining this plane. Consider now the case where a different set of conditions is applied. Different values will be obtained for these parameters, thus redefining the reference plane. Following a similar reasoning, $\Gamma(s)$ can be thought of as the warping function obtained when the conditions are chosen to lead to $x_{2r} = x_{3r} = a = 0$.

In general, assume a warping function Ψ was found based on a particular, unknown normalization. The warping function may be renormalized using any set of conditions on N_1, M_2 and M_3 as

$$\Psi_{\text{new}} = \Psi + \lambda_2 x_3 - \lambda_3 x_2 + \mu, \tag{27}$$

where the three unknown coefficients λ_2, λ_3 and μ are computed by solving a system of equilibrium equations similar to Eq. (24)

$$\begin{bmatrix} S & Sx_{3c} & -Sx_{2c} \\ Sx_{3c} & H^o_{22} & -H^o_{23} \\ -Sx_{2c} & -H^o_{23} & H^o_{33} \end{bmatrix} \begin{Bmatrix} \mu \\ \lambda_2 \\ \lambda_3 \end{Bmatrix} = \begin{Bmatrix} \frac{N_1}{\kappa_1} - \int_{\mathcal{C}} E\Psi t \, \mathrm{d}s \\ \frac{M_2}{\kappa_1} - \int_{\mathcal{C}} E\Psi x_3 t \, \mathrm{d}s \\ \frac{M_3}{\kappa_1} + \int_{\mathcal{C}} E\Psi x_2 t \, \mathrm{d}s \end{Bmatrix}. \tag{28}$$

This fact will be applied in Chapter 5. In particular, to compute the classical warping function, for which the sectional loads are zero, one would simply set $N_1 = M_2 = M_3 = 0$; this is equivalent to using the earlier equation, Eq. (24), if Γ is substituted with Ψ, and the solution is now $\{\mu, \lambda_2, \lambda_3\}^T$. As before, the cross-sectional axes centered on the chosen origin do not need to be the principal axes of bending centered on the centroid. However, whenever possible, choosing these axes simplifies

the formulation.

4.1.2 Modified theory

In order to analyze the proposed concept, the classical theory is not adequate. Indeed, this theory assumes no constraints outside of the beam boundary conditions, and as a consequence places the center of twist at the location of the shear center. However, in this concept, the deformable aft section of the blade will be connected to the D-spar, which imposes restrictions on the ways in which the cross-section can warp out of plane. Referring back to Fig. 17, the double joint specifically restricts the center about which the cross-section rotates to a particular location which in general is not the shear center. Clearly, the theory must be modified by imposing the values of x_{2r} and x_{3r} rather than compute them as properties of the cross-section. The warping function now depends not only on the cross-sectional characteristics, but on the constraints imposed on that cross-section as well.

In fact, the first of the three equations presented in Eq. (24) still holds, but x_{2r} and x_{3r} are now given quantities, and the integration constant a is still computed using

$$a = -x_{3c}x_{2r} + x_{2c}x_{3r} - \frac{1}{S}\int_{\mathcal{C}} E\Gamma t \, \mathrm{d}s. \tag{29}$$

However, the second and third equations of Eq. (24) do not hold anymore, due to the non-zero bending moments required to force the center of twist into a particular location. It is interesting to note that if the origin is at the centroid, $x_{2c} = x_{3c} = 0$ and the expression for a is identical to Eq. (25).

Using a reasoning similar to that of the previous section, it is clear that the modified warping function is related to the classical one through a redefinition of the reference plane. Assuming the classical warping function Ψ_c is known, as well as the location of the centroid and the shear center of the cross-section, the modifed function

Ψ_m can simply be obtained using

$$\Psi_m = \Psi_c + (x_{2r}^m - x_{2r})(x_3 - x_{3c}) - (x_{3r}^m - x_{3r})(x_2 - x_{2c}), \tag{30}$$

where x_{2r}^m and x_{3r}^m describe the location of the constrained center of rotation.

As will be shown in the next section, in addition to typical cross-sectional properties, the behavior of a beam experiencing out-of-plane warping is also determined by coefficients computed using the characteristic warping function of the cross-section. Clearly, the values of these properties will be modified as well, and the response of the beam to external loading and actuation will be affected. It will be shown that the deformable blade's response is accurately modeled by the updated warping coefficients, while the classical properties do not capture its behavior, justifying the need to introduce these modifications.

Appendix B provides a relevant example illustrating the different results obtained with both the classical theory and the modified approach presented here. The warping function and associated cross-sectional properties of a thin-walled open triangular section are provided for the study of the warping-actuated blade.

4.1.3 Energy approach to non-uniform torsion

Once the sectional coefficients related to warping are determined, it is possible to analyze the response of beams under twisting and warping. Examples of problems that can be tackled are: response due to concentrated end torques and/or a distributed torque along the span of the beam; response due to concentrated axial warping actuation at the ends of the beam; response due to distributed axial warping actuation along the span of the beam. In this section the analytical formulation leading to the force-displacement relationship for beams under torsion and warping actuation is described.

An energy approach is used to investigate the behavior of the structure under different applied loads and boundary conditions. We assume a displacement field of

the form

$$u_1(x_1, s) = \Psi(s)\,\alpha(x_1), \tag{31a}$$

$$u_2(x_1, s) = -\,(x_3 - x_{3r})\,\phi_1(x_1), \tag{31b}$$

$$u_3(x_1, s) = \quad (x_2 - x_{2r})\,\phi_1(x_1), \tag{31c}$$

where the axial displacement is assumed to be proportional to an unknown function $\alpha(x_1)$ through the warping function $\Psi(s)$. As before, the inplane displacement components describe the rotation of the cross-section by an angle ϕ_1 about the center of twist. Using the strain-displacement relationships, the non-zero strain field components can be written

$$\varepsilon_1 = \Psi(s)\,\frac{\mathrm{d}\alpha}{\mathrm{d}x_1}, \tag{32a}$$

$$\gamma_{12} = \frac{\partial \Psi}{\partial x_2}\,\alpha - (x_3 - x_{3r})\,\kappa_1, \tag{32b}$$

$$\gamma_{13} = \frac{\partial \Psi}{\partial x_3}\,\alpha + (x_2 - x_{2r})\,\kappa_1. \tag{32c}$$

The normal shear strain $\gamma_n = \tau_n/G \approx 0$ is neglected as before, and the tangential shear strain component along curve $\mathcal{C}$ is

$$\gamma_s = \gamma_{12}\frac{\mathrm{d}x_2}{\mathrm{d}s} + \gamma_{13}\frac{\mathrm{d}x_3}{\mathrm{d}s} = \frac{\mathrm{d}\Psi}{\mathrm{d}s}\,\alpha + r_r\,\kappa_1, \tag{33}$$

where, similarly to r_o in previous sections, we have introduced

$$r_r = (x_2 - x_{2r})\frac{\mathrm{d}x_3}{\mathrm{d}s} - (x_3 - x_{3r})\frac{\mathrm{d}x_2}{\mathrm{d}s} = r_o - x_{2r}\frac{\mathrm{d}x_3}{\mathrm{d}s} + x_{3r}\frac{\mathrm{d}x_2}{\mathrm{d}s}. \tag{34}$$

The expression for γ_s may be simplified by using Eq. (22) to finally yield the following non-vanishing strain field components

$$\varepsilon_1 = \Psi(s)\,\frac{\mathrm{d}\alpha}{\mathrm{d}x_1}, \qquad \gamma_s = (\kappa_1 - \alpha)\,r_r. \tag{35}$$

For a linearly elastic, isotropic material, the corresponding stress components are

$$\sigma_1 = E\,\Psi(s)\,\frac{\mathrm{d}\alpha}{\mathrm{d}x_1}, \qquad \tau_s = G\,(\kappa_1 - \alpha)\,r_r. \tag{36}$$

The strain energy of the beam

$$A = \frac{1}{2}\int_0^L \int_{\mathcal{C}} \left[\sigma_1 \varepsilon_1 + \tau_s \gamma_s\right] t \, \mathrm{d}s \, \mathrm{d}x_1 \tag{37}$$

only includes contributions from the non-vanishing stress and strain components, and can be written as

$$A = \frac{1}{2}\int_0^L \left[\left(\int_{\mathcal{C}} E\Psi^2 t \, \mathrm{d}s\right)\left(\frac{\mathrm{d}\alpha}{\mathrm{d}x_1}\right)^2 + \left(\int_{\mathcal{C}} G r_r^2 t \, \mathrm{d}s\right)(\kappa_1 - \alpha)^2\right] \mathrm{d}x_1. \tag{38}$$

This expression was obtained by considering the vanishing of τ_s on $\mathcal{C}$, and hence does not include the linear through-the-thickness variation of the tangential shear strain that is found for open thin-walled sections in torsion. Therefore, the classical strain energy term associated with torsion is added to Eq. (38), and finally

$$A = \frac{1}{2}\int_0^L \left[H_{11w}\left(\frac{\mathrm{d}\alpha}{\mathrm{d}x_1}\right)^2 + I_p\left(\kappa_1 - \alpha\right)^2 + H_{11}\kappa_1^2\right] \mathrm{d}x_1, \tag{39}$$

where

$$H_{11w} = \int_{\mathcal{C}} E\Psi^2 t \, \mathrm{d}s \tag{40}$$

and

$$I_p = \int_{\mathcal{C}} G r_r^2 t \, \mathrm{d}s \tag{41}$$

represent cross-sectional coefficients describing the warping behavior of the beam in torsion, and H_{11} is the usual torsional stiffness.

In order to analyse the response of beams under torsional applied loads and warping actuation, the associated potentials of externally applied loads are computed. They are obtained as the negative of the work done by these applied loads. The potential associated with concentrated torques applied at the root, Q_1^0, and at the tip, Q_1^L, is

$$V_1 = Q_1^0 \, \phi_1(0) - Q_1^L \, \phi_1(L). \tag{42}$$

That associated with a distributed torque along the span of the beam, $q_1(x_1)$, is

$$V_2 = -\int_0^L q_1 \phi_1 \, \mathrm{d}x_1. \tag{43}$$

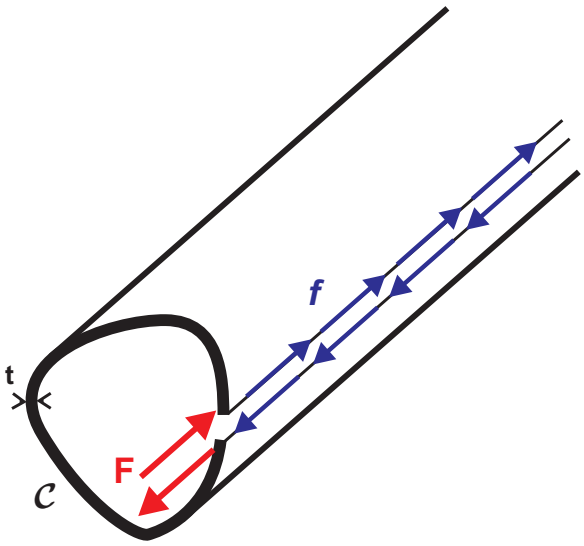

Figure 21: Concentrated and distributed warping actuation forces

Next, we consider the potential arising from warping forces applied in pairs. First, we consider the case of two concentrated forces applied at the root section of the beam, as illustrated in Fig. 21. The forces are parallel, of equal magnitude F^0, and opposite directions, applied at two different points A and B of the cross-section. The following convention is adopted: the axial force applied at A acts in the positive direction for sectional axial forces at the root, while that applied at B acts in the negative direction. Then, the potential of each applied force is

$$V^A_{F,0} = \quad F^0\, u_1(0, s_A) = \quad F^0\, \Psi(s_A)\, \alpha(0), \tag{44a}$$

$$V^B_{F,0} = -F^0\, u_1(0, s_B) = -F^0\, \Psi(s_B)\, \alpha(0), \tag{44b}$$

and the total potential for this pair of concentrated warping forces becomes

$$V_{F,0} = F^0\, \Delta\Psi_{F,0}\, \alpha(0), \quad \text{where} \qquad \Delta\Psi_{F,0} = \Psi(s_A) - \Psi(s_B). \tag{45}$$

More generally, if $N_{c,0}$ pairs of concentrated warping forces F^0_i are applied at the root section of the beam, then the total potential associated with all concentrated warping actuation forces at the root is

$$V_{c,0} = \hat{F}^0\, \alpha(0), \quad \text{with} \qquad \hat{F}^0 = \sum_{i=1}^{N_{c,0}} F^0_i \Delta\Psi^0_i, \tag{46}$$

where it should be understood that, for each pair of forces, $\Delta\Psi_i^0$ is the difference between the value of the warping function at the point of application of positive warping force (as determined by the positive direction of sectional axial force at the root section) and its value at the point of application of negative warping force. Likewise, it is found that the total potential of all concentrated warping actuation forces at the tip section, if any exist, is

$$V_{c,L} = -\hat{F}^L\,\alpha(L), \quad \text{with} \qquad \hat{F}^L = \sum_{i=1}^{N_{c,L}} F_i^L \Delta\Psi_i^L, \tag{47}$$

where the same convention is used to define $\Delta\Psi_i^L$ for each pair of warping forces (remembering that the positive direction of sectional axial force is in the positive $\bar{\imath}_1$ direction for the tip section, as opposed to the root section). Finally, the potential associated with *all* concentrated actuation forces is

$$V_3 = V_{c,0} + V_{c,L} = \hat{F}^0\,\alpha(0) - \hat{F}^L\,\alpha(L), \tag{48}$$

for which $\hat{F}^0$ and $\hat{F}^L$ are defined in Eqs. (46) and (47). In a similar fashion, one finds the potential of distributed actuation forces to be

$$V_4 = -\int_0^L \hat{f}(x_1)\alpha(x_1)\,\mathrm{d}x_1, \quad \text{where} \qquad \hat{f}(x_1) = \sum_{i=1}^{N_d} f_i(x_1)\Delta\Psi_i^d. \tag{49}$$

As before, the distributed loading is applied in pairs of distributed forces, of magnitude $f_i(x_1)$ and opposite signs, and $\Delta\Psi_i^d$ is the difference between the value of the cross-sectional warping function at the point of application of the axial force in the positive $\bar{\imath}_1$ direction and its value at the point of application of the opposite force. Note that $\Delta\Psi_i^d$ does not depend on x_1; this is consistent with the initial kinematic assumptions, according to which Ψ only depends on the curvilinear coordinate s.

The total potential energy Π is the sum of the strain energy A and all the potentials of externally applied loads V_i,

$$\Pi = A + V_1 + V_2 + V_3 + V_4. \tag{50}$$

The principle of minimum total potential energy states that Π is strictly minimized if and only if the beam is in equilibrium. This principle is applied by considering all kinematically admissible displacement fields, and determining the real displacement field that minimizes the total potential energy. The first variation of Π is

$$\delta\Pi = \delta A + \delta V_1 + \delta V_2 + \delta V_3 + \delta V_4, \tag{51}$$

and this principle requires that $\delta\Pi = 0$. This condition leads to the actual displacement field at the stationary point of Π; the positive-definiteness of the strain energy ensures that it is in fact a strict minimum.

The first variation of the strain energy computed in Eq. (39) is

$$\begin{aligned}\delta A = \int_0^L \Bigg[& H_{11} \frac{\mathrm{d}\phi_1}{\mathrm{d}x_1} \delta\left(\frac{\mathrm{d}\phi_1}{\mathrm{d}x_1}\right) + H_{11w} \frac{\mathrm{d}\alpha}{\mathrm{d}x_1} \delta\left(\frac{\mathrm{d}\alpha}{\mathrm{d}x_1}\right) \\ & + I_p \left(\frac{\mathrm{d}\phi_1}{\mathrm{d}x_1} - \alpha\right)\left(\delta\left(\frac{\mathrm{d}\phi_1}{\mathrm{d}x_1}\right) - \delta\alpha\right)\Bigg] \,\mathrm{d}x_1.\end{aligned} \tag{52}$$

Integrating relevant terms by parts,

$$\begin{aligned}\delta A = \int_0^L \Bigg[& -H_{11} \frac{\mathrm{d}^2\phi_1}{\mathrm{d}x_1^2} \delta\phi_1 - I_p \frac{\mathrm{d}}{\mathrm{d}x_1}\left(\frac{\mathrm{d}\phi_1}{\mathrm{d}x_1} - \alpha\right)\delta\phi_1 \\ & - H_{11w} \frac{\mathrm{d}^2\alpha}{\mathrm{d}x_1^2}\delta\alpha - I_p\left(\frac{\mathrm{d}\phi_1}{\mathrm{d}x_1} - \alpha\right)\delta\alpha\Bigg] \,\mathrm{d}x_1 \\ & + \left[I_p\left(\frac{\mathrm{d}\phi_1}{\mathrm{d}x_1} - \alpha\right)\delta\phi_1\right]_0^L + \left[H_{11}\frac{\mathrm{d}\phi_1}{\mathrm{d}x_1}\delta\phi_1\right]_0^L \\ & + \left[H_{11w}\frac{\mathrm{d}\alpha}{\mathrm{d}x_1}\delta\alpha\right]_0^L.\end{aligned} \tag{53}$$

The first variations of the potentials of externally applied loads computed in Eqs. (42), (43), (48) and (49) are

$$\delta V_1 = Q_1^0\,\delta\phi_1(0) - Q_1^L\,\delta\phi_1(L), \tag{54a}$$

$$\delta V_2 = -\int_0^L q_1(x_1)\delta\phi_1(x_1)\,\mathrm{d}x_1, \tag{54b}$$

$$\delta V_3 = \hat{F}^0\,\delta\alpha(0) - \hat{F}^L\,\delta\alpha(L), \tag{54c}$$

$$\delta V_4 = -\int_0^L \hat{f}(x_1)\delta\alpha(x_1)\,\mathrm{d}x_1. \tag{54d}$$

Hence, the first variation of the total potential energy becomes

$$\begin{aligned}\delta\Pi = \int_0^L \Bigg[& \left(-I_p \frac{\mathrm{d}}{\mathrm{d}x_1}\left(\frac{\mathrm{d}\phi_1}{\mathrm{d}x_1} - \alpha\right) - H_{11}\frac{\mathrm{d}^2\phi_1}{\mathrm{d}x_1^2} - q_1\right)\delta\phi_1 \\ & + \left(-H_{11w}\frac{\mathrm{d}^2\alpha}{\mathrm{d}x_1^2} - I_p\left(\frac{\mathrm{d}\phi_1}{\mathrm{d}x_1} - \alpha\right) - \hat{f}\right)\delta\alpha\Bigg]\,\mathrm{d}x_1 \\ & + \left[-I_p\left(\frac{\mathrm{d}\phi_1}{\mathrm{d}x_1}(0) - \alpha(0)\right) - H_{11}\frac{\mathrm{d}\phi_1}{\mathrm{d}x_1}(0) + Q_1^0\right]\delta\phi_1(0) \\ & + \left[\ I_p\left(\frac{\mathrm{d}\phi_1}{\mathrm{d}x_1}(L) - \alpha(L)\right) + H_{11}\frac{\mathrm{d}\phi_1}{\mathrm{d}x_1}(L) - Q_1^L\right]\delta\phi_1(L) \\ & + \left[-H_{11w}\frac{\mathrm{d}\alpha}{\mathrm{d}x_1}(0) + \hat{F}^0\right]\delta\alpha(0) \\ & + \left[\ H_{11w}\frac{\mathrm{d}\alpha}{\mathrm{d}x_1}(L) - \hat{F}^L\right]\delta\alpha(L). \end{aligned} \tag{55}$$

Setting $\delta\Pi = 0$ for all arbitrary, independent virtual changes in ϕ_1 and α, we finally obtain a set of differential equations

$$H_{11}\frac{\mathrm{d}^2\phi_1}{\mathrm{d}x_1^2} + I_p\frac{\mathrm{d}}{\mathrm{d}x_1}\left(\frac{\mathrm{d}\phi_1}{\mathrm{d}x_1} - \alpha\right) = -q_1, \tag{56}$$

$$H_{11w}\frac{\mathrm{d}^2\alpha}{\mathrm{d}x_1^2} + I_p\left(\frac{\mathrm{d}\phi_1}{\mathrm{d}x_1} - \alpha\right) = -\hat{f}, \tag{57}$$

with boundary conditions at $x_1 = 0$

$$H_{11}\frac{\mathrm{d}\phi_1}{\mathrm{d}x_1}(0) + I_p\left(\frac{\mathrm{d}\phi_1}{\mathrm{d}x_1}(0) - \alpha(0)\right) = Q_1^0 \quad \text{or} \quad \delta\phi_1(0) = 0, \tag{58}$$

$$H_{11w}\frac{\mathrm{d}\alpha}{\mathrm{d}x_1}(0) = \hat{F}^0 \quad \text{or} \quad \delta\alpha(0) = 0, \tag{59}$$

and with boundary conditions at $x_1 = L$

$$H_{11}\frac{\mathrm{d}\phi_1}{\mathrm{d}x_1}(L) + I_p\left(\frac{\mathrm{d}\phi_1}{\mathrm{d}x_1}(L) - \alpha(L)\right) = Q_1^L \quad \text{or} \quad \delta\phi_1(L) = 0, \tag{60}$$

$$H_{11w}\frac{\mathrm{d}\alpha}{\mathrm{d}x_1}(L) = \hat{F}^L \quad \text{or} \quad \delta\alpha(L) = 0. \tag{61}$$

The general solution is of the form

$$\alpha(x_1) = C_1\sinh\left(\frac{kx_1}{L}\right) + C_2\cosh\left(\frac{kx_1}{L}\right) - \frac{q_1}{H_{11}}x_1 + C_3, \tag{62}$$

$$\theta_1(x_1) = \frac{C_1 L}{k_w}\cosh\left(\frac{kx_1}{L}\right) + \frac{C_2 L}{k_w}\sinh\left(\frac{kx_1}{L}\right) - \frac{q_1}{H_{11}}\frac{x_1^2}{2} + \left(C_3 - \frac{\hat{f}}{I_p}\right)x_1 + C_4, \tag{63}$$

in which we have introduced the positive non-dimensional coefficients k, k_w and k_p such that

$$k_w^2 = \frac{H_{11}L^2}{H_{11w}}, \tag{64a}$$

$$k_p^2 = \frac{I_p}{I_p + H_{11}} = \frac{1}{1 + H_{11}/I_p}, \tag{64b}$$

$$k^2 = k_w^2 k_p^2 = \frac{H_{11}L^2}{H_{11w}} \frac{I_p}{I_p + H_{11}}, \tag{64c}$$

and where the coefficients C_1, C_2, C_3 and C_4 can be determined for a particular set of boundary conditions. Note that I_p is often much larger than H_{11}, in which case $k_p \approx 1$.

Consider the case of concentrated actuation F provided at the root of the beam. At the root $x_1 = 0$, $\phi_1 = 0$ and $H_{11w}\frac{\mathrm{d}\alpha}{\mathrm{d}x_1} = F$, while the two homogeneous natural boundary conditions are applied at the free tip of the beam. Then, the tip section rotation and applied load can be determined in terms of the root relative axial displacement d as

$$\phi_1(L) = \frac{\Delta\Psi}{H_{11}} F, \tag{65}$$

$$F = \frac{H_{11w}}{\Delta\Psi^2} \frac{d}{L} k \tanh k. \tag{66}$$

In these expressions, $\Delta\Psi$ refers to the difference between the warping function values at the two points of application of F, as defined in Eq. (46).

Similar equations can be obtained for different loading configurations, such as the prescribed displacement d or distributed load f cases, which both result in the same analytical solution

$$\phi_1(L) = \frac{\Delta\Psi}{H_{11}} fL, \tag{67}$$

$$fL = \frac{H_{11w}}{\Delta\Psi^2} \frac{d}{L} k^2. \tag{68}$$

These results will be used in following sections.

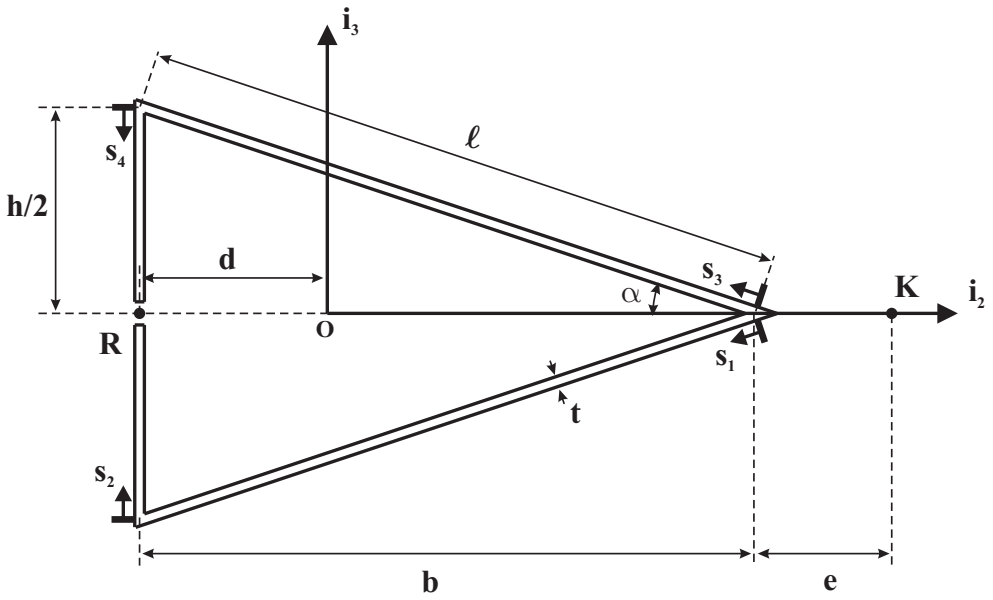

Figure 22: Open triangular section representing blade aft part

4.2 Static analysis of an early design

4.2.1 Validation of modified theory

In this section, the design described at the beginning of this chapter will be analyzed. As Fig. 22 shows, the analysis may be reduced to the triangular aft section of the blade, since the front D-spar remains essentially unchanged. Only the aft part undergoes torsional deformation through out-of-plane warping actuation. Clearly, it can be modeled as a triangular open section with its center of rotation constrained at the location of the double joint. As pointed out in the previous sections, this requires that the modified warping function and cross-sectional coefficients be taken into consideration.

To verify the validity of the analytical formulations, a finite element shell model of the section illustrated in Fig. 23 was created using ABAQUS. Figure 23 shows a representative model. The FE analysis used 3D shell elements, with different boundary conditions along the edges where the section is cut open, depending on the desired actuation mechanism, as well as on the presence of a constraint on the center of twist.

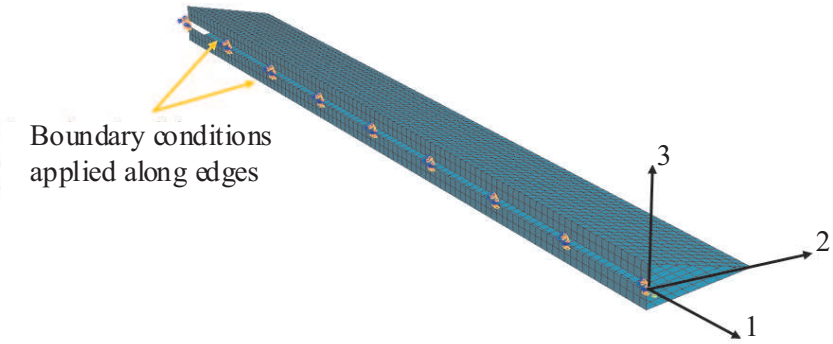

Figure 23: ABAQUS shell model of blade aft part

The dimensions of the model were chosen to approximate those of the UH-60 helicopter. Its span L is 8 m long, while the width b is chosen to be 70% of the typical chord length $c = 0.533$ m. By definition of the NACA0012 airfoil, its height h was set to be 12% of the chord length. Finally, a thickness $t = 0.01b$ ensures that the thin-walled assumption is adequate.

As stated earlier, in a typical rotor blade application, the flap section has to be attached to the D-spar of the rotor blade through a sliding joint allowing out-of-plane warping to occur freely. This is achieved by co-locating the actuation and the axis of rotation by a double joint type connection. On one hand, it allows for relative sliding between the lower and the upper lip of the cut for out-of-plane warping; and on the other hand, it allows rotation of the aft blade section as a rigid body about this axis. The boundary conditions on the ABAQUS model were defined to reflect this modification. The in-plane motions were constrained while free rotation about the slider joint axis was maintained for all nodes contained in the upper and lower lips. For concentrated actuation, only the nodes at the root had applied axial forces; in the distributed actuation case, the relative warping displacement was identically set at all nodes of the lips.

Figures 24 and 25 show the numerical results obtained using the ABAQUS model

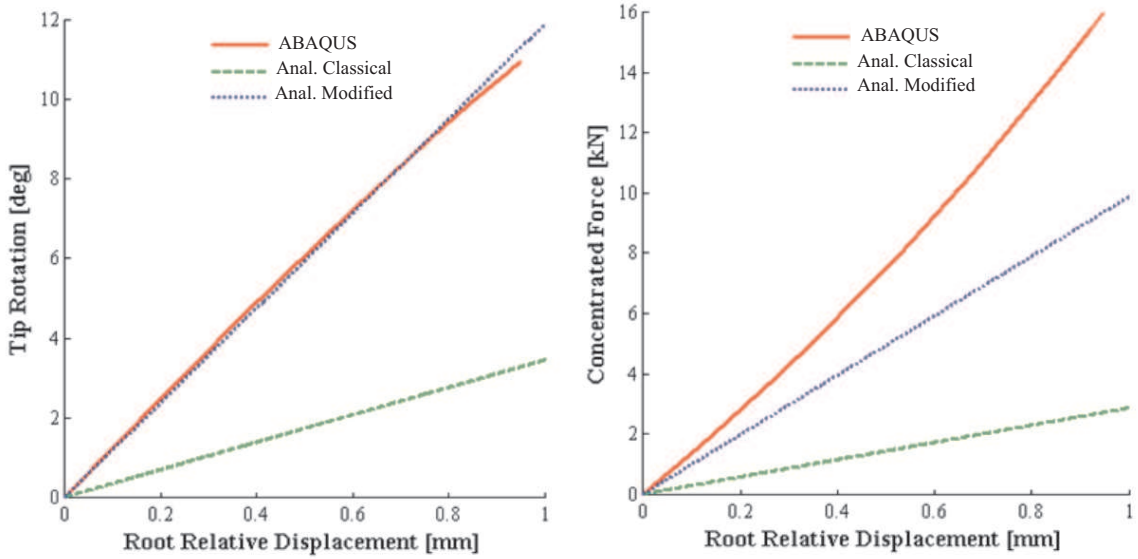

Figure 24: Tip rotation and total applied force as a function of relative warping displacement at the root, for concentrated actuation with double joint connection

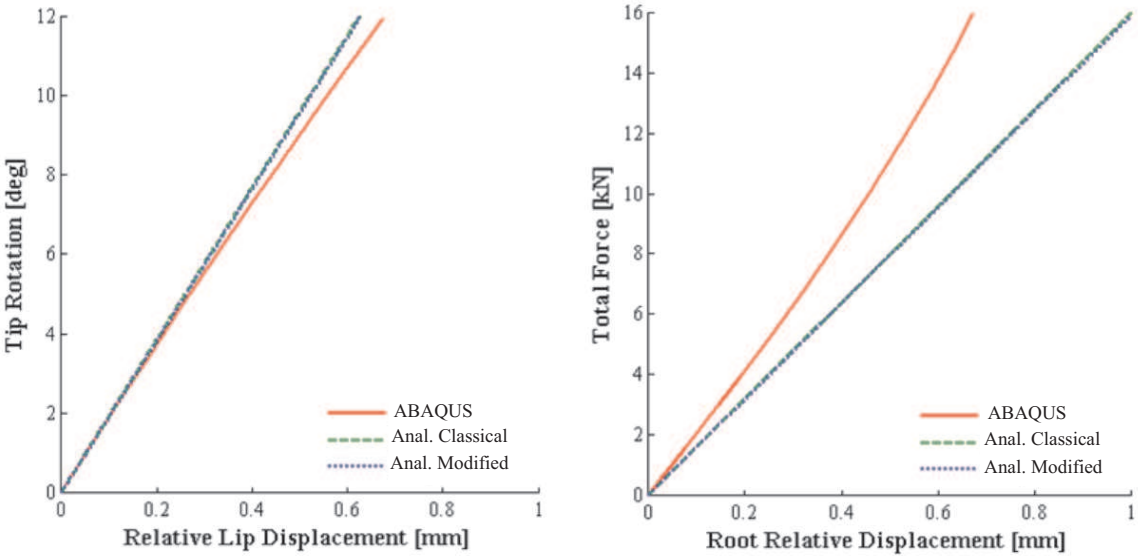

Figure 25: Tip rotation and total applied force as a function of spanwise relative warping displacement, for distributed actuation with double joint connection

including the boundary conditions modeling the slider ("ABAQUS"), as well as analytical results obtained for both this set of boundary conditions ("Anal. Modified") and the set of free boundary conditions used in the classical approach to warping ("Anal. Classical"). The results of the analysis for concentrated actuation in Fig. 24 show that the predictions of the analytical formulation with the correct sectional constants correlate well with the ABAQUS shell model predictions for the kinematic relationship. However, the force-displacement relationships do not correlate as well due to the inclusion of nonlinear effects in the numerical simulations. In addition, it is clear that the classical theory does not predict the correct results. Similar observations can be made for the distributed actuation case shown in Fig. 25. Note that the two analytical solutions are very close, as can be seen from Eqs. (67) and (68) when written in terms of H_{11} and k_p, since $k_p = \frac{I_p}{I_p+H_{11}} \approx 1$ in both constrained and unconstrained cases. Based on these analyses, we conclude that the Vlasov beam theory properly models the kinematics of the 3D warping concept provided that the assumptions made are correct.

4.2.2 Distributed and concentrated actuation

The actuation of the system can be achieved in two distinct ways: distributed actuation along the edge, or concentrated actuation where a single point load is applied at one end of the structure. In this section, the effects of these two options will be investigated using static ABAQUS analyses. Figure 26 shows a similar model with a constant 200 N/m^2 applied surface load. The purpose is to determine how efficiently this external loading can be reacted by out-of-plane warping actuators.

A varying set of actuators was located along the span of the blade, as described in Table 2. Case 1 corresponds to the presence of pure concentrated actuation at the root. Cases 2 and 3 illustrate situations in which an increasing number of actuators would be used: case 2 involves two in total, at points A and C, while case 3 includes

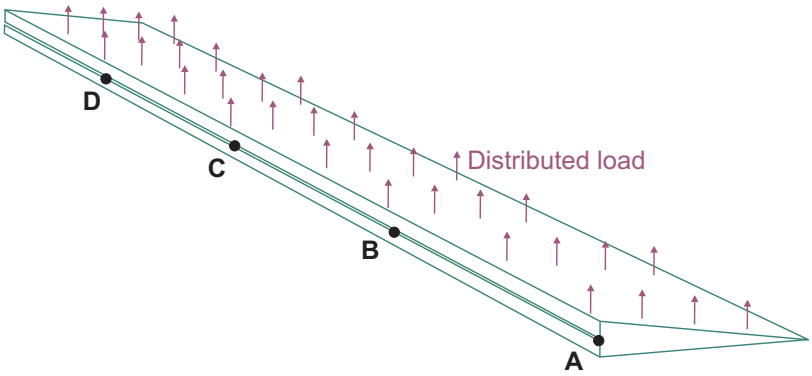

Figure 26: Static ABAQUS model with various possible locations (denoted by A, B, C, D) for actuator placement

Table 2: Various combinations of actuator locations

Case	Actuator locations
1	A (concentrated actuation)
2	A, C
3	A, B, C, D
4	Idealized distributed actuation

four actuators located at points A, B, C and D. Finally, case 4 in the table represents an idealized distributed actuation case where the load is assumed to be applied continuously along the open lips. In practice for this last case, the number of reaction points, which are located at all nodes along the cut edges, depends on the chosen mesh size. As the mesh is refined, the simulation more closely models the theoretical, distributed actuation scenario.

The results of this analysis are shown in Fig. 27. The total reaction represents the actuation load required to prescribe a vanishing axial relative displacement at the load application points, under the effect of the applied external load. The concentrated actuation case is very compliant compared to the distributed actuation case and cannot react the externally applied load efficiently. For equal total reaction of 10000 N, the structure exhibits about 20 degrees of blade tip rotation in the concentrated actuation case, while in the distributed actuation case, the structure barely

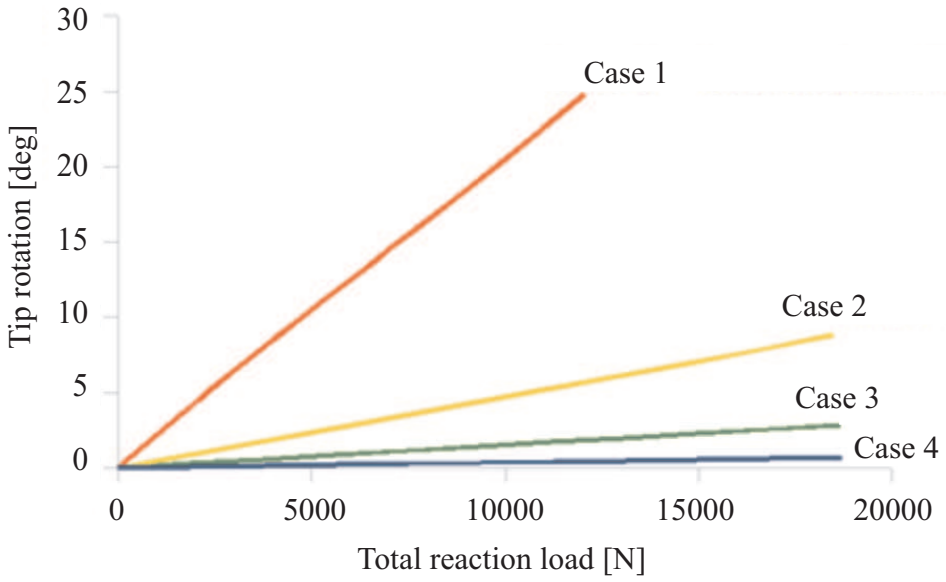

Figure 27: Reaction to the external load based on different actuation cases

rotates at the blade tip. It is however interesting to note that, with only a few concentrated point actuators scattered along the blade span, it is possible to drastically improve the structure's response and to mimic a distributed actuation scenario quite effectively. The results show that distributed actuation (case 4) would have a better control authority for the success of the 3D warping concept, but close to ideal actuation performance can also be achieved when multiple point load actuators are distributed along the blade span (case 3).

4.2.3 Axial reinforcement

The results of the above analysis raise questions regarding the ability of the concentrated actuation system to carry its reaction capability across the blade span. One means of improving its performance in this respect would be to stiffen the line of action of the applied load along the blade span, such that its effects are better transmitted and can be felt farther from the point of application. Figure 28 illustrates the stiffening of the section at location R.

This section was analyzed in ABAQUS with different stiffness values assigned to

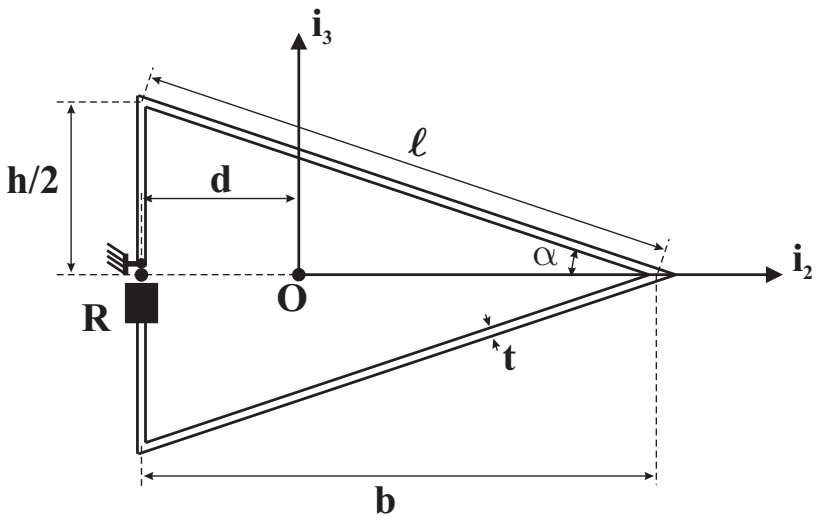

Figure 28: Stiffened line of action at R

the support region, while the rest of the cross-section is assumed to be aluminum. The results of this analysis are shown in Fig. 29. Expectedly, the overall stiffness of the structure increases with increasing support modulus. The associated drawback is the ever more stringent requirement on the maximum actuator output for a given tip rotation target. However, comparing the concentrated and distributed actuation cases for increasing support stiffness, it can be seen that the responses become ever more similar, or in other words, the differences between the structural deformations for the two actuation methods shrink. This suggests that the presence of a stiffened line of action may improve the performance of a design involving few actuators. Note that to clearly demonstrate this evolution, unrealistically high values of the support's Young's modulus are necessary.

In fact, a compromise would have to be struck between increased efficiency of a limited number of actuators, and reduced morphing capability through twisting. The actual number of actuators would naturally have to be included as a parameter in this design optimization process. Overall, these initial results indicate that the number of warping force application points along the cut plays a far greater role than the potential presence of a support structure for load transmission.

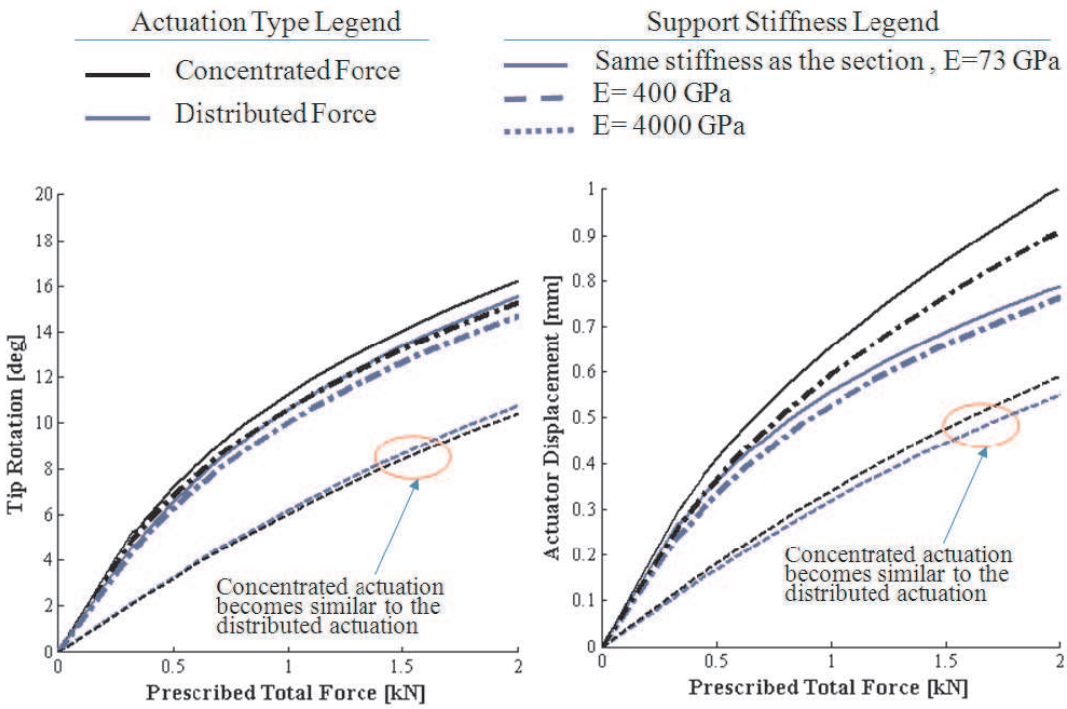

Figure 29: Concentrated and distributed actuation for different values of the support stiffness

4.3 Dynamic analysis of an early design

4.3.1 Inertial effects

In dynamic environments, inertial forces must be taken into account, and dynamic forces are also typically higher than their static counterparts. These effects have been reported to become a barrier to the success of many active actuation concepts. To investigate the inertial effects, ABAQUS dynamic analysis procedures were used to study the behavior of the double-jointed 75% flap configuration. In the model used for this analysis, several linear dashpots were placed along the span of the blade to add damping to the structure. This could for example simulate aerodynamic damping which typically arises in unsteady airflows. The out-of-plane warping was controlled by applying a prescribed sinusoidal relative displacement between the open lips.

In dynamic cases, inertial forces increase the actuation load requirement compared to the static case, unless the excitation and the system's natural frequencies

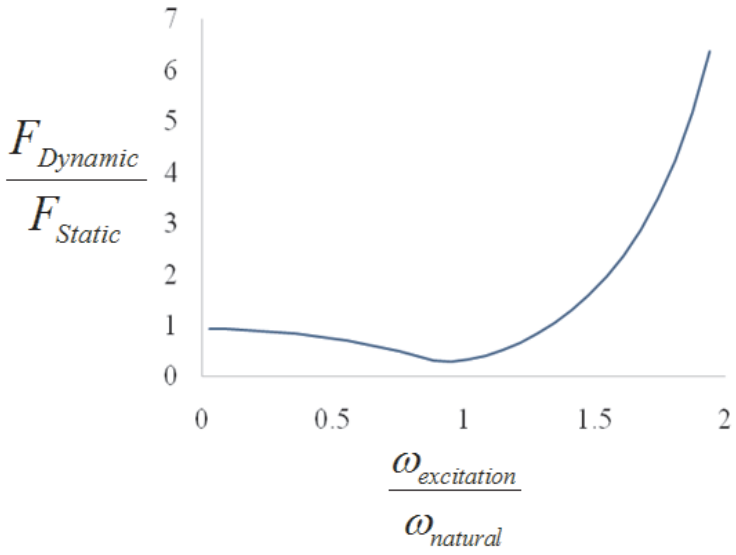

Figure 30: Effect of resonant design on actuator load requirement

are made to coincide, either by tailoring the structure's properties to given actuation frequencies, or by choosing control frequencies matching the natural frequencies associated with a particular blade design. Figure 30 illustrates the effect of excitation at the resonant frequency. For $\omega_{\text{excitation}} = \omega_{\text{natural}}$, the dynamic load requirement is minimum and is less than the static load requirement.

In applying the 3D warping concept to swashplateless rotors, the interest lies with excitations of the system at 1/rev. However, typically, rotor blades are tailored to restrict the first torsional frequency to be above the 4/rev frequency to avoid adverse effects. Since this novel concept essentially creates an open section with respect to the actuator load, it would however be possible to tailor the flap configuration's first torsional frequency to be closer to 1/rev to take advantage of the resonant design. To investigate this possibility, a configuration with a composite sandwich wall design was used. Table 3 details the layup used for the sandwich wall around the triangular cross-section.

A linear perturbation analysis in ABAQUS identified the system's first torsional frequency as 3.877 Hz. Then, the system was excited at 4.3 Hz, the 1/rev frequency

Table 3: Composite sandwich wall lay-up

Material	Thickness (mm)	Ply angle (deg)
Carbon-Epoxy	1	0
Carbon-Epoxy	1	90
Balsa	12	0
Carbon-Epoxy	1	90
Carbon-Epoxy	1	0

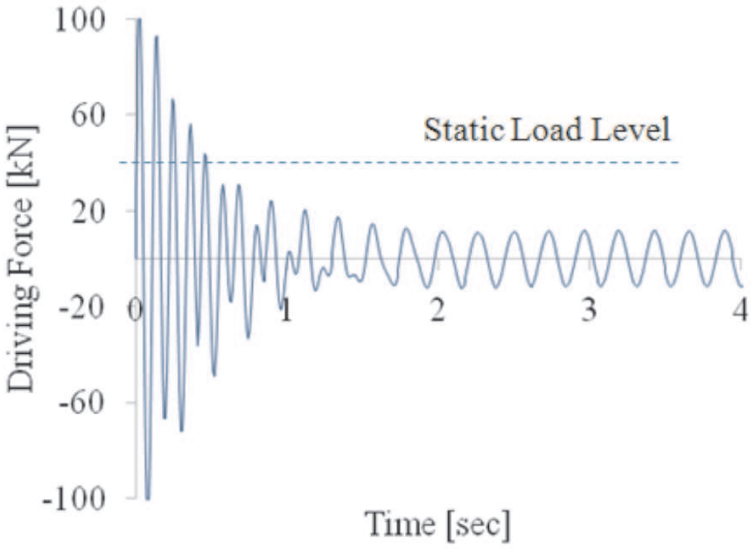

Figure 31: Dynamic response to excitation at 4.3 Hz

for a typical UH-60 rotor, using a prescribed relative displacement time history $\Delta(t) = 1.5\sin(2\cdot\pi\cdot4.3\cdot t)$ mm. Figure 31 shows the time history of the required actuation load to sustain the prescribed sinusoidal relative displacement. It is seen that the system requires considerably lower steady state actuation loads compared to the static case. Hence, careful design of the warping-enabled section to take advantage of resonances would lead to more efficient systems.

4.3.2 Effect of unsteady aerodynamic loads

The response of the warping actuated blade to estimated applied aerodynamic loads in forward flight was also investigated. Theodorsen's theory for a thin airfoil with a flap (Ref. 84) was used in order to determine the aerodynamic load levels to be reacted by the system. Figure 32 graphically shows a comparison between the conventional case where the whole section rotates about the quarter chord location according to collective and cyclic inputs controlled by the swashplate, and the case at hand where the rotation is limited to the 75% aft portion of the blade section.

Reference 84 provides aerodynamic loads expressions for a thin airfoil of chord $2b$ in simple harmonic motion, with a flap whose hinge is located at a distance $c\,b$ from the center of the airfoil toward the trailing edge. The airfoil, which extends from the leading edge of coordinate $-b$ to the trailing edge at $+b$, rotates about a point a distance $a\,b$ away from the center toward the trailing edge. Clearly, $-1 \leq a \leq +1$ and $-1 \leq c \leq +1$. The degrees-of-freedom under consideration are: the vertical displacement h of the axis of rotation, measured positive downward; the angle of attack α of the airfoil, measured positive in the clockwise direction from the horizontal; and the angle β of the aileron with respect to the undeflected position relative to the airfoil, defined to be positive in the clockwise direction as well. The air of density ρ has a wind velocity v along the horizontal. Appendix C (section C.1) provides a summary of the original equations derived by Theodorsen.

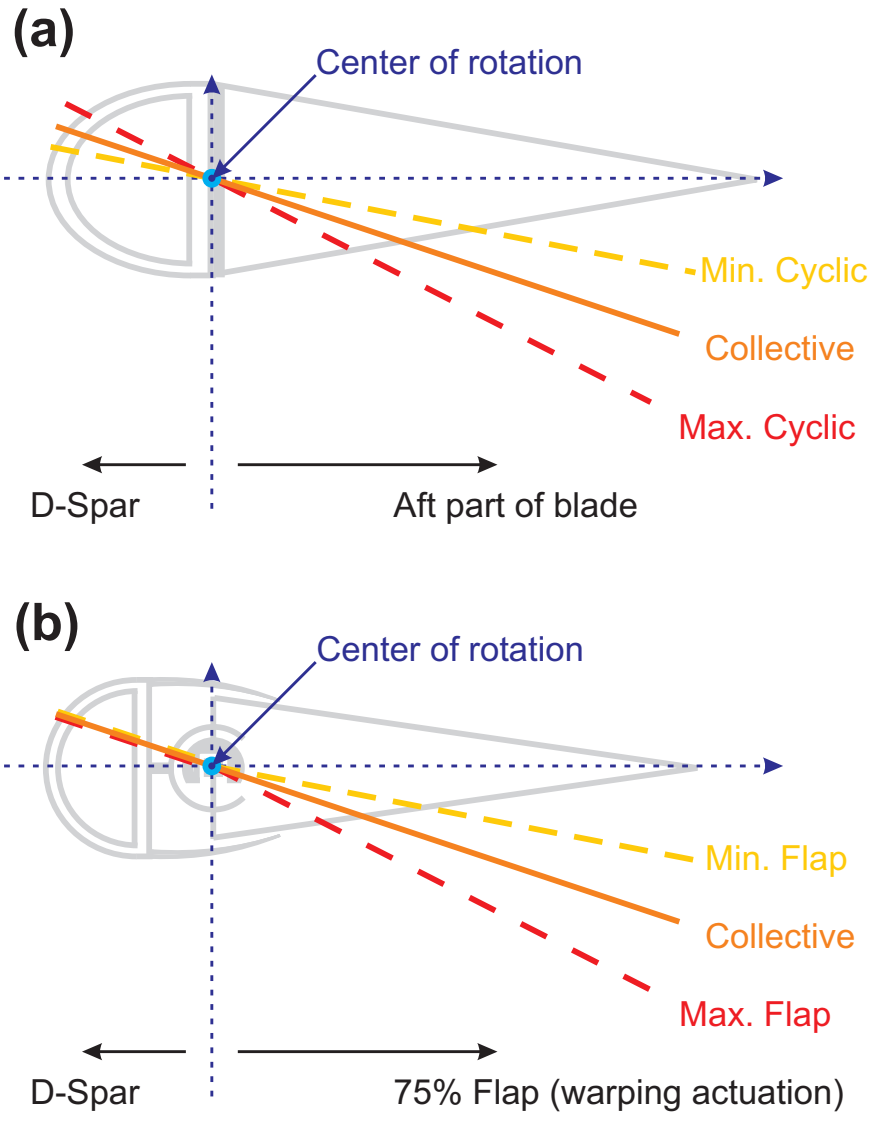

Figure 32: (a) Typical rotor blade, and (b) 75% flap configuration

We turn to the specific problem of comparing the typical design with swashplate to the newly proposed design. Considering the collective angle to be the same in both situations, we want to contrast the effect of the cyclic variation of angle of attack in the baseline design with that of cyclic variation of the flap angle. Specifically, we will derive the condition ensuring that each form of cyclic control provides the same amount of lift. In other words, the value of the amplitude of flap angle variation will be determined as a function of the amplitude of the baseline cyclic angle of attack, such that the lift provided in both cases is identical. This will effectively provide an approximate way of relating the performance of the swashplateless design compared to typical system.

Based on the expressions in Appendix C, the sectional lift generated in the first case due to cyclic variation of the angle of attack, with $h = \beta = 0$ and the angle of attack $\alpha = \alpha_I = \hat{\alpha}_I e^{i\Omega t}$ in simple harmonic motion at the 1/rev frequency Ω, is $P_I = \hat{P}_I e^{i\Omega t}$ and its complex amplitude is

$$\hat{P}_I = -\rho b^2 \left(v\pi i\Omega\hat{\alpha}_I + \pi b a \Omega^2 \hat{\alpha}_I \right) - 2\pi\rho v b C(K) \left[v\hat{\alpha}_I + b\left(\frac{1}{2} - a\right) i\Omega\hat{\alpha}_I \right], \tag{69}$$

where $K = b\Omega/v$ was introduced, and $C(K)$ is the Theodorsen function described in the Appendix. This can be simplified to

$$\mathcal{N} = \frac{\hat{P}_I}{-2\pi\rho b v^2 \hat{\alpha}_I} = i\frac{K}{2} + a\frac{K^2}{2} + C(K)\left[1 + i\left(\frac{1}{2} - a\right)K\right]. \tag{70}$$

Likewise, the sectional lift generated in the second case due to cyclic variation of the flap angle, with $h = \alpha = 0$ and the flap angle $\beta = \beta_{II} = \hat{\beta}_{II} e^{i\Omega t}$ in simple harmonic motion at frequency Ω, is $P_{II} = \hat{P}_{II} e^{i\Omega t}$, with complex amplitude

$$\hat{P}_{II} = -\rho b^2 \left(-vT_4 i\Omega\hat{\beta}_{II} + T_1 b\Omega^2 \hat{\beta}_{II} \right) - 2\pi\rho v b C(K) \left(\frac{1}{\pi} T_{10} v\hat{\beta}_{II} + b\frac{1}{2\pi} T_{11} i\Omega\hat{\beta}_{II} \right), \tag{71}$$

which can also be simplified as

$$\mathcal{D} = \frac{\hat{P}_{II}}{-2\pi\rho b v^2 \hat{\beta}_{II}} = -i\frac{T_4}{\pi}\frac{K}{2} + \frac{T_1}{\pi}\frac{K^2}{2} + C(K)\left(\frac{T_{10}}{\pi} + i\frac{T_{11}}{\pi}\frac{K}{2}\right). \tag{72}$$

Now, setting $\hat{P}_I = \hat{P}_{II}$, we find that the requirement for the equivalence of lift per unit span becomes

$$\hat{\beta}_{II} = \frac{\mathcal{N}}{\mathcal{D}}\hat{\alpha}_I = \frac{i\frac{K}{2} + a\frac{K^2}{2} + C(K)\left[1 + i\left(\frac{1}{2} - a\right)K\right]}{-i\frac{T_4}{\pi}\frac{K}{2} + \frac{T_1}{\pi}\frac{K^2}{2} + C(K)\left[\frac{T_{10}}{\pi} + i\frac{T_{11}}{\pi}\frac{K}{2}\right]}\hat{\alpha}_I. \tag{73}$$

Unfortunately, this equivalence does not carry over when considering the total lift generated in both cases. Indeed, for a helicopter rotor, the airspeed varies linearly along the radial direction, $v(x_1) = (e + x_1)\Omega$, in which e is the blade root offset distance defined in Chapter 3. The additional air speed associated with forward flight will be ignored to simplify this preliminary analysis. $\hat{\alpha}_I$ is constant along the length of the beam, but in case II, $\hat{\beta}_{II}$ is not constant. Indeed, the rotation of the warping-actuated flap is zero at the root and increases along the blade due to the generated twist rate. We will make the simplifying assumption that this twist rate is constant, so that $\hat{\beta}_{II}(x_1) = \hat{\beta}_{\text{tip}}\frac{x_1}{L}$, where $\hat{\beta}_{\text{tip}}$ is the maximum flap rotation at the tip of the blade. This is indeed a good assumption in the case of distributed warping actuation. Finally, we will take into account a tip loss factor $\eta(x_1) = \tanh\left(\frac{1-x_1/L}{1-\lambda}\right)$ with $\lambda = 0.95$ to simulate the loss of sectional lift toward the tip of the blade. Note that the effect of the tip loss factor can be removed by setting λ to be very close to 1. The total lift on the entire blade is then obtained by integrating the sectional lift over the length of the beam.

In case I, the total lift associated with cyclic control of the pitch angle is $\mathcal{P}_I = \hat{\mathcal{P}}_I e^{i\Omega t}$ where

$$\hat{\mathcal{P}}_I = \int_0^L \hat{P}_I \eta(x_1)\,\mathrm{d}x_1 = -2\pi\rho b\int_0^L v^2\mathcal{N}(v)\hat{\alpha}_I\eta(x_1)\,\mathrm{d}x_1. \tag{74}$$

In case II, the total lift associated with cyclic variation of the tip flap rotation angle is $\mathcal{P}_{II} = \hat{\mathcal{P}}_{II}e^{i\Omega t}$ and

$$\hat{\mathcal{P}}_{II} = \int_0^L \hat{P}_{II}\eta(x_1)\,\mathrm{d}x_1 = -2\pi\rho b\int_0^L v^2\mathcal{D}(v)\hat{\beta}_{II}(x_1)\eta(x_1)\,\mathrm{d}x_1. \tag{75}$$

As before, these can be set to be equal, and the resulting requirement for equivalence between the two cases in terms of total generated lift is

$$\hat{\beta}_{\text{tip}} = \mathcal{Z}\,\hat{\alpha}_I = \frac{\int_0^L v^2 \mathcal{N}(v)\eta(x_1)\,\mathrm{d}x_1}{\int_0^L v^2 \mathcal{D}(v)(x_1/L)\eta(x_1)\,\mathrm{d}x_1}\,\hat{\alpha}_I. \tag{76}$$

These integrals are computed numerically, and this relationship provides a preliminary estimate of the value of cyclic tip rotation needed in the warping-actuated system so that the generated lift by the rotor blade is equal to that of a typical rotor blade pitched cyclically by a swashplate.

Figure 33 shows the evolution of the required cyclic flap angle as the flap length changes, such that the total lift generated is identical to that of a rigid blade with a cyclic pitch angle as indicated on the figure. It can be seen that, above 60% flap length, the required cyclic pitch angles are close. This result suggests that the 3D warping concept with 75% flap could be a viable option for designing a swashplateless rotor in terms of the generated lift. Small flaps ($< 20\%$ chord) would, however, require very large pitch angles to achieve the same result.

Following these observations, the equations from Theodorsen's theory (see Appendix C) were used to calculate the blade loads to be used as inputs to a simplified structural analysis of the system. The total blade loads, as measured at the blade root, are shown in Fig. 34 for a typical baseline rigid blade and a blade with 75% flap. Notice that the total lifts were made to match in both cases. It can be seen that the flap pitch moments about the flap hinge are much higher than the total airfoil pitch moments about the quarter chord. The flap hinge moment is about 2000 Nm, whereas the total quarter chord moment is around 400 Nm for the flapped blade and 50 Nm for the rigid blade. Unfortunately, the 75% flap design must react the large 2000 Nm aerodynamic moment.

To confirm the issues posed by such large forces, an ABAQUS model was used to statically evaluate the response of the 75% flap to this level of aerodynamic flap moment about the hinge. A distributed pressure load was applied to simulate the

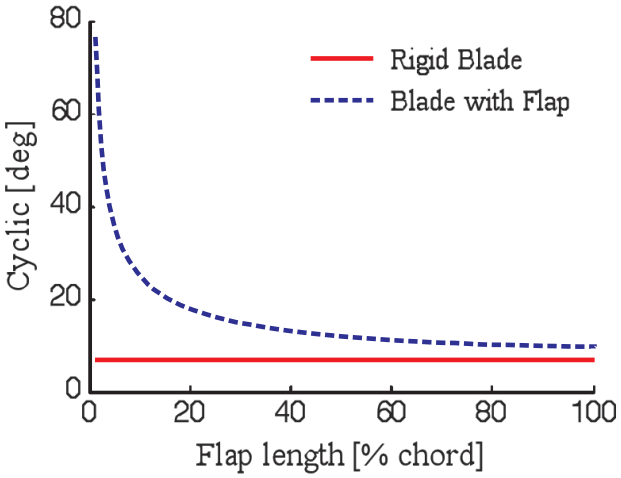

Figure 33: Cyclic angle comparison for equal total lift

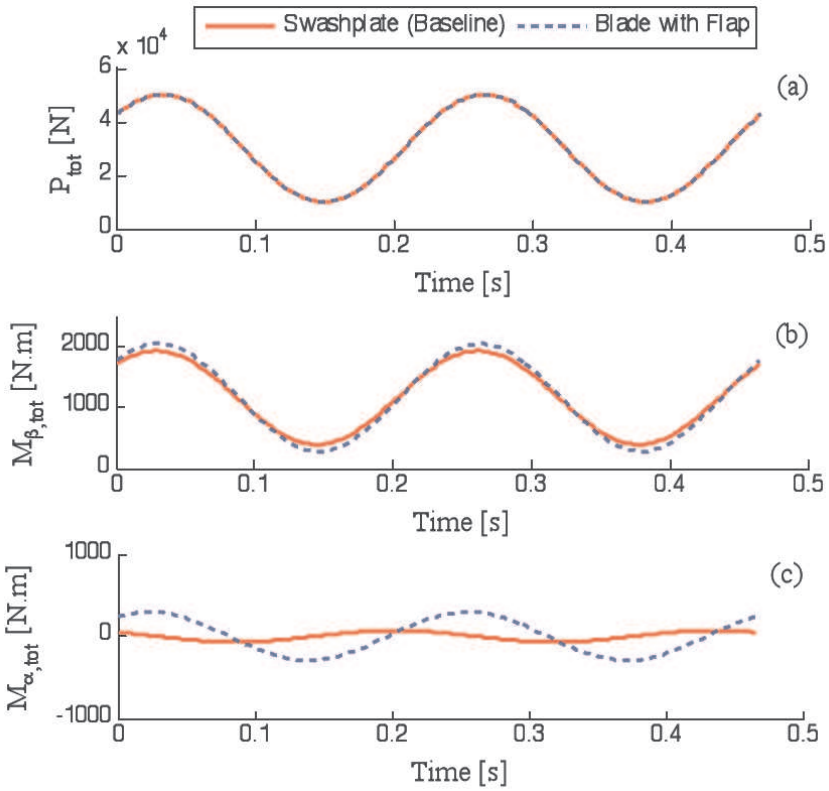

Figure 34: Total lift, total flap moment about flap hinge, and total pitching moment about the quarter chord

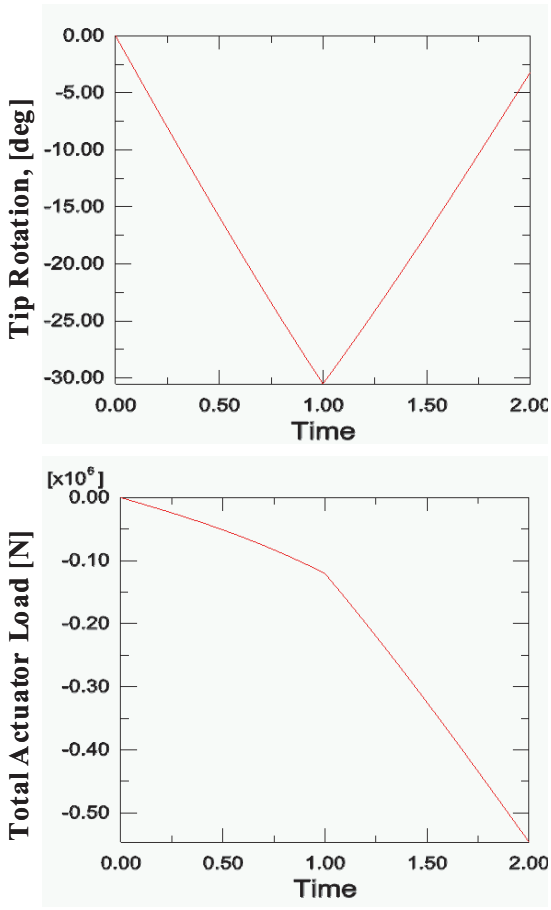

Figure 35: Response of 75% flap configuration to external piching moments

aerodynamic pressure on the structure, leading to a total root moment of about 2000 Nm. It was found that the system requires an elevated actuator load of more than 400 kN to react this moment. Next, a two-step analysis procedure was performed, in which the structure was first twisted by warping actuation resulting in about 30 degrees of blade tip twist, and afterward was loaded with the same external pitching moment (2000 Nm). Figure 35 shows that the system requires very large actuator loads above 500 kN to react the external loads. Moreover, the twist achieved by warping actuation was drastically reduced, due to the opposite elastic twist of the blade under the aerodynamic moments.

These results point to the leverage effect generated by the 3D warping actuation concept with 75% flap. The essence of this concept resides in the fact that small

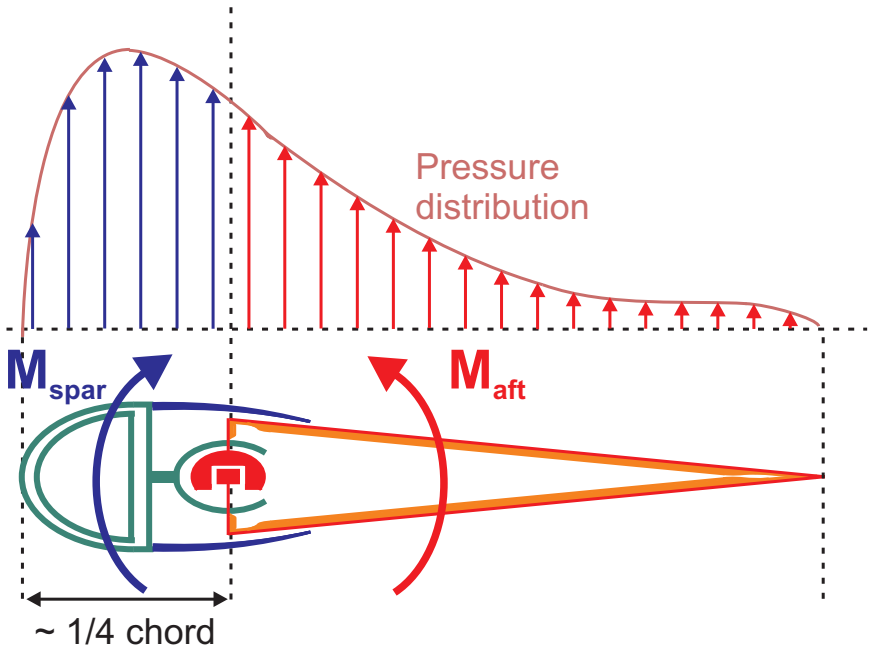

Figure 36: Typical pressure distribution over a rotor blade airfoil

warping displacements create large tip rotations, thus creating the desired amplification; however, it also results in the fact that small applied tip torques will require large equilibrating action forces as well.

4.4 Full blade warping control

While the concept presented above seemed promising in certain aspects, the study of the warping actuated blade's response under aerodynamic loading also showed its shortcomings, especially for large flap lengths. Figure 36 illustrates a typical lift distribution over an airfoil. The way the double-jointed concept is constructed, the warping actuated flap has to react the moment generated by the lift over the aft section of the rotor blade. This flap moment can be relatively large, even though the total moment of the whole airfoil about the quarter-chord may be minimal, as the air pressures generated in front and behind the quarter-chord tend to balance out.

Based on this observation, the design is modified to an innovative full-blade warping concept introduced in Ref. 88, where the blade is cut open along the entire length

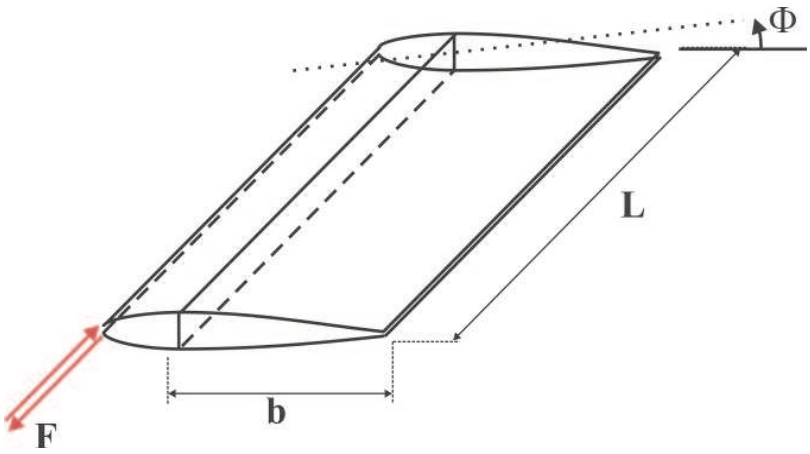

Figure 37: Full-blade warping concept

of both the leading and the trailing edges, thus forming a torsionally compliant structure. This unique structure takes the general shape of an I-beam with curved upper and lower flanges, and with the airfoil vertical web forming the I-beam's vertical web, as shown schematically in Fig. 37. When actuated along the leading edge, the entire airfoil rotates as a rigid body around the pitch axis, resulting in large relative tip rotations as before. Ideally, the D-spar is located close to the quarter chord location to take advantage of the low total aerodynamic moments.

An ABAQUS model of this new concept was constructed based on 3D shell elements and is shown in its deformed configuration in Fig. 38. A static prescribed displacement analysis was performed to demonstrate the twisting of the new blade configuration. The results are shown in Fig. 39. The concept allows the blade to achieve a 30 degree tip rotation for as little as 2 mm of relative displacement applied along the leading edge open lips. This analysis verifies that the morphing capability of a warping actuation concept is not inherent to any particular shape of the airfoil and is effective for open sections of any shape, thus providing unique and great design flexibility.

The response of the full-blade warping concept to static external loads was investigated as well. It was found that the 50 Nm aerodynamic pitching moment about the

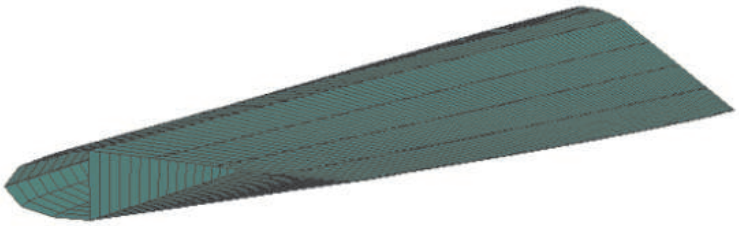

Figure 38: Deformed configuration due to prescribed warping displacement

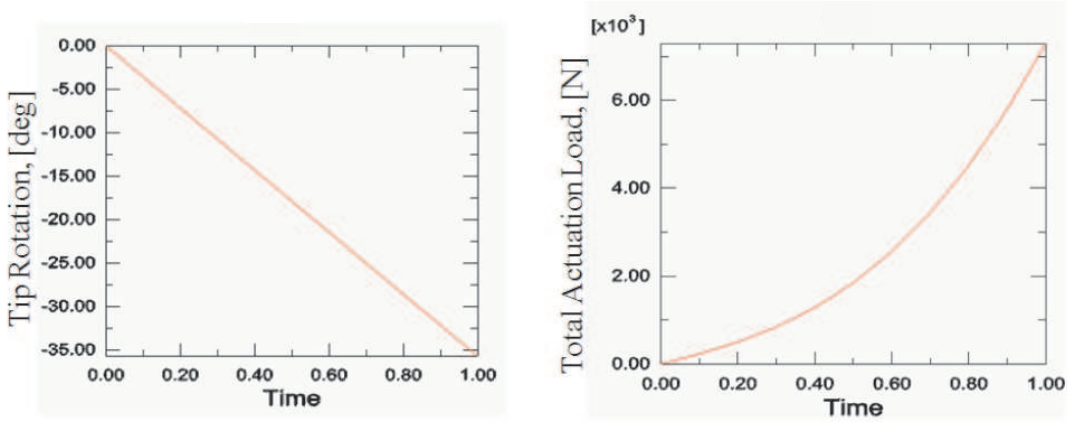

Figure 39: Tip rotation and total actuation load under prescribed warping displacement

quarter chord would require only about 20 kN of actuator load, resulting in less than 0.5 degrees of (unwanted) tip rotation. By comparison, the 75% flap design required over 400 kN of actuation load to react a total moment of about 2000 Nm.

4.5 Summary

A preliminary design analysis was conducted to assess the feasibility of a warping-actuated rotor blade. The study of an initial design involving a torsionally compliant aft part, while the D-spar remained essentially unaltered, was shown to be impractical due to large aerodynamic moments, and a full-blade warping concept was proposed instead. In general, warping actuation is not inherent to a particular shape of the airfoil. It was found that regardless of the specific form of the open section, a small relative axial displacement can induce large blade tip rotations. The blade section should rotate rigidly about a point, and therefore Vlasov beam theory was shown to properly model the system's behavior if proper constraints were included. The performance of distributed actuation was far superior to that of concentrated actuation, but a more practical approach involves several small actuators spread out along a potentially stiffened line of action. This concept enjoys great design flexibility, allowing for the possibility to benefit from dynamic effects such as resonances. However, the sensitivity of the concept to external loads, in particular unsteady aerodynamic forces and moments, was shown to be important, and this consideration weighed heavily in settling on the final design.

CHAPTER V

NUMERICAL IMPLEMENTATION OF OUT-OF-PLANE WARPING

As Chapter 4 has shown, the ability to model the behavior of warping in open thin-walled beams is essential to study the proposed warping-actuated morphing rotor blade. In this chapter, existing tools will be extended to include the analysis of beams undergoing both twisting and warping. SECTIONBUILDER, a finite element tool for the analysis of beam cross-sections, and DYMORE, a finite-element-based flexible multibody dynamics code, are complementary programs for the analysis of beam structures. Beams are three-dimensional deformable structures for which one dimension is much larger than the other two dimensions. In such a case, the 3D elasticity problem for the beam can be decoupled into a linear 2D analysis (cross-sectional analysis) and a nonlinear 1D analysis of the deformation of the reference line along the larger dimension. SECTIONBUILDER provides the sectional properties associated with the first problem, while DYMORE uses these parameters as inputs to solve the second problem. Both codes will be modified to provide the necessary cross-sectional properties related to the warping behavior of beams, and to compute the correct deformations of beams that are actuated by warping forces.

5.1 Overview of relevant numerical analysis tools

5.1.1 SECTIONBUILDER

SECTIONBUILDER is a finite element tool for the analysis of arbitrary composite beam cross-sections. This code is tailored towards the modeling of rotor blade sections, which can involve different types of metals, complex lay-ups of composite

materials, honeycomb cores, sandwich structures, and complex cellular geometries. It offers several predefined configurations such as simple airfoil sections, I-sections, circular and rectangular geometries, etc. Each section's shape is parametrically defined, and different material properties can be associated with different parts of each section. It also includes a builder allowing the definition of arbitrary cross-sections with arbitrary composite lay-up sequences. Such sections are composed of walls joined by different types of connectors, as well as optional core materials such as honeycombs. Once a model is defined, its cross-sectional properties can be obtained, and stress distributions associated with specific sectional forces and moments can be computed.

As detailed in Ref. 29, a cross-section is analyzed in SECTIONBUILDER in three main steps. First, the model definition phase allows the user to define the topology, geometry and material composition of the cross-section. Next, the computational phase consists of a meshing step and a finite element analysis. The finite element analysis is based on VABS, the Variational Asymptotic Beam Sectional Analysis method originally implemented as a toolset in ANSYS. The concept was introduced in Ref. 27, and References 47, 96, 97 provide further developments and validations of this method. Finally, the post-processing phase allows the user to retrieve the sectional properties, and to visualize stress and strain distributions in 3D.

5.1.2 DYMORE

DYMORE is a comprehensive finite element based multibody dynamics code, described in Ref. 8, that allows modeling and analysis of complex systems such as rotorcraft. It includes an extensive library of: joint elements such as revolute joints, prismatic joints, planar joints and so on; components such as beam elements, rigid body elements or cable elements; boundary conditions and prescribed displacements; and additional elements and properties for modeling specific physical phenomena:

friction, backlash, hydraulic dampers, aerodynamic loading, etc. The code can perform both static and dynamic analyses, as well as additional post-processing tasks, such as Fourier analysis, stability analysis, or signal conditioning. Some of its capabilities have already been demonstrated in Chapter 2, and they will be further extended in this chapter.

The modeling of complex systems in DYMORE is structured in three levels. First, the topology of the system is defined: this step determines the connectivity between the elements without considering the type of the elements or their geometry. Most elements, such as joints, beams or rigid bars, are represented by an edge which has two vertices. Two edges are connected if they share a vertex. A few elements are represented by a vertex alone (such as boundary conditions, point masses, etc.) More complex topological entities such as faces (4 edges on the sides and 4 vertices at the corners) are also possible. This topological description ensures that fundamental properties such as continuity are satisfied.

The second step is the definition of the geometry of the model: this step defines the overall shape, position and orientation of the system in space. Points are attached to vertices and define the coordinates at that location. Curves are used to represent the shape of the reference axis of elements such as beams and cables. Additional geometric entities are available to accurately define the system.

Finally, the element properties are assigned: in this step the properties and characteristics of the elements associated with the topological and geometric entities are defined. For example, the stiffness matrix and inertia characteristics must be defined for beams.

5.1.3 Improvements for analysis of out-of-plane warping concept

As Chapter 4 indicates, the ability to compute warping functions and warping sectional properties is fundamental in the analysis of the new rotor blade morphing

concept. This was achieved by extending SECTIONBUILDER to include these capabilities. This tool provides an ideal platform, since the warping function, after some minor adjustments, is essentially already provided. Standard cross-sectional properties, in particular relevant ones such as the shear center or the torsional stiffness, are also included. Additional computations will therefore be implemented as a post-processing step to produce all required quantities. The theoretical basis of this program extension is presented in Section 5.2.1, while the practical implementation aspects are discussed and validated in Section 5.3.

The ability to analyze the behavior of beam structures in the presence of warping deformation is equally fundamental to assessing this concept. Again, DYMORE already provides some of the necessary capabilities, such as the dynamic analysis of rotor blades. However, its beam models do not include the additional warping degree-of-freedom α. Several steps need to be taken to include warping deformations in DYMORE. In terms of the definition of a model containing warping effects, little needs to change. The definition of the topology of the system, as well as of its geometry, is hardly changed. The existing element properties are unchanged as well, but new properties need to be included based on the expanded analysis in SECTIONBUILDER. In particular, boundary conditions involving warping must be treated appropriately. Most changes to the code will occur in the meshing and finite element stages. The computation must accomodate the presence of a new degree-of-freedom. This alters the treatment of nodes and nodal values, as well as the computation of elemental matrices and elemental load vectors. The assembly of elemental matrices into the global matrices is naturally affected. Theoretical aspects of these modifications can be found in Sections 5.2.2 and 5.2.3. The implementation and its validation are tackled in Section 5.4.

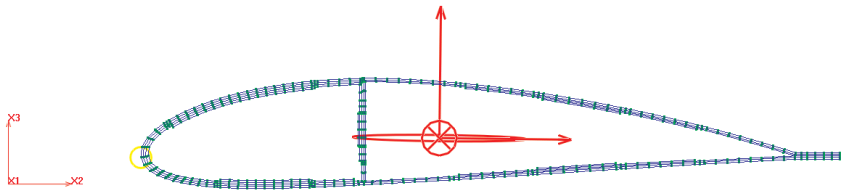

Figure 40: A blade cross-section model in SECTIONBUILDER

5.2 Theoretical foundation

5.2.1 Two-dimensional cross-sectional analysis

Vlasov beam theory for warping and torsion of beams with open thin-walled sections is effective to derive analytical results for simple cross-sectional geometries. However, for more complicated geometries, potentially including complex lay-ups of composite materials, a numerical solution of the cross-sectional properties associated with torsion and out-of-plane warping is required. The beam cross-sectional analysis code SECTIONBUILDER which was introduced in the previous section will therefore be used. Beams with arbitrary cross-sections can be analyzed, such as the one depicted in Fig. 40, and the code is tailored towards the modeling of rotor blades.

The theoretical formulation presented in Chapter 4 relies on the characteristics of the beam section to simplify a two-dimensional problem in the plane of the cross-section into a one-dimensional problem along the contour defining it. On the other hand, SECTIONBUILDER performs a general analysis of arbitrary cross-sections in two dimensions; no assumptions are made about the geometry. In other words, whereas the warping function computed by the classical theory depends only on a single variable, the arc length along the curve, the warping function computed by SECTIONBUILDER varies along both cross-sectional coordinates x_2 and x_3, shown in Fig. 41. A new set of sectional coefficients describing the out-of-plane warping behavior needs to be computed and integrated to the existing analysis in SECTIONBUILDER. Since this code already provides the warping function, it is assumed to be

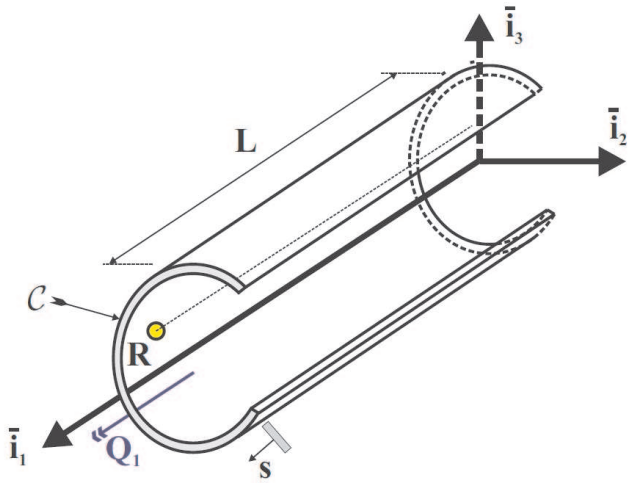

Figure 41: Coordinate system associated with a typical thin-walled open section

known and the following developments will detail the computation of the associated properties. They will be obtained using a process similar to that of Chapter 4.

Let x_1 be the coordinate along the length of the beam, and x_2 and x_3 those in the plane of the cross-section $\mathcal{A}$. Let x_{2r} and x_{3r} be the coordinates of the center of twist in the plane of the section, and $\Psi(x_2, x_3)$ the warping function for that cross-section. Using the following kinematic assumptions for the displacement of the beam cross-section

$$u_1(x_1, x_2, x_3) = \Psi(x_2, x_3)\,\alpha(x_1), \tag{77a}$$

$$u_2(x_1, x_2, x_3) = -\,(x_3 - x_{3r})\,\phi_1(x_1), \tag{77b}$$

$$u_3(x_1, x_2, x_3) = \quad (x_2 - x_{2r})\,\phi_1(x_1), \tag{77c}$$

the non-zero components of the stress field, under the assumption of small displacements and linear elastic isotropic material, are found to be

$$\sigma_1 = E\,\Psi(x_2, x_3)\,\frac{\mathrm{d}\alpha}{\mathrm{d}x_1}, \tag{78a}$$

$$\tau_{12} = G\,\frac{\partial \Psi}{\partial x_2}\,\alpha - G\,(x_3 - x_{3r})\,\kappa_1, \tag{78b}$$

$$\tau_{13} = G\,\frac{\partial \Psi}{\partial x_3}\,\alpha + G\,(x_2 - x_{2r})\,\kappa_1. \tag{78c}$$

The strain energy of the beam undergoing twisting and warping is

$$A = \frac{1}{2}\int_0^L \int_{\mathcal{A}} \left[\frac{\sigma_1^2}{E} + \frac{\tau_{12}^2}{G} + \frac{\tau_{13}^2}{G}\right] \mathrm{d}\mathcal{A}\,\mathrm{d}x_1. \tag{79}$$

After substituting into A the expressions for σ_1, τ_{12} and τ_{13}, one finds

$$A = \frac{1}{2}\int_0^L \left[I_0 \left(\frac{\mathrm{d}\phi_1}{\mathrm{d}x_1}\right)^2 - 2I_1 \frac{\mathrm{d}\phi_1}{\mathrm{d}x_1}\,\alpha + I_2\,\alpha^2 + H_{11w}\left(\frac{\mathrm{d}\alpha}{\mathrm{d}x_1}\right)^2\right] \mathrm{d}x_1, \tag{80}$$

in which the following warping-related coefficients were introduced

$$I_0 = \int_{\mathcal{A}} G\left[(x_2 - x_{2r})^2 + (x_3 - x_{3r})^2\right] \mathrm{d}\mathcal{A}, \tag{81a}$$

$$I_1 = \int_{\mathcal{A}} G\left[(x_3 - x_{3r})\frac{\partial \Psi}{\partial x_2} - (x_2 - x_{2r})\frac{\partial \Psi}{\partial x_3}\right] \mathrm{d}\mathcal{A}, \tag{81b}$$

$$I_2 = \int_{\mathcal{A}} G\left[\left(\frac{\partial \Psi}{\partial x_2}\right)^2 + \left(\frac{\partial \Psi}{\partial x_3}\right)^2\right] \mathrm{d}\mathcal{A}, \tag{81c}$$

and

$$H_{11w} = \int_{\mathcal{A}} E\Psi^2\,\mathrm{d}\mathcal{A}. \tag{82}$$

It is interesting to introduce $\bar{I}_0 = I_0 - H_{11}$ where H_{11} is the usual torsional stiffness of the beam, so that

$$A = \frac{1}{2}\int_0^L \left[H_{11}\left(\frac{\mathrm{d}\phi_1}{\mathrm{d}x_1}\right)^2 + \bar{I}_0\left(\frac{\mathrm{d}\phi_1}{\mathrm{d}x_1}\right)^2 - 2I_1\frac{\mathrm{d}\phi_1}{\mathrm{d}x_1}\,\alpha + I_2\,\alpha^2 + H_{11w}\left(\frac{\mathrm{d}\alpha}{\mathrm{d}x_1}\right)^2\right] \mathrm{d}x_1, \tag{83}$$

If we substituted the notation I_p instead of $\bar{I}_0$, I_1 and I_2, the three terms involving these constants would reduce to $I_p(\kappa_1 - \alpha)^2$, and the strain energy would have the same form as in Chapter 4.

For comparison purposes, Table 4 shows the correspondence between this new set of coefficients and those obtained under the thin-walled beam assumption. A simple formula for the torsional stiffness may be used in the latter case (a derivation may be found in Ref. 9), while H_{11}^{sb} is the same quantity as computed by SECTIONBUILDER. Of course, when analyzing a thin-walled section in this code, the torsional stiffness computed numerically would approximately be equal to the corresponding

Table 4: Sectional coefficients computed using the classical theory and using SECTIONBUILDER

Coefficient	Vlasov theory for thin-walled beams	2D theory suitable for SECTIONBUILDER
Torsional stiffness	$H_{11} = \frac{1}{3}Glt^3$	H_{11}^{sb}
Warping stiffness	$H_{11w} = \int_{\mathcal{C}} E\Psi^2 t \, \mathrm{d}s$	$H_{11w} = \int_{\mathcal{A}} E\Psi^2 \mathrm{d}\mathcal{A}$
Additional constants	$I_p = \int_{\mathcal{C}} G r_r^2 t \, \mathrm{d}s$	$I_0 = \int_{\mathcal{A}} G \left[(x_2 - x_{2r})^2 + (x_3 - x_{3r})^2\right] \mathrm{d}\mathcal{A}$
		$I_1 = \int_{\mathcal{A}} G \left[(x_3 - x_{3r}) \frac{\partial \Psi}{\partial x_2} - (x_2 - x_{2r}) \frac{\partial \Psi}{\partial x_3}\right] \mathrm{d}\mathcal{A}$
		$I_2 = \int_{\mathcal{A}} G \left[\left(\frac{\partial \Psi}{\partial x_2}\right)^2 + \left(\frac{\partial \Psi}{\partial x_3}\right)^2\right] \mathrm{d}\mathcal{A}$

simple theoretical result. The expressions for the warping stiffness H_{11w} are essentially identical. Finally, additional constants are required, and they take different forms depending on the assumptions made.

This summary shows that if Ψ is available from SECTIONBUILDER, all warping-related quantities can be computed, using numerical differentiation based on the finite element interpolation functions for the partial derivatives of Ψ, and numerical integration over all elemental Gauss points to compute the integrals over the surface $\mathcal{A}$. The extraction of the warping function using SECTIONBUILDER consists of applying a unit sectional twisting moment and determining the corresponding out-of-plane (axial) displacement throughout the cross-section. It should be emphasized it is obtained without any constraints on the location of the center of twist. The modified function for the same section with a slider constraint may simply be obtained through the transformation detailed in Section 4.1.2.

The out-of-plane displacement output from SECTIONBUILDER is normalized with respect to a different reference plane than that defined by the vanishing of the

axial force and bending moments. As highlighted in Section 4.1.1, a simple redefinition of the reference plane can be applied to ensure equilibrium conditions are imposed. In fact, this renormalization can be performed without explicit knowledge of the previous normalization. Let us denote by $\Psi_{\text{sb}}(x_2, x_3)$ the original result computed by SECTIONBUILDER. The renormalized form is then found as

$$\Psi = \Psi_{\text{sb}} + \lambda_2 x_3 - \lambda_3 x_2 + \mu, \tag{84}$$

where the coefficients λ_2, λ_3 and μ can be computed by solving

$$\begin{bmatrix} S & Sx_{3c} & -Sx_{2c} \\ Sx_{3c} & H^o_{22} & -H^o_{23} \\ -Sx_{2c} & -H^o_{23} & H^o_{33} \end{bmatrix} \begin{Bmatrix} \mu \\ \lambda_2 \\ \lambda_3 \end{Bmatrix} = \begin{Bmatrix} -\int_{\mathcal{A}} E\Psi \,\mathrm{d}\mathcal{A} \\ -\int_{\mathcal{A}} E\Psi x_3 \,\mathrm{d}\mathcal{A} \\ \int_{\mathcal{A}} E\Psi x_2 \,\mathrm{d}\mathcal{A} \end{Bmatrix} \tag{85}$$

about an arbitrarily chosen point O of the cross-section. As before, choosing principal centroidal axes of bending simplifies the formulation.

5.2.2 One-dimensional beam equations

As was detailed in Chapter 4, once the sectional coefficients related to warping are determined, it is possible to analyze the response of beams under twisting and warping. In anticipation of the implementation of warping degrees-of-freedom in DYMORE for dynamic analyses, dynamic beam equations will be derived. The static equations will be treated as a special case.

The strain energy for a beam under twisting and warping deformation is given by Eq. (83), where the sectional coefficients H_{11}, I_0, I_1, I_2 and H_{11w} are assumed to be known. Note that variables $\phi_1 = \phi_1(x_1, t)$ and $\alpha = \alpha(x_1, t)$ now depend both on the spatial coordinate along the beam's reference axis, and time. As a consequence, derivatives with respect to x_1 should be replaced with partial derivatives.

The kinetic energy of a differential element of material in the beam is

$$\mathrm{d}^3 K = \frac{1}{2}(\rho \,\mathrm{d}\mathcal{A}\,\mathrm{d}x_1)\, v^2, \tag{86}$$

where ρ denotes the material density. The speed of that differential element, v, is obtained by differentiating Eqs. (77)

$$\frac{\partial u_1}{\partial t} = \Psi(x_2, x_3)\,\frac{\partial \alpha}{\partial t}(x_1, t), \tag{87a}$$

$$\frac{\partial u_2}{\partial t} = -\,(x_3 - x_{3r})\,\frac{\partial \phi_1}{\partial t}(x_1, t), \tag{87b}$$

$$\frac{\partial u_3}{\partial t} = \quad (x_2 - x_{2r})\,\frac{\partial \phi_1}{\partial t}(x_1, t), \tag{87c}$$

so that finally

$$v^2 = \Psi^2 \left(\frac{\partial \alpha}{\partial t}\right)^2 + (x_3 - x_{3r})^2 \left(\frac{\partial \phi_1}{\partial t}\right)^2 + (x_2 - x_{2r})^2 \left(\frac{\partial \phi_1}{\partial t}\right)^2. \tag{88}$$

Integrating over the volume of the beam yields the total kinetic energy

$$K = \frac{1}{2}\int_0^L \int_{\mathcal{A}} \left\{ \rho\Psi^2 \left(\frac{\partial \alpha}{\partial t}\right)^2 + \rho\left[(x_2 - x_{2r})^2 + (x_3 - x_{3r})^2\right] \left(\frac{\partial \phi_1}{\partial t}\right)^2 \right\} \mathrm{d}\mathcal{A}\,\mathrm{d}x_1, \tag{89}$$

which may be expressed as

$$K = \frac{1}{2}\int_0^L \left\{ M_w \left(\frac{\partial \alpha}{\partial t}\right)^2 + I_r \left(\frac{\partial \phi_1}{\partial t}\right)^2 \right\} \mathrm{d}x_1, \tag{90}$$

where $M_w = \int_{\mathcal{A}} \rho\Psi^2\,\mathrm{d}\mathcal{A}$ is an inertial sectional property associated with out-of-plane warping deformation, and $I_r = \int_{\mathcal{A}} \rho\left[(x_2 - x_{2r})^2 + (x_3 - x_{3r})^2\right]\mathrm{d}\mathcal{A}$ is the sectional polar moment of inertia about the center of rotation.

Finally, based on expressions in Chapter 4 and adding the dependency on time of all relevant quantities, the virtual work done by the externally applied forces and moments is composed of

$$\overline{\delta W}_1 = -Q_1^0(t)\,\delta\phi_1(0,t) + Q_1^L(t)\,\delta\phi_1(L,t), \tag{91a}$$

$$\overline{\delta W}_2 = \int_0^L q_1(x_1,t)\delta\phi_1(x_1,t)\,\mathrm{d}x_1, \tag{91b}$$

$$\overline{\delta W}_3 = -\hat{F}^0(t)\,\delta\alpha(0,t) + \hat{F}^L(t)\,\delta\alpha(L,t), \tag{91c}$$

$$\overline{\delta W}_4 = \int_0^L \hat{f}(x_1,t)\delta\alpha(x_1,t)\,\mathrm{d}x_1, \tag{91d}$$

where all quantities are defined as before. Note that the $\Delta\Psi$ terms in the definitions of $\hat{F}^0$, $\hat{F}^L$ and $\hat{f}$ are now simply determined by the x_2 and x_3 coordinates of the points of application of axial warping forces, rather than the curvilinear coordinate s.

Application of Hamilton's Extended Principle allows us to find the equations of motion. For arbitrary times t_1 and t_2,

$$\int_{t_1}^{t_2} \left[\delta(K - A) + \overline{\delta W}\right] \, \mathrm{d}t = 0 \quad \text{and} \quad \delta\phi_1 = \delta\alpha = 0 \text{ at } t_1, \, t_2. \tag{92}$$

Substituting in the expressions for K, A and $\overline{\delta W}$,

$$\begin{aligned} 0 = \int_{t_1}^{t_2} \Bigg\{ \int_0^L \Bigg[& M_w \frac{\partial\alpha}{\partial t}\frac{\partial\delta\alpha}{\partial t} + I_r \frac{\partial\phi_1}{\partial t}\frac{\partial\delta\phi_1}{\partial t} - H_{11w}\frac{\partial\alpha}{\partial x_1}\frac{\partial\delta\alpha}{\partial x_1} - I_0 \frac{\partial\phi_1}{\partial x_1}\frac{\partial\delta\phi_1}{\partial x_1} \\ & + I_1\left(\frac{\partial\delta\phi_1}{\partial x_1}\alpha + \frac{\partial\phi_1}{\partial x_1}\delta\alpha\right) - I_2\alpha\delta\alpha + q_1\delta\phi_1 + \hat{f}\delta\alpha \Bigg] \, \mathrm{d}x_1 \\ & - Q_1^0\delta\phi_1(0,t) + Q_1^L\delta\phi_1(L,t) - \hat{F}^0(t)\delta\alpha(0,t) + \hat{F}^L(t)\delta\alpha(L,t) \Bigg\} \, \mathrm{d}t. \end{aligned} \tag{93}$$

Next, integration by parts in time is performed on all terms involving time derivatives of variations, and the generated boundary terms are set to zero by virtue of the vanishing of $\delta\phi_1$ and $\delta\alpha$ at times t_1 and t_2. Since this time interval is arbitrary, the integrand must be zero for all t and the integral over time may be removed to find

$$\begin{aligned} 0 = \int_0^L \Bigg[& \frac{\partial}{\partial t}\left(M_w\frac{\partial\alpha}{\partial t}\right)\delta\alpha + \frac{\partial}{\partial t}\left(I_r\frac{\partial\phi_1}{\partial t}\right)\delta\phi_1 - H_{11w}\frac{\partial\alpha}{\partial x_1}\frac{\partial\delta\alpha}{\partial x_1} - I_0\frac{\partial\phi_1}{\partial x_1}\frac{\partial\delta\phi_1}{\partial x_1} \\ & + I_1\left(\frac{\partial\delta\phi_1}{\partial x_1}\alpha + \frac{\partial\phi_1}{\partial x_1}\delta\alpha\right) - I_2\alpha\delta\alpha + q_1\delta\phi_1 + \hat{f}\delta\alpha \Bigg] \, \mathrm{d}x_1 \\ & - Q_1^0\delta\phi_1(0,t) + Q_1^L\delta\phi_1(L,t) - \hat{F}^0(t)\delta\alpha(0,t) + \hat{F}^L(t)\delta\alpha(L,t). \end{aligned} \tag{94}$$

As in Section 4.1.3, all terms involving spatial derivatives of variations are integrated by parts, and finally, the arbitrariness of $\delta\phi_1$ and $\delta\alpha$ is used to obtain the partial differential equations of motion

$$\frac{\partial}{\partial t}\left(I_r\frac{\partial\phi_1}{\partial t}\right) + \frac{\partial}{\partial x_1}\left(H_{11}\frac{\partial\phi_1}{\partial x_1}\right) + \frac{\partial}{\partial x_1}\left(\bar{I}_0\frac{\partial\phi_1}{\partial x_1} - I_1\alpha\right) = -q_1, \tag{95a}$$

$$\frac{\partial}{\partial t}\left(M_w\frac{\partial\alpha}{\partial t}\right) + \frac{\partial}{\partial x_1}\left(H_{11w}\frac{\partial\alpha}{\partial x_1}\right) + \left(I_1\frac{\partial\phi_1}{\partial x_1} - I_2\alpha\right) = -\hat{f}, \tag{95b}$$

as well as the boundary conditions at $x_1 = 0$

$$H_{11}\frac{\partial \phi_1}{\partial x_1}(0,t) + \bar{I}_0\frac{\partial \phi_1}{\partial x_1}(0,t) - I_1\alpha(0,t) = Q_1^0(t) \qquad \text{or} \qquad \delta\phi_1(0,t) = 0, \tag{96}$$

$$H_{11w}\frac{\partial \alpha}{\partial x_1}(0,t) = \hat{F}^0(t) \qquad \text{or} \qquad \delta\alpha(0,t) = 0, \tag{97}$$

and at $x_1 = L$

$$H_{11}\frac{\partial \phi_1}{\partial x_1}(L,t) + \bar{I}_0\frac{\partial \phi_1}{\partial x_1}(L,t) - I_1\alpha(L,t) = Q_1^L(t) \qquad \text{or} \qquad \delta\phi_1(L,t) = 0, \tag{98}$$

$$H_{11w}\frac{\partial \alpha}{\partial x_1}(L,t) = \hat{F}^L(t) \qquad \text{or} \qquad \delta\alpha(L,t) = 0, \tag{99}$$

These equations will form the basis of the developments in the next section.

As was pointed out earlier, the corresponding equations for the application of the Vlasov theory for thin-walled open section beams can be retrieved as a special case of these equations. The substitution

$$\bar{I}_0 = I_1 = I_2 = I_p \tag{100}$$

would yield the correct equations.

After removing all time derivatives, the static differential equations are

$$\frac{\mathrm{d}}{\mathrm{d}x_1}\left(H_{11}\frac{\mathrm{d}\phi_1}{\mathrm{d}x_1}\right) + \frac{\mathrm{d}}{\mathrm{d}x_1}\left(\bar{I}_0\frac{\mathrm{d}\phi_1}{\mathrm{d}x_1} - I_1\alpha\right) = -q_1, \tag{101a}$$

$$\frac{\mathrm{d}}{\mathrm{d}x_1}\left(H_{11w}\frac{\mathrm{d}\alpha}{\mathrm{d}x_1}\right) + \left(I_1\frac{\mathrm{d}\phi_1}{\mathrm{d}x_1} - I_2\alpha\right) = -\hat{f}, \tag{101b}$$

and the boundary conditions are identical to those listed in Eqs. (96), (97), (98) and (99), with the time dependency removed. Assuming q_1 and $\hat{f}$ to be constant distributed forces along the span of the beam, the general solution of these differential equations has the form

$$\alpha(x_1) = C_1\sinh(\omega x_1) + C_2\cosh(\omega x_1) - \frac{I_1 q_1}{I_0 I_2 - I_1^2}\,x_1 + C_3, \tag{102a}$$

$$\phi_1(x_1) = \frac{I_1 C_1}{I_0\omega}\cosh(\omega x_1) + \frac{I_1 C_2}{I_0\omega}\sinh(\omega x_1) - \frac{I_2 q_1}{I_0 I_2 - I_1^2}\,\frac{x_1^2}{2} + \frac{I_2 C_3 - \hat{f}}{I_1}\,x_1 + \frac{I_2 C_4}{I_1}, \tag{102b}$$

in which the constant ω was defined as

$$\omega = \sqrt{\frac{I_0 I_2 - I_1^2}{I_0 H_{11w}}}, \tag{103}$$

and where coefficients C_1, C_2, C_3 and C_4 can be determined by choosing a particular set of boundary conditions.

It will now be shown that $I_0 I_2 - I_1^2 \geq 0$, and hence ω is a real constant. We denote the usual Euclidean inner product by $\cdot$ and the associated Euclidean norm by $\|\cdot\|_2$. We also define

$$< \underline{f}, \underline{g} >= \int_{\mathcal{A}} \underline{f} \cdot \underline{g} \, \mathrm{d}\mathcal{A} \qquad \text{and} \qquad \|\underline{f}\| = \left[\int_{\mathcal{A}} \|\underline{f}\|_2^2 \, \mathrm{d}\mathcal{A} \right]^{1/2}, \tag{104}$$

which can easily be shown to be an inner product and a norm respectively. The Cauchy-Schwartz inequality therefore holds

$$| < \underline{f}, \underline{g} > | \leq \|\underline{f}\| \|\underline{g}\|. \tag{105}$$

Introducing

$$\underline{f} = \begin{Bmatrix} -\sqrt{G}\,(x_2 - x_{2r}) \\ \sqrt{G}\,(x_3 - x_{3r}) \end{Bmatrix} \qquad \text{and} \qquad \underline{g} = \begin{Bmatrix} \sqrt{G}\,\frac{\partial \Psi}{\partial x_3} \\ \sqrt{G}\,\frac{\partial \Psi}{\partial x_2} \end{Bmatrix}, \tag{106}$$

I_0, I_1 and I_2 can be written in terms of this inner product and this norm as

$$I_0 = \|\underline{f}\|^2, \qquad I_1 =< \underline{f}, \underline{g} >, \qquad I_2 = \|\underline{g}\|^2. \tag{107}$$

Applying the Cauchy-Schwartz inequality, we finally find that

$$I_1^2 \leq I_0 I_2, \tag{108}$$

and hence, ω is indeed a real constant.

Table 5 summarizes the values of coefficients C_1, C_2, C_3 and C_4 for several combinations of boundary conditions and distributed loads. Case I refers to a cantilevered beam with constrained warping displacement at the root and an externally applied

Table 5: Solution constants for several cases

	C_1	C_2	C_3	C_4
Case I	$\frac{I_1 Q \tanh(\omega L)}{I_0 I_2 - I_1^2}$	$-\frac{I_1 Q}{I_0 I_2 - I_1^2}$	$\frac{I_1 Q}{I_0 I_2 - I_1^2}$	$-\frac{I_1^2}{I_0 I_2 \omega}\frac{I_1 Q \tanh(\omega L)}{I_0 I_2 - I_1^2}$
Case II	0	0	$\frac{I_1 Q}{I_0 I_2 - I_1^2}$	0
Case III	$\frac{\hat{F}}{\omega H_{11w}}$	$-\frac{\hat{F}}{\omega H_{11w}\tanh(\omega L)}$	0	$-\frac{\hat{F}}{I_0\left(\frac{I_2}{I_1}\right)^2 - I_2}$
Case IV	0	0	$\frac{\hat{f}}{\omega^2 H_{11w}}$	0

end torque Q. Case II is similar to case I, but leaves α free at the root. Case III is a cantilevered beam with a free end but applied concentrated root actuation $\hat{F} = F\Delta\Psi$, while case IV has applied distributed warping actuation $\hat{f} = f\Delta\Psi$ instead. Again, it should be remembered that these equations apply in the framework of the Vlasov thin-walled beam theory with the proper substitutions, see Eq. (100).

5.2.3 Application to finite element formulation in DYMORE

First, the dynamic equations from the previous section will be cast in a more appropriate form for implementation in DYMORE. For a typical beam element in DYMORE, the equations of motion can be expressed in their most general form as

$$\underline{\mathcal{F}}^I - \underline{\mathcal{F}}^{C\prime} + \underline{\mathcal{F}}^D = \underline{\mathcal{F}}^G + \underline{\mathcal{F}}^{\text{ext}}, \tag{109}$$

where $\underline{\mathcal{F}}^I$ represents the inertial forces associated with the beam element, $\underline{\mathcal{F}}^C$ and $\underline{\mathcal{F}}^D$ the elastic forces (which may include dissipative forces as well as the effect of extension-twist material coupling), $\underline{\mathcal{F}}^G$ the gravity forces, and $\underline{\mathcal{F}}^{\text{ext}}$ the external forces applied to the beam (distributed forces and moments). $(\cdot)'$ indicates differentiation with respect to the spatial coordinate along the beam reference line. Detailed expressions for these forces may be found in the DYMORE user manual (Ref. 5). Furthermore, since these forces are in general nonlinear, a linearization is required for

the computational process. If we introduce the incremental arrays of displacement, velocity and acceleration

$$\Delta \underline{q} = \begin{Bmatrix} \Delta \underline{u} \\ \Delta \underline{c} \end{Bmatrix}, \qquad \Delta \underline{\dot{q}} = \begin{Bmatrix} \Delta \underline{\dot{u}} \\ \Delta \underline{\dot{c}} \end{Bmatrix}, \qquad \Delta \underline{\ddot{q}} = \begin{Bmatrix} \Delta \underline{\ddot{u}} \\ \Delta \underline{\ddot{c}} \end{Bmatrix}, \tag{110}$$

where $\dot{()}$ represents differentiation with respect to time, $\underline{u}$ is the reference line displacement vector and $\underline{c}$ the array of rotation parameters representing finite rotations, then the increments of the inertial and elastic forces can be shown to have the following general expressions

$$\Delta \underline{\mathcal{F}}^I = \mathcal{K}^I \Delta \underline{q} + \mathcal{G}^I \Delta \underline{\dot{q}} + \mathcal{M}^I \Delta \underline{\ddot{q}}, \tag{111}$$

$$\Delta \underline{\mathcal{F}}^C = \mathcal{S}\, \Delta \underline{q}' + \mathcal{O}\, \Delta \underline{q}, \tag{112}$$

$$\Delta \underline{\mathcal{F}}^D = \mathcal{P}\, \Delta \underline{q}' + \mathcal{Q}\, \Delta \underline{q}. \tag{113}$$

Detailed derivations and results can be found in Ref. 5. In order to include the effect of warping, the equations of motion were modified to include warping terms, and an additional warping equation was added based on the developments of the previous section

$$\underline{\mathcal{F}}^I - \underline{\mathcal{F}}^{C\prime} + \underline{\mathcal{F}}^D + \underline{\mathcal{F}}_\alpha^{P\prime} - \underline{\mathcal{F}}_\alpha^{Q\prime} = \underline{\mathcal{F}}^G + \underline{\mathcal{F}}^{\text{ext}}, \tag{114a}$$

$$\underline{\mathcal{F}}_\alpha^I - \underline{\mathcal{F}}_\alpha^{R\prime} + \underline{\mathcal{F}}_\alpha^S - \underline{\mathcal{F}}_\alpha^T = \underline{\mathcal{F}}_\alpha^{\text{dist}}, \tag{114b}$$

where

$$\underline{\mathcal{F}}_\alpha^I = [M_w \ddot{\alpha}\,,\, 0\,,\, 0\,,\, 0\,,\, 0\,,\, 0]^T, \tag{115a}$$

$$\underline{\mathcal{F}}_\alpha^P = [0\,,\, 0\,,\, 0\,,\, I_1 \alpha\,,\, 0\,,\, 0]^T, \tag{115b}$$

$$\underline{\mathcal{F}}_\alpha^Q = \left[0\,,\, 0\,,\, 0\,,\, \bar{I}_0 \kappa_1\,,\, 0\,,\, 0\right]^T = \left[(\underline{N}^Q)^T\,,\, (\underline{M}^Q)^T\right]^T, \tag{115c}$$

$$\underline{\mathcal{F}}_\alpha^R = [H_{11w} \alpha'\,,\, 0\,,\, 0\,,\, 0\,,\, 0\,,\, 0]^T, \tag{115d}$$

$$\underline{\mathcal{F}}_\alpha^S = [I_2 \alpha\,,\, 0\,,\, 0\,,\, 0\,,\, 0\,,\, 0]^T, \tag{115e}$$

$$\underline{\mathcal{F}}_\alpha^T = [I_1 \kappa_1\,,\, 0\,,\, 0\,,\, 0\,,\, 0\,,\, 0]^T = \left[(\underline{N}^T)^T\,,\, (\underline{M}^T)^T\right]^T, \tag{115f}$$

$$\underline{\mathcal{F}}_\alpha^{\text{dist}} = \left[\hat{f}\,,\, 0\,,\, 0\,,\, 0\,,\, 0\,,\, 0\right]^T. \tag{115g}$$

Note that $\underline{\mathcal{F}}_\alpha^I$, $\underline{\mathcal{F}}_\alpha^R$, $\underline{\mathcal{F}}_\alpha^S$, $\underline{\mathcal{F}}_\alpha^T$ and $\underline{\mathcal{F}}_\alpha^{\text{dist}}$ are all 6-by-1 arrays in which the first element is the only non-zero one. Essentially, the warping equation was simply augmented with five identically zero equations for ease of implementation, as explained in later sections.

As before, the expressions for the incremental forces are needed in order to linearize the equations. They are of the form

$$\Delta\underline{\mathcal{F}}_\alpha^I = X_\alpha^I \, \Delta\underline{\ddot{w}}, \tag{116a}$$

$$\Delta\underline{\mathcal{F}}_\alpha^P = X_\alpha^P \, \Delta\underline{w}, \tag{116b}$$

$$\Delta\underline{\mathcal{F}}_\alpha^Q = X_\alpha^Q \, \Delta\underline{q}' + Y_\alpha^Q \, \Delta\underline{q}, \tag{116c}$$

$$\Delta\underline{\mathcal{F}}_\alpha^R = X_\alpha^R \, \Delta\underline{w}, \tag{116d}$$

$$\Delta\underline{\mathcal{F}}_\alpha^S = X_\alpha^S \, \Delta\underline{w}, \tag{116e}$$

$$\Delta\underline{\mathcal{F}}_\alpha^T = X_\alpha^T \, \Delta\underline{q}' + Y_\alpha^T \, \Delta\underline{q}, \tag{116f}$$

where $\underline{w} = [\alpha, 0, 0, 0, 0, 0]^T$. Defining the set of 6-by-6 matrices $\mathcal{E}_{kl}$ whose components are

$$(\mathcal{E}_{kl})_{i,j} = \begin{cases} 1 & \text{if } i = k \text{ and } j = l, \\ 0 & \text{otherwise,} \end{cases} \tag{117}$$

the 6-by-6 matrices involved in these incremental force equations are

$$X_\alpha^I = M_w \mathcal{E}_{11}, \tag{118a}$$

$$X_\alpha^P = I_1 \mathcal{E}_{41}, \tag{118b}$$

$$X_\alpha^R = H_{11w} \mathcal{E}_{11}, \tag{118c}$$

$$X_\alpha^S = I_2 \mathcal{E}_{11}, \tag{118d}$$

as well as

$$X_\alpha^Q = \bar{C}_0 \begin{bmatrix} I_{3\times3} & 0_{3\times3} \\ 0_{3\times3} & H \end{bmatrix}, \tag{119a}$$

$$Y_\alpha^Q = \begin{bmatrix} 0_{3\times3} & (\tilde{N}^Q)^T H \\ 0_{3\times3} & (\tilde{M}^Q)^T H \end{bmatrix} + \bar{C}_0 \begin{bmatrix} 0_{3\times3} & \tilde{E}_1 H \\ 0_{3\times3} & H' \end{bmatrix}, \tag{119b}$$

in which $\bar{C}_0 = \bar{I}_0 \mathcal{E}_{44}$, and

$$X_\alpha^T = C_1 \begin{bmatrix} I_{3\times3} & 0_{3\times3} \\ 0_{3\times3} & H \end{bmatrix}, \tag{120a}$$

$$Y_\alpha^T = \begin{bmatrix} 0_{3\times3} & (\tilde{N}^T)^T H \\ 0_{3\times3} & (\tilde{M}^T)^T H \end{bmatrix} + C_1 \begin{bmatrix} 0_{3\times3} & \tilde{E}_1 H \\ 0_{3\times3} & H' \end{bmatrix}, \tag{120b}$$

in which $C_1 = I_1 \mathcal{E}_{14}$. $0_{3\times3}$ is the 3-by-3 null matrix, $I_{3\times3}$ the 3-by-3 identity matrix, $\underline{E}_1$ is the unit vector normal to the deformed beam reference cross-sectional plane, H is the operator relating the derivatives of the finite rotation parameters to the components of the angular velocity vector, and $\tilde{a}$ indicates the 3-by-3 skew-symmetric matrix associated with a 3-by-1 vector $\underline{a}$ according to

$$\tilde{a} = \begin{bmatrix} 0 & -a_3 & a_2 \\ a_3 & 0 & -a_1 \\ -a_2 & a_1 & 0 \end{bmatrix}. \tag{121}$$

As described in Ref. 5, a weighted-residual formulation is used to derive the finite element equations for the beam element in terms of nodal values of displacement, velocity and acceleration, as well as nodal values of the warping quantity α and its derivatives. The following notations are introduced first

$$\underline{v}(x_1) = \dot{\underline{q}}(x_1)\,, \qquad \underline{a}(x_1) = \ddot{\underline{q}}(x_1), \tag{122}$$

$$\underline{v}_w(x_1) = \dot{\underline{w}}(x_1)\,, \qquad \underline{a}_w(x_1) = \ddot{\underline{w}}(x_1). \tag{123}$$

Defining $W(x_1)$ as the matrix of assumed shape functions, we can introduce the following interpolations

$$\underline{q}(x_1) = W(x_1)\hat{\underline{q}}, \tag{124a}$$

$$\underline{q}'(x_1) = W'(x_1)\hat{\underline{q}}, \tag{124b}$$

$$\underline{v}(x_1) = W(x_1)\hat{\underline{v}}, \tag{124c}$$

$$\underline{a}(x_1) = W(x_1)\hat{\underline{a}}, \tag{124d}$$

where $\hat{\underline{q}}$, $\hat{\underline{v}}$ and $\hat{\underline{a}}$ are the nodal values of displacement, velocity and acceleration, and

$$\underline{w}(x_1) = W(x_1)\hat{\underline{w}}, \tag{125a}$$

$$\underline{w}'(x_1) = W'(x_1)\hat{\underline{w}}, \tag{125b}$$

$$\underline{v}_w(x_1) = W(x_1)\hat{\underline{v}}_w, \tag{125c}$$

$$\underline{a}_w(x_1) = W(x_1)\hat{\underline{a}}_w, \tag{125d}$$

in which $\hat{\underline{w}}$, $\hat{\underline{v}}_w$ and $\hat{\underline{a}}_w$ are the nodal values of warping displacement, velocity and acceleration.

The weighted-residual form of the dynamic equations of motion, Eqs. (114), is

$$\int_0^L W^T \left(\underline{\mathcal{F}}^I - \underline{\mathcal{F}}^{C\prime} + \underline{\mathcal{F}}^D + \underline{\mathcal{F}}_\alpha^{P\prime} - \underline{\mathcal{F}}_\alpha^{Q\prime} - \underline{\mathcal{F}}^G - \underline{\mathcal{F}}^{\text{ext}} \right) \mathrm{d}x_1 = 0, \tag{126a}$$

$$\int_0^L W^T \left(\underline{\mathcal{F}}_\alpha^I - \underline{\mathcal{F}}_\alpha^{R\prime} + \underline{\mathcal{F}}_\alpha^S - \underline{\mathcal{F}}_\alpha^T - \underline{\mathcal{F}}_\alpha^{\text{dist}} \right) \mathrm{d}x_1 = 0. \tag{126b}$$

In an identical process to that presented in Ref. 5, integration by parts is performed on the weighted-residual form. This step is similar to the integration by parts step in previous derivations of the twisting and warping differential equations under several torques and warping actuation loads. Next, the linearized forms of the various force arrays are introduced in the formulation, in order to cast the equations in terms of incremental quantities. This linearization step, along with the introduction of the previously defined interpolations, finally leads to the weak statement of dynamic

equilibrium, which can be written in the following form

$$\hat{M}\Delta\underline{\hat{a}} + \hat{G}\Delta\underline{\hat{v}} + \hat{K}\Delta\underline{\hat{q}} + \hat{K}^c_\alpha\Delta\underline{\hat{w}} = \underline{\hat{F}}^G + \underline{\hat{F}}^{\text{ext}} - \underline{\hat{F}}^{(1)} + \left[W^T\underline{\mathcal{F}}^C - W^T\underline{\mathcal{F}}^P_\alpha + W^T\underline{\mathcal{F}}^Q_\alpha\right]_0^L, \quad (127a)$$

$$\hat{M}_\alpha\Delta\underline{\hat{a}}_w + \hat{K}_\alpha\Delta\underline{\hat{w}} + \hat{K}^c\Delta\underline{\hat{q}} = \underline{\hat{F}}^{\text{dist}}_\alpha - \underline{\hat{F}}^{(2)} + \left[W^T\underline{\mathcal{F}}^R_\alpha\right]_0^L, \quad (127b)$$

where we have introduced the following matrices

$$\hat{M} = \int_0^L W^T\mathcal{M}^I W\,\mathrm{d}x_1, \quad (128a)$$

$$\hat{G} = \int_0^L W^T\mathcal{G}^I W\,\mathrm{d}x_1, \quad (128b)$$

$$\hat{K} = \int_0^L \left[W^T\mathcal{K}^I W + W'^T\mathcal{S}W' + W'^T\mathcal{O}W + W^T\mathcal{P}W' + W^T\mathcal{Q}W + W'^T X^Q_\alpha W' + W'^T Y^Q_\alpha W\right]\mathrm{d}x_1, \quad (128c)$$

$$\hat{K}^c_\alpha = \int_0^L \left[-W'^T X^P_\alpha W\right]\mathrm{d}x_1, \quad (128d)$$

$$\hat{M}_\alpha = \int_0^L W^T X^I_\alpha W\,\mathrm{d}x_1, \quad (128e)$$

$$\hat{K}_\alpha = \int_0^L \left[W'^T X^R_\alpha W' + W^T X^S_\alpha W\right]\mathrm{d}x_1, \quad (128f)$$

$$\hat{K}^c = \int_0^L \left[-W^T X^T_\alpha W' - W^T Y^T_\alpha W\right]\mathrm{d}x_1, \quad (128g)$$

as well as the right-hand side load vectors

$$\underline{\hat{F}}^G = \int_0^L W^T\underline{\mathcal{F}}^G\,\mathrm{d}x_1, \quad (129a)$$

$$\underline{\hat{F}}^{\text{ext}} = \int_0^L W^T\underline{\mathcal{F}}^{\text{ext}}\,\mathrm{d}x_1, \quad (129b)$$

$$\underline{\hat{F}}^{(1)} = \int_0^L \left[W^T\underline{\mathcal{F}}^I + W'^T\underline{\mathcal{F}}^C + W^T\underline{\mathcal{F}}^D - W'^T\underline{\mathcal{F}}^P_\alpha + W'^T\underline{\mathcal{F}}^Q_\alpha\right]\mathrm{d}x_1, \quad (129c)$$

$$\underline{\hat{F}}^{\text{dist}}_\alpha = \int_0^L W^T\underline{\mathcal{F}}^{\text{dist}}_\alpha\,\mathrm{d}x_1, \quad (129d)$$

$$\underline{\hat{F}}^{(2)} = \int_0^L \left[W^T\underline{\mathcal{F}}^I_\alpha + W'^T\underline{\mathcal{F}}^R_\alpha + W^T\underline{\mathcal{F}}^S_\alpha - W^T\underline{\mathcal{F}}^T_\alpha\right]\mathrm{d}x_1. \quad (129e)$$

As will be seen in later sections on the DYMORE implementation of these equations, for a given node in a given beam element, the typical six degrees-of-freedom $\underline{\hat{q}}$ and

the additional warping measure $\underline{\hat{w}}$ are combined in a single array of twelve variables $\{\underline{\hat{q}}^T \ \underline{\hat{w}}^T\}^T$. Note that the last five elements of this array are identically zero and will therefore not be used. They are simply included for ease of implementation. The equations can therefore be combined in the compact form

$$\begin{bmatrix} \hat{M} & 0_{6\times6} \\ 0_{6\times6} & \hat{M}_\alpha \end{bmatrix} \begin{Bmatrix} \Delta\underline{\hat{a}} \\ \Delta\underline{\hat{a}}_w \end{Bmatrix} + \begin{bmatrix} \hat{G} & 0_{6\times6} \\ 0_{6\times6} & 0_{6\times6} \end{bmatrix} \begin{Bmatrix} \Delta\underline{\hat{v}} \\ \Delta\underline{\hat{v}}_w \end{Bmatrix} + \begin{bmatrix} \hat{K} & \hat{K}^c_\alpha \\ \hat{K}^c & \hat{K}_\alpha \end{bmatrix} \begin{Bmatrix} \Delta\underline{\hat{q}} \\ \Delta\underline{\hat{w}} \end{Bmatrix}$$
$$= \begin{Bmatrix} \underline{\hat{F}}^G + \underline{\hat{F}}^{\text{ext}} \\ \underline{\hat{F}}^{\text{dist}}_\alpha \end{Bmatrix} - \begin{Bmatrix} \underline{\hat{F}}^{(1)} \\ \underline{\hat{F}}^{(2)} \end{Bmatrix} + \left[\begin{Bmatrix} W^T\underline{\mathcal{F}}^C - W^T\underline{\mathcal{F}}^P_\alpha + W^T\underline{\mathcal{F}}^Q_\alpha \\ W^T\underline{\mathcal{F}}^R_\alpha \end{Bmatrix} \right]_0^L . \quad (130)$$

5.3 Implementation in SECTIONBUILDER

5.3.1 General procedure

The computation of the warping function and its associated sectional properties is implemented as an additional post-processing step of the current SECTIONBUILDER code. First, the modeling and finite element analysis are mostly unchanged. At the end of the computation phase, the out-of-plane warping displacement over the entire cross-section associated with a unit torque, $u^{\text{unit}}_{1,\text{warp}}(x_2, x_3)$, is available. According to the first of Eqs. (18), and recalling that $\kappa_1 = M_1/H_{11}$, the warping function $\Psi(x_2, x_3)$ is related to this SECTIONBUILDER output through

$$\Psi = H_{11} u^{\text{unit}}_{1,\text{warp}}, \quad (131)$$

H_{11} being also obtained numerically. However, as was discussed in previous sections, this warping function is normalized differently than in the classical Vlasov theory. Regardless of the initial normalization, the reference plane of the warping function can be adjusted using the process described in Section 5.2.1. Next, the new sectional coefficients, which the code does not yet provide, are computed as integrals over the surface of the cross-section according to Eqs. (81) and (82). These integrals are numerically calculated based on a discrete summation of the integrands' values at all

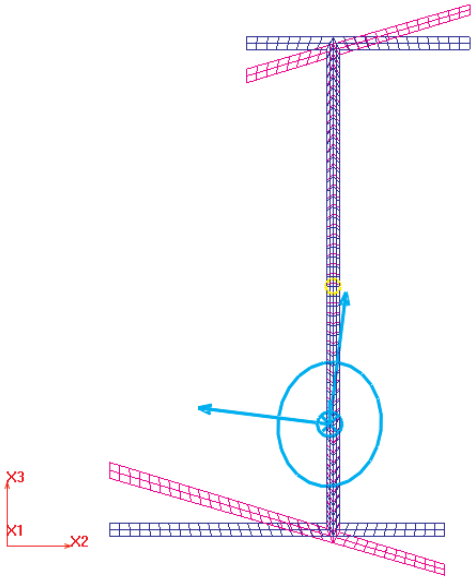

Figure 42: I-beam cross-section as modeled in SECTIONBUILDER, and the corresponding warping function

the Gauss points of the elements of the model. Based on its values at each node, the integrand is interpolated at each of the Gauss points and this contribution is then added to the total numerical integral. Once this process is completed, the sectional warping coefficients are printed in an output file to be used in beam analyses. Finally, the user can analyse the results and visualize them in the last stage.

5.3.2 Validation of cross-sectional properties

The implementation was tested on various I-beam configurations for which these coefficients could be computed by hand. The most general case for which a reasonably simple analytical result could be obtained is that of an I-beam with four flanges of different lengths, as represented in Fig. 42.

The warping function obtained analytically and that computed by SECTIONBUILDER are compared in Fig. 43. It reveals extremely good correlation between them, which shows the efficiency of the renormalization process in yielding the correct warping function. Note that the analytical result under the thin wall assumption is

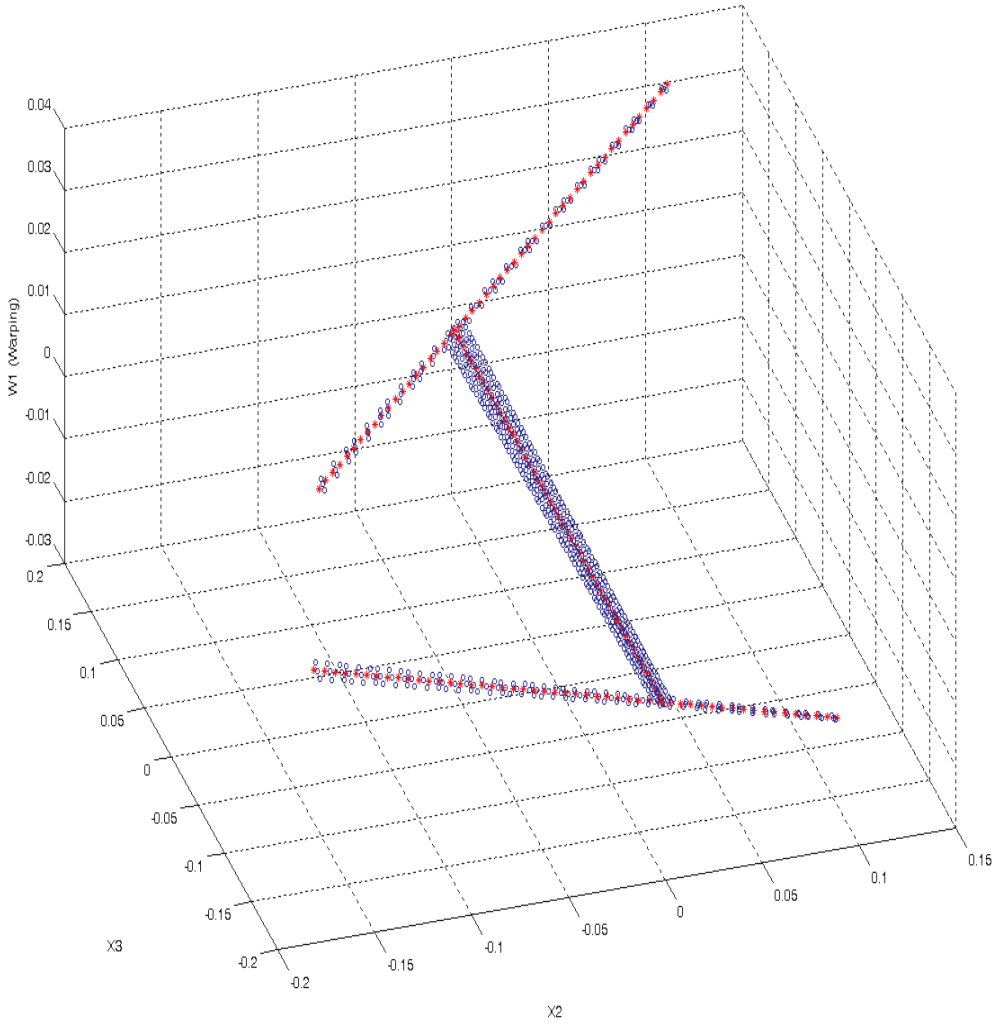

Figure 43: Warping functions from the thin-walled beam theory (∗) and from SECTIONBUILDER (∘)

Table 6: Comparison of the sectional coefficients from the theory and from SECTIONBUILDER

			Theory	SECTIONBUILDER
Shear Center	[m]	x_{2k}	$-2.7363 \cdot 10^{-3}$	$-2.7854 \cdot 10^{-3}$
	[m]	x_{3k}	$-1.1073 \cdot 10^{-1}$	$-1.1049 \cdot 10^{-1}$
Torsional stiffness	[N·m^2]	H_{11}	$7.8615 \cdot 10^{3}$	$7.8430 \cdot 10^{3}$
Warping stiffness	[N·m^4]	H_{11w}	$4.5464 \cdot 10^{4}$	$4.5311 \cdot 10^{4}$
Additional constants	[N·m^2]	I_p	$5.2630 \cdot 10^{6}$	
	[N·m^2]	I_0		$8.6055 \cdot 10^{6}$
	[N·m^2]	$\bar{I}_0$		$8.5977 \cdot 10^{6}$
	[N·m^2]	I_1		$8.5977 \cdot 10^{6}$
	[N·m^2]	I_2		$8.5977 \cdot 10^{6}$

represented by the curve along the contour line. The variation through the thickness is not available due to the simplifying assumption. It is however included in the numerical result, but as mentioned in Section 4.1.1, that additional contribution is very small compared to the relatively large global out-of-plane deformation of the open section.

Table 6 shows a quantitative comparison between analytical and SECTIONBUILDER based results for various cross-sectional parameters. The section was assumed isotropic with Young's modulus of 73GPa and Poisson's ratio of 0.3. The results from SECTIONBUILDER match those from the theory very closely. Fair agreement exists between I_p and its more general counterparts. The comparison of the theoretical expressions for I_p and I_0 for example shows that in general, they will result in different values. Indeed, both involve similar integrals, but the former involves a factor r_r^2 related to the distance between R and the tangent to the contour line, while the latter involves a factor d_r^2 where d_r is simply the distance between R and the contour line. Clearly, these factors are in general different, and there is no reason to believe their respective integrals would yield the same values. The discrepancy observed here is a manifestation of these differences, and other simple examples could be constructed to demonstrate this point. I_0, I_1 and I_2 are however of the same order of magnitude

as I_p. Note also that $I_0 - H_{11} = I_1 = I_2$.

For most typical open thin-walled sections, I_p is much larger than H_{11}. This I-beam section is a clear example. To illustrate this point, consider a homogeneous section with torsional stiffness $H_{11} = 1/3\, Glt^3$ and warping coefficient $I_p = Gt \int_{\mathcal{C}} r_k^2 \, \mathrm{d}s$. Introduce $r_{\min}$ the positive number such that $r_{\min}^2 = \min_{\mathcal{C}}(r_k^2)$. Then, $I_p/H_{11} \geq 3(r_{\min}/t)^2$. As long as $r_{\min}$ is sensibly larger than t, a fairly common situation for open thin-walled sections, H_{11} will be an order of magnitude smaller than I_p or more. Even if $r_{\min}$ is small, chances are high that a reasonable portion of the open section would still have r_k much larger than t, in which case the same conclusion holds. The subsequent inference is that, in most cases, if a discrepancy exists between I_p and I_0, as is the case here, a similar discrepancy will remain between I_p and $\bar{I}_0$. In other words, the difference is not attributable to whether the torsional stiffness is taken into account or not.

5.3.3 Validation of beam equations

First, a long cantilevered beam with the cross-section shown in Fig. 42 and whose sectional properties are listed in Tab. 6 is analyzed. The beam is assumed to have constrained warping at the root and to be subjected to an end torque. Figures 44 and 45 show nondimensionalized analysis results. The Saint-Venant results refer to the case of uniform torsion without considering warping. It represents the limiting case in which the beam is infinite and the localized effect of warping at the root becomes insignificant. Next, the same comparison was made for the case of concentrated axial actuation at the root in Figures 46 and 47. In this case, a Saint-Venant solution is not available since warping deformation is necessarily involved. Both cases show an excellent agreement between the analytical solutions obtained under the thin wall assumption and those involving the coefficients computed with SECTIONBUILDER. This strong correlation is not particularly surprising, since the only terms that are

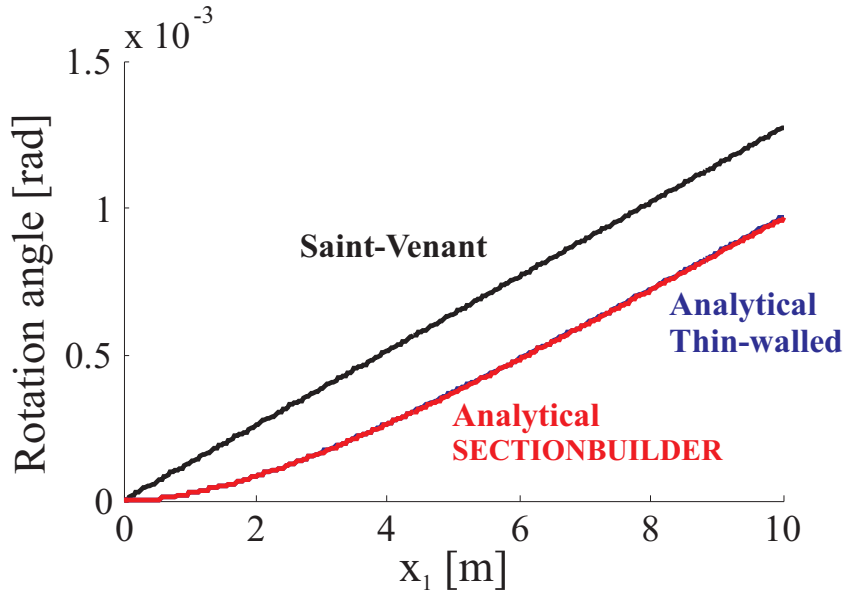

Figure 44: Spanwise rotation angle for cantilevered beam with end torque

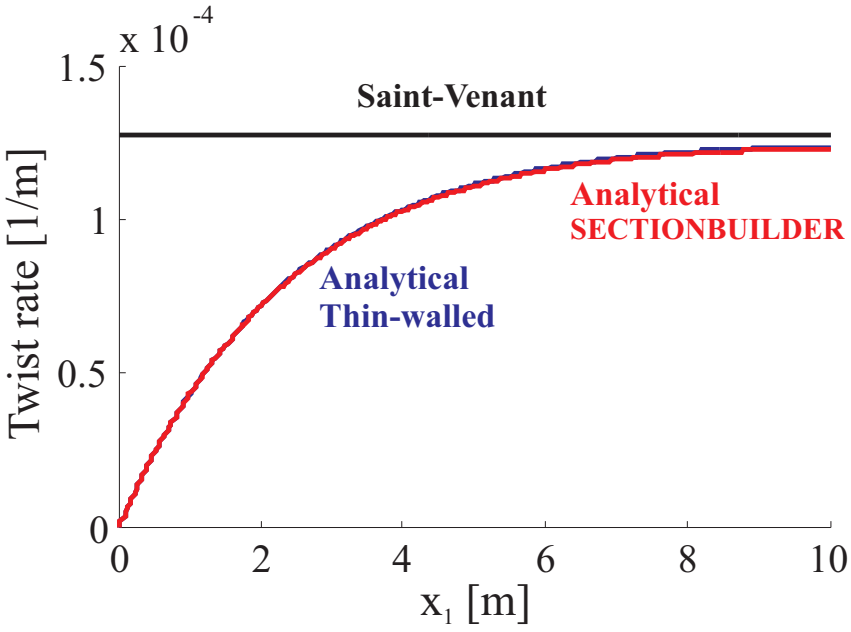

Figure 45: Spanwise twist rate for cantilevered beam with end torque

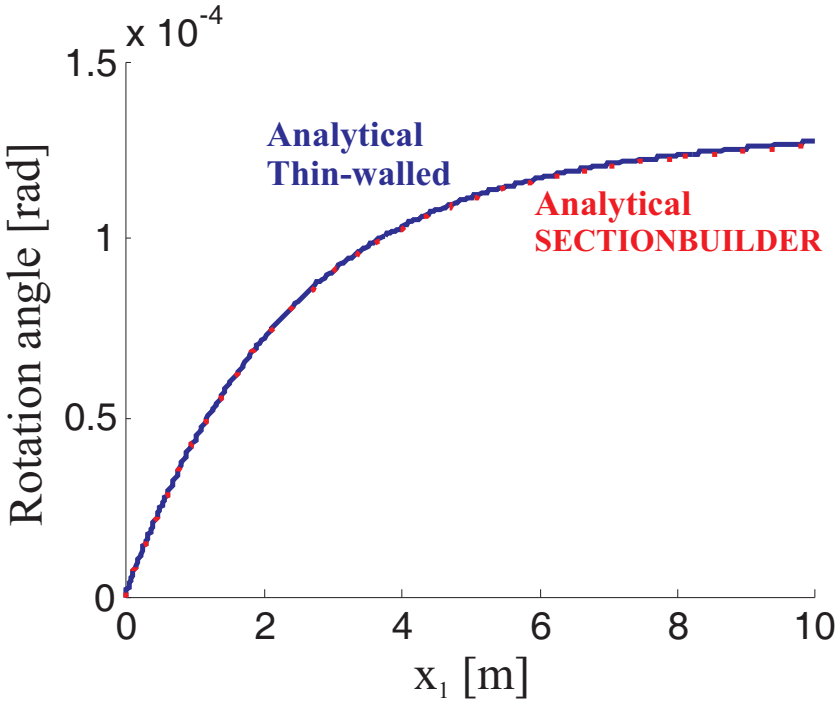

Figure 46: Spanwise rotation angle for beam with concentrated root actuation

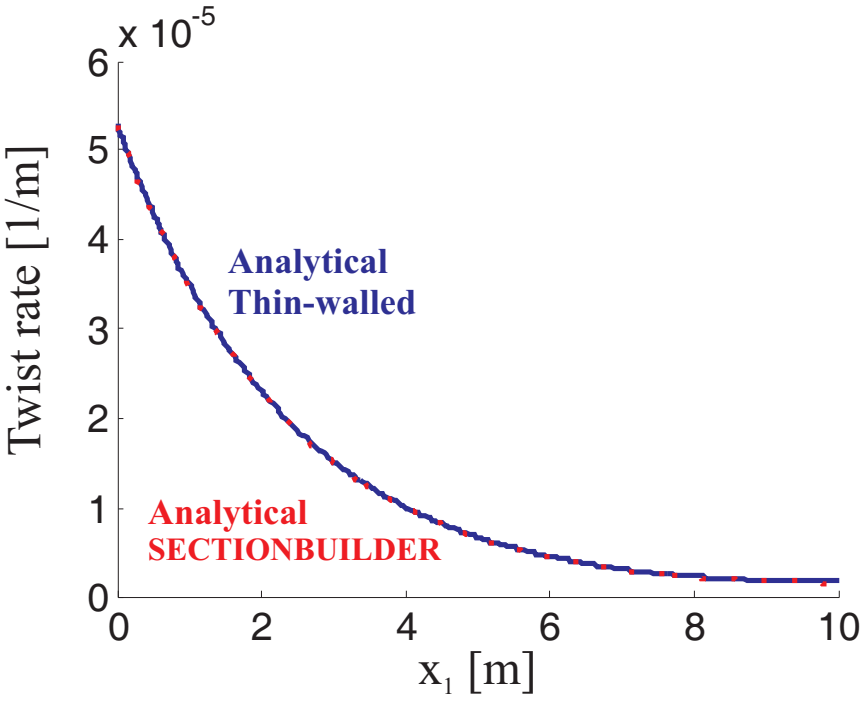

Figure 47: Spanwise twist rate for beam with concentrated root actuation

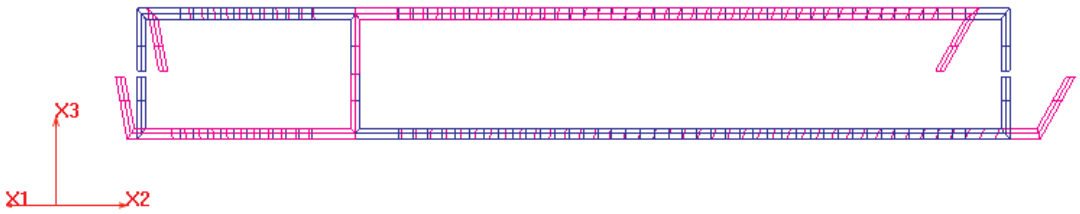

Figure 48: Cross-section as modeled in SECTIONBUILDER

affected in the differential equations are $I_p(\kappa_1 - \alpha)$ in the former case, and $\bar{I}_0(\kappa_1 - \alpha)$ in the latter (note that we made use of the fact that $\bar{I}_0 = I_1 = I_2$ for this section). In both situations, since coefficients I_p and $\bar{I}_0$ (regardless of their differences in values) are much larger than other constants in the equations, they tend to equally well enforce the condition that $\alpha \approx \kappa_1$ in a manner similar to penalty terms used in certain applications to enforce constraints. In other words, for many sections which are characterized by high values of I_p or $\bar{I}_0$, the behavior of the beam is mainly driven by H_{11} and H_{11w}, and different values of I_p or $\bar{I}_0$ do not generally influence the result, as long as they are of the same order of magnitude.

Next, the solutions obtained using the above beam theory with the SECTIONBUILDER coefficients were compared to the twist response obtained from a full finite element analysis in ABAQUS, for a different cross-section. The SECTIONBUILDER model of the cross-section can be visualized in Fig. 48, while the corresponding ABAQUS model using shell elements to perform a full 3D analysis is shown in Fig. 49. This cross-section is an open double box with two openings at the "leading edge" and the "trailing edge." Its dimensions were chosen to approximate the proportions of a NACA0012 airfoil. The ABAQUS model represents a cantilevered beam with free axial displacement at the beam root, allowing out-of-plane warping. Other degrees-of-freedom were constrained to set the root rotation to zero and to avoid bending in the model.

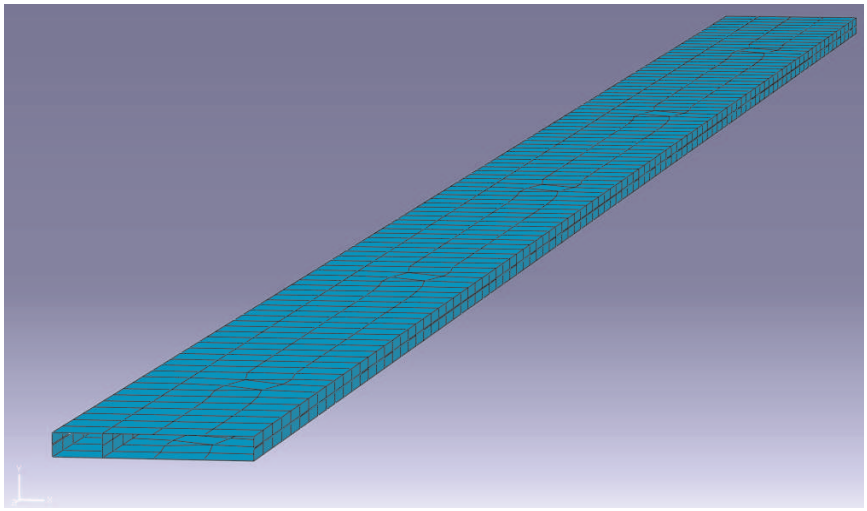

Figure 49: Beam as modeled in ABAQUS

Figures 50, 51 and 52 show all three cases: beam with end torque, beam with concentrated root actuation, and beam with distributed axial actuation, respectively. For each case, three analysis results are compared: the solution as obtained with the beam theory developed earlier and the coefficients as computed using SECTION-BUILDER, the result of an ABAQUS simulation taking geometric nonlinearity into account, and the corresponding run with the assumption of linear geometry.

The first case, beam with an end torque, represents a comparison for a well-known case. Good agreement is found. Away from the root section, the ABAQUS results behave exactly like those from the theoretical results since the slopes, *i.e.*, the twist rates, are nearly identical. Only at the root, where the localized effects of the boundary conditions are felt, is the behavior slightly different.

The other two cases involving concentrated and distributed actuation represent two options for the warping actuation mechanism. In both cases, the same total force is applied, *i.e.*, the distributed force integrated over the length of the beam has the same value as the concentrated force. According to the theoretical results, we see that in the concentrated case, most of the twist deformation occurs close to the root section, where the large axial force is applied. Far from the root, the twist rate

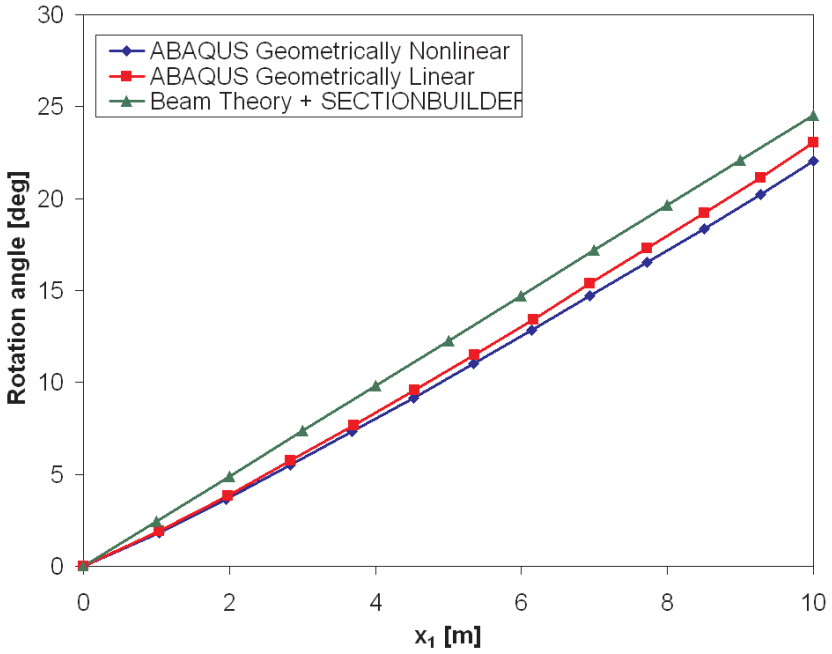

Figure 50: Spanwise variation of the rotation angle with applied end torque

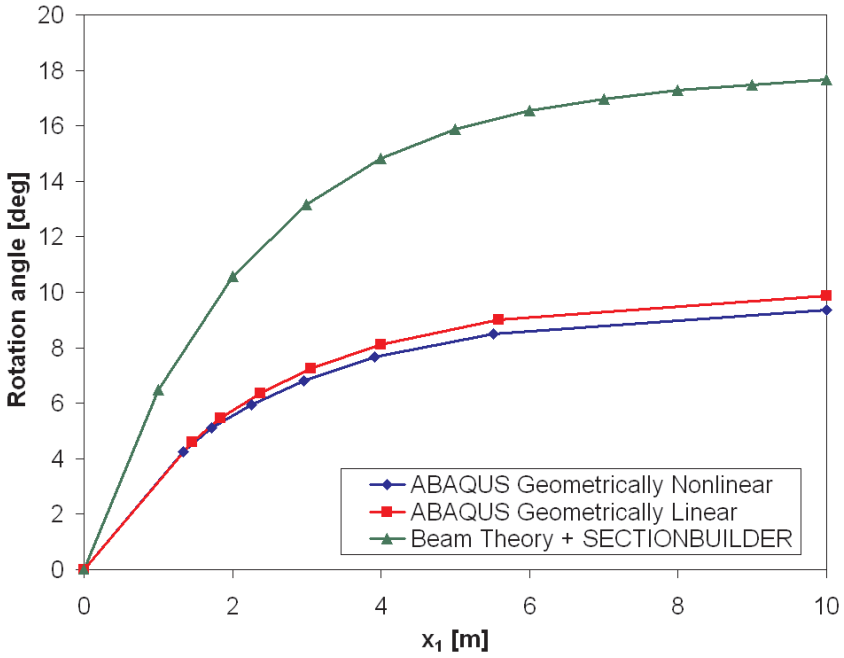

Figure 51: Spanwise variation of the rotation angle with concentrated root warping actuation

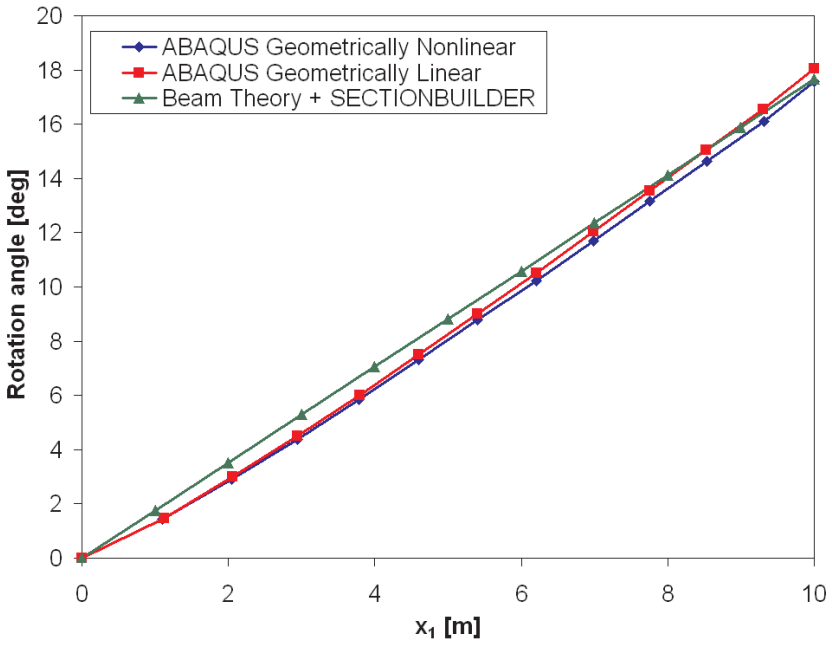

Figure 52: Spanwise variation of the rotation angle with distributed warping actuation

decreases and approaches zero. On the contrary, the twist rate is essentially constant throughout the length of the beam in the distributed case. For the same total force, both cases lead to the same tip angle, although with different behaviors toward the root and along the span of the beam.

In the distributed actuation case, the ABAQUS shell model and our beam analysis results are in good agreement. However, it is not the case for the concentrated actuation application. The ABAQUS results for the concentrated case are quite different and show a loss of tip rotation. This is explained by the presence of important shell deformation patterns close to the root section where a large force is applied. These deformation modes are not captured by the beam analysis. In this case, it is obvious that measures would need to be taken to reinforce the lips of the leading edge cut to prevent these shell bending modes to appear.

Simulations where a prescribed displacement was enforced instead of a prescribed axial force were also considered. Figure 53 shows the results which were obtained with

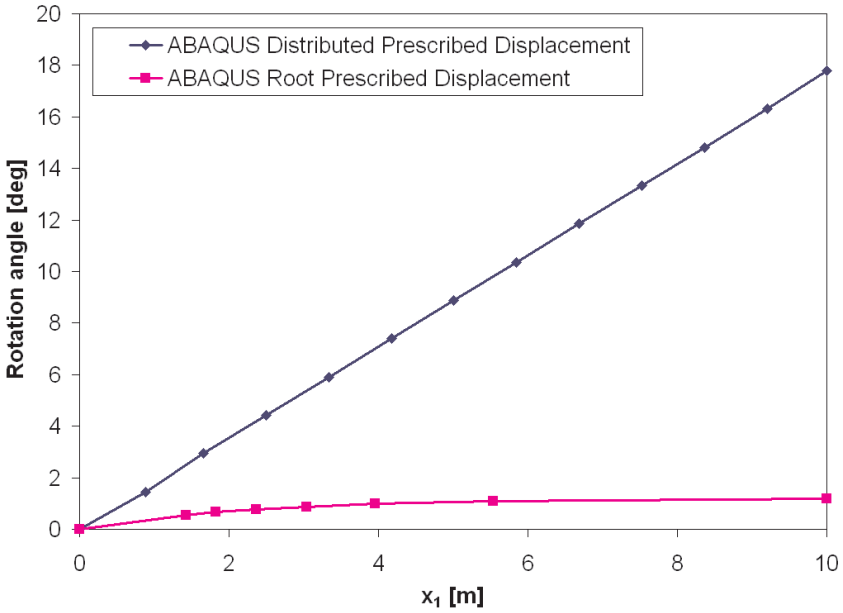

Figure 53: Spanwise variations of the rotation angle in different cases of prescribed axial displacements

geometrically nonlinear simulations in ABAQUS. It clearly shows that even though the root relative displacement of the lips of the cut may have identical values, the distributed case provides a far larger twist rate, and hence a much larger tip rotation. This shows that to obtain a given tip rotation, even though the total force may be the same, a much larger root relative displacement will be needed in the concentrated case than in the distributed one.

5.4 Implementation in DYMORE

5.4.1 General approach

The finite element formulation is based on the definition of elements and their associated nodes that contain the degrees-of-freedom of the discretized system. Each node originally has 6 degrees-of-freedom representing 3 displacements and 3 rotations. The implementation of the Vlasov beam theory into DYMORE necessitates an additional 7th degree-of-freedom representing a measure of warping in beam elements. In traditional representations of beam deformations, one considers 6 strain measures: one

extension strain measure, two transverse strain measures and three measures of curvature. These are then related to the three displacement and three rotation parameters used in DYMORE, which are defined at each node of the discretized model. With the implementation of Vlasov theory, an additional measure of warping is included.

Based on the fundamental principles upon which the code is constructed, there is no simple way of including additional warping degrees-of-freedom. Two main options were considered to achieve this:

1. The warping parameter can be defined as an additional degree-of-freedom. The number of degrees-of-freedom per node can be changed from 6 to 7, the 7th degree-of-freedom being the warping parameter. This allows for the topological definition of the model to automatically enforce continuity of warping from one beam element to the next. However, the code inherently relies on the assumption that there are only 6 degrees-of-freedom per node (3 displacements, 3 rotations), so that changing this parameter would entail very extensive modifications affecting all subroutines of the code.

2. The warping parameter can be defined as a special additional node. In this approach the number of degrees-of-freedom per node remains at 6, but additional special nodes defining the warping deformation can be added. This is beneficial because it would mainly affect the beam element in the code, with minimal interference with the definition and treatment of all other elements. However, these special nodes cannot be used for topology definitions and hence, continuity cannot automatically be enforced. This necessitates additional subroutines to be implemented to artificially maintain deformation continuity.

Since changing the number of degrees-of-freedom in a node leads to a complete reorganization of the code, it seems more judicious to keep the number of degrees-of-freedom per node at 6 and add nodes dedicated to including warping in the only

element that can realistically feature it, the beam element. These additional warping nodes, which share the same location as regular beam element nodes, are topologically different from regular beam element nodes. Among other things, the boundary and continuity conditions which the warping-enabled elements of the model must satisfy need to be artificially enforced.

Some of the main modifications needed to incorporate warping in DYMORE are:

- modifying the input file's property definitions to account for warping;
- implementing the additional degree-of-freedom representing warping in a beam element;
- converting the inputs into constraints and/or continuity conditions in the code;
- incorporating the new sectional coefficients into beam element matrices.

A multibody system is defined in input files that are read by the program, and this data is stored in data structures used by the code. These reading and storage functions were generalized to include the interpretation of warping related inputs. The input file should define whether any beams undergo warping deformation. If so, the associated boundary conditions must be specified. The typical definition of a beam described in Ref. 5 is expanded with a warping flag `@WARPING_FLAG` which can have the `WrpFlg` values "Yes" or "No" (default: "No"), as well as two fields `BCat0` and `BCat1` for the warping boundary conditions `@WARPING_BOUNDARY_CONDITIONS`:

```
@BEAM_DEFINITION {
    @BEAM_NAME {BeamName} {
        @EDGE_NAME {EdgeName}
        @BEAM_PROPERTY_NAME {BldPropName}
        @INITIAL_COORDINATE {si}
        @STRATEGY_PARAMETERS {Er}
```

```
        @SHAPE_NAME {ShapeName}
        @GRAPHICAL_PARAMETERS_NAME {GrfParamName}
        @WARPING_FLAG {WrpFlg}
        @WARPING_BOUNDARY_CONDITIONS {BCat0,BCat1}
    }
}
```

A boundary could have free or fixed warping, or one may want to enforce continuity of warping between two beams. This latter situation may arise when one single beam must be separated into two parts to allow for additional connections at the splitting point. Each field `BCat0` and `BCat1` can therefore have one of the following values: "Free" for free warping at this end of the beam; "Fixed" for zero prescribed warping at this end of the beam; "Continuous" for continuous warping if this end of the beam is attached to another warping-enabled beam. As an example, a warping-enabled helicopter blade fixed to a rotor hub would require a free warping boundary condition at the root attachment, in order to allow for warping deformations.

Additionally, the sectional properties that were identified earlier as characteristics of a beam's warping behavior must be taken into account in DYMORE simulations. After analyzing the cross-sections of the beam with SECTIONBUILDER, the warping coefficients can be manually transferred to the DYMORE input file.

The next step consists in the meshing of the multibody model. This step refers to the discretization of the full model into a set of elements and their associated nodes, whose degrees-of-freedom will be solved for. This process affects all components of the model (flexible bodies, joints, rigid bodies...) Based on the chosen strategy for the inclusion of warping degrees-of-freedom, modifications are only made to the meshing of beams.

Most elements in DYMORE are associated with an edge and have internal nodes of a specific type. Figure 54 shows a revolute joint element as a simple example. An

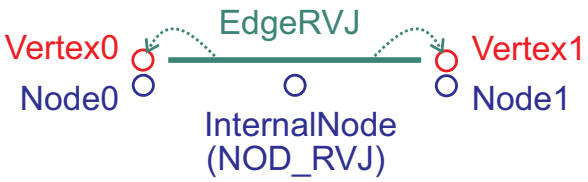

Figure 54: Revolute joint

edge `EdgeRVJ` is associated with the revolute joint element. It points to two vertices `Vertex0` and `Vertex1`, which will be shared with other elements connected to the revolute joint. These vertices have associated nodes `Node0` and `Node1` respectively. Finally, this edge contains an internal node of type `NOD_RVJ`. An internal node is a node attached to an edge, but which does not correspond to either of the two vertices. It is an additional node which carries information about the sole element to which it corresponds, but not about the other elements it is connected to (unlike the nodes associated with the vertices, which are shared with other elements connected at those vertices). In this particular case, the internal node allows the code to enforce the constraints related to a revolute joint.

A similar approach is taken for the implementation of warping in DYMORE. The warping information will be carried through additional internal nodes. Figure 55 shows the difference between the existing beam element (for which warping is not activated) and the new proposed implementation of beam elements for which warping is enabled. The beam element shown in Fig. 55(a) is a 3^{rd} order beam element with four nodes in total. The two additional internal nodes `Node2` and `Node3` facilitate the implementation of a cubic beam element. The same idea is extended in Fig. 55(b) to warping with the additional 4 internal warping nodes associated with each of the regular nodes. Linear elements would have 2 nodes (with an equal number of warping nodes), quadratic elements 3 nodes (and 3 warping nodes). The regular internal beam node type is denoted `NOD_BLD`, while the warping internal nodes will be considered to be of type `NOD_BLW`.

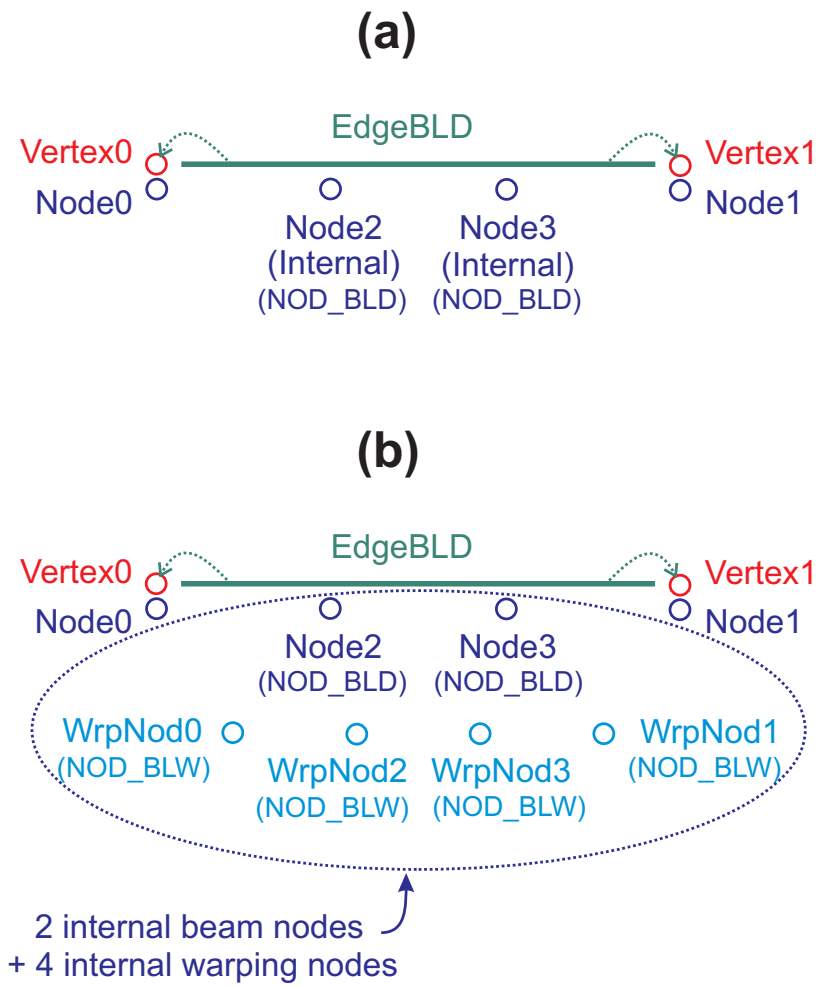

Figure 55: Beam element (a) without warping and (b) with warping

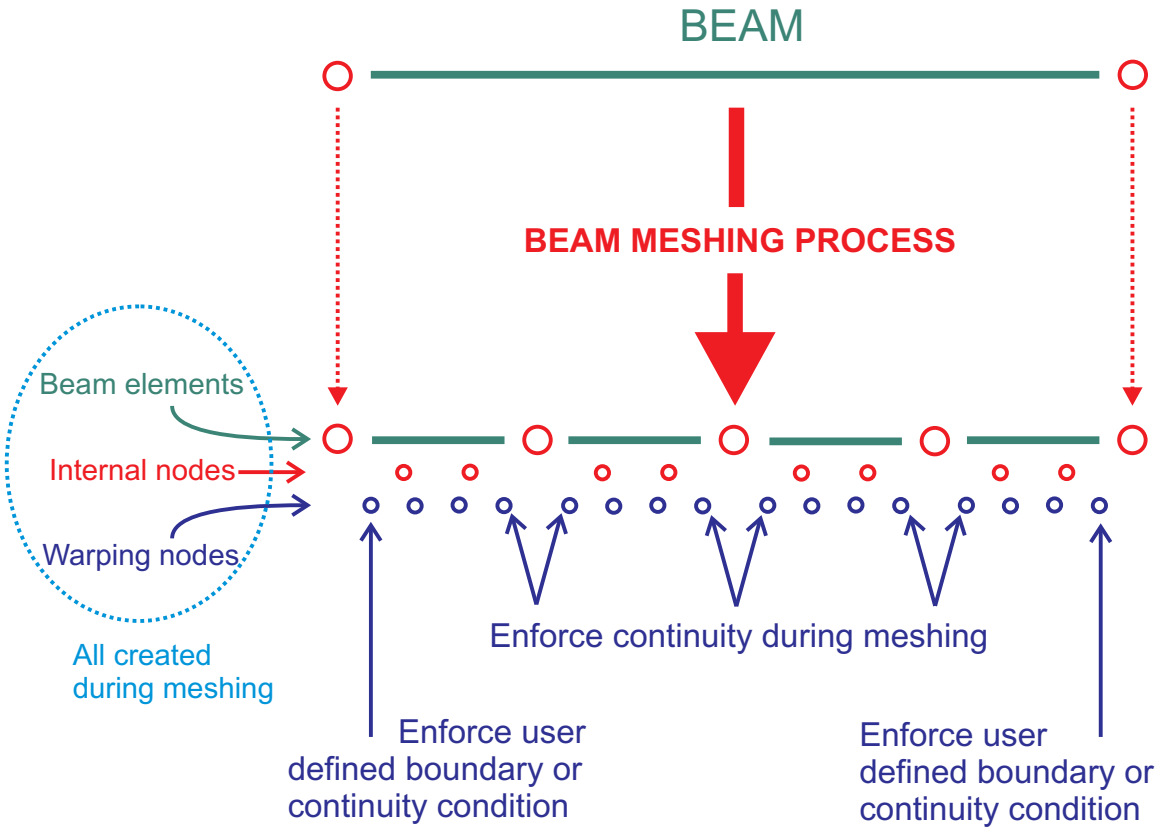

Figure 56: Meshing of a beam presenting warping

The meshing process for beams is also affected by the inclusion of these warping internal nodes. Figure 56 shows how a beam is meshed when warping is present. Starting at the first vertex of the beam, a vertex is created, as well as the first beam element between these two vertices. Internal nodes are added depending on the order of the finite elements, and next internal warping nodes are created. The first warping node is constrained to the user defined boundary or continuity conditions as described earlier. Next, starting at the created vertex, a new beam element is generated with an end vertex as well as all the needed internal nodes. Here, it is imperative to enforce a continuity condition on warping between the last warping node of the previous element and the first warping node of the current element. This process is repeated until the whole beam is discretized, and the final boundary or continuity condition is enforced.

The system having been discretized, the finite element solution of the problem can be computed. The time integration scheme controls the solution process from the initial time to the final time; at each time step, a number of iterations is needed for a converged solution. The updating process of the warping degrees-of-freedom was added to the numerical time-stepping scheme. At each iteration, the structural matrices and loads are computed. The challenge is to incorporate the structural terms and equations related to the treatment of beams with warping into the finite element formulation, as detailed in Section 5.2.3. Essentially, the usual 6-by-6 matrices (stiffness matrix, mass matrix, and so on) for each node must be expanded into 12-by-12 matrices including the warping coefficients, and must be assembled in expanded global matrices. Note that given the chosen implementation of the warping degrees-of-freedom, most terms associated with the warping degrees-of-freedom in the elemental matrices are zero.

Once the solution process is complete, a phase of postprocessing analysis allows the user to extract meaningful information from the full solution of the problem. In this case, an additional sensor was needed to extract values of the warping measure at given time steps and locations. Finally, output files and plots are created to allow the user to review results after the simulation.

5.4.2 Validation of static cases

We consider a beam with the asymmetric cross-section of Fig. 42. A DYMORE input model was defined in which a beam with warping deformation is subjected to a tip torque. The beam was modeled using 8 cubic beam elements. The root boundary condition was here chosen to be clamped with fixed warping. Figs. 57 and 58 show the spanwise rotation angle and warping measure obtained with DYMORE, compared to the results from the analytical formulation using the coefficients computed by SECTIONBUILDER. The correlation is excellent in both plots. In addition, Fig. 57

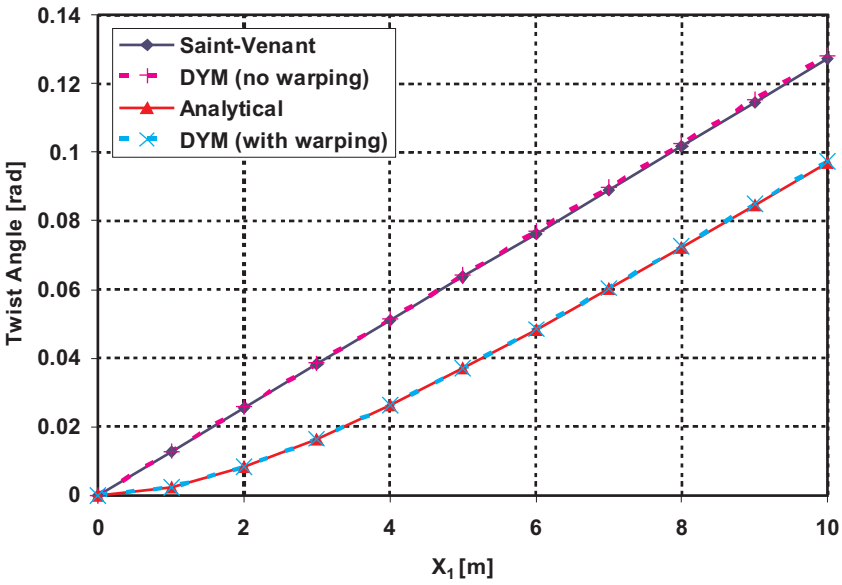

Figure 57: Spanwise rotation angle ϕ_1 in the static analysis of a beam subjected to a tip torque

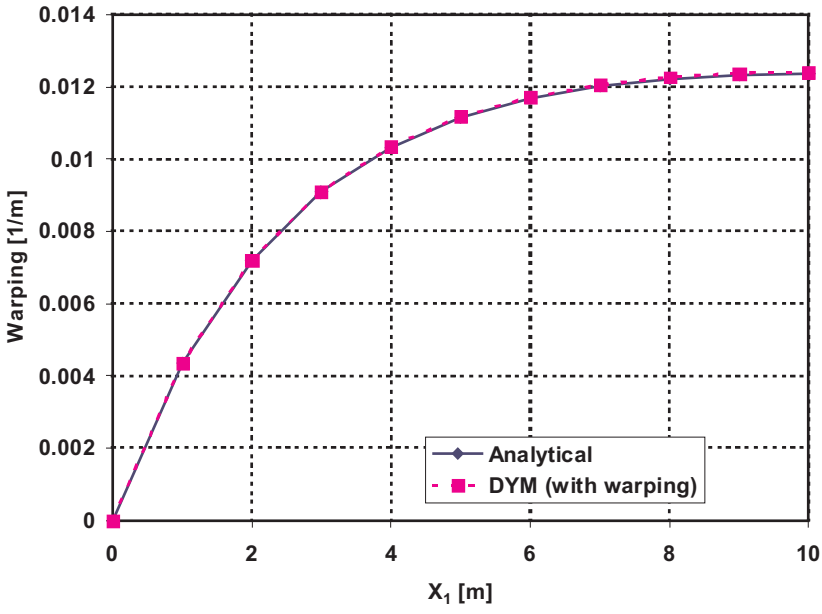

Figure 58: Spanwise warping α in the static analysis of a beam subjected to a tip torque

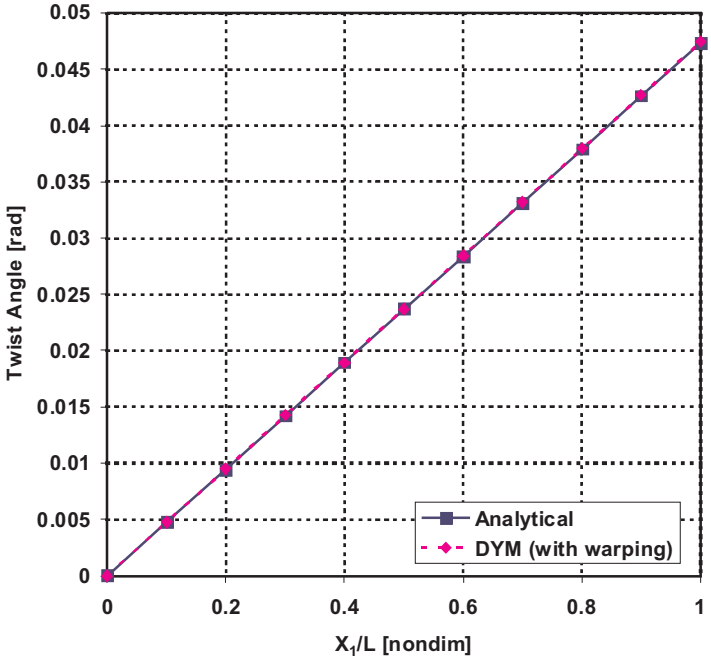

Figure 59: Spanwise rotation angle ϕ_1 in the static analysis of a beam subjected to distributed warping actuation

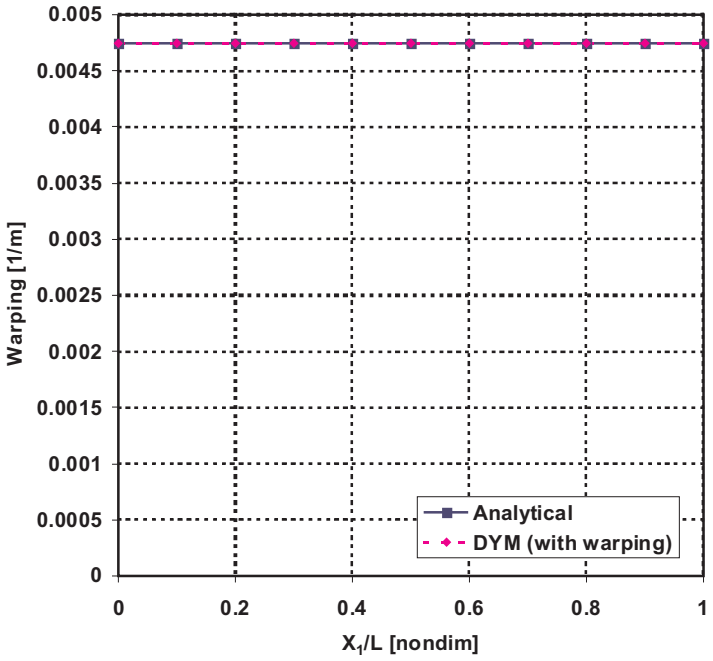

Figure 60: Spanwise warping α in the static analysis of a beam subjected to distributed warping actuation

also includes the analytical Saint-Venant twist and the twist variation obtained with the original DYMORE code. These results also correlate extremely well, as would be expected.

Next, an identical beam was considered; in this case however, a distributed warping force is applied, and warping is free at both ends. The results of the comparison between the analytical formulas and DYMORE can be found in Figs. 59 and 60. Again, excellent correlation is found between them.

5.4.3 Example dynamic cases

Finally, dynamic analyses were run in the same cases. The tip torque of the first case was now applied as a step function at the initial time, and the resulting vibration of the beam is observed. Structural damping was added to obtain time-decaying solutions. Figures 61 and 62 show the time histories of the rotation angle and warping at several stations along the length of the beam (at 20%, 40%, 70% and 100% of the span from the root). It is interesting to note that the steady-state values obtained after a few seconds all correlate perfectly with the corresponding static results from the previous paragraph.

Figures 63 and 64 show similar results for the 40%, 70% and 100% span locations, in the case where a distributed warping actuation force is applied as a step force starting at the initial time. It is clear again that the steady-state values correspond to the static response. This shows that consistent results are found in both the static and dynamic case using the new implementation of warping deformation in DYMORE.

5.5 Summary

SECTIONBUILDER and DYMORE are finite-element-based codes for the analysis of arbitrary beam cross-sections and the analysis of flexible multibody dynamic systems, respectively. They were modified to provide additional capabilities for the analysis of

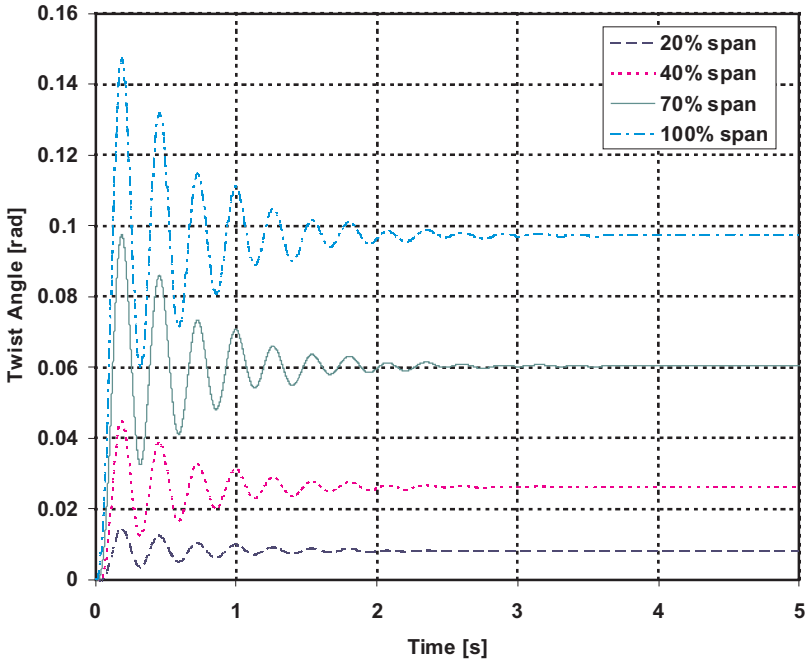

Figure 61: Time history of rotation angle ϕ_1 at several spanwise locations in the dynamic analysis of a beam subjected to a tip torque

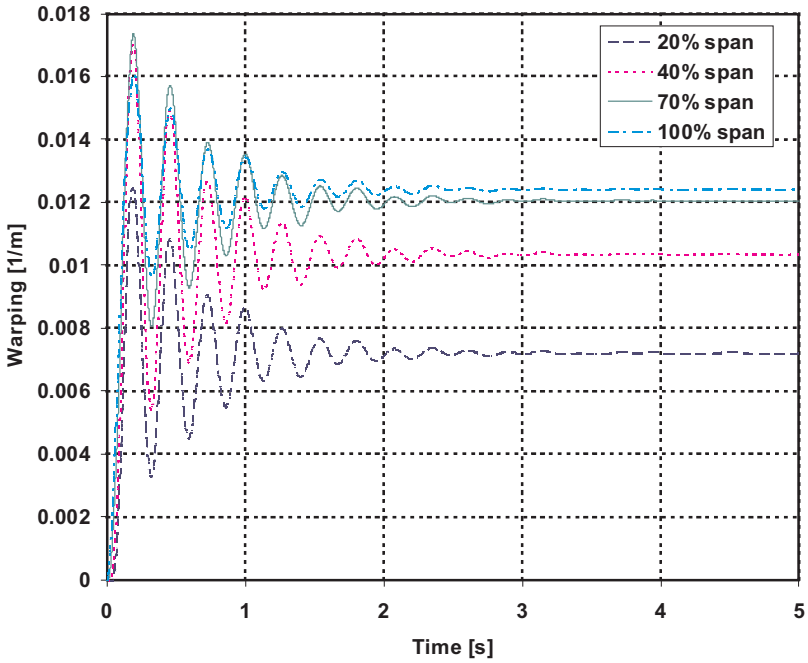

Figure 62: Time history of warping α at several spanwise locations in the dynamic analysis of a beam subjected to a tip torque

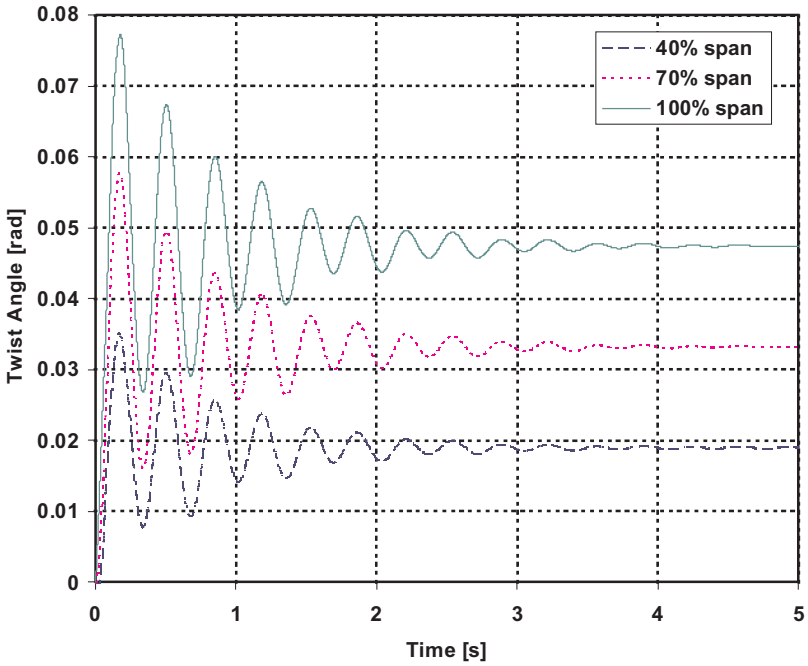

Figure 63: Time history of rotation angle ϕ_1 at several spanwise locations in the dynamic analysis of a beam subjected to a distributed warping force

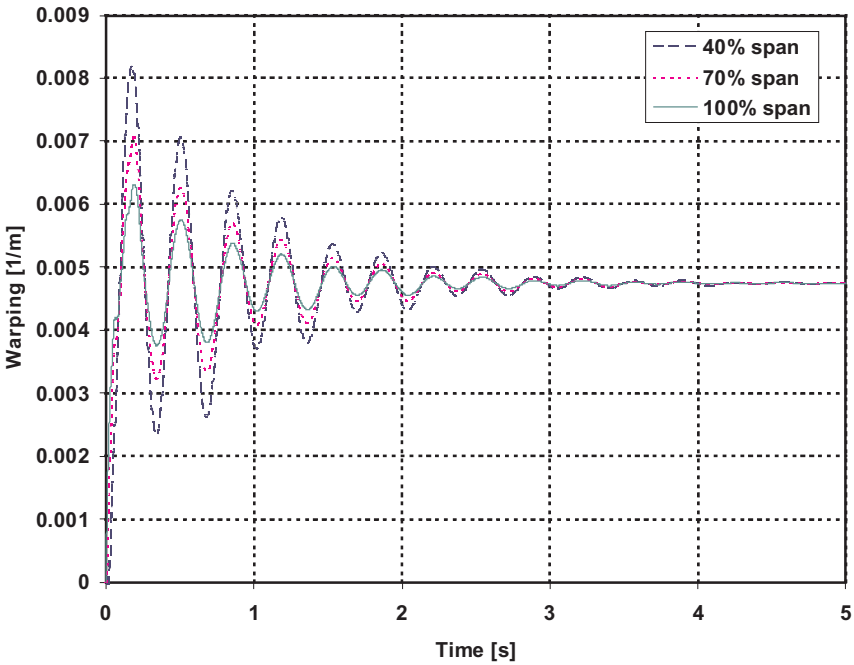

Figure 64: Time history of warping α at several spanwise locations in the dynamic analysis of a beam subjected to a distributed warping force

warping-actuated beams. SECTIONBUILDER was extended to provide additional sectional properties that are fundamental for the modeling of beams undergoing both twisting and warping. Reworking the Vlasov theory that was presented in Chapter 4 without the thin wall assumption provided the foundation for these modifications. The implementation of these ideas was validated by comparing these numerically computed cross-sectional properties with analytical results obtained with the thin-walled beam assumption. Further validation was provided with ABAQUS.

DYMORE was modified to include the additional warping degree-of-freedom in multibody simulations. The properties and constraints associated with this new degree-of-freedom were included in the analysis. The extensive changes to the code, particularly for beam elements which were affected by these changes, were described. They rely on the theoretical developments providing the dynamic partial differential equations for a beam under twisting and warping, and their inclusion in a weighted-residual formulation leading to the extended finite element implementation of beam elements. The results for static cases obtained with DYMORE correlate extremely well with analytical solutions using the coefficients computed by SECTIONBUILDER, while the results for dynamic cases were found to be consistent with those from the static cases.

CHAPTER VI

CHIRAL-NETWORK-BASED VARIABLE-CAMBER ROTOR BLADES

A second approach to morphing rotor blades is proposed in this chapter. While the concept of Chapter 4 enabled blade morphing strictly through variable twist, this new concept will make use of a special type of cellular structure to induce variable camber in the blade's airfoil shape. The controlled camber deformation could vary along its span, as well as vary in time. The change in shape is obtained through distributed internal straining of the cellular structure shown in Fig. 65. Locally generated deformations lead to global morphing of the structure.

Several possible designs using chiral lattice geometries can be envisioned. A first design shown in Fig. 66 would integrate a chiral core into the deformable airfoil instead of the typical honeycomb core. Another possibility is suggested in Fig. 67, in which the active chiral network would be used to generate the rotation of a trailing-edge flap. Finally, one could envision using chiral "spars" placed at an angle with

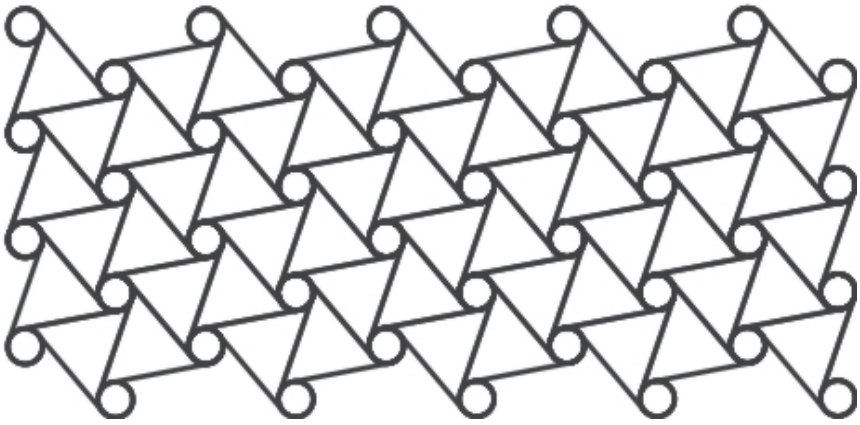

Figure 65: Hexagonal chiral lattice

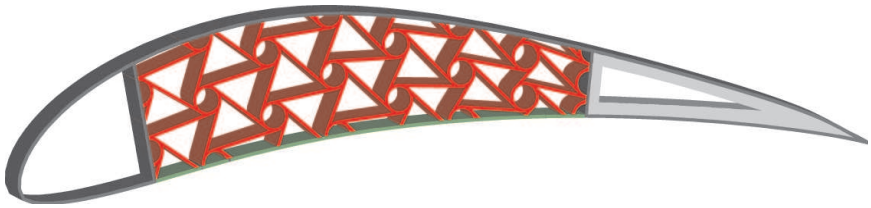

Figure 66: Deformable airfoil with chiral core

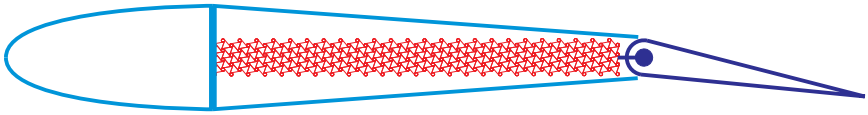

Figure 67: Flap actuated by chiral actuator

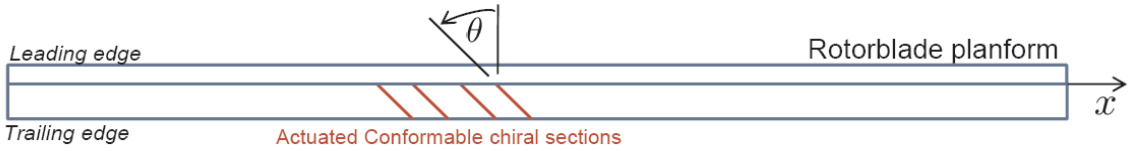

Figure 68: Conformable sections inducing both camber change and blade twist

respect to the elastic axis, as illustrated in Fig. 68. Such conformable sections would simultaneously induce camber change and blade twist, and may benefit from insight gained in Chapters 4 and 5.

First, general features and characteristics of chiral lattice networks will be introduced. Piezoelectric materials, and especially piezo-benders, are particularly well suited to be integrated as smart actuators into these networks. Their properties will briefly be introduced as well. Next, the passive behavior of chiral structures will be investigated, leading to a few interesting facts. Finally, a preliminary assessment of active chiral structures incorporating piezoelectric actuators will be conducted through static analyses. Several simple actuation schemes will be explored, and their performance will be determined in a simplified steady aerodynamic environment.

6.1 Chiral networks and piezoelectric actuators

6.1.1 Chiral networks

The structures that will be considered here are based on a particular kind of cellular solid known as hexagonal chiral lattices (Fig. 65). An important feature of deterministic cellular solids such as these is their spatial periodicity: the structure's geometry is constructed from the replication of a unit cell. The particular lattice under consideration is *hexagonal* due to the geometric invariance through a rotation of $\frac{2\pi}{6}\text{rad} = 60°$, and *chiral* because the original structure and its image through a reflection cannot be made to coincide. Figure 69 visually elucidates these three fundamental facets of hexagonal chiral lattices. In the remainder of this work, structures based on these lattices will simply be called *chiral networks* or *chiral structures*.

Chiral structures present some unique features which make this type of design particularly suited for the present work. Contrary to typical truss-like architectures, the elements of the network are connected to form a system of non-central forces, as indicated in Fig. 70. In particular, the tangential force applied to the circular "nodes" by the ligaments is not directed toward the center of these nodes. The subsequent circle rotations and associated bending deformation modes of the ligaments define the unique deformation patterns of chiral structures, and lead to their large deflection capabilities. Another interesting feature is the design flexibility that such a system affords. Depending on its topology, both at the unit cell level and at the global scale, the behavior of a chiral network can vary drastically. For example, the relative size of circles compared to the length of the ligaments or the total number of cells have been shown to affect the compliance of such a structure (Ref. 79, 80).

Additional features of chiral structures are particularly advantageous for the design of active compliant systems. First, the actuation can be embedded into the structure, resulting in an active compliant system in which the actuation elements are integrally part of the flexible structure. The actuation force is transmitted through

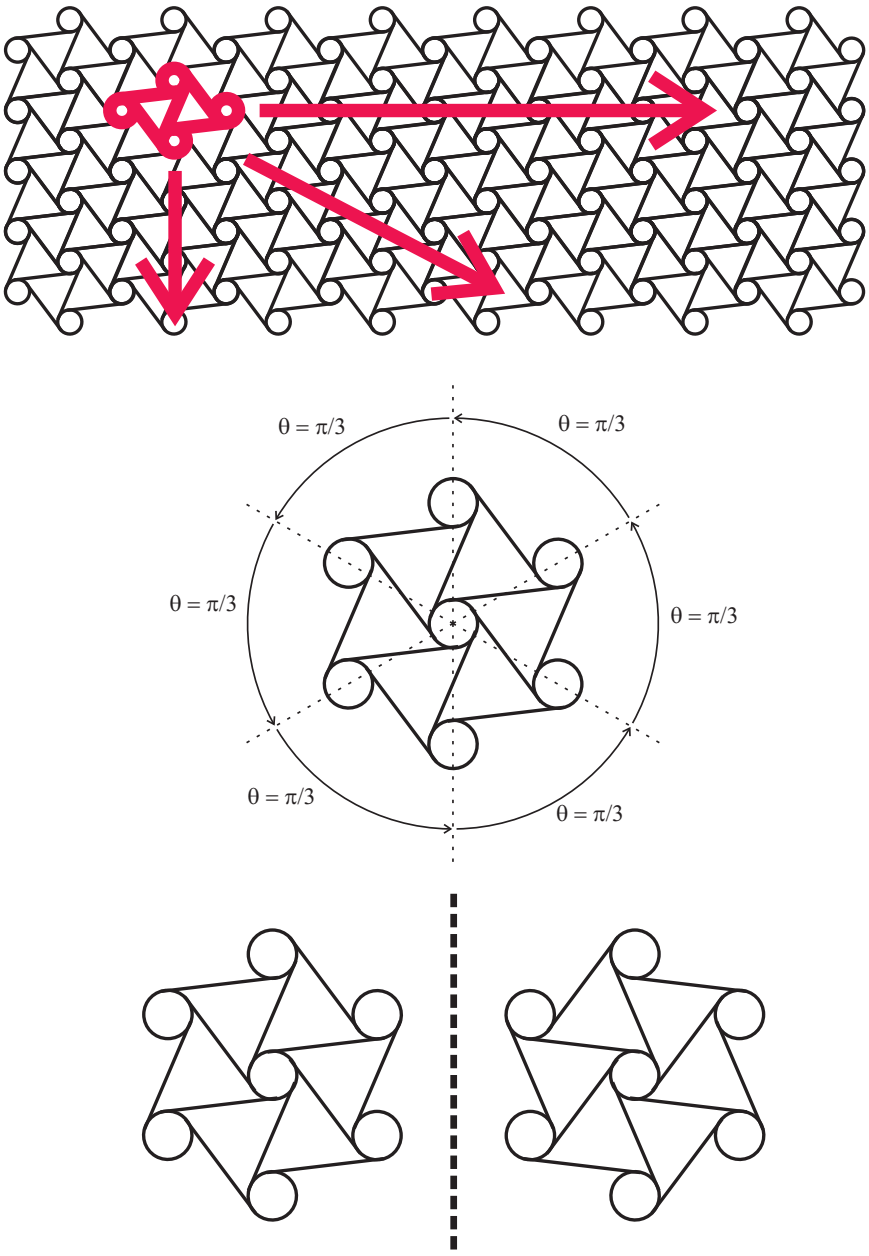

Figure 69: Three fundamental aspects of hexagonal chiral structures: periodicity, invariance through a 60° rotation, and chirality

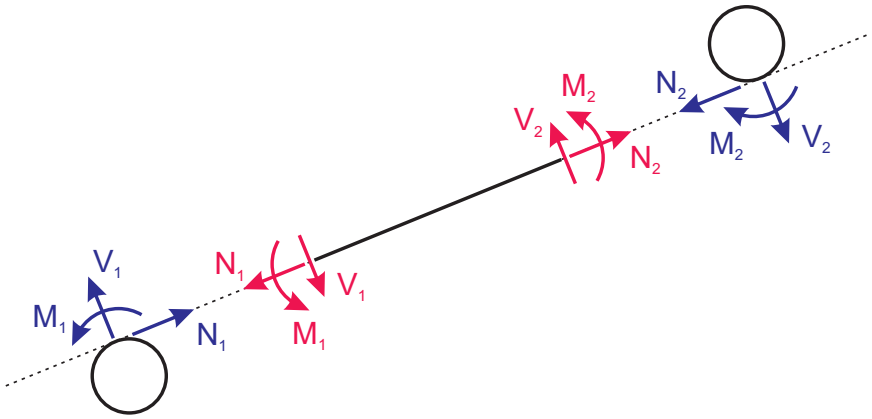

Figure 70: Non-central forces applied to circular nodes of a chiral structure

the stiffness of the structure, while the deformation capability is provided by its flexibility. Next, the structural redundancy can be used to implement distributed actuation strategies, whereby the combined straining of multiple ligaments is amplified to provide large global deflections while keeping the deformation of individual ligaments below the elastic limit of the selected material. By controlling the deformation of several ligaments independently, many different deformed configurations can be generated. In addition, such a system would not involve any mechanical parts or joints, avoiding the typical wear and tear found in mechanical systems that are often complex.

A final advantage of these types of structures is the possibility of using composite materials for a truly practical design. These materials often feature high stiffness-to-weight ratios, an undeniable advantage for aerospace applications. Structural tailoring of the material stiffness is also possible by careful design of the lay-up sequence; more freedom is attainable if the lay-up sequence is individually determined for each ligament. Finally, composites can have higher yield limits, allowing larger deformations without inducing failure.

Figure 71 shows the important geometric parameters that characterize a chiral structure. R is the distance between the centers of two circles of radii r, and L is the length of the ligaments joining these nodes. β denotes the angle between the

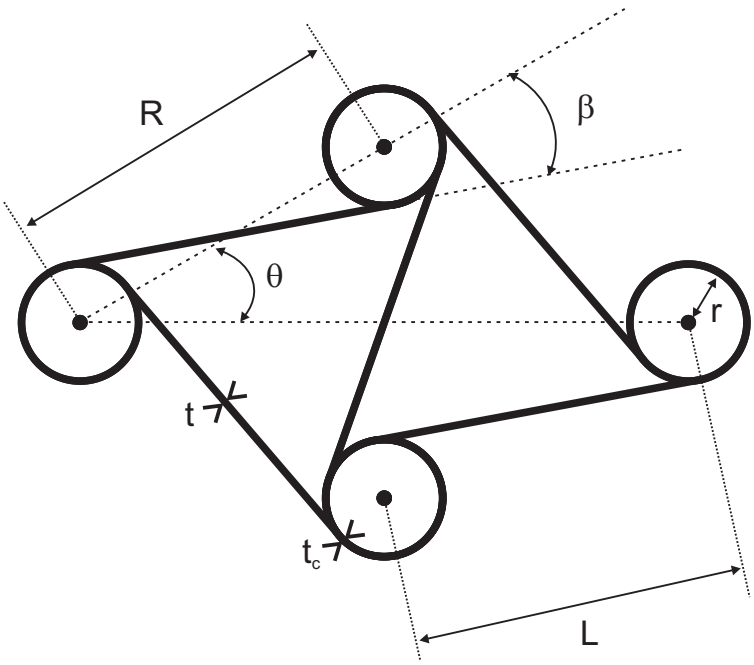

Figure 71: Basic geometric parameters characterizing a chiral structure

line joining the centers of two circles and the corresponding ligament, while t and t_c represent the thickness of a ligament and of a circle, respectively. These two quantities may be different, and in fact probably would be in practical applications. The manufacturing process of composite chiral structures described in Ref. 20 leads to configurations where $t_c \approx 2t$. Furthermore, although deformation of the ligaments is desirable, deformation of the nodes should be minimized; increasing their thickness would provide the adequate level of stiffness in them. It is easily shown that

$$\beta = \arccos(\rho), \tag{132}$$

$$r = \frac{R}{2}\sin(\beta) = \frac{L}{2}\tan(\beta), \tag{133}$$

where we introduced the notation $\rho = \frac{L}{R}$. In other words, the unit cell configuration of a particular chiral network is determined by the definition of ρ, R (or L), t, and t_c. Typically, the value of R determines the approximate size of the unit cell. Parameters t and t_c directly influence the stiffness of the structure. And, as shown in Fig. 72, ρ determines the relative size of the circles compared to the length of the ligaments.

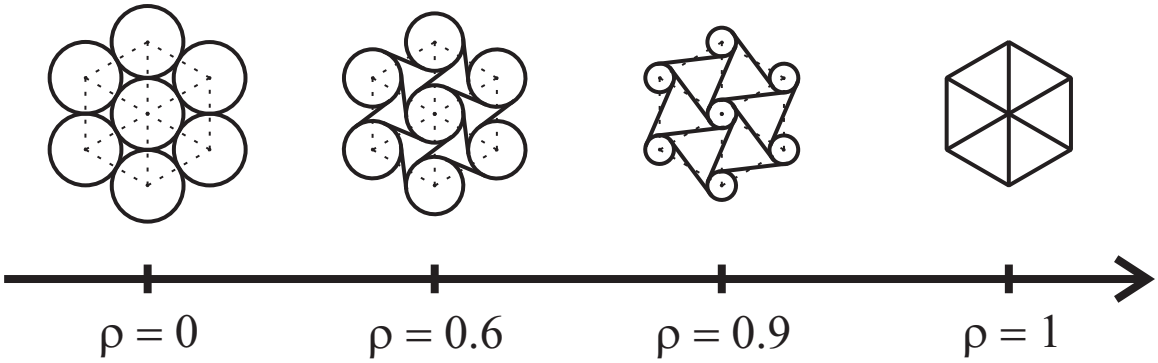

Figure 72: Topology variations with ρ

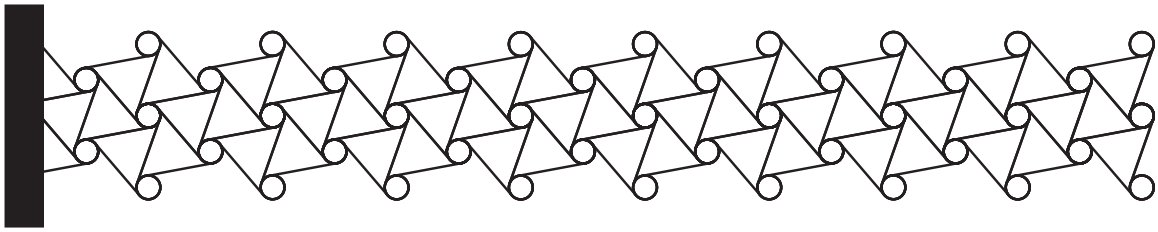

Figure 73: Rectangular chiral structure

When $\rho = 0$ on the lower end, the ligaments are inexistant ($L = 0$), while the circle radius reaches its maximum value $r_{\max} = \frac{R}{2}$. When $\rho = 1$ on the upper bound, the ligaments have maximum length $L_{\max} = R$, and the circles are nonexistant ($r = 0$).

A few additional important parameters pertain to the overall dimensions of the structure. As shown in Fig. 73, we will mostly consider long rectangular chiral structures (referred to as "chiral beams") constrained at one end. One important parameter is the orientation of the chiral cells. As shown in Fig. 74, if one draws the line connecting a circle center to the center of the first adjacent circle above the horizontal when traveling in the anticlockwise direction, the angle between this line and the horizontal can be 30° or 60°. This angle θ will be used to describe the orientation of chiral cells in the structure. Other important geometric variables are the out-of-plane width w of the structure and the number of cells in each direction. If one denotes by $\hat{l} = R\cos(\theta)$ and $\hat{h} = R\sin(\theta)$ the units of length in the horizontal and vertical directions respectively, one can define the total number of units of length

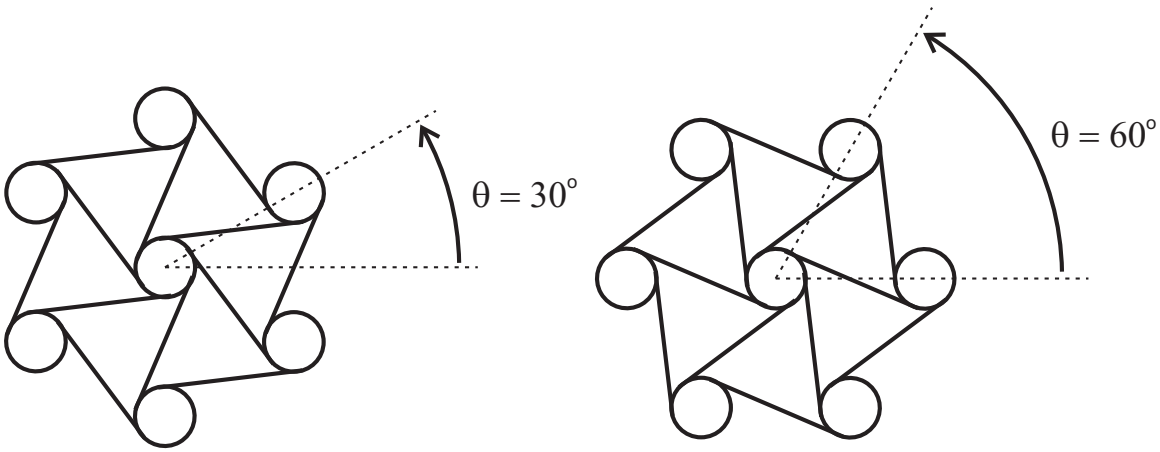

Figure 74: Possible cell orientations

in each direction, N_l and N_h, so that the total lengths will be $l = N_l\,\hat{l}$ and $h = N_h\,\hat{h}$, respectively. Any circle in the structure can conveniently be located by its integer coordinates $0 \leq n_l \leq N_l$ and $0 \leq n_h \leq N_h$. For given dimensions of the structure, increasing N_l and N_h increases the density of unit cells. Finally, the material properties must be chosen. In the current work, the emphasis has been on chiral networks made of a homogeneous, isotropic and linear material such as aluminum, a common metal in aerospace applications. Of course, composite materials would offer yet another level of design flexibility.

6.1.2 Piezoelectric actuators

The piezoelectric effect, described in detail in Ref. 72, couples the electrical and mechanical constitutive equations in a material. The *direct piezoelectric effect* refers to its property of generating an electrical charge in response to an externally applied loading. This effect allows them to be used as sensors, the applied force being measured by the level of electrical charge. The *inverse piezoelectric effect* is the property that the application of an electric field in the direction of polarization of the material induces straining in the material. This makes them behave as actuators, generating material deformations due to the electric field input.

Two main uses of piezoelectric materials exist for actuation purposes, as shown in

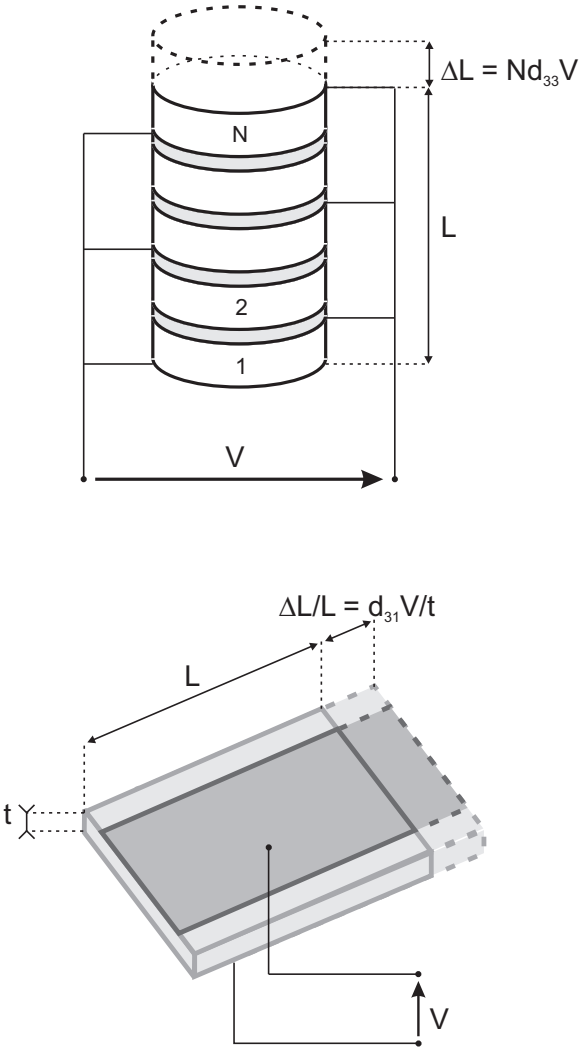

Figure 75: Two actuator designs using piezoelectric materials: linear piezo-stack and laminar piezo-bender

Fig. 75. The first consists in using it as a linear actuator, usually featuring a piezo-stack and optionally including an amplification device. In this case, the direction of polarization, the direction of the applied electric field and the direction of expansion are all identical, and the main mode of deformation is determined by the piezoelectric constant d_{33}. Such linear actuators are often used in truss-like architectures to replace certain truss members (Ref. 72). This possibility will not be investigated here, since such an actuator does not lend itself to easy integration into the chiral network. The other approach, also shown in Fig. 75, involves using the d_{31} piezoelectric constant, which induces a linear strain in the direction normal to the direction of the applied electric field, which coincides with the direction of polarization of the material. This electric field is generated by applying a voltage between two thin electrodes bonded on either side of the piezoelectric laminate. This is particularly well suited to our case, since this laminar type of actuator can simply be bonded to a ligament of the chiral structure to deform it. In essence, this layer of piezoelectric material is embedded as part of the compliant system. In this case, the actuator creates axial strain on the top and/or bottom edges of the shell-like ligament, inducing a bending type of deformation. Hence, we will also refer to these laminar actuators as "piezo-benders". As a final note, it is clear that these piezo-benders use the inverse piezoelectric effect, generating material deformation from the application of a voltage. Likewise, laminar sensors using the direct piezoelectric effect could be bonded to the structure to measure the deformation of a ligament.

6.2 Passive static analysis

6.2.1 Passive response of a chiral structure

First, we will investigate the passive static response of a chiral beam to applied forces and moments. ANSYS will be used to perform the analysis, while MATLAB will allow the post-processing of the analysis results. This should provide some insight

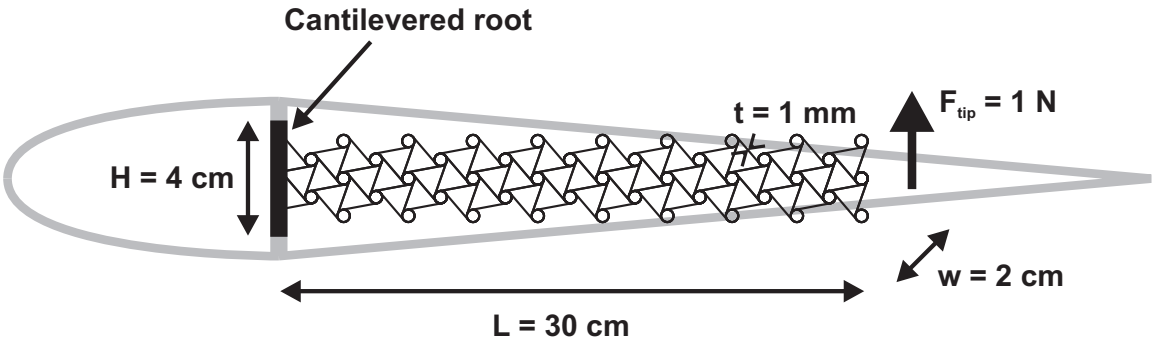

Figure 76: Clamped chiral beam with unit tip transverse force

in the attainable displacements under various loading conditions, for given values of the design parameters. It would also provide a "map" highlighting which ligaments undergo the largest deformations. Figure 76 shows the first problem under consideration. A chiral beam is clamped on the left-hand side, for example to the vertical web of the front D-spar of a typical rotor blade, while a unit transverse tip force is applied on the right-hand side (towards the trailing edge). The output displacement of interest is the tip deflection. The overall dimensions of the chiral structure were chosen to provide a reasonable fit for a UH-60 blade: its size is representative of a chiral core filling the aft part of the blade, while also being close to that of a chiral actuator used to deflect a flap.

The resulting deformed configuration is shown in Fig. 77. Figures 78 and 79 show the direct axial strain and the curvature that develop in the ligaments. Clearly, high localized strains are found close to the cantilevered root, while little deformation occurs towards the tip of the structure. In other words, the mechanical deformation is not distributed throughout the structure. Figures 80 and 81 show the transverse deflection field and the in-plane rotation of the circles. This last quantity is a measure computed from the average tangential displacement of the finite element nodes on each circle. These figures again emphasize the very limited contribution of the right half of the chiral network to the deformation capability. High gradients of rotation at the root generate high global curvature of the chiral beam, while the near-constant

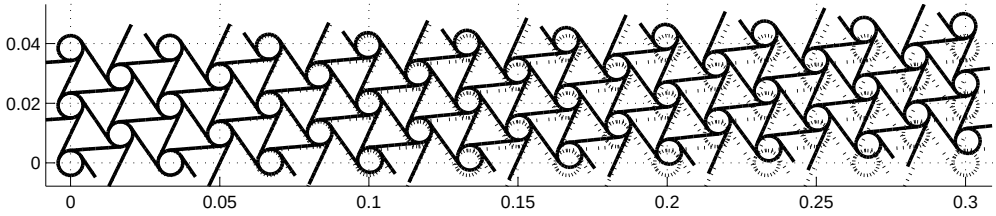

Figure 77: Deformed configuration due to unit tip transverse force (scaling factor = 10)

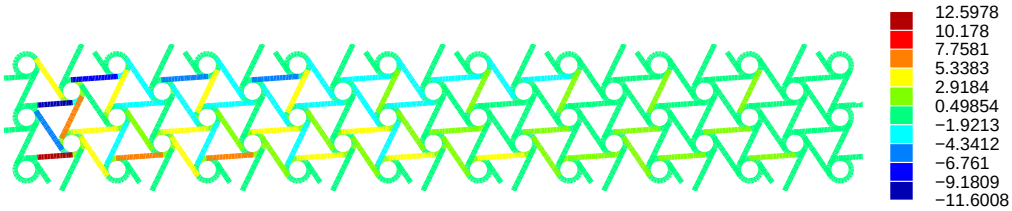

Figure 78: Direct axial strain (in μ-strain) due to unit tip transverse force

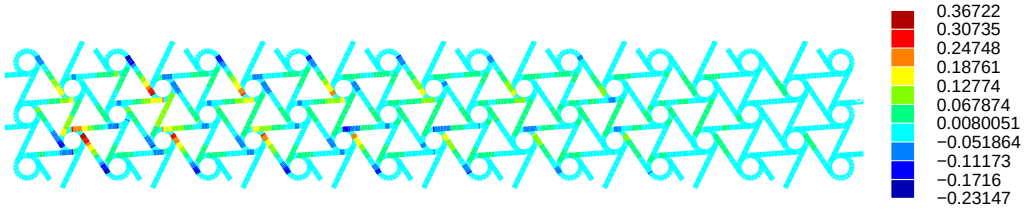

Figure 79: Ligament curvature (in 1/m) due to unit tip transverse force

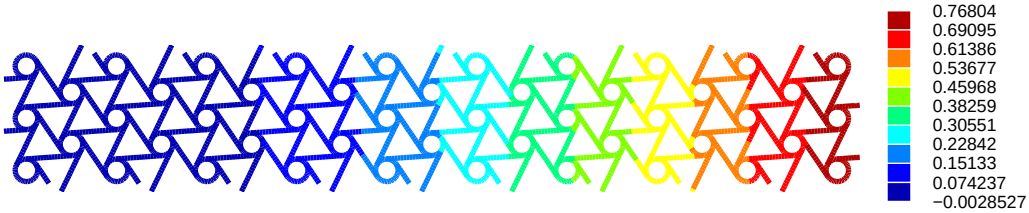

Figure 80: Transverse displacement (in mm) due to unit tip transverse force

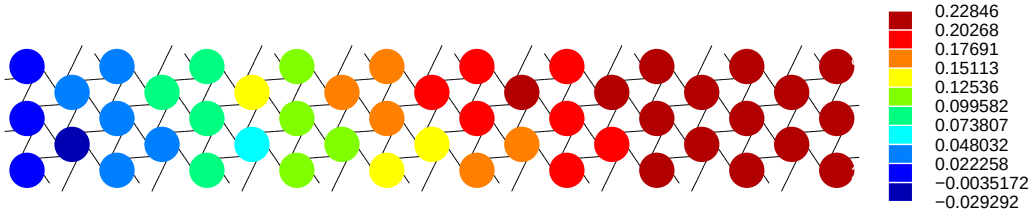

Figure 81: Circle rotation (in deg) due to unit tip transverse force

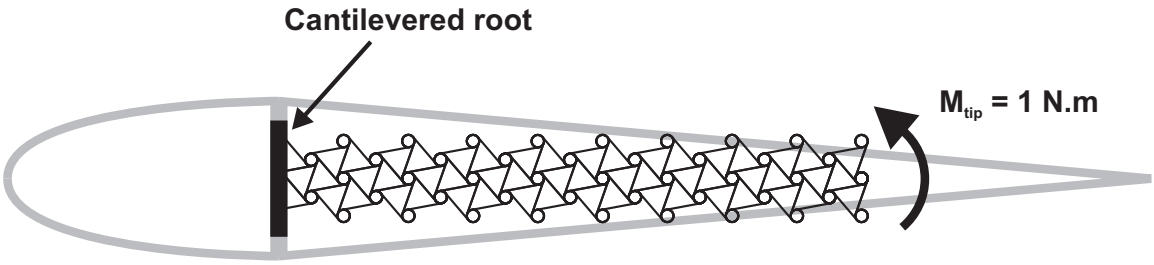

Figure 82: Clamped chiral beam with unit tip moment

rotation and linear deflection patterns hint at "rigid body rotation" toward the tip.

Next, the same chiral beam was loaded by a unit tip moment (Fig. 82), and its deformed configuration is shown in Fig. 83. Figures 84 and 85 show the direct axial strain and curvature respectively. It is clear that a periodic strain pattern arises over the length of the structure, showing that the deformation is periodically distributed throughtout the structure. Figures 86 and 87 show the transverse deflection and circle rotation respectively. The continuous gradient of rotation indicates that no rigid body type behavior occurs. Hence, the entire structure contributes to the deformation capability.

Figure 88 shows a blown-up view of a hexagonal cell, whose deformation pattern is repeated along the length of the chiral network. In addition to the periodicity, certain "symmetries" are revealed within this unit cell. Looking at the variation of curvature over the length of various ligaments (Fig. 89), it is clear that the plots are mirror images of each other. For example, the curvature in ligament #2 is identical to that in ligament #5 through a rotation of 180°. Similar symmetries would be found on those ligaments for the axial strain. Similar symmetries would also be observed on the inner ligaments of the hexagonal cell. Both of these features, repeatability and symmetry, could be used to simplify the problem of analyzing a chiral structure. Considering smaller unit cells may simplify the design process by affording a better grasp on the influence of certain parameters and by reducing simulation times. Control procedures could also be simplified, and equivalent mechanical properties could be obtained for

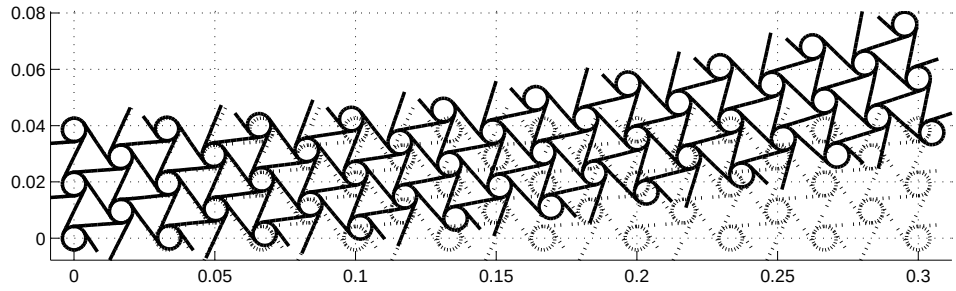

Figure 83: Deformed configuration due to unit tip moment (scaling factor = 10)

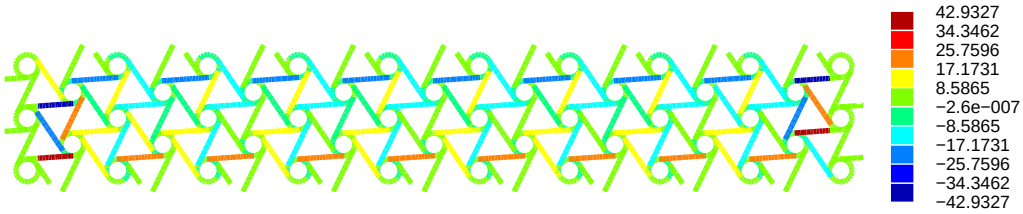

Figure 84: Direct axial strain (in μ-strain) due to unit tip moment

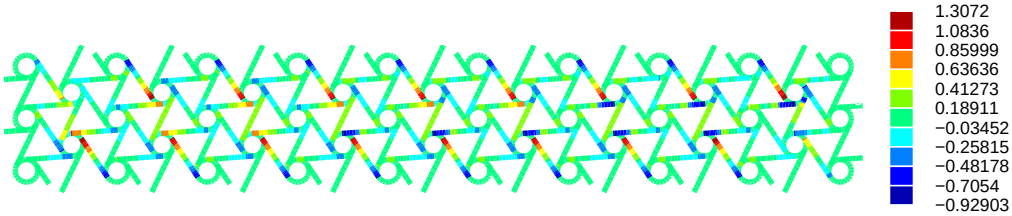

Figure 85: Ligament curvature (in 1/m) due to unit tip moment

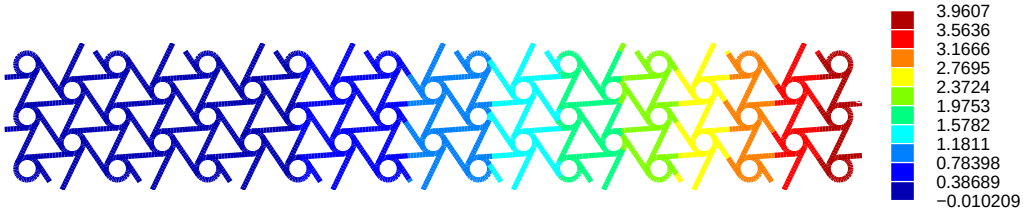

Figure 86: Transverse displacement (in mm) due to unit tip moment

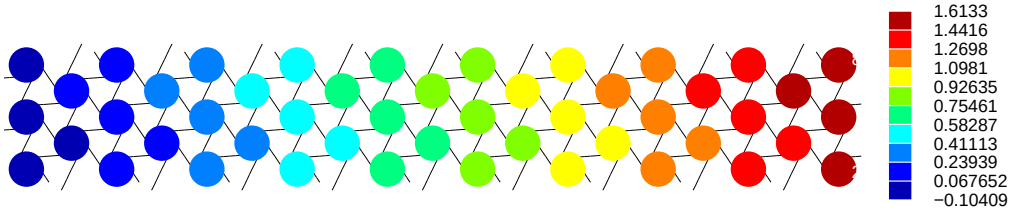

Figure 87: Circle rotation (in deg) due to unit tip moment

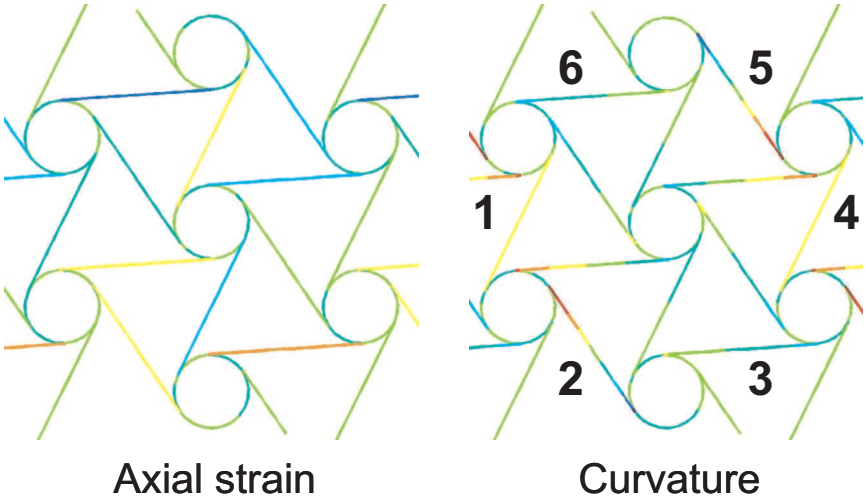

Figure 88: View of a single hexagonal cell in the unit tip moment case: axial strain and curvature

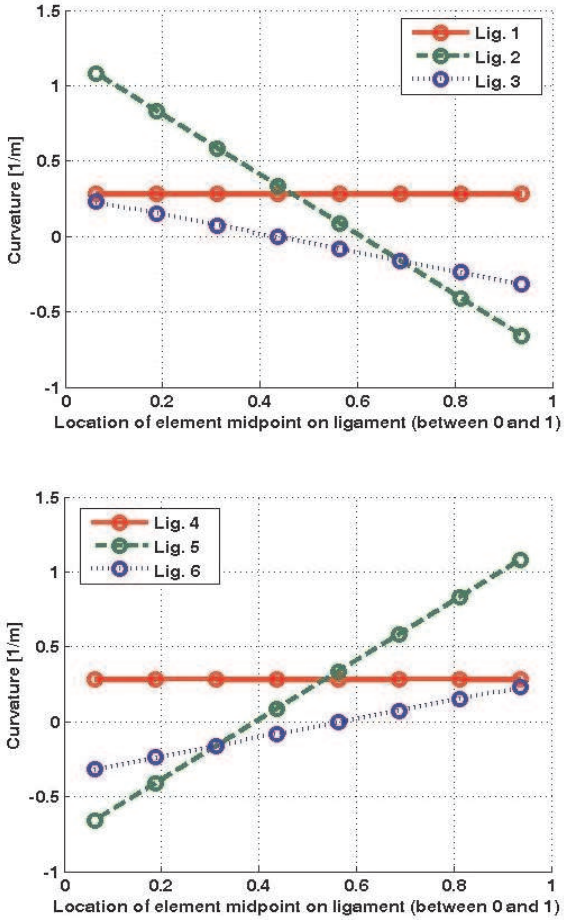

Figure 89: Curvatures of 6 ligaments as indicated in Fig. 88

use in comprehensive analyses of the full aeroelastic behavior of variable camber rotor blades.

6.2.2 Equivalent bending stiffness

In this section, it will be shown that a chiral structure can be represented as a beam with an equivalent bending stiffness. In order to obtain this coefficient, a vertical slice of the considered structure is subjected to bending moments at its left and right ends. The resulting deformation is measured by computing the angle made by the line joining the circles on the left-hand side in its deformed configuration relative to its undeformed configuration, and repeating this for the circles on the right-hand side. The total angle variation divided by the length of the considered slice provides an approximate measure of the global curvature of the chiral structure. The coefficient of proportionality between the applied moment and this curvature will be the equivalent bending stiffness of the chiral network. Then, this value can be used in standard solutions for cantilevered beams to approximate the deflection of the structure. First, we considered the case shown in Fig. 90, where $N_h = 4$ is even. Figures 91 and 92 show the deflection and angle of the reference line along the span, for a tip unit moment and a tip unit transverse force, respectively. It shows that very good agreement can be found based on the equivalent mechanical properties.

Figure 93 shows a similar case, but with $N_h = 5$ odd now, and the results are included in Figs. 94 and 95. Again, good agreement is found between the two models. It is noteworthy that in this case, there is no smooth variation of the deflection of each vertical line of circles along the length; however, the equivalent model captures the average behavior of the structure well. Hence, it is possible to approximate the behavior of the chiral beam using Euler-Bernoulli beam equations and the computed equivalent bending stiffness.

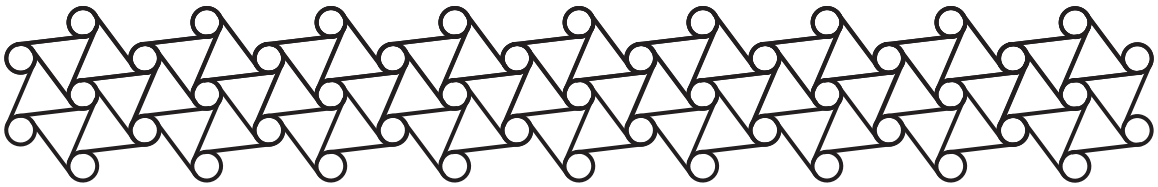

Figure 90: Chiral network with $N_l = 18$ and $N_h = 4$

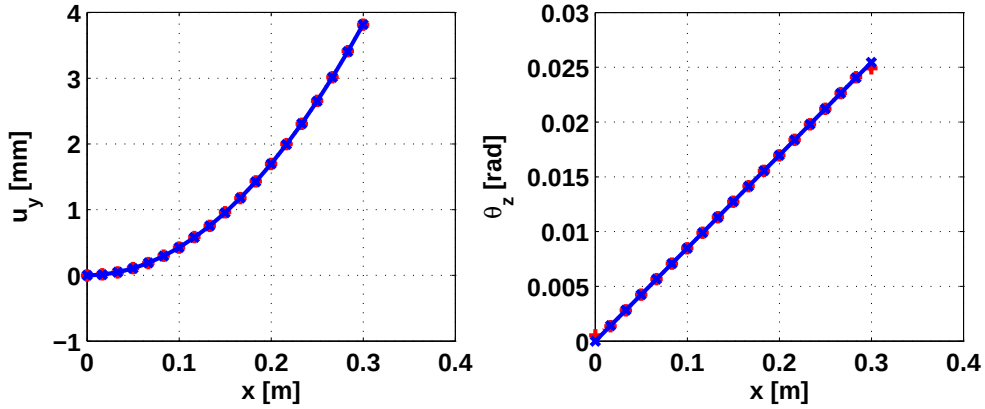

Figure 91: Deflection and angle of the reference line (chiral +, beam ×), when subjected to a unit tip moment, for the case $N_h = 4$

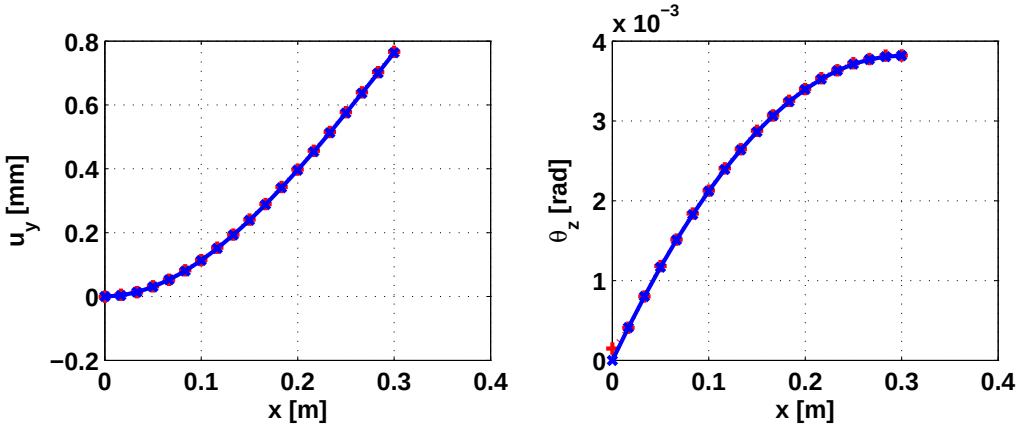

Figure 92: Deflection and angle of the reference line (chiral +, beam ×), when subjected to a unit tip transverse force, for the case $N_h = 4$

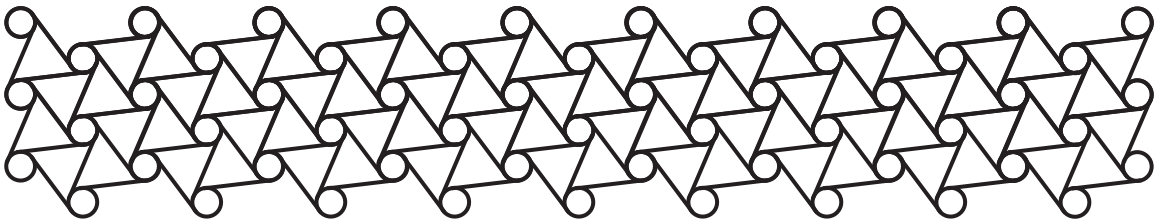

Figure 93: Chiral network with $N_l = 18$ and $N_h = 5$

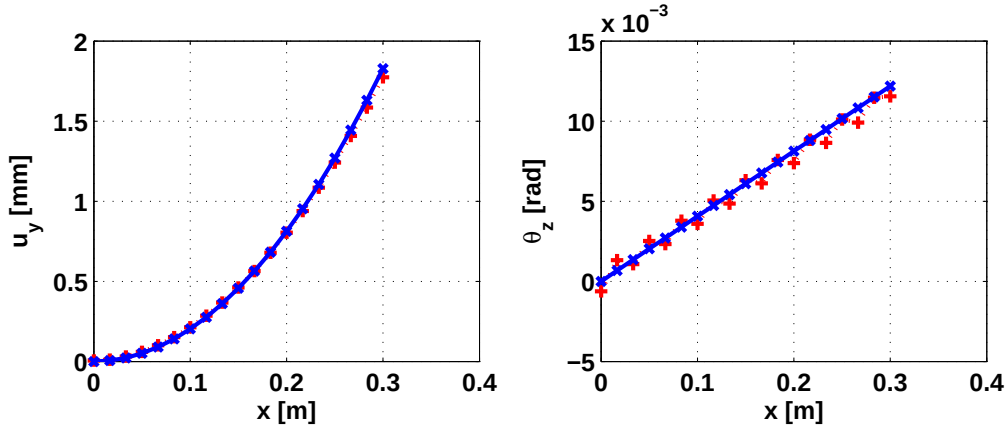

Figure 94: Deflection and angle of the reference line (chiral +, beam ×), when subjected to a unit tip moment, for the case $N_h = 5$

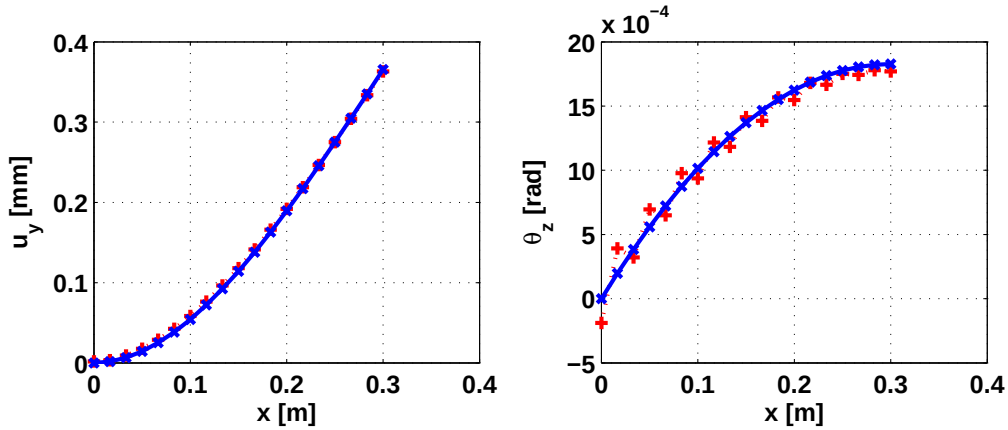

Figure 95: Deflection and angle of the reference line (chiral +, beam ×), when subjected to a unit tip transverse force, for the case $N_h = 5$

6.3 Active chiral networks

6.3.1 Piezoelectric actuation model

In order to include the effect of piezoelectric benders on the ligaments of the ANSYS model, a piezoelectric actuation model needed to be derived. ANSYS offers 3D solid elements with piezoelectric capabilities, but their integration into a beam or shell model for the chiral network is highly impractical. Furthermore, their inclusion would dramatically increase the computational cost of a simulation. Hence, an indirect approach was required and a simplified model was derived based on the demonstrable equivalence between the effect of a laminar piezoelectric actuator and the application of a gradient of temperature through the thickness of a ligament, in the framework of Euler-Bernoulli or Timoshenko beam theory. Figure 96 shows the two configurations under consideration. The results of Timoshenko beam theory can be derived while including additional terms due to thermal strains and the piezoelectric coupling terms in the constitutive equations.

The beam under consideration has Young's modulus E, thermal expansion coefficient α_{th}, width w, and thickness (or height) t. We consider the case where two piezo strips may be bonded to the beam representing a ligament, one on the top surface and one on the bottom one. The piezoelectric material is characterized by its Young's modulus E_p and its piezoelectric constant d_{21p} (the direction of polarization is $\bar{\imath}_2$). The piezo strips have thickness t_p. The electrodes on both piezo strips may have varying width, w_b on the bottom strip and w_t for the top one, and are subjected to voltages V_b and V_t. In addition, a linear temperature gradient may occur through the thickness

$$\Delta T(x_1, x_2) = \tau^T(x_2)\, \Delta T_1(x_1), \qquad \tau^T(x_2) = \tau_c^T + \tau_l^T x_2. \tag{134}$$

In this particular expression, x_2 has its origin at the ligament midplane, even though principal centroidal axes with their origin at the centroid will be chosen for the following derivation.

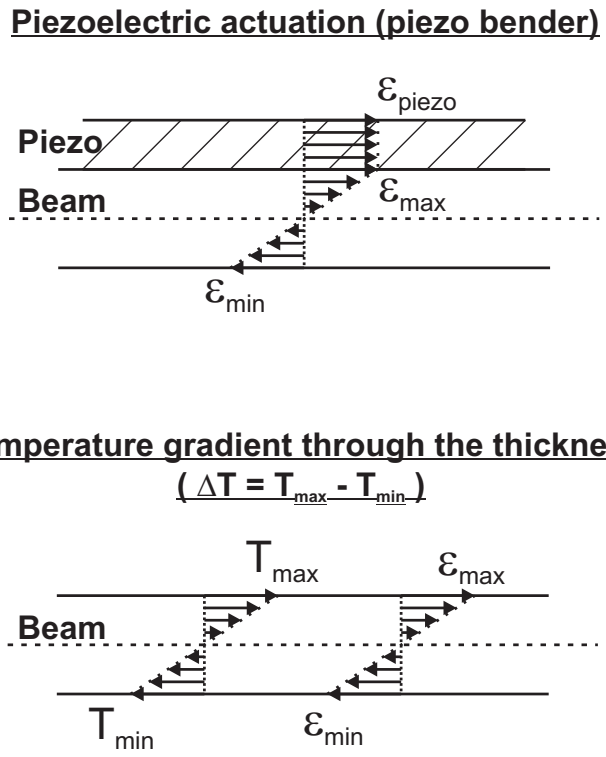

Figure 96: Equivalence between piezoelectric actuation and temperature gradient through the thickness

Based on the kinematic assumptions of Timoshenko beam theory, the displacement field reduces to

$$u_1(x_1, x_2, x_3) = \bar{u}_1(x_1) - x_2\Phi_3(x_1), \tag{135a}$$

$$u_2(x_1, x_2, x_3) = \bar{u}_2(x_1). \tag{135b}$$

The associated non-vanishing strain field components are then

$$\varepsilon_{11}(x_1, x_2, x_3) = \bar{\varepsilon}_1 - x_2\kappa_3, \tag{136a}$$

$$\gamma_{12}(x_1, x_2, x_3) = \bar{u}_2' - \Phi_3, \tag{136b}$$

where $(\cdot)'$ indicates differentiation with respect to x_1, and where we introduced

$$\bar{\varepsilon}_1(x_1) = \bar{u}_1'(x_1), \qquad \kappa_3(x_1) = \bar{u}_2''(x_1). \tag{137}$$

Following the standard beam assumption that the normal stresses besides σ_{11} are comparatively very small and can be neglected, the constitutive relationship including

the effect of the piezoelectric benders and the temperature gradient is

$$\varepsilon_{11} = \frac{1}{E}\sigma_{11} + d_{21}(x_2)\frac{V_j(x_1)}{t_j(x_1)} + \alpha_{\text{th}}(x_2)\Delta T(x_1, x_2), \tag{138a}$$

$$\gamma_{12} = \frac{1}{G}\tau_{12}. \tag{138b}$$

d_{21} varies with x_2 in the sense that it is 0 in the ligament, and constant equal to d_{21p} in the piezoelectric strips. Likewise, since the temperature gradient is only assumed to act in the beam, α_{th} may be assumed to be zero in the piezoelectric material. The subscript j can refer to either piezoelectric strip (the bottom one b or the top one t), or the ligament itself. For the ligament, $t_j = t$ and V_j is irrelevant. For either piezobender, t_j is the thickness of the piezo strip and V_j is either V_b or V_t.

The axial force is defined as

$$N_1(x_1) = \int_{\mathcal{A}} \sigma_{11}\,\mathrm{d}\mathcal{A}, \tag{139}$$

which, upon substituting in the expression for σ_{11} from the constitutive equations and carrying out the integrations, becomes

$$\begin{aligned} N_1(x_1) = S\bar{\varepsilon}_1(x_1) - Etw\alpha_{\text{th}}\tau_c^T\Delta T_1(x_1) \\ - E_p d_{21p} w_b(x_1) V_b(x_1) - E_p d_{21p} w_t(x_1) V_t(x_1), \end{aligned} \tag{140}$$

$S = \int_{\mathcal{A}} E\,\mathrm{d}\mathcal{A}$ is the axial stiffness of the entire section (including any piezobenders), and centroidal axes were chosen to simplify this expression. Similarly, the shear force defined as

$$V_2(x_1) = \int_{\mathcal{A}} \tau_{12}\,\mathrm{d}\mathcal{A} \tag{141}$$

is simply found to be

$$V_2(x_1) = K_{22}\left(\bar{u}_2' - \Phi_3\right). \tag{142}$$

K_{22} is here the shear stiffness associated with Timoshenko beam theory. Euler-Bernoulli beam theory can be recovered by considering the limiting case in which

$K_{22} \to \infty$. Finally, the bending moment

$$M_3(x_1) = \int_{\mathcal{A}} -x_2 \sigma_{11} \, \mathrm{d}\mathcal{A} \tag{143}$$

can similarly be computed, and is found to be

$$\begin{aligned} M_3(x_1) = H^c_{33}\kappa_3(x_1) - Etw\alpha_{\text{th}} \left(\tau_c^T d_{2c} - \tau_l^T \frac{t^2}{12} \right) \Delta T_1(x_1) \\ - E_p d_{21p} \left(\frac{t+t_p}{2} + d_{2c} \right) w_b(x_1) V_b(x_1) \\ + E_p d_{21p} \left(\frac{t+t_p}{2} - d_{2c} \right) w_t(x_1) V_t(x_1), \end{aligned} \tag{144}$$

where $H^c_{33} = \int_{\mathcal{A}} E x_2^2 \, \mathrm{d}\mathcal{A}$ is the bending stiffness for the section (which includes the piezo strips), and d_{2c} denotes the location of the centroid from the midplane. To summarize, the sectional loads can be written in the form

$$N_1(x_1) = S \, \bar{\varepsilon}_1(x_1) - N_{1\text{th}}(x_1) - N_{1p}(x_1), \tag{145a}$$

$$V_2(x_1) = K_{22} \left(\bar{u}_2' - \Phi_3 \right), \tag{145b}$$

$$M_3(x_1) = H^c_{33} \, \kappa_3(x_1) - M_{3\text{th}}(x_1) - M_{3p}(x_1), \tag{145c}$$

where $N_{1p} = N_{1b} + N_{1t}$, $M_{3p} = M_{3b} + M_{3t}$, and introducing the notations $\chi_b(x_1) = w_b(x_1)V_b(x_1)$ and $\chi_t(x_1) = w_t(x_1)V_t(x_1)$, these individual terms can be written as

$$N_{1\text{th}}(x_1) = E \, t \, w \, \alpha_{\text{th}} \, \tau_c^T \, \Delta T_1(x_1), \tag{146a}$$

$$N_{1b}(x_1) = E_p \, d_{21p} \, \chi_b(x_1), \tag{146b}$$

$$N_{1t}(x_1) = E_p \, d_{21p} \, \chi_t(x_1), \tag{146c}$$

$$M_{3\text{th}}(x_1) = E \, t \, w \, \alpha_{\text{th}} \left(\tau_c^T d_{2c} - \tau_l^T \frac{t^2}{12} \right) \Delta T_1(x_1), \tag{146d}$$

$$M_{3b}(x_1) = \quad E_p \, d_{21p} \left(\frac{t+t_p}{2} + d_{2c} \right) \chi_b(x_1), \tag{146e}$$

$$M_{3t}(x_1) = -E_p \, d_{21p} \left(\frac{t+t_p}{2} - d_{2c} \right) \chi_t(x_1). \tag{146f}$$

Of course, if any (or both) of the piezo strips are removed, the corresponding terms simply need to be removed from the equations.

By simple application of Newton's laws to an infinitesimal cross-sectional slice of material in the beam (details may be found in Ref. 9), the equilibrium equations governing the behavior of this Timoshenko beam are

$$N_1' = -p_1(x_1), \tag{147a}$$

$$V_2' = -p_2(x_1), \tag{147b}$$

$$M_3' + V_2 = -q_3(x_1). \tag{147c}$$

Taking a derivative of the third equation and using the second, another form of the third equation can be obtained

$$M_3'' = p_2(x_1) - q_3'(x_1). \tag{148}$$

Substituting the expressions of the sectional forces and moments obtained earlier into these equations yields the governing equations of the problem

$$S\bar{u}_1'' = -p_1 + N_{1\text{th}}' + N_{1p}', \tag{149a}$$

$$K_{22}\left(\bar{u}_2' - \Phi_3\right)' = -p_2, \tag{149b}$$

$$H_{33}^c\bar{u}_2''' + K_{22}\left(\bar{u}_2' - \Phi_3\right) = -q_3 + M_{3\text{th}}' + M_{3p}'. \tag{149c}$$

It is now clear that if we set the values of w_b, w_t, V_b, V_t and ΔT such that

$$N_{1b}(x_1) + N_{1t}(x_1) = N_{1\text{th}}(x_1), \qquad M_{3b}(x_1) + M_{3t}(x_1) = M_{3\text{th}}(x_1), \tag{150}$$

then the effects on the beam's behavior of the thermal loading and of the piezo-benders will be identical. In other words, these relationships allow us to determine the temperature gradient needed to represent the effect of piezoelectric actuation. Therefore, in the following simulations run in ANSYS, the piezoelectric actuators and their associated desired input voltages will be included through linear through-the-thickness temperature gradients in the active ligaments.

In order to validate this equivalence based on beam theory, several models of simple cantilevered beams where tested: an ANSYS 3D solid model of a piezoelectric

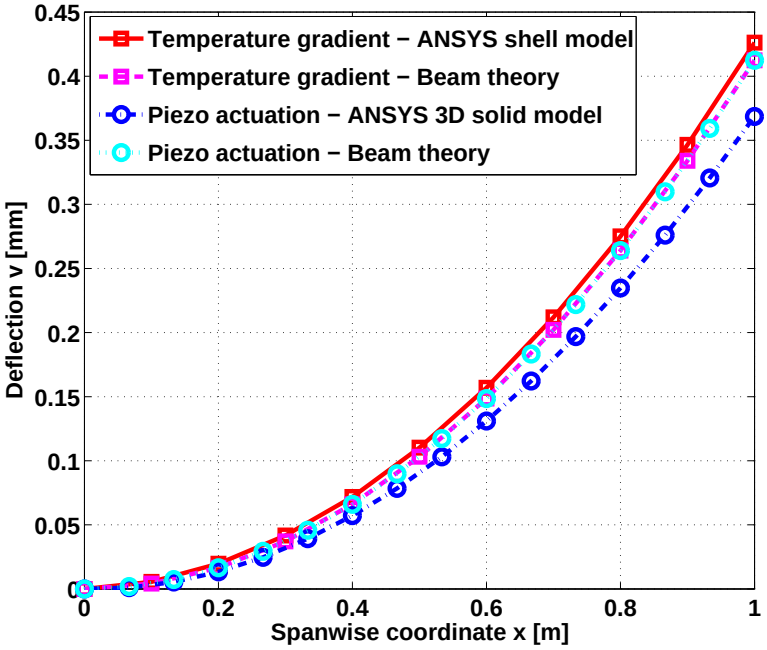

Figure 97: Comparison of four models of a cantilevered beam with actuation

material on top of a beam; an ANSYS shell model of a beam with a temperature gradient through the thickness; and analytical beam theory results for these same two cases. The results shown in Fig. 97 display very good correlation. As one would expect, the analytical results are identical, and unsurprisingly as well, the shell model results are closer to the beam solution than the 3D solid ones. Similar correlation was found with pinned-pinned boundary conditions.

6.3.2 Performance of simple actuation strategies

Several simple actuation strategies using laminar piezoelectric actuators were initially considered to deform the ligaments and induce a global deformation of the chiral structure. As shown in Fig. 98, a first option is to cover the full length of one side of the ligament with a laminar actuator capable of inducing a constant curvature along the full span of the ligament. This will be referred to as *simple bending* actuation. A second option, referred to as *double bending* actuation, is shown in Fig. 99. In this

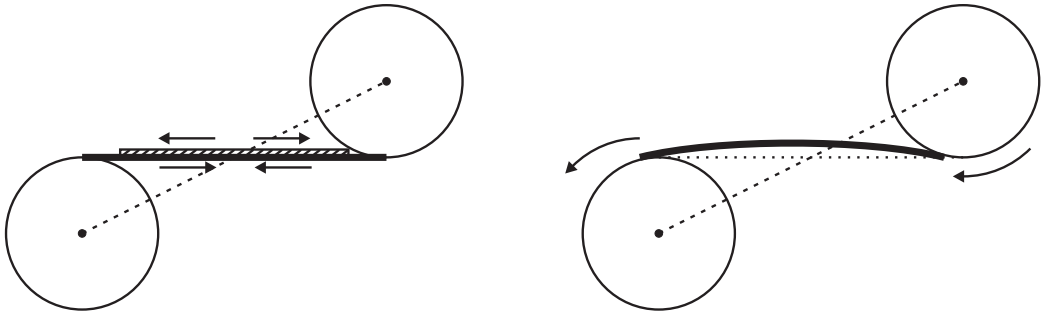

Figure 98: Configuration of piezoelectric actuators and deformation pattern for "simple bending" actuation

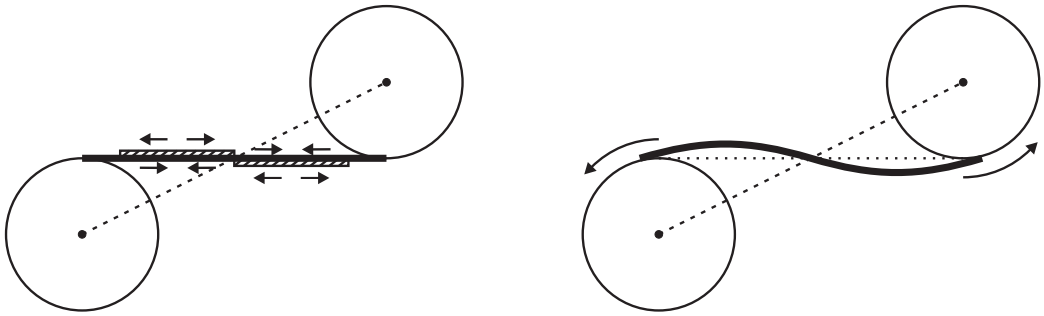

Figure 99: Configuration of piezoelectric actuators and deformation pattern for "double bending" actuation

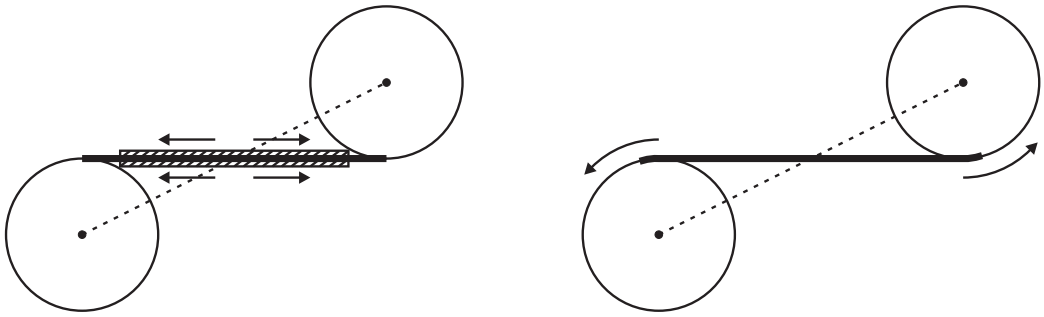

Figure 100: Configuration of piezoelectric actuators and deformation pattern for axial actuation

case, half of one side of the ligament is covered with a piezo-bender, while another actuator is added to the other side of the other half of the ligament. A piece-wise constant curvature is therefore created, with equal magnitudes but opposite signs on the two halves, which generates the deformation pattern highlighted in Fig. 99. Note that the same effect can be obtained by having both piezo-benders on the same side, but with opposite polarizations or opposite applied voltages. Finally, a third option, which does not take advantage of the bending-dominated deformation patterns of chiral networks, is shown for completeness in Fig. 100. One could imagine bonding two laminar actuators on the ligament, one on each side, to generate a constant axial strain through the thickness of the ligament (strains of equal magnitudes on the top and bottom). The ligament exhibits no curvature, so that the deformation due to the actuation is purely axial.

A set of simulations was run in ANSYS in which each ligament was individually actuated with each of the three actuation mechanisms described in the previous section, and the lateral tip displacement was reported. To reduce simulation times, a smaller chiral structure with fewer ligaments was considered (a total of 54 ligaments). They are ordered such that ligament numbers increase from the root of the structure (left-most ligaments) to the tip (right-most ligaments). The results may be found in Fig. 101. It is clear that axial straining yields very poor results in most of the network, except for a few ligaments at the root which generate a relatively large rigid-body rotation of the chiral beam. In these cases, a hinging phenomenon occurs at the root. It is also obvious that ligaments at the tip of the structure do not have any sizeable effect on the output. Any tip deflection measured there is only a reflection of local deformations, not of any desirable global deformations. Finally, we see that globally, for relevant ligament positions away from the extremities, double bending actuation works better than simple bending. These simple cases show that the choice of actuation mechanism greatly affects the results, as well as the choice of actuated

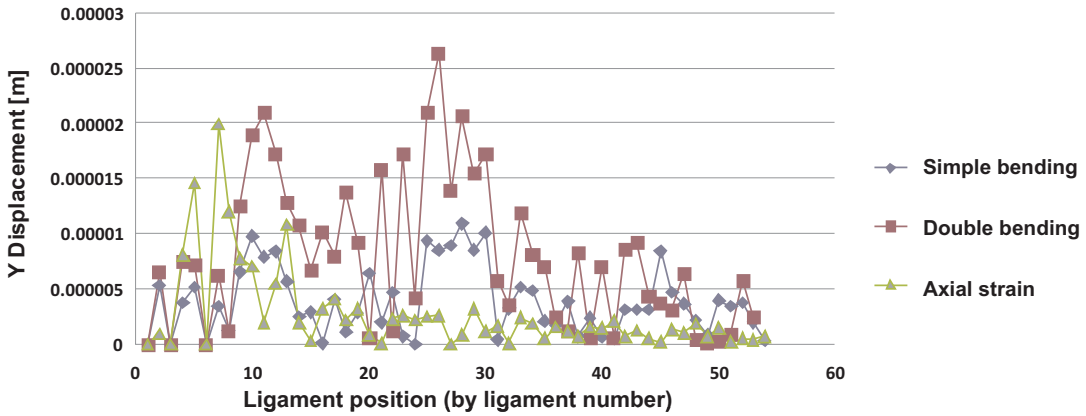

Figure 101: Tip lateral displacement as a function of actuated ligament location and actuation mechanism

ligament positions. As a final remark, it can be noticed that "simple bending" may be viewed as a special case of "double bending", if the control input allows for setting the voltages of the two halves as equal or opposite. In this case, it would be possible to choose the best actuation mechanism for each individual ligament separately, leading to a mixture of simply and doubly actuated ligaments in the same chiral network.

As an example, the global deformation due to actuation of ligament # 26 is shown for all three cases in Figs. 102, 103 and 104 (scaling factor 1000). The double bending strategy clearly provides the best result for this ligament, while the axial straining strategy comparatively has no noticeable effect.

6.3.3 Application of static aerodynamic loads

In this section, the actuated chiral network's ability to react typical aerodynamic load levels found on rotorcraft will be assessed. An estimate was obtained using the time history of total lift on a UH-60 rotor blade in high speed forward flight (Fig. 34). Based on the maximum value of lift encountered over a full rotation, and assuming a constant aerodynamic pressure over the entire planform of the blade, "typical" orders of magnitude were found for the aerodynamic forces and moments one could expect an airfoil section with chiral structure to carry. These load levels were then statically

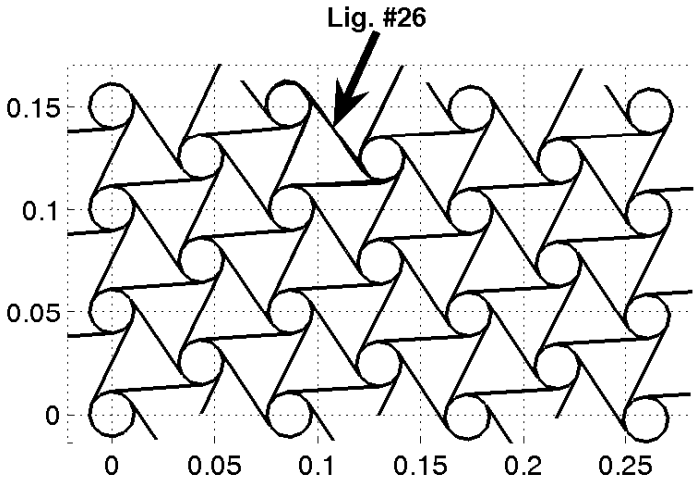

Figure 102: Structural deformation due to axial straining in ligament # 26

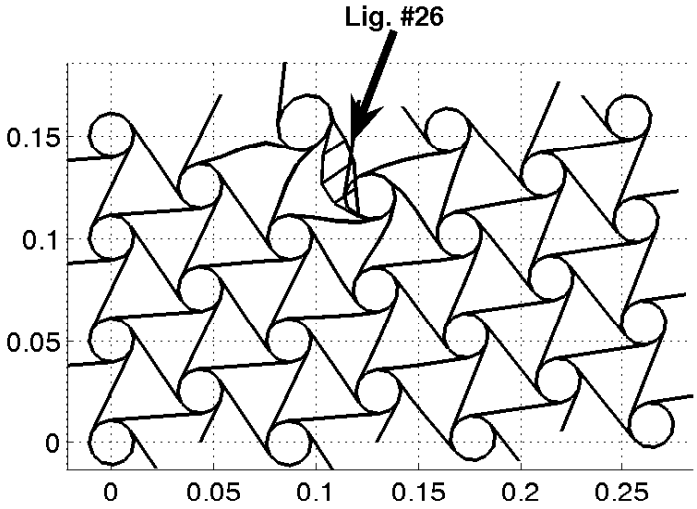

Figure 103: Structural deformation due to simple bending actuation in ligament # 26

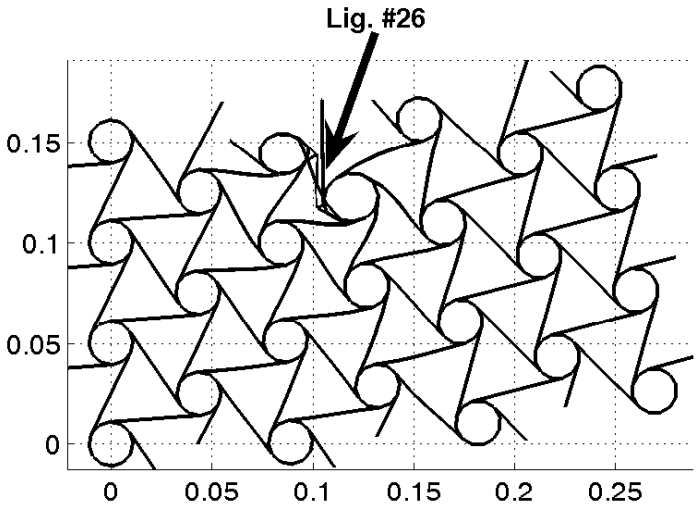

Figure 104: Structural deformation due to double bending actuation in ligament # 26

applied to the structure. Figure 105 shows the applied forces on the chiral structure to represent the aerodynamic pressure on the airfoil.

The deflection of the 75%-of-chord aft part of the airfoil was studied under the combined effects of the applied steady aerodynamic loads and/or piezoelectric actuation. Parametric studies were undertaken to determine the influence of several geometric variables defining the chiral network: $\rho = \frac{L}{R}$ ratio, number of cells in the transverse direction N_h, ligament thickness, and piezoelectric bender thickness. Selected results are shown in Figs. 106, 107, 108, and 109. Each figure corresponds to a particular set of values for t and t_p, and shows the tip deflection as it varies with ρ and N_h in three cases: passively loaded structure; actuated structure with double bending strategy; and actuated structure under aerodynamic loads.

These studies show that using the actuation capabilities of chiral networks in a static manner to react aerodynamic loads may not provide the authority needed for a successful concept. For reasonable values of the parameters, deflections do not reach sufficient levels. Configurations may be found where the aerodynamic loads can be

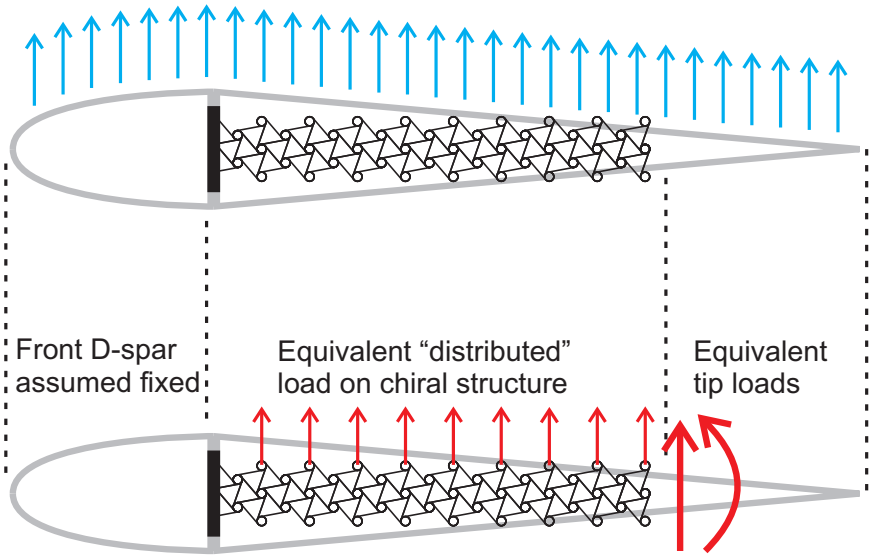

Figure 105: Equivalent forces and moments to represent the steady aerodynamic pressure

successfully reacted, but the stiffness of the structure becomes too important in those situations.

However, it is known that many concepts involving morphing of rotor blades rely on the unsteady nature of the airflow on the rotor blades to achieve sizeable results. Similarly, our concept may perform better when considered in a dynamic environment where the coupling with unsteady aerodynamics may amplify the currently available actuation capability.

6.4 Summary

A novel concept for continuous camber deformation of rotor blades was proposed based on a particular type of cellular structure. Chiral lattice networks are fitting candidates for such an application. Embedded actuation using piezoelectric materials can be distributed throughout the structure to generate local deformations which then compound into global morphing. Such a "chiral actuator" may be used to deflect flaps or to directly change the camber of a rotor blade's aft section. Studies of the passive case lead to a few general observations on the properties of deformations of passively

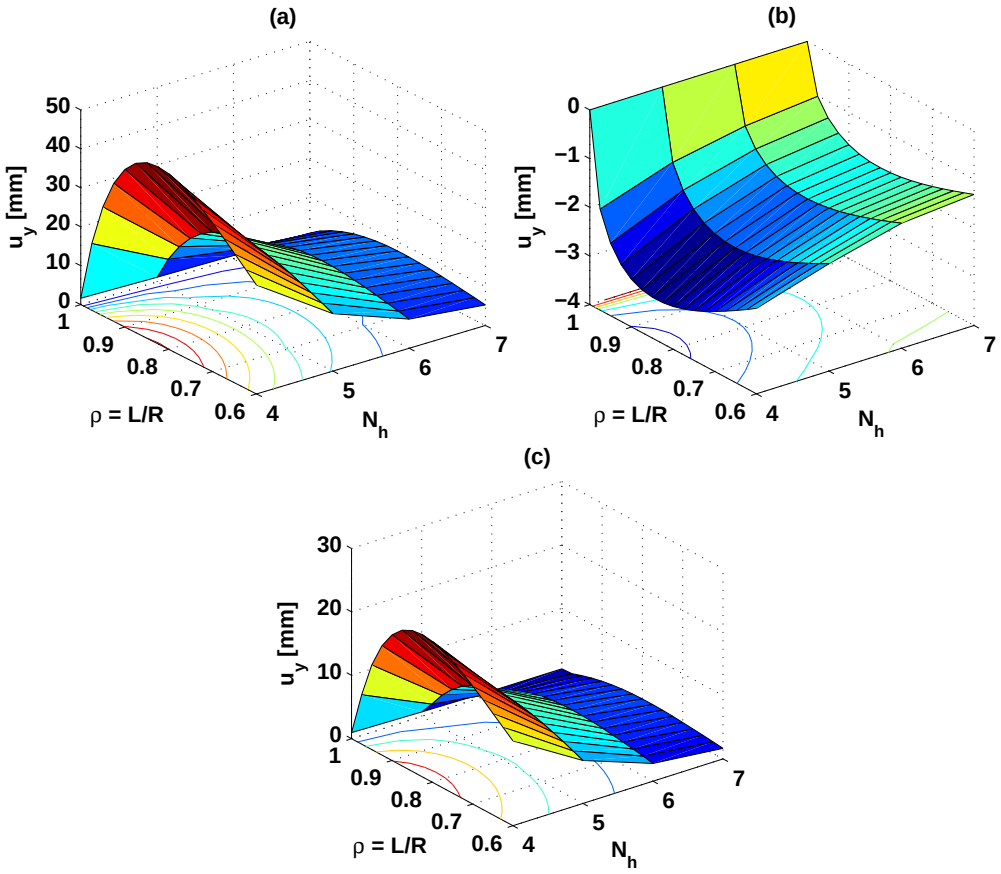

Figure 106: Tip deflection under estimated aerodynamic loads with varying number of cells and varying ρ, in the case $t = 0.5$ mm and $t_p = 0.5$ mm: (a) passively loaded structure; (b) double bending actuation only; (c) airloads and actuation

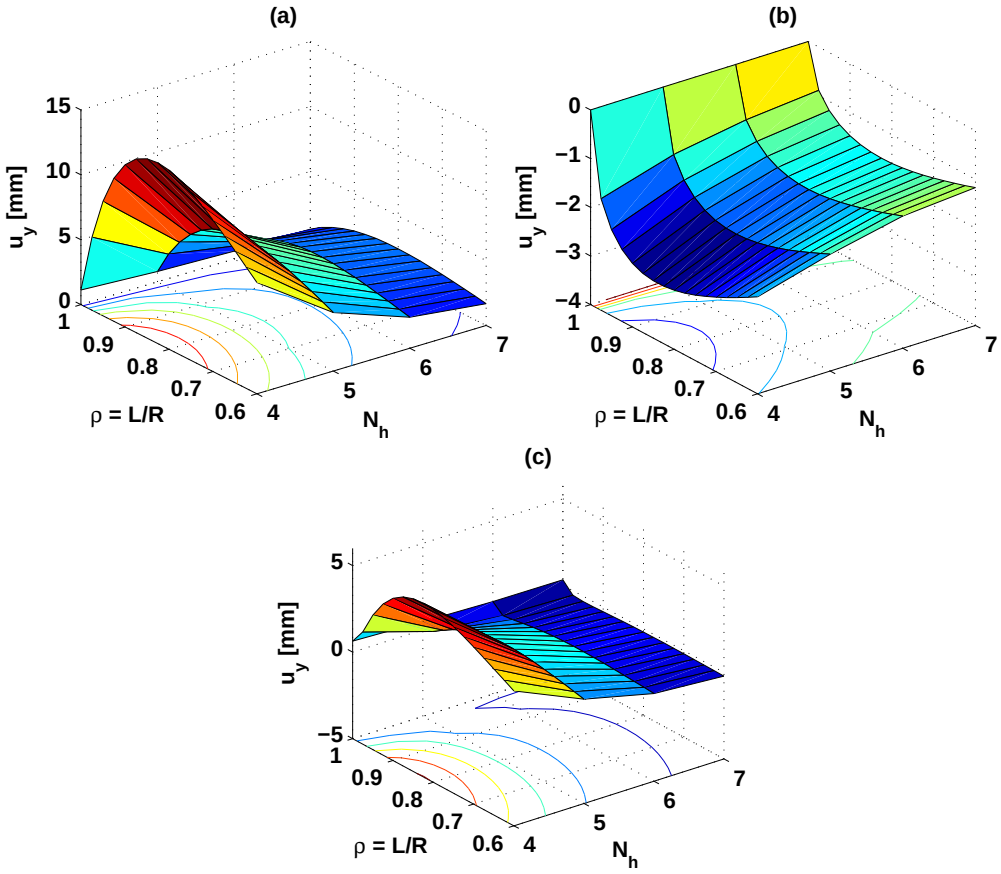

Figure 107: Tip deflection under estimated aerodynamic loads with varying number of cells and varying ρ, in the case $t = 0.5$ mm and $t_p = 1$ mm: (a) passively loaded structure; (b) double bending actuation only; (c) airloads and actuation

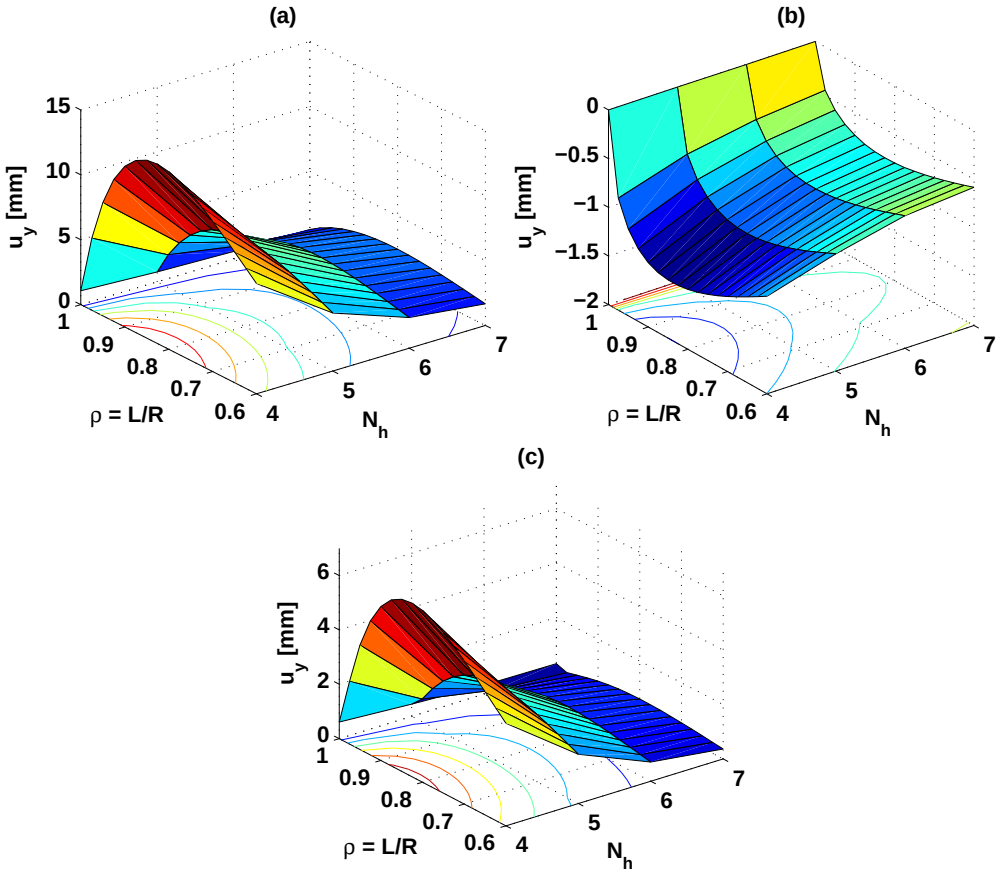

Figure 108: Tip deflection under estimated aerodynamic loads with varying number of cells and varying ρ, in the case $t = 1$ mm and $t_p = 0.5$ mm: (a) passively loaded structure; (b) double bending actuation only; (c) airloads and actuation

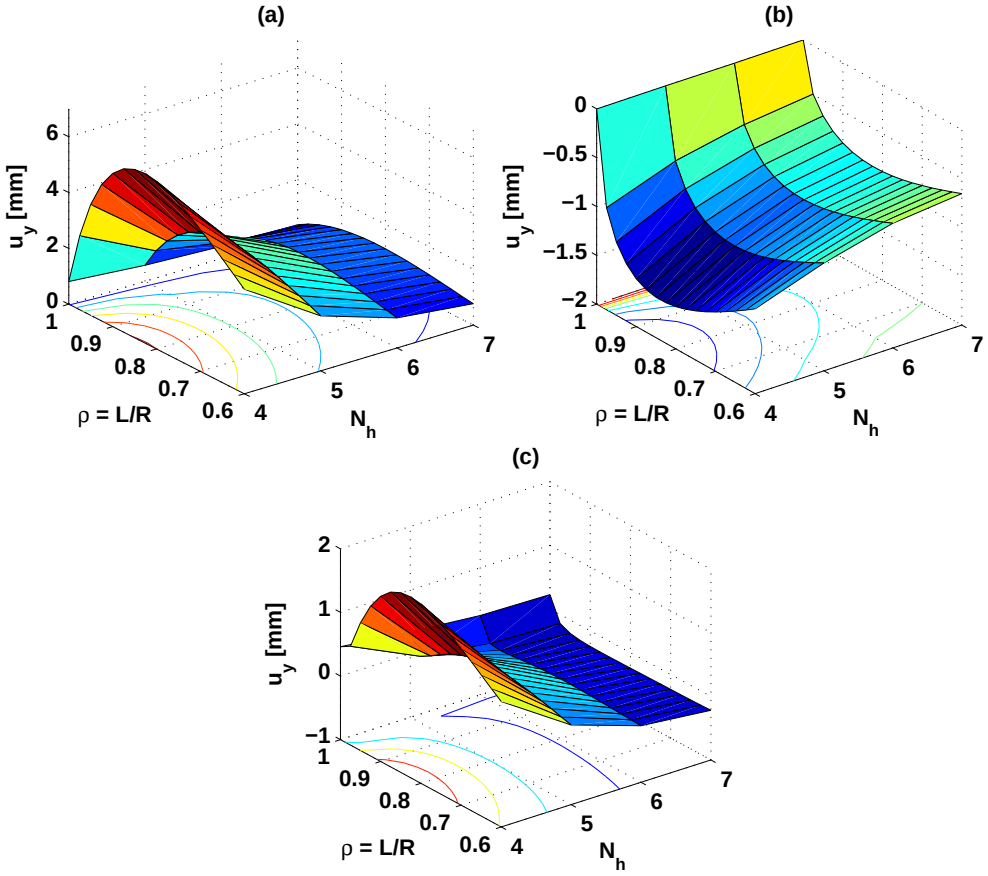

Figure 109: Tip deflection under estimated aerodynamic loads with varying number of cells and varying ρ, in the case $t = 1$ mm and $t_p = 1$ mm: (a) passively loaded structure; (b) double bending actuation only; (c) airloads and actuation

loaded structures. Interestingly, the overall reference line deformation of a rectangular chiral network can be modeled by regular Euler-Bernoulli beam equations with an equivalent bending stiffness value. Preliminary studies of the active case were based on a simplified actuation model in ANSYS. Several simple actuation schemes were investigated, and "double bending" actuation was determined to be more efficient in general. Exploratory simulations assessed the ability of such structures to react typical values of aerodynamic loads on UH-60 rotor blades, and it was shown that the control authority provided by piezoelectric materials was not sufficient in a steady aerodynamic environment.

CHAPTER VII

AEROELASTIC ANALYSIS OF CHIRAL ACTUATORS

The approach that was followed in Chapter 6 for the static analysis of passive and active chiral networks involved the use of the commercial software ANSYS, and relied on the theoretical equivalence between piezo-benders bonded to the ligaments and temperature gradients through the thickness of the ligaments. This effectively allowed the interpretation of the response of thermally loaded chiral structures as a deformation generated through piezoelectric actuation. Simple actuation schemes could be modeled this way.

Unfortunately, this approach has several shortcomings. First of all, the high computational cost of static analyses of such structures in ANSYS is detrimental to the design process. This process could require that many geometric configurations be studied, with varying actuation methods and different actuator placement schemes. For preliminary design stages, simple, efficient numerical analyses are clearly necessary. This becomes even more crucial when dynamic simulations are needed, possibly including a coupled aerodynamics model as well. Second, using the equivalence mentioned above proves to be difficult to implement and time-consuming to use. Applying temperature gradients to the structural model is a convoluted way of dealing with mechanical loading. More importantly, the equivalence is imperfect because it is only established for theoretical beam models. The models used in ANSYS are shell models, which may exhibit slightly different properties than theoretical beams, or even beam elements available in ANSYS. The temperature gradients are applied as prescribed nodal temperatures; if the modeling of thermal loading is not entirely understood, one runs the risk of misinterpreting the results. Some of the physics of thermal effects

that are included in the analysis may not be taken into consideration in the simple equivalence relationship, implying that it is only approximative. More generally, possible unknown effects may violate the assumptions made to derive the equivalence equations, so as to render them unreliable, and therefore impractical. Finally, temperature gradients in ANSYS can only realistically model very simple actuator configuration, such as the simple and double bending schemes presented previously. A tool is needed that can simulate more complicated actuation strategies.

In this chapter, a code will be presented that accomodates different types of actuation at a reduced computational cost. It is based on explicit assumptions and models, so results are easily interpreted and their limitations clearly understood. It considers each ligament as an Euler-Bernoulli or Timoshenko beam, and represents the circular nodes as rigid bodies. For static analyses, an exact analytical solution is found for a typical ligament in terms of the center displacements of the associated circles. This solution includes the effect of piezoelectric actuation as an applied distributed load. A MATLAB program is then used to assemble all the ligaments of a chiral network, in a manner similar to the way finite elements are assembled in standard FEA, to obtain the structure's stiffness matrix. The degrees-of-freedom of the system are the two in-plane displacements of the center of each circle, as well as the in-plane rotation of those nodes. Finally, boundary conditions as well as additional external loads are applied, and the resulting system of equations is solved for the degrees-of-freedom of the system. This approach was shown to yield similar results to ANSYS on the simpler cases (for which the circles were defined as rigid bodies, and beam elements were used), but with much shorter simulation times.

In order to evaluate the reasonableness of the rigid circle assumption, a number of ANSYS simulations were run with varying circle compliance, by varying the thickness of the circles relative to that of the ligaments (which remained unchanged). The results summarized in the logarithmic plot of Fig. 110 show the tip deflection of the

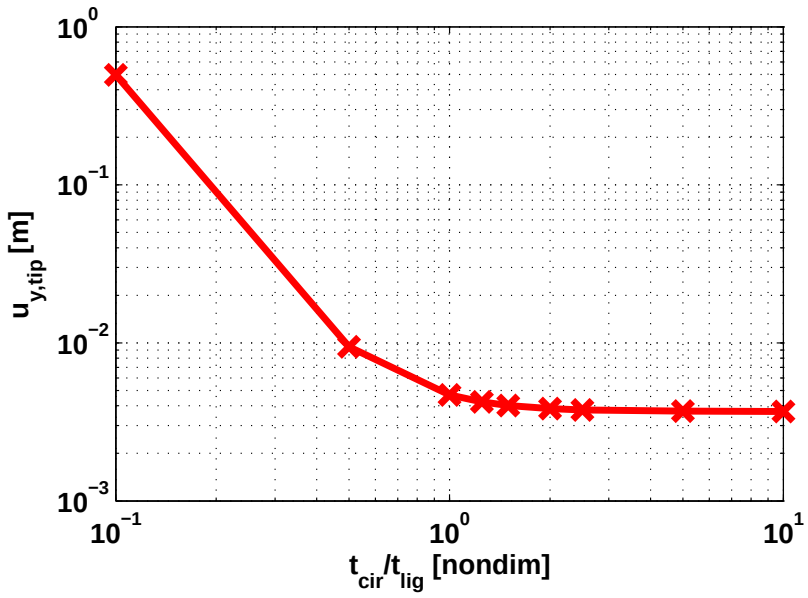

Figure 110: Tip transverse deflection for varying thickness of the circles (nondimensionalized by the thickness of the ligaments)

chiral structure as it varies with circle thickness. It is clear that for the range of values of interest, where the thickness of the circles is at least that of the ligaments, the overall deformation is only slightly affected by the compliance of the circles. Considering manufacturing constraints with composite materials as well, in which case the thickness of the circles would be at least twice that of the ligaments, we see that the compliance of the circles only minimally affects the final results. Therefore, it is a fair simplifying assumption to consider the nodes to be rigid. Furthermore, increasing their stiffness to prevent uncontrollable deformations in the circles would be highly desirable.

7.1 Theoretical foundation for static analysis of active chiral networks

7.1.1 Ligament model

In this section, we consider the 2D axial and transverse behavior of a single ligament with rectangular cross-section of length L, height t and width w, as shown in Fig. 111.

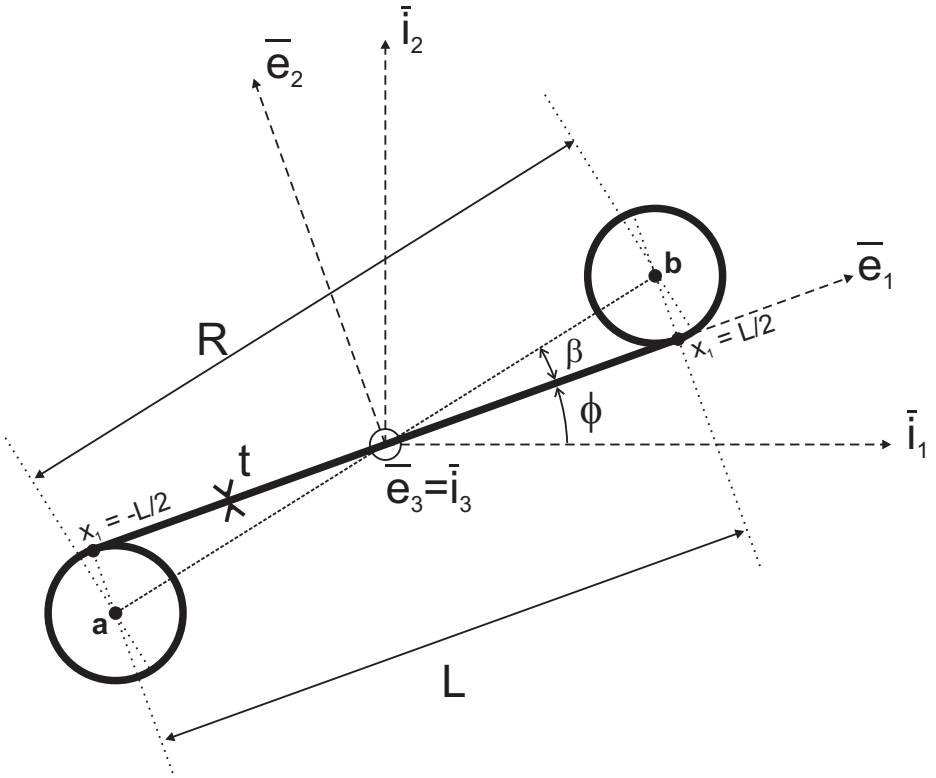

Figure 111: Single ligament with rigid circles

The axial unit vector $\bar{e}_1$ is along the reference line and the associated coordinate x_1 has its origin at the center point of the beam. In other words, the "left" end is located at $x_1 = x_{1a} = -L/2$, while the "right" extremity is at $x_1 = x_{1b} = L/2$. For any vector function $\underline{f}(x_1)$, we will use the following notation: $\underline{f}(x_{1a}) = \underline{f}_a$ and $\underline{f}(x_{1b}) = \underline{f}_b$. Axes $\bar{e}_2$ and $\bar{e}_3$ are in the plane of the cross-section, $\bar{e}_2$ in the plane of bending (normal to the thin ligament) and $\bar{e}_3$ along the width. The ligament has applied distributed loads: distributed axial force $p_1(x_1)$ along $\bar{e}_1$, distributed transverse force $p_2(x_1)$ along $\bar{e}_2$, and distributed bending moment $q_3(x_1)$ about $\bar{e}_3$. In addition, the displacements and rotation of the centers of the rigid circles attached to the extremities of the ligament are prescribed: u_a^e and v_a^e are the displacements of the "left" node along $\bar{e}_1$ and $\bar{e}_2$, respectively; θ_a^e is its rotation about $\bar{e}_3$; and u_b^e, v_b^e and θ_b^e are the corresponding quantities for the "right" node.

The displacements of the "left" extremity of the ligament, $\bar{u}_a^e$ and $\bar{v}_a^e$, and the

rotation at that point, $\bar{\theta}_a^e$, as well the corresponding quantities at the other end, $\bar{u}_b^e$, $\bar{v}_b^e$ and $\bar{\theta}_b^e$, are related to the displacements and the rotation of those circle centers. Assuming small displacements and angles,

$$\bar{u}_a^e = u_a^e - r\theta_a^e, \qquad \bar{v}_a^e = v_a^e, \qquad \bar{\theta}_a^e = \theta_a^e, \tag{151}$$

and

$$\bar{u}_b^e = u_b^e + r\theta_b^e, \qquad \bar{v}_b^e = v_b^e, \qquad \bar{\theta}_b^e = \theta_b^e, \tag{152}$$

where r is the radius of the circles. Introducing the arrays $\underline{u}^{e\,T} = \{u_a^e\,,\, v_a^e\,,\, \theta_a^e\,,\, u_b^e\,,\, v_b^e\,,\, \theta_b^e\}$ and $\underline{\bar{u}}^{e\,T} = \{\bar{u}_a^e\,,\, \bar{v}_a^e\,,\, \bar{\theta}_a^e\,,\, \bar{u}_b^e\,,\, \bar{v}_b^e\,,\, \bar{\theta}_b^e\}$, these equations can be cast in matrix form

$$\underline{\bar{u}}^e = \underline{\underline{F}}\,\underline{u}^e, \tag{153}$$

where

$$\underline{\underline{F}} = \begin{bmatrix} 1 & 0 & -r & 0 & 0 & 0 \\ 0 & 1 & 0 & 0 & 0 & 0 \\ 0 & 0 & 1 & 0 & 0 & 0 \\ 0 & 0 & 0 & 1 & 0 & r \\ 0 & 0 & 0 & 0 & 1 & 0 \\ 0 & 0 & 0 & 0 & 0 & 1 \end{bmatrix} \tag{154}$$

If $\bar{u}_1^e$, $\bar{u}_2^e$ and Φ_3^e are the axial cross-sectional displacement, the transverse cross-sectional displacement, and the cross-sectional rotation, respectively, then the differential equations for a statically loaded Timoshenko beam are

$$\frac{\mathrm{d}}{\mathrm{d}x_1}\left(S\frac{\mathrm{d}\bar{u}_1^e}{\mathrm{d}x_1}\right) = -p_1(x_1), \tag{155a}$$

$$\frac{\mathrm{d}}{\mathrm{d}x_1}\left(H_{33}^c\frac{\mathrm{d}\Phi_3^e}{\mathrm{d}x_1}\right) + K_{22}\left(\frac{\mathrm{d}\bar{u}_2^e}{\mathrm{d}x_1} - \Phi_3^e\right) = -q_3(x_1), \tag{155b}$$

$$\frac{\mathrm{d}}{\mathrm{d}x_1}\left[K_{22}\left(\frac{\mathrm{d}\bar{u}_2^e}{\mathrm{d}x_1} - \Phi_3^e\right)\right] = -p_2(x_1), \tag{155c}$$

where S, H_{33}^c and K_{22} are the axial stiffness, the bending stiffness and the shear stiffness, respectively. Assuming constant properties along the span of the beam, and

introducing $\check{p}_1(x_1)$, $\check{p}_2(x_1)$ and $\check{q}_3(x_1)$ such that

$$\frac{\mathrm{d}^2\check{p}_1}{\mathrm{d}x_1^2} = \frac{p_1}{S}, \qquad \frac{\mathrm{d}^4\check{p}_2}{\mathrm{d}x_1^4} = \frac{p_2}{H_{33}^c}, \qquad \frac{\mathrm{d}^3\check{q}_3}{\mathrm{d}x_1^3} = \frac{q_3}{H_{33}^c}, \tag{156}$$

as well as the shear flexibility parameter $\Omega = \frac{H_{33}^c}{K_{22}L^2}$, they can be rewritten as

$$\frac{\mathrm{d}^2\bar{u}_1^e}{\mathrm{d}x_1^2} = -\frac{\mathrm{d}^2\check{p}_1}{\mathrm{d}x_1^2}, \tag{157a}$$

$$\Omega L^2\frac{\mathrm{d}^2\Phi_3^e}{\mathrm{d}x_1^2} + \frac{\mathrm{d}\bar{u}_2^e}{\mathrm{d}x_1} - \Phi_3^e = -\Omega L^2\frac{\mathrm{d}^3\check{q}_3}{\mathrm{d}x_1^3}, \tag{157b}$$

$$\frac{\mathrm{d}^2\bar{u}_2^e}{\mathrm{d}x_1^2} - \frac{\mathrm{d}\Phi_3^e}{\mathrm{d}x_1} = -\Omega L^2\frac{\mathrm{d}^4\check{p}_2}{\mathrm{d}x_1^4}. \tag{157c}$$

It will be convenient to introduce $(\cdot)'$ as a derivative with respect to x_1, as well as the following notations

$$\check{p}_{1a}^{(i)} = \frac{\mathrm{d}^i\check{p}_1}{\mathrm{d}x_1^i}\left(-\frac{L}{2}\right), \qquad \check{p}_{1b}^{(i)} = \frac{\mathrm{d}^i\check{p}_1}{\mathrm{d}x_1^i}\left(\frac{L}{2}\right), \tag{158a}$$

$$\check{p}_{2a}^{(i)} = \frac{\mathrm{d}^i\check{p}_2}{\mathrm{d}x_1^i}\left(-\frac{L}{2}\right), \qquad \check{p}_{2b}^{(i)} = \frac{\mathrm{d}^i\check{p}_2}{\mathrm{d}x_1^i}\left(\frac{L}{2}\right), \tag{158b}$$

$$\check{q}_{3a}^{(i)} = \frac{\mathrm{d}^i\check{q}_3}{\mathrm{d}x_1^i}\left(-\frac{L}{2}\right), \qquad \check{q}_{3b}^{(i)} = \frac{\mathrm{d}^i\check{q}_3}{\mathrm{d}x_1^i}\left(\frac{L}{2}\right). \tag{158c}$$

Using these new notations and rearranging the differential equations, one finds

$$(\bar{u}_1^e)'' = -\check{p}_1^{(2)}, \tag{159a}$$

$$(\bar{u}_2^e)'''' = \check{p}_2^{(4)} - \check{q}_3^{(4)} - \Omega L^2\check{p}_2^{(6)}, \tag{159b}$$

$$(\Phi_3^e)''' = \check{p}_2^{(4)} - \check{q}_3^{(4)}. \tag{159c}$$

Introducing

$$\underline{\mathcal{P}}(x_1) = \begin{Bmatrix}\mathcal{P}_1(x_1)\\ \mathcal{P}_2(x_1)\\ \mathcal{P}_3(x_1)\end{Bmatrix} = \begin{Bmatrix}-\check{p}_1\\ \check{p}_2 - \check{q}_3 - \Omega L^2\check{p}_2^{(2)}\\ \check{p}_2^{(1)} - \check{q}_3^{(1)}\end{Bmatrix} \tag{160}$$

the equations simply become

$$(\bar{u}_1^e - \mathcal{P}_1)'' = 0, \tag{161a}$$

$$(\bar{u}_2^e - \mathcal{P}_2)'''' = 0, \tag{161b}$$

$$(\Phi_3^e - \mathcal{P}_3)''' = 0. \tag{161c}$$

These equations can be solved for by using the given boundary conditions prescribing the displacements and rotations at the edges. It should be emphasized that since the order of differentiation has been increased, there will be more constants of integration than the number of given boundary conditions. The solution should be substituted in the original differential equations to find the remaining constants of integration. After completing this process, the solution is found to be

$$\underline{\mathcal{U}}^e(x_1) = \begin{Bmatrix} \bar{u}_1^e(x_1) \\ \bar{u}_2^e(x_1) \\ \Phi_3^e(x_1) \end{Bmatrix} = \underline{\underline{N}}(x_1)\underline{\underline{T}}\,\underline{\bar{u}}^e - \underline{\underline{N}}(x_1)\underline{\underline{T}}\,\underline{\mathcal{P}}^+ + \underline{\mathcal{P}}(x_1), \tag{162}$$

where

$$\underline{\underline{N}}(x_1) = \begin{bmatrix} x_1 & 1 & 0 & 0 & 0 & 0 \\ 0 & 0 & x_1^3 - 6\Omega L^2 x_1 & x_1^2 & x_1 & 1 \\ 0 & 0 & 3x_1^2 & 2x_1 & 1 & 0 \end{bmatrix}, \tag{163}$$

$$\underline{\underline{T}} = \begin{bmatrix} -\frac{1}{L} & 0 & 0 & \frac{1}{L} & 0 & 0 \\ \frac{1}{2} & 0 & 0 & \frac{1}{2} & 0 & 0 \\ 0 & \frac{2}{L^3\Omega_1} & \frac{1}{L^2\Omega_1} & 0 & -\frac{2}{L^3\Omega_1} & \frac{1}{L^2\Omega_1} \\ 0 & 0 & -\frac{1}{2L} & 0 & 0 & \frac{1}{2L} \\ 0 & -\frac{3}{2L\Omega_1} & -\frac{\Omega_2}{4\Omega_1} & 0 & \frac{3}{2L\Omega_1} & -\frac{\Omega_2}{4\Omega_1} \\ 0 & \frac{1}{2} & \frac{L}{8} & 0 & \frac{1}{2} & -\frac{L}{8} \end{bmatrix}, \tag{164}$$

where $\Omega_1 = 1 + 12\,\Omega$, $\Omega_2 = 1 - 24\,\Omega$, and finally $\underline{\mathcal{P}}^+ = \{\underline{\mathcal{P}}_a^T\,,\, \underline{\mathcal{P}}_b^T\}^T$. Recalling the relationship from Eq. (153) between the degrees-of-freedom of the ligament ends and those of the associated circle centers, this result becomes

$$\underline{\mathcal{U}}^e(x_1) = \underline{\underline{N}}(x_1)\underline{\underline{T}}\,\underline{\underline{F}}\,\underline{u}^e - \underline{\underline{N}}(x_1)\underline{\underline{T}}\,\underline{\mathcal{P}}^+ + \underline{\mathcal{P}}(x_1). \tag{165}$$

The strain measures associated with the displacement field for such a beam are

$$\bar{\varepsilon}_1^e(x_1) = \frac{\mathrm{d}\bar{u}_1^e}{\mathrm{d}x_1}, \qquad \kappa_3^e(x_1) = \frac{\mathrm{d}\Phi_3^e}{\mathrm{d}x_1}, \qquad \gamma_{12}^e(x_1) = \frac{\mathrm{d}\bar{u}_2^e}{\mathrm{d}x_1} - \Phi_3^e. \tag{166}$$

Then, the array of strain measures is defined as

$$\underline{\mathcal{E}}^e(x_1) = \begin{Bmatrix} \bar{\varepsilon}_1^e(x_1) \\ \kappa_3^e(x_1) \\ \gamma_{12}^e(x_1) \end{Bmatrix}, \tag{167}$$

and using the result of Eq. (165)

$$\underline{\mathcal{E}}^e(x_1) = \underline{\underline{B}}(x_1)\underline{\underline{T}}\,\underline{\underline{F}}\,\underline{u}^e - \underline{\underline{B}}(x_1)\underline{\underline{T}}\,\underline{\mathcal{P}}^+ + \underline{\mathcal{Q}}(x_1). \tag{168}$$

where

$$\underline{\underline{B}}(x_1) = \begin{bmatrix} 1 & 0 & 0 & 0 & 0 & 0 \\ 0 & 0 & 6x_1 & 2 & 0 & 0 \\ 0 & 0 & -6L^2\Omega & 0 & 0 & 0 \end{bmatrix}, \tag{169}$$

$$\underline{\mathcal{Q}}(x_1) = \begin{Bmatrix} -\check{p}_1^{(1)} \\ \check{p}_2^{(2)} - \check{q}_3^{(2)} \\ -L^2\Omega\check{p}_2^{(3)} \end{Bmatrix}. \tag{170}$$

The corresponding stress resultants are $N_1^e = S\bar{\varepsilon}_1^e$, $M_3^e = H_{33}^c\kappa_3^e$ and $V_2^e = K_{22}\gamma_{12}^e$. Defining the array of stress resultants

$$\underline{\mathcal{S}}^e(x_1) = \begin{Bmatrix} N_1^e(x_1) \\ M_3^e(x_1) \\ V_2^e(x_1) \end{Bmatrix} \tag{171}$$

and the constitutive matrix

$$\underline{\underline{C}} = \begin{bmatrix} S & 0 & 0 \\ 0 & H_{33}^c & 0 \\ 0 & 0 & K_{22} \end{bmatrix}, \tag{172}$$

the resultants can be expressed in a compact form as

$$\underline{\mathcal{S}}^e(x_1) = \underline{\underline{C}}\,\underline{\mathcal{E}}^e(x_1) = \underline{\underline{C}}\,\underline{\underline{B}}(x_1)\underline{\underline{T}}\,\underline{\underline{F}}\,\underline{u}^e - \underline{\underline{C}}\,\underline{\underline{B}}(x_1)\underline{\underline{T}}\,\underline{\mathcal{P}}^+ + \underline{\underline{C}}\,\underline{\mathcal{Q}}(x_1). \tag{173}$$

The degrees-of-freedom associated with the centers of the circles to which the ligament is attached can be resolved in the inertial frame $\mathcal{I}$ (with unit vectors $\bar{\imath}_1$, $\bar{\imath}_2$ and $\bar{\imath}_3$) instead, and can be related to the degrees-of-freedom written in the local frame (indicated by superscript $(\cdot)^e$) attached to the ligament. The array of degrees-of-freedom in $\mathcal{I}$ for the ligament is $\underline{u}^{i\,T} = \{u_a^i\,,\, v_a^i\,,\, \theta_a^i\,,\, u_b^i\,,\, v_b^i\,,\, \theta_b^i\}$. If ϕ is the angle from the horizontal $\bar{\imath}_1$ to the reference axis of the ligament $\bar{e}_1$, the relationship between $\underline{u}^e$ and $\underline{u}^i$ has the form

$$\underline{u}^e = \underline{\underline{R}}\,\underline{u}^i, \tag{174}$$

where

$$\underline{\underline{R}} = \begin{bmatrix} \underline{\underline{\hat{R}}} & 0 \\ 0 & \underline{\underline{\hat{R}}} \end{bmatrix} \tag{175}$$

and

$$\underline{\underline{\hat{R}}} = \begin{bmatrix} \cos(\phi) & \sin(\phi) & 0 \\ -\sin(\phi) & \cos(\phi) & 0 \\ 0 & 0 & 1 \end{bmatrix}. \tag{176}$$

If x_{1ca}^i and x_{2ca}^i are the center coordinates of the "left" circle, and x_{1cb}^i and x_{2cb}^i those of the "right" one, then

$$\cos(\phi) = \frac{x_{1cb}^i - x_{1ca}^i}{R}\cos(\beta) + \frac{x_{2cb}^i - x_{2ca}^i}{R}\sin(\beta), \tag{177a}$$

$$\sin(\phi) = \frac{x_{2cb}^i - x_{2ca}^i}{R}\cos(\beta) - \frac{x_{1cb}^i - x_{1ca}^i}{R}\sin(\beta), \tag{177b}$$

where R and β were introduced in Fig. 71. Introducing this new relationship into Eqs. (165) and (168), the arrays of displacements, strains and stress resultants can be expressed in terms of the degrees-of-freedom in the global frame as

$$\underline{\mathcal{U}}^e(x_1) = \underline{\underline{N}}(x_1)\underline{\underline{T}}\,\underline{\underline{F}}\,\underline{\underline{R}}\,\underline{u}^i - \underline{\underline{N}}(x_1)\underline{\underline{T}}\,\underline{\mathcal{P}}^+ + \underline{\mathcal{P}}(x_1), \tag{178a}$$

$$\underline{\mathcal{E}}^e(x_1) = \underline{\underline{B}}(x_1)\underline{\underline{T}}\,\underline{\underline{F}}\,\underline{\underline{R}}\,\underline{u}^i - \underline{\underline{B}}(x_1)\underline{\underline{T}}\,\underline{\mathcal{P}}^+ + \underline{\mathcal{Q}}(x_1), \tag{178b}$$

$$\underline{\mathcal{S}}^e(x_1) = \underline{\underline{C}}\,\underline{\underline{B}}(x_1)\underline{\underline{T}}\,\underline{\underline{F}}\,\underline{\underline{R}}\,\underline{u}^i - \underline{\underline{C}}\,\underline{\underline{B}}(x_1)\underline{\underline{T}}\,\underline{\mathcal{P}}^+ + \underline{\underline{C}}\,\underline{\mathcal{Q}}(x_1). \tag{178c}$$

To summarize, Eqs. (178) provide the full local displacement, strain and stress field in an arbitrarily oriented ligament in terms of the degrees-of-freedom in a global frame of the two nodes connected to it. These results depend on the expressions of the distributed forces and moments that are applied to it.

7.1.2 Total ligament potential

The strain energy of a single ligament is

$$A^{\text{lig}} = \frac{1}{2}\int_{-\frac{L}{2}}^{\frac{L}{2}} \underline{\mathcal{E}}^{e\,T}(x_1)\underline{\underline{C}}\,\underline{\mathcal{E}}^{e}(x_1)\,\mathrm{d}x_1, \tag{179}$$

where $\underline{\mathcal{E}}^e$ is given by Eq. (178) and the constitutive matrix $\underline{\underline{C}}$ is defined in Eq. (172). Substituting in the expression for the strain array, one finds

$$A^{\text{lig}} = \frac{1}{2}\underline{u}^{i\,T}\underline{\underline{K}}^{i}\underline{u}^{i} + \underline{u}^{i\,T}\underline{f}^{i} + g^{i}, \tag{180}$$

where

$$\underline{\underline{K}}^{i} = \underline{\underline{R}}^{T}\underline{\underline{F}}^{T}\underline{\underline{T}}^{T}\mathcal{I}(\underline{\underline{B}},\underline{\underline{B}})\,\underline{\underline{T}}\,\underline{\underline{F}}\,\underline{\underline{R}}, \tag{181a}$$

$$\underline{f}^{i} = \underline{\underline{R}}^{T}\underline{\underline{F}}^{T}\underline{\underline{T}}^{T}\left(\mathcal{I}(\underline{\underline{B}},\underline{\mathcal{Q}}) - \mathcal{I}(\underline{\underline{B}},\underline{\underline{B}})\,\underline{\underline{T}}\,\underline{\mathcal{P}}^{+}\right), \tag{181b}$$

$$g^{i} = \frac{1}{2}\mathcal{I}(\underline{\mathcal{Q}},\underline{\mathcal{Q}}) - \underline{\mathcal{P}}^{+\,T}\underline{\underline{T}}^{T}\mathcal{I}(\underline{\underline{B}},\underline{\mathcal{Q}}) + \frac{1}{2}\underline{\mathcal{P}}^{+\,T}\underline{\underline{T}}^{T}\mathcal{I}(\underline{\underline{B}},\underline{\underline{B}})\,\underline{\underline{T}}\,\underline{\mathcal{P}}^{+}, \tag{181c}$$

where the notation

$$\mathcal{I}(\underline{\underline{X}},\underline{\underline{Y}}) = \int_{-\frac{L}{2}}^{\frac{L}{2}} \underline{\underline{X}}^{T}\underline{\underline{C}}\,\underline{\underline{Y}}\,\mathrm{d}x_1. \tag{182}$$

was used. Based on the expression of $\underline{\underline{B}}$ in Eq. (169), $\mathcal{I}(\underline{\underline{B}},\underline{\underline{B}})$ can be computed through simple integration

$$\mathcal{I}(\underline{\underline{B}},\underline{\underline{B}}) = \begin{bmatrix} SL & 0 & 0 & 0 & 0 & 0 \\ 0 & 0 & 0 & 0 & 0 & 0 \\ 0 & 0 & 3H_{33}^{c}L^{3}\Omega_1 & 0 & 0 & 0 \\ 0 & 0 & 0 & 4H_{33}^{c}L & 0 & 0 \\ 0 & 0 & 0 & 0 & 0 & 0 \\ 0 & 0 & 0 & 0 & 0 & 0 \end{bmatrix}. \tag{183}$$

The other integrals depend on the particular expression of the distributed loads applied to the ligament. Using the definition of $\underline{\mathcal{Q}}$ in Eq. (170), the general form of $\mathcal{I}(\underline{\underline{B}}, \underline{\mathcal{Q}})$ is found to be

$$\mathcal{I}(\underline{\underline{B}}, \underline{\mathcal{Q}}) = \mathcal{I}(\underline{\underline{B}}, \underline{\underline{B}})\, \underline{\underline{T}}\, \underline{\mathcal{P}}^{+}, \tag{184}$$

so that simply

$$\underline{f}^{i} = \underline{0}. \tag{185}$$

Using this fact, g^i can also be simplified to

$$2g^{i} = \mathcal{I}(\underline{\mathcal{Q}}, \underline{\mathcal{Q}}) - \underline{\mathcal{P}}^{+\,T}\, \underline{\underline{T}}^{T}\, \mathcal{I}(\underline{\underline{B}}, \underline{\underline{B}})\, \underline{\underline{T}}\, \underline{\mathcal{P}}^{+}. \tag{186}$$

Externally applied concentrated forces and moments, which will be referred to as circle loads, may be applied to the centers of the circles to which the ligament is attached. If the loads applied to circle "a" are denoted by F^i_{1a}, F^i_{2a} and M^i_{3a} in the global frame, and those applied to circle "b" F^i_{1b}, F^i_{2b} and M^i_{3b}, then the work associated with these loads is simply

$$W^{\text{lig}}_{\text{cir}} = \underline{u}^{i\,T}\, \underline{f}^{i}_{\text{cir}}, \tag{187}$$

where

$$\underline{f}^{i}_{\text{cir}} = \left\{ F^i_{1a}\,,\, F^i_{2a}\,,\, M^i_{3a}\,,\, F^i_{1b}\,,\, F^i_{2b}\,,\, M^i_{3b} \right\}^{T}. \tag{188}$$

The applied distributed loads on that same ligament are $p_1(x_1)$, $p_2(x_1)$ and $q_3(x_1)$. The work of these externally applied loads can be computed as

$$W^{\text{lig}}_{\text{dist}} = \int_{-\frac{L}{2}}^{\frac{L}{2}} \underline{\mathcal{U}}^{e\,T}(x_1) \begin{Bmatrix} p_1(x_1) \\ p_2(x_1) \\ q_3(x_1) \end{Bmatrix} \mathrm{d}x_1. \tag{189}$$

Introducing the expression for $\underline{\mathcal{U}}^e$ from Eq. (178), the following compact expression is obtained

$$W^{\text{lig}}_{\text{dist}} = \underline{u}^{i\,T}\, \underline{f}^{i}_{\text{dist}} + g^{i}_{\text{dist}}, \tag{190}$$

where

$$\underline{f}^i_{\text{dist}} = \underline{\underline{R}}^T \underline{\underline{F}}^T \underline{\underline{T}}^T \int_{-\frac{L}{2}}^{\frac{L}{2}} \underline{\underline{N}}^T(x_1) \begin{Bmatrix} p_1(x_1) \\ p_2(x_1) \\ q_3(x_1) \end{Bmatrix} \mathrm{d}x_1, \tag{191a}$$

$$g^i_{\text{dist}} = -\underline{\mathcal{P}}^{+T} \underline{\underline{T}}^T \int_{-\frac{L}{2}}^{\frac{L}{2}} \underline{\underline{N}}^T(x_1) \begin{Bmatrix} p_1(x_1) \\ p_2(x_1) \\ q_3(x_1) \end{Bmatrix} \mathrm{d}x_1 + \int_{-\frac{L}{2}}^{\frac{L}{2}} \underline{\mathcal{P}}^T(x_1) \begin{Bmatrix} p_1(x_1) \\ p_2(x_1) \\ q_3(x_1) \end{Bmatrix} \mathrm{d}x_1. \tag{191b}$$

These quantities clearly depend on the particular expressions of the distributed loads that are applied. Note that if the distributed loads are all constant along the length of the ligament, the expression for $\underline{f}^i_{\text{dist}}$ simplifies to

$$\underline{f}^i_{\text{dist}} = \underline{\underline{R}}^T \underline{\underline{F}}^T \underline{\underline{T}}^T \underline{\underline{\mathcal{N}}}^T_{\text{ctt}} \begin{Bmatrix} p_1 \\ p_2 \\ q_3 \end{Bmatrix}, \tag{192}$$

with

$$\underline{\underline{\mathcal{N}}}_{\text{ctt}} = \begin{bmatrix} 0 & L & 0 & 0 & 0 & 0 \\ 0 & 0 & 0 & \frac{L^3}{12} & 0 & L \\ 0 & 0 & \frac{L^3}{4} & 0 & L & 0 \end{bmatrix}. \tag{193}$$

Another special case involves distributed loads that are proportional to a Dirac function, effectively defining concentrated loads on the interior of the ligament. The array of distributed forces and moments is of the form

$$\begin{Bmatrix} p_1(x_1) \\ p_2(x_1) \\ q_3(x_1) \end{Bmatrix} = \begin{Bmatrix} P_1 \\ P_2 \\ Q_3 \end{Bmatrix} \delta(x_1 - x_\delta), \tag{194}$$

and the expression for $\underline{f}^i_{\text{dist}}$ simplifies to

$$\underline{f}^i_{\text{dist}} = \underline{\underline{R}}^T \underline{\underline{F}}^T \underline{\underline{T}}^T \underline{\underline{\mathcal{N}}}^T_{\text{drc}} \begin{Bmatrix} P_1 \\ P_2 \\ Q_3 \end{Bmatrix}, \tag{195}$$

with

$$\underline{\underline{\mathcal{N}}}_{\text{drc}} = \underline{\underline{N}}(x_\delta). \tag{196}$$

More general cases may be treated with the general formula above, either analytically or through numerical quadrature.

In particular, sectional forces and moments may be applied on the ends of the ligament; such loads can be represented as distributed loads proportional to the Dirac function, with $x_\delta = -L/2$ and $x_\delta = L/2$, respectively. If one denotes by N_a, V_a and M_a those at end "a" of the ligament, and N_b, V_b and M_b those at end "b", then the associated work takes the form

$$W^{\text{lig}}_{\text{end}} = \underline{u}^{i\,T}\,\underline{f}^i_{\text{end}} + g^i_{\text{end}}, \tag{197}$$

where

$$\underline{f}^i_{\text{end}} = \underline{\underline{R}}^T\,\underline{\underline{F}}^T\,\underline{\underline{T}}^T \left(\underline{\underline{N}}^T(-L/2) \begin{Bmatrix} -N_a \\ -V_a \\ -M_a \end{Bmatrix} + \underline{\underline{N}}^T(+L/2) \begin{Bmatrix} N_b \\ V_b \\ M_b \end{Bmatrix} \right). \tag{198}$$

Using the expressions for $\underline{\underline{T}}$ and $\underline{\underline{N}}$, it can easily be shown that

$$\underline{\underline{N}}(-L/2)\underline{\underline{T}} = \left[\underline{\underline{I}}_{3\times3}\,,\, \underline{\underline{O}}_{3\times3} \right], \tag{199a}$$

$$\underline{\underline{N}}(+L/2)\underline{\underline{T}} = \left[\underline{\underline{O}}_{3\times3}\,,\, \underline{\underline{I}}_{3\times3} \right], \tag{199b}$$

where $\underline{\underline{I}}_{3\times3}$ is the 3-by-3 identity matrix, and $\underline{\underline{O}}_{3\times3}$ the 3-by-3 zero matrix. Hence, the expression for $\underline{f}^i_{\text{end}}$ simplifies to

$$\underline{f}^i_{\text{end}} = \underline{\underline{R}}^T\,\underline{\underline{F}}^T \begin{Bmatrix} -N_a & -V_a & -M_a & N_b & V_b & M_b \end{Bmatrix}^T. \tag{200}$$

Finally, if we introduce

$$\underline{\underline{\tilde{I}}} = \begin{bmatrix} -\underline{\underline{I}}_{3\times3} & \underline{\underline{O}}_{3\times3} \\ \underline{\underline{O}}_{3\times3} & \underline{\underline{I}}_{3\times3} \end{bmatrix}, \tag{201}$$

the result can finally be written in a compact form

$$\underline{f}^i_{\text{end}} = \underline{\underline{R}}^T\,\underline{\underline{F}}^T\,\underline{\underline{\tilde{I}}}\,\underline{F}_{\text{end}}, \tag{202}$$

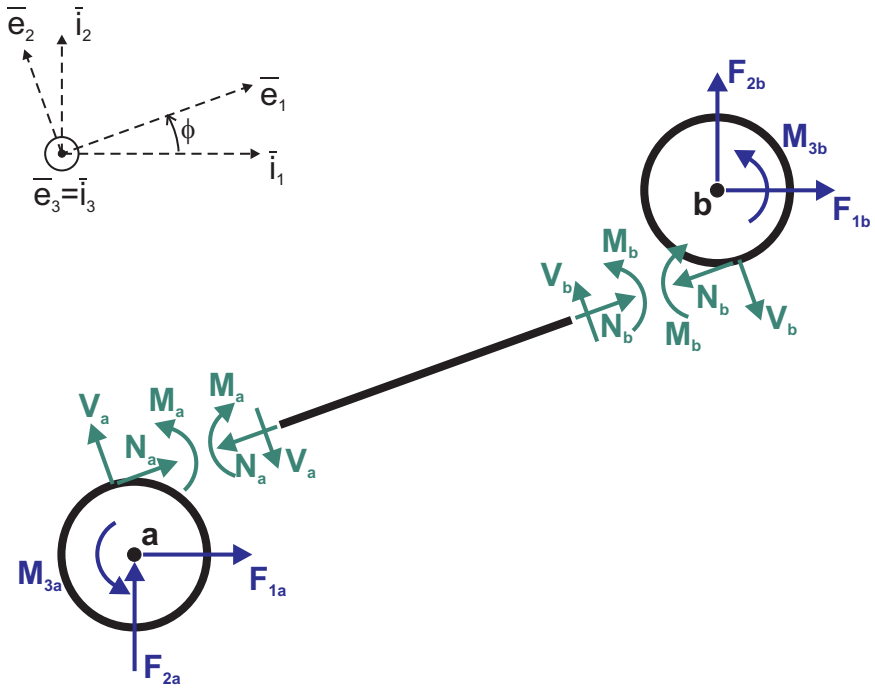

Figure 112: Free-body diagram of ligament and associated circle nodes

where

$$\underline{F}^T_{\text{end}} = \left\{ N_a \quad V_a \quad M_a \quad N_b \quad V_b \quad M_b \right\}. \tag{203}$$

Another approach for computing the work done by such sectional loads at the extremities of the ligament is to use circle equilibrium considerations to define the equivalent forces and moments that need to be applied at each circle center to achieve the same effect. Referring to the free-body diagrams of Fig. 112, and denoting those loads by F^i_{1a}, F^i_{2a} and M^i_{3a} for circle "a", and F^i_{1b}, F^i_{2b} and M^i_{3b} for the other, we have

$$F^i_{1a} = -N_a \cos(\phi) + V_a \sin(\phi), \tag{204a}$$

$$F^i_{2a} = -N_a \sin(\phi) - V_a \cos(\phi), \tag{204b}$$

$$M^i_{3a} = -M_a + rN_a, \tag{204c}$$

$$F^i_{1b} = \quad N_b \cos(\phi) - V_b \sin(\phi), \tag{204d}$$

$$F^i_{2b} = \quad N_b \sin(\phi) + V_b \cos(\phi), \tag{204e}$$

$$M^i_{3b} = \quad M_b + rN_b. \tag{204f}$$

Recalling the definitions of $\underline{\underline{R}}$, $\underline{\underline{F}}$ and $\underline{\underline{\tilde{I}}}$, these relationships can be cast in matrix form as

$$\underline{f}^i_{\text{cir}} = \underline{\underline{R}}^T \underline{\underline{F}}^T \underline{\underline{\tilde{I}}}\, \underline{F}_{\text{end}}. \tag{205}$$

Clearly, the results are identical with both approaches. Note also that this last relationship can simply be inverted if end sectional loads on a ligament need to be computed when associated circle loads are known.

Finally, the total potential associated with this ligament is $\Pi^{\text{lig}} = A^{\text{lig}} - W^{\text{lig}}$, and specifically, when considering all circle loads and all distributed loads, it has the general form

$$\Pi^{\text{lig}} = \frac{1}{2} \underline{u}^{i\,T} \underline{\underline{K}}^i \underline{u}^i - \underline{u}^{i\,T} \hat{\underline{f}}^i + \hat{g}^i, \tag{206}$$

where

$$\hat{\underline{f}}^i = \underline{f}^i_{\text{cir}} + \underline{f}^i_{\text{dist}}, \tag{207a}$$

$$\hat{g}^i = g^i - g^i_{\text{dist}}. \tag{207b}$$

7.1.3 Inclusion of piezoelectric actuation

In this section, the special case of piezoelectric actuation on a ligament is presented in detail. It will be shown that, following the developments in Ref. 72, the effect of bonded piezoelectric strips on the ligament can be modeled by distributed loads along the span of the ligament, as well as sectional loads at its edges. Having demonstrated this representation, it will be clear that the developments of the previous section may be applied to determine the load arrays associated with this type of actuation. Of course, by virtue of the equivalence between such piezo actuation and thermal loading due to a temperature gradient through the thickness of the ligament, one could similarly treat the latter case. However, it will not be necessary here, since a piezoelectric actuation model is readily available.

In section 6.3.1, it was shown that in the presence of piezoelectric actuators, the

sectional loads take the form

$$N_1(x_1) = S\,\bar{\varepsilon}_1(x_1) - N_{1p}(x_1), \tag{208a}$$

$$V_2(x_1) = K_{22}\left(\bar{u}_2' - \Phi_3\right), \tag{208b}$$

$$M_3(x_1) = H_{33}^c\,\kappa_3(x_1) - M_{3p}(x_1), \tag{208c}$$

where $N_{1p} = N_{1b} + N_{1t}$, $M_{3p} = M_{3b} + M_{3t}$, and the individual expressions of these different contributions are given in Eqs. (146). As pointed out earlier, if any (or both) of the piezoelectric strips are removed, the corresponding terms simply need to be removed. These terms may be recombined in the following way

$$N_{1p}(x_1) = E_p d_{21p}\left(\chi_b(x_1) + \chi_t(x_1)\right), \tag{209a}$$

$$M_{3p}(x_1) = E_p d_{21p}\frac{t+t_p}{2}\left(\chi_b(x_1) - \chi_t(x_1)\right) + E_p d_{21p} d_{2c}\left(\chi_b(x_1) + \chi_t(x_1)\right). \tag{209b}$$

If both are present, then $d_{2c} = 0$ and the second term in M_{3p} vanishes. If the electrodes are mirror images about the midplane and the applied voltages are the same, the first term vanishes as well, but N_{1p} is non zero and corresponds to axial actuation. If the electrodes are identical and the applied voltages are opposites, N_{1p} vanishes but M_{3p} is then non-zero and a curvature is generated in the ligament. If only one of the piezoelectric strips is present, *e.g.*, the top one, there will be a combination of non-zero N_{1p} and M_{3p}; note that in this case, $d_{2c} \neq 0$ and the second term in M_{3p} remains.

It was also shown in section 6.3.1 that the equilibrium equations become

$$S\bar{u}_1'' = -p_1 + N_{1p}', \tag{210a}$$

$$K_{22}\left(\bar{u}_2' - \Phi_3\right)' = -p_2, \tag{210b}$$

$$H_{33}^c\bar{u}_2''' + K_{22}\left(\bar{u}_2' - \Phi_3\right) = -q_3 + M_{3p}'. \tag{210c}$$

From these developments, it becomes apparent that the piezoelectric effect due to one or two piezobenders bonded to the ligament is equivalent to the application of

distributed spanwise forces and moments

$$p_{1p}(x_1) = -N'_{1p} = -E_p d_{21p} \left(\chi'_b + \chi'_t\right), \tag{211a}$$

$$p_{2p}(x_1) = 0, \tag{211b}$$

$$q_{3p}(x_1) = -M'_{3p} = -E_p d_{21p} \frac{t + t_p}{2} \left(\chi'_b - \chi'_t\right) - E_p d_{21p} d_{2c} \left(\chi'_b + \chi'_t\right), \tag{211c}$$

as well as the application of sectional forces and moments at the left boundary at $x_1 = -L/2$

$$N_{1a} = E_p d_{21p} \left(\chi_{b,a} + \chi_{t,a}\right), \tag{212a}$$

$$V_{2a} = 0, \tag{212b}$$

$$M_{3a} = E_p d_{21p} \frac{t + t_p}{2} \left(\chi_{b,a} - \chi_{t,a}\right) + E_p d_{21p} d_{2c} \left(\chi_{b,a} + \chi_{t,a}\right), \tag{212c}$$

and at the right boundary at $x_1 = L/2$

$$N_{1b} = E_p d_{21p} \left(\chi_{b,b} + \chi_{t,b}\right), \tag{213a}$$

$$V_{2b} = 0, \tag{213b}$$

$$M_{3b} = E_p d_{21p} \frac{t + t_p}{2} \left(\chi_{b,b} - \chi_{t,b}\right) + E_p d_{21p} d_{2c} \left(\chi_{b,b} + \chi_{t,b}\right). \tag{213c}$$

Hence, the developments on the work done by applied distributed loads and applied sectional loads of the previous section can be exploited to include this type of actuation.

With the method outlined here, very general types of piezoelectric actuation can be implemented. The electrodes could have complicated shapes, the applied voltage could vary along the length of a ligament, or different materials and geometries could be used on different ligaments. For this analysis tool, the following simple setup was specifically implemented. Zero, one or two piezo strips may be present on each ligament, and if only one is included, it can be placed on either side of the ligament ("top" or "bottom"). The width variation of any electrode was constrained to be linear, so that it could be defined completely by two parameters, the slope and width

at the midpoint, or alternatively, the width at both ends of the ligament. In addition, each electrode can be separated into two halves along the span, one half denoted by "a" on the "left" side of the ligament, $-\frac{L}{2} \leq x_1 \leq 0$, the other denoted by "$b$" on the "right" side, $0 \leq x_1 \leq \frac{L}{2}$. This allows for actuation schemes such as the double bending strategy studied previously. On each half, the width of the electrode varies linearly. The applied voltage is constant on each half, but may be different between the two sides.

To represent these assumptions, the following expressions are introduced

$$\chi_b(x_1) = \left(w^c_{b,a} + w^l_{b,a}x_1\right) V_{b,a}H(-x_1) + \left(w^c_{b,b} + w^l_{b,b}x_1\right) V_{b,b}H(x_1), \tag{214a}$$

$$\chi_t(x_1) = \left(w^c_{t,a} + w^l_{t,a}x_1\right) V_{t,a}H(-x_1) + \left(w^c_{t,b} + w^l_{t,b}x_1\right) V_{t,b}H(x_1), \tag{214b}$$

where $H(x_1)$ represents the Heaviside function. The first subscript refers to the bottom ("b") or the top ("t") of the ligament. The second subscript refers to the left side "a" or the right side "b". A superscript c refers to the constant term in each electrode's width, while l refers to the linear term (slope). The sectional loads associated with piezoelectric actuation are then

$$N_{1a} = E_p d_{21p}\left(w^*_{b,a}V_{b,a} + w^*_{t,a}V_{t,a}\right), \tag{215a}$$

$$V_{2a} = 0, \tag{215b}$$

$$M_{3a} = E_p d_{21p}\frac{t+t_p}{2}\left(w^*_{b,a}V_{b,a} - w^*_{t,a}V_{t,a}\right) + E_p d_{21p}d_{2c}\left(w^*_{b,a}V_{b,a} + w^*_{t,a}V_{t,a}\right), \tag{215c}$$

and

$$N_{1b} = E_p d_{21p}\left(w^*_{b,b}V_{b,b} + w^*_{t,b}V_{t,b}\right), \tag{216a}$$

$$V_{2b} = 0, \tag{216b}$$

$$M_{3b} = E_p d_{21p}\frac{t+t_p}{2}\left(w^*_{b,b}V_{b,b} - w^*_{t,b}V_{t,b}\right) + E_p d_{21p}d_{2c}\left(w^*_{b,b}V_{b,b} + w^*_{t,b}V_{t,b}\right), \tag{216c}$$

where the following boundary quantities were introduced

$$w^*_{b,a} = w^c_{b,a} - w^l_{b,a}\frac{L}{2}, \tag{217a}$$

$$w^*_{t,a} = w^c_{t,a} - w^l_{t,a}\frac{L}{2}, \tag{217b}$$

$$w^*_{b,b} = w^c_{b,b} + w^l_{b,b}\frac{L}{2}, \tag{217c}$$

$$w^*_{t,b} = w^c_{t,b} + w^l_{t,b}\frac{L}{2}. \tag{217d}$$

The distributed loads associated with piezoelectric actuation are

$$p_{1p}(x_1) = -E_p d_{21p}\left(\chi'_b + \chi'_t\right), \tag{218a}$$

$$p_{2p}(x_1) = 0, \tag{218b}$$

$$q_{3p}(x_1) = -E_p d_{21p}\frac{t+t_p}{2}\left(\chi'_b - \chi'_t\right) - E_p d_{21p} d_{2c}\left(\chi'_b + \chi'_t\right), \tag{218c}$$

where

$$\begin{aligned}\chi'_b \pm \chi'_t = {} & w^l_{b,a}V_{b,a}H(-x_1) + w^l_{b,b}V_{b,b}H(x_1) \pm w^l_{t,a}V_{t,a}H(-x_1) \pm w^l_{t,b}V_{t,b}H(x_1) \\ & - \left(w^c_{b,a} + w^l_{b,a}x_1\right)V_{b,a}\delta(-x_1) + \left(w^c_{b,b} + w^l_{b,b}x_1\right)V_{b,b}\delta(x_1) \\ & \mp \left(w^c_{t,a} + w^l_{t,a}x_1\right)V_{t,a}\delta(-x_1) \pm \left(w^c_{t,b} + w^l_{t,b}x_1\right)V_{t,b}\delta(x_1),\end{aligned} \tag{219}$$

and $\delta(x_1)$ is the Dirac function.

7.1.4 General procedure

Assume a full chiral structure needs to be analyzed. The model may involve piezoelectric actuation on any of the ligaments, as well as prescribed forces and moments at the circular nodes. The displacements and rotations of certain circles may be constrained to be zero, or be prescribed to a constant value. In order to avoid rigid body modes which result in a noninvertible system of equations, the model should be sufficiently constrained.

The first step consists in a numbering process akin to the definition of a mesh in standard FEA. However, whereas a model needs to be discretized into elements

and nodes in the latter, the "elements" and "nodes" to be defined in this method are self-evident: the centers of rigid circles, with their three associated degrees-of-freedom, will fill the role of "nodes", while the ligaments correspond to "elements". The numbering process orders the nodes and provides a connectivity table linking ligaments to their corresponding nodes. As in standard FEA, any two elements that are connected share a node, and hence share the same degrees-of-freedom at their junction. The chiral lattice topology translates directly to the connectivity of the system. In fact, a chiral structure is modeled in rather the same way as simple trusses; what differs is the physics of the connection between two nodes (typically, an axial spring-like behavior is assumed in simple trusses), as well as the number of degrees-of-freedom (typically, rotations are not considered in simple trusses since the truss members are assumed to be loaded in tension and compression).

Based on this meshing process, it is possible to define, for each ligament, a matrix $\underline{\underline{A}}^{\text{lig}}$ such that

$$\underline{u}^i = \underline{\underline{A}}^{\text{lig}}\,\underline{U}, \tag{220}$$

where $\underline{U}$ is the full array of ordered degrees-of-freedom of the entire system. Recalling the general expression for the total potential Π^{lig} in Eq. (206), it can therefore be written as

$$\Pi^{\text{lig}} = \frac{1}{2}\underline{U}^T\,\underline{\underline{A}}^{\text{lig}\,T}\,\underline{\underline{K}}^i\,\underline{\underline{A}}^{\text{lig}}\underline{U} - \underline{u}^{i\,T}\,\underline{\underline{A}}^{\text{lig}\,T}\,\underline{\hat{f}}^i + \hat{g}^i, \tag{221}$$

and summing all contributions of all ligaments, the total potential Π of the structure becomes

$$\Pi = \sum_{\text{lig}} \Pi^{\text{lig}} = \frac{1}{2}\underline{U}^T\,\underline{\underline{K}}\,\underline{U} - \underline{u}^{i\,T}\,\underline{\hat{f}} + \hat{g}, \tag{222}$$

in which the following quantities were defined

$$\underline{\underline{K}} = \sum_{\text{lig}} \underline{\underline{A}}^{\text{lig}\,T}\,\underline{\underline{K}}^i\,\underline{\underline{A}}^{\text{lig}}, \qquad \underline{\hat{f}} = \sum_{\text{lig}} \underline{\underline{A}}^{\text{lig}\,T}\,\underline{\hat{f}}^i, \qquad \hat{g} = \sum_{\text{lig}} \hat{g}^i. \tag{223}$$

Taking the variation of the total potential and setting it equal to zero, one finds

$$\delta\Pi = 0 \qquad \rightarrow \qquad \underline{\underline{K}}\,\underline{U} = \underline{\hat{f}}, \tag{224}$$

where $\underline{\underline{K}}$ is the global stiffness matrix, and $\underline{\hat{f}}$ is the global load vector.

Next, constraints are applied to the degrees-of-freedom. This system of equations can be partitioned based on known (or prescribed) and unknown degrees-of-freedom; the latter must be solved for to completely determine the static configuration of the structure under loading. Collecting all unknown degrees-of-freedom in an array $\underline{U}_u$ and all known ones in $\underline{U}_k$, the equation may formally be written as

$$\begin{bmatrix} \underline{\underline{K}}_{uu} & \underline{\underline{K}}_{uk} \\ \underline{\underline{K}}_{ku} & \underline{\underline{K}}_{kk} \end{bmatrix} \begin{Bmatrix} \underline{U}_u \\ \underline{U}_k \end{Bmatrix} = \begin{Bmatrix} \underline{\hat{f}}_k \\ \underline{\hat{f}}_u \end{Bmatrix}. \tag{225}$$

Extracting the first equation

$$\underline{\underline{K}}_{uu}\,\underline{U}_u = \underline{\hat{f}}_k - \underline{\underline{K}}_{uk}\,\underline{U}_k, \tag{226}$$

the unknown degrees-of-freedom can be solved for, and since the others are known, the full array $\underline{U}$ is completely determined. Then, through Eqs. (178), the full local displacement, strain and stress fields on any ligament can be found.

7.2 Static validations and simulations

7.2.1 Validation of single ligament response

This first validation demonstrates the basic modeling of one ligament and its solution process under loading and constraints. It also validates the implementation of piezoelectric effects due to bonded piezo strips. A single ligament is considered such that the line of node centers is at a 30° angle. The left node is fixed in all three nodal degrees-of-freedom; this naturally implies that the left boundary of the ligament is essentially cantilevered. Forces and moments are applied at the other circle center. These loads translate into applied tip sectional loads on the ligament. Additionally, piezoelectric actuators are attached on top and underneath the ligament. The top one is assumed to have an electrode of varying width, while the bottom one has constant width, but different voltages are applied on both halves. Hence, a mixed type of actuation is considered here.

Table 7: Comparison of degree-of-freedom values under loading

		Tip loading	
		New code	Analytical
u_b	[m]	$1.159615712 \cdot 10^{-4}$	$1.159615712 \cdot 10^{-4}$
v_b	[m]	$-1.890016101 \cdot 10^{-4}$	$-1.890016101 \cdot 10^{-4}$
θ_b	[rad]	$-4.209987706 \cdot 10^{-3}$	$-4.209987706 \cdot 10^{-3}$
		Piezo actuation	
		New code	Analytical
u_b	[m]	$-2.346217855 \cdot 10^{-5}$	$-2.346217855 \cdot 10^{-5}$
v_b	[m]	$-4.108043658 \cdot 10^{-5}$	$-4.108043658 \cdot 10^{-5}$
θ_b	[rad]	$9.425064701 \cdot 10^{-4}$	$9.425064701 \cdot 10^{-4}$

Two approaches were used to analyze this problem. First, the new code was used to compute the static values under loading of the unconstrained degrees-of-freedom of the model. Furthermore, the variation of $\bar{u}_1^e$, $\bar{u}_2^e$ and Φ_3^e over the entire ligament was obtained to ascertain that the solution is correct on the interior of the "element." These quantities were computed separately for the cases of tip loading and piezoelectric actuation. Next, the same results were obtained from a fully analytical solution of the same problem. This procedure uses the same theories as those presented in section 7.1, but does not use the energy approach. The solution is obtained directly through integration of the differential equations under the constraints and loading mentioned above.

Table 7 shows the extremely good correlation between the two approaches in determining the displacements and rotations of the center of the tip circle. Any errors (which are truncated in the table) are simply numerical in nature. The results are also just as good in the tip loading case as in the piezoelectric actuation case. Next, Figs. 113 and 114 also exhibit perfect correlation, which confirms not only the ability of the code to compute the correct discrete degrees-of-freedom, but also the full displacements and rotations of all points in the structure.

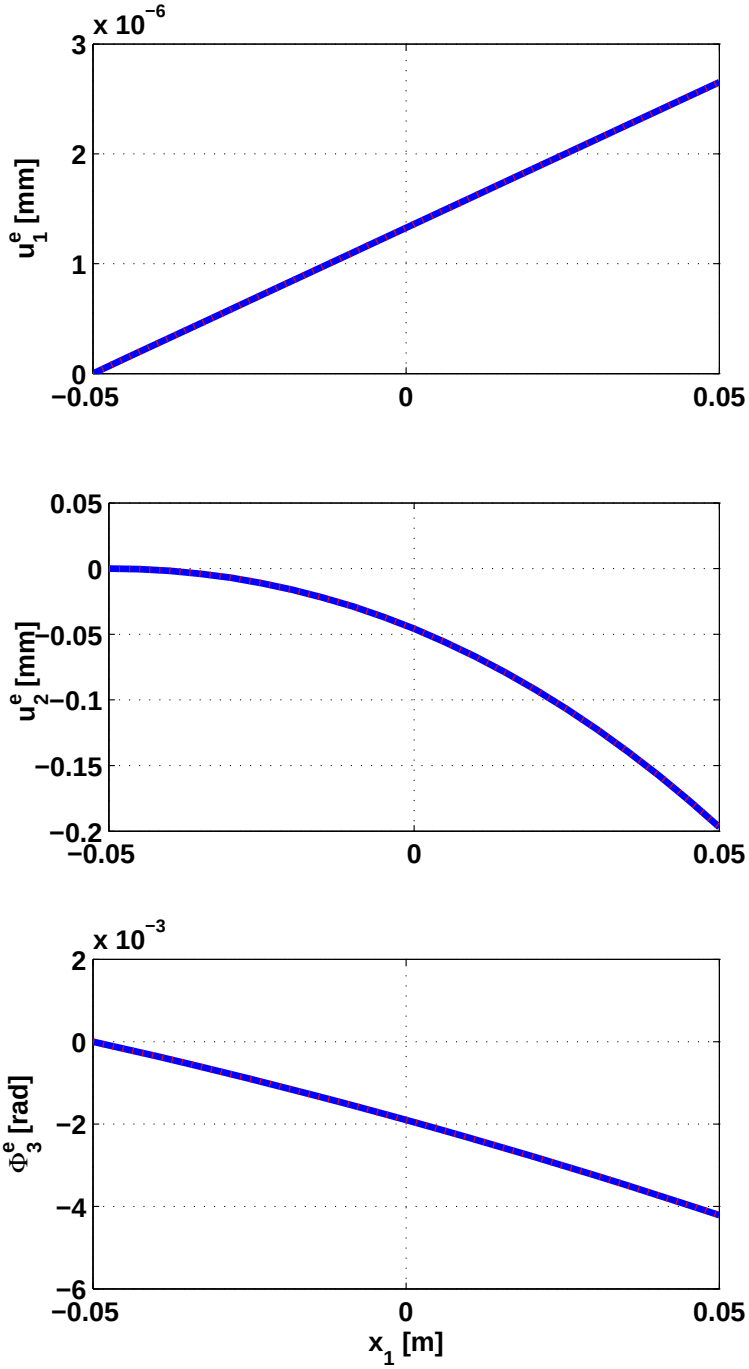

Figure 113: Ligament response under tip loads: analytical (blue, solid) and numerical (red, dotted)

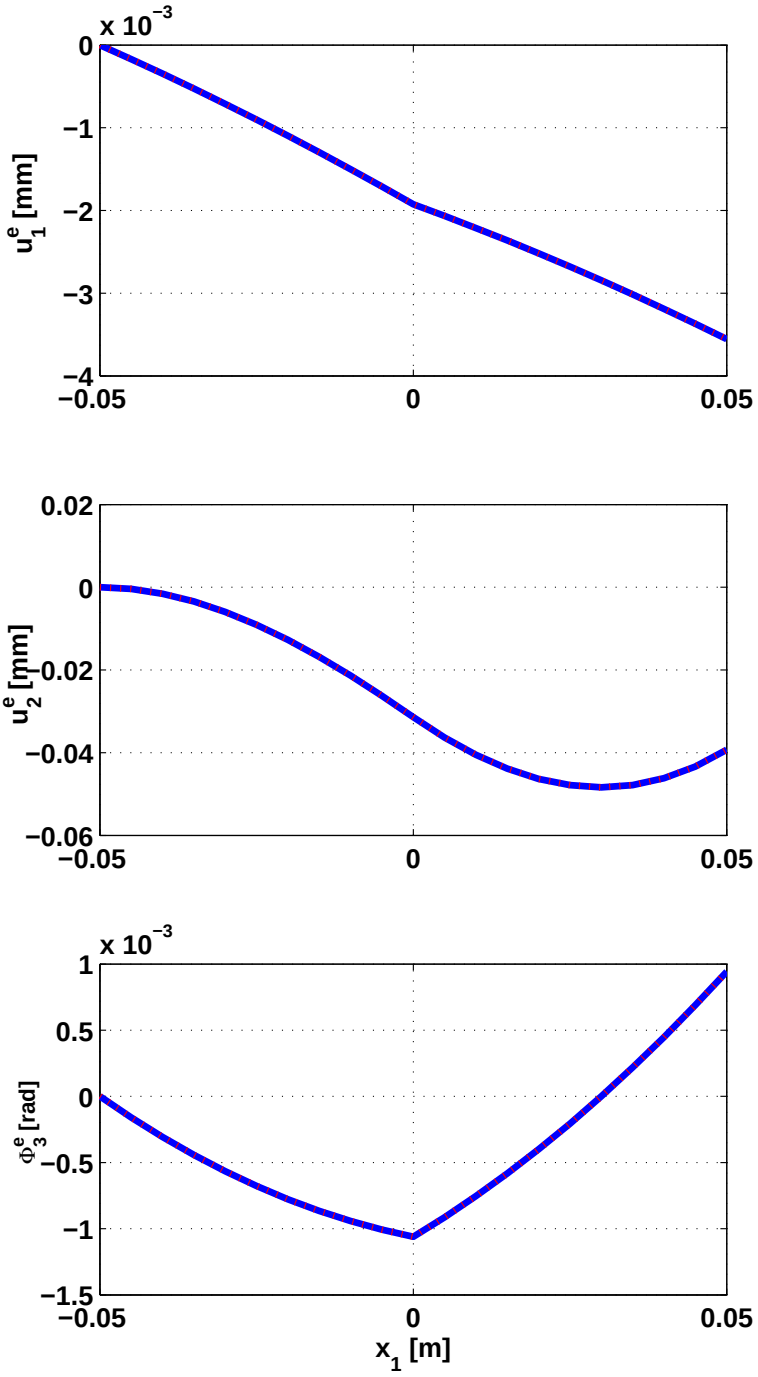

Figure 114: Ligament response under piezoelectric actuation: analytical (blue, solid) and numerical (red, dotted)

7.2.2 Response of chiral network

In order to further validate the implementation, and specifically the assembly of the global stiffness matrix and the global load vector, the cases from section 6.2.1 were run again. This time, the simplified code was used instead of the model in ANSYS. Figures 115, 116, 117, 118 and 119 (scaling factor 10) show the results for a unit tip force. Note that only the connectivity of the chiral structure is represented. Each line represents a ligament, and the connecting points indicate circular nodes. The computed response is generally close to that obtained earlier with ANSYS. The difference can be attributed to the flexibility of the circular nodes in the ANSYS model, as indicated at the beginning of this chapter. The results are also slightly affected by the differences in post-processing of the ANSYS output and that of the simplified tool.

As in section 6.2.1, a unit tip moment can be applied as well. The results obtained with the simplified code, see Figs. 120, 121, 122, 123, and 124, are again satisfactorily validated.

When the model of section 6.2.1 is constrained so that all finite element nodes associated with elements on the circles are rigidly connected, the tip deflection response is essentially identical to that obtained with the simplified code. Considering the case in which a tip transverse force is applied, while the former yields 0.721293 mm of tip displacement, the latter provides 0.721292 mm. The plots in Figs. 125 and 126 are selected results of displacement-level quantities showing the excellent correlation between these two simulations. The perfect correlation of the second plot with the result of Fig. 119 is a manifestation of the fact that identical solutions are found for the degrees-of-freedom, which are the displacements and rotations of all circle centers. The results in Figs. 125 and 118 show very good correlation, but small discrepancies persist due to the differences in post-processing of the results. Nevertheless, these two sets of results are clearly much closer than either is to the original ANSYS solution.

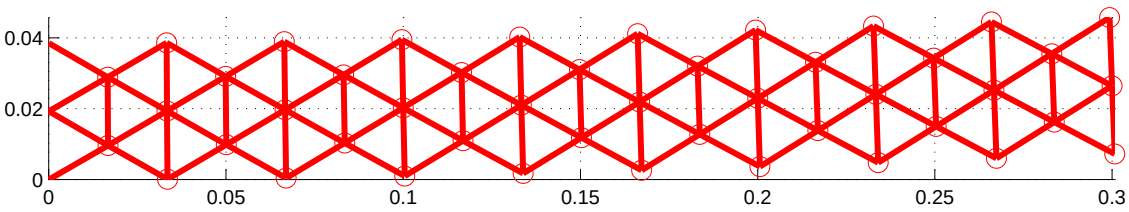

Figure 115: Deformed configuration under unit tip force

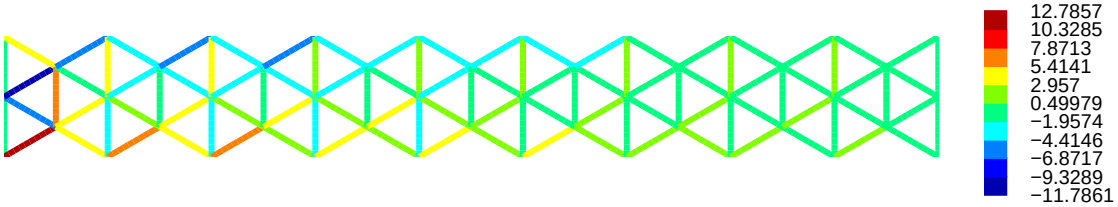

Figure 116: Axial strain (in μ-strain) under unit tip force

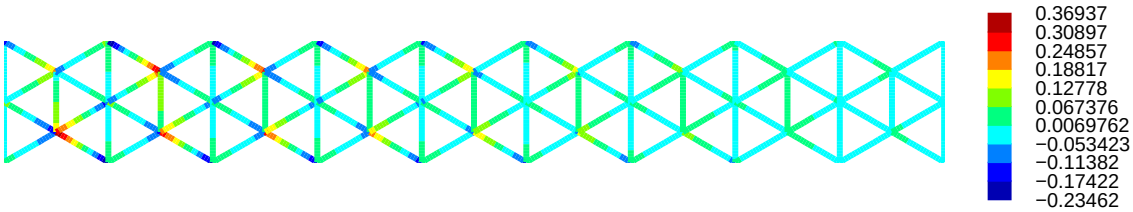

Figure 117: Ligament curvature (in 1/m) under unit tip force

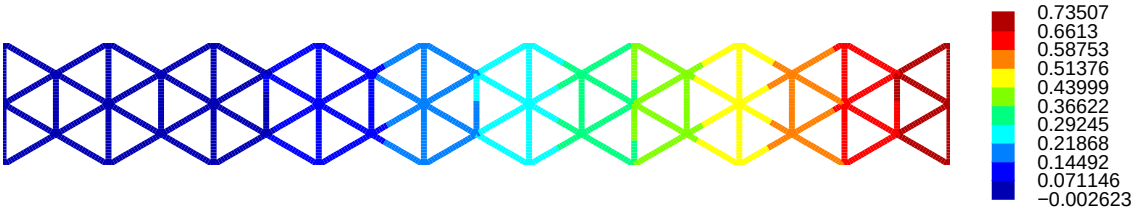

Figure 118: Lateral deflection (in mm) under unit tip force

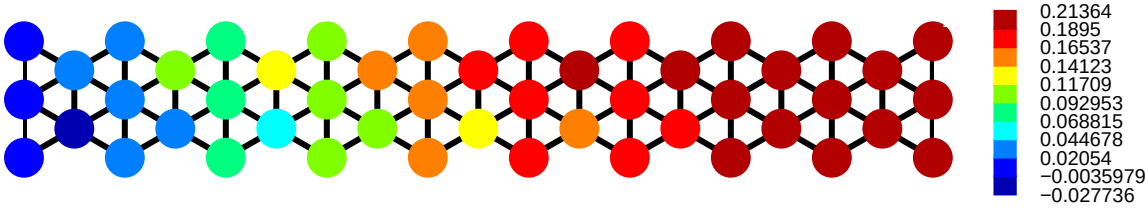

Figure 119: Circle rotation (in deg) under unit tip force

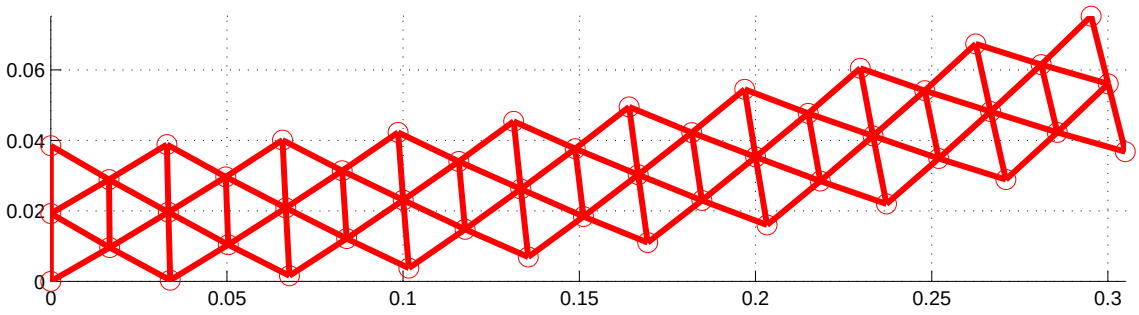

Figure 120: Deformed configuration under unit tip moment

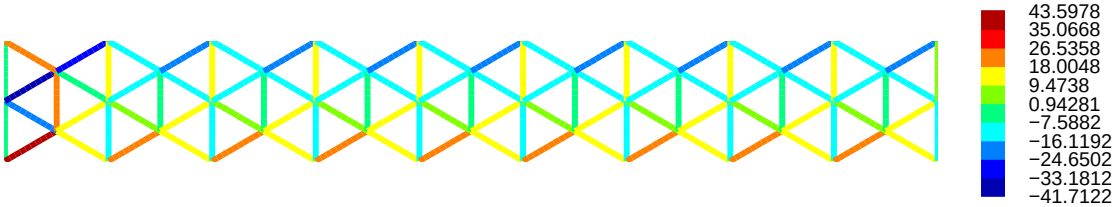

Figure 121: Axial strain (in μ-strain) under unit tip moment

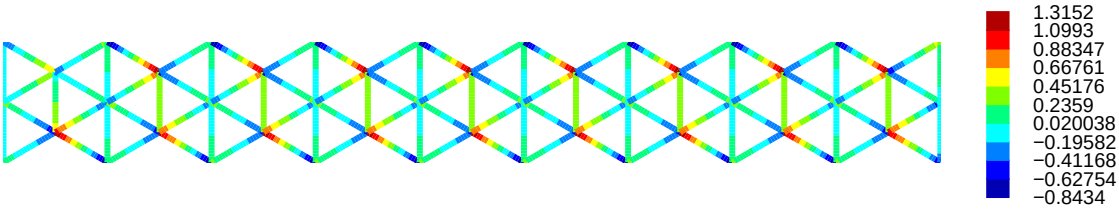

Figure 122: Ligament curvature (in 1/m) under unit tip moment

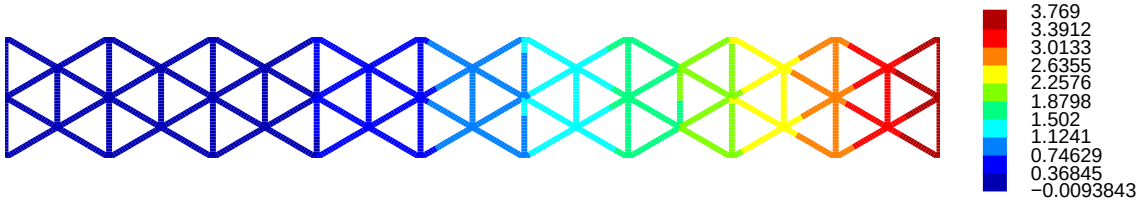

Figure 123: Lateral deflection (in mm) under unit tip moment

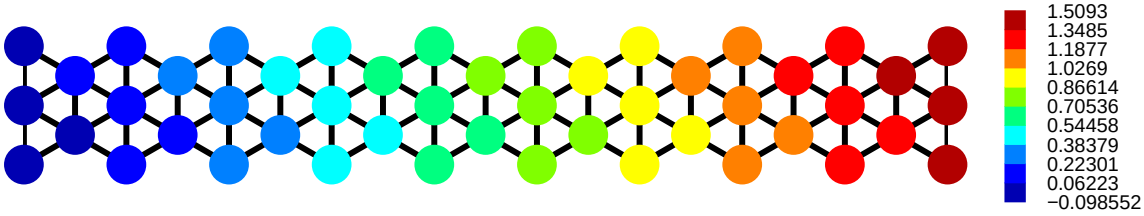

Figure 124: Circle rotation (in deg) under unit tip moment

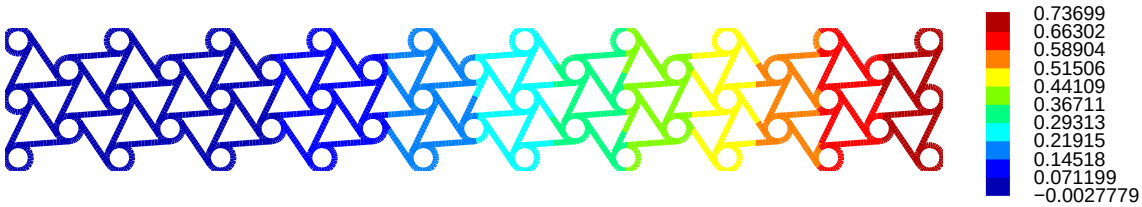

Figure 125: Lateral deflection (in mm) under unit tip force, ANSYS simulation with rigid circles

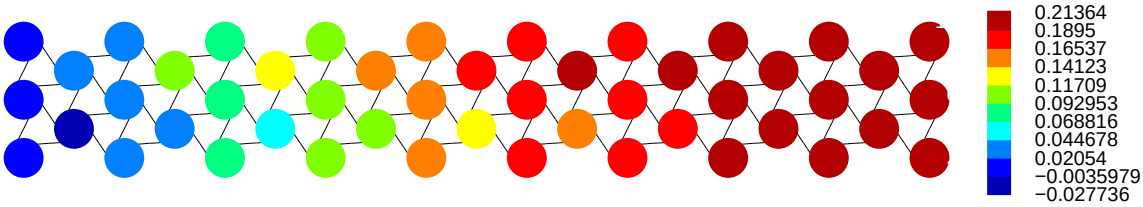

Figure 126: Circle rotation (in deg) under unit tip force, ANSYS simulation with rigid circles

7.2.3 Refined actuation strategy

The performance of an actuation strategy that tries to replicate passive deformation patterns will now be assessed. Referring back to Figs. 88 and 89, it is clear that to reproduce the structural deformation obtained under an applied tip moment using piezoelectric actuation, it is necessary to be able to apply linear curvature variations over the span of the ligaments. Two approaches could achieve such control. Figure 127 shows a first option in which the electrode is shaped to have a linearly varying width. Since the equivalent bending moment applied by the piezoelectric bender is proportional to the electrode's width, a linearly varying curvature can very naturally be enforced on the ligament. A different approach is illustrated in Fig. 128. This concept would approximate the linear variation by a piecewise constant function. Each piece of electrode would have a different applied voltage, chosen to provide the closest approximation possible to the desired linearly varying curvature. The advantage of the first approach is its simplicity of implementation: all that is required is that the electrode be shaped according to the desired control. However, once the shape of the

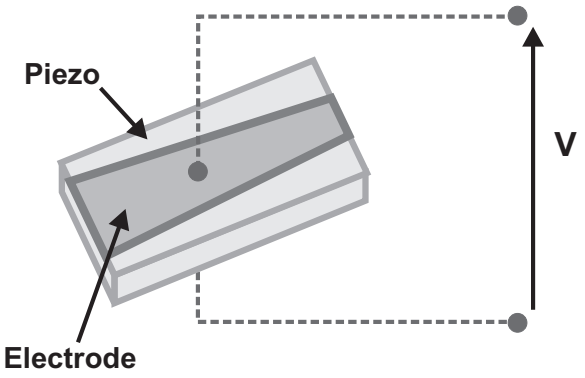

Figure 127: Piezoelectric material with electrode of varying width

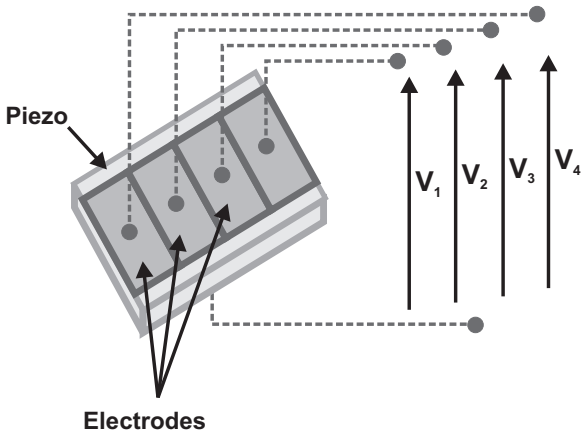

Figure 128: Piezoelectric material with multiple electrodes along the length

electrode has been chosen, it cannot be changed, should a new type of actuation be necessary. The second approach eliminates this issue by allowing the various input voltages to be applied independently. However, implementing this approach could be more involved since several electrodes with their own wiring and control inputs are needed.

Figures 129 and 130 show the deformed configuration of the chiral structure under simple and double bending actuation, respectively, using the new code (scaling factor 100). The associated maximum tip deflections are found to be 0.566 mm and 0.989 mm, respectively. These results confirm the earlier findings of section 6.3.2 about the performance of double bending actuation relative to simple bending actuation.

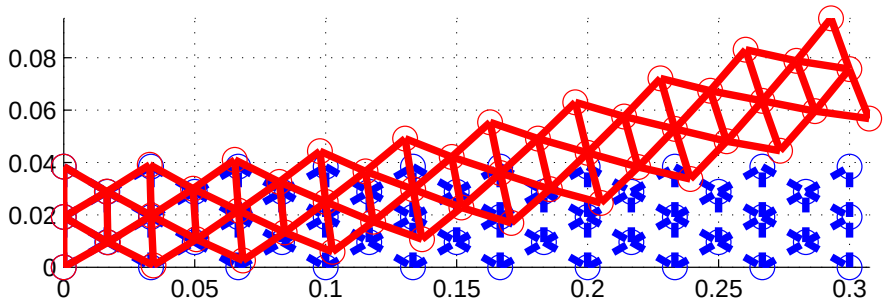

Figure 129: Chiral network actuated by simple bending control strategy (scale factor 100): undeformed configuration (blue, dotted); actuated deformed configuration (red, solid)

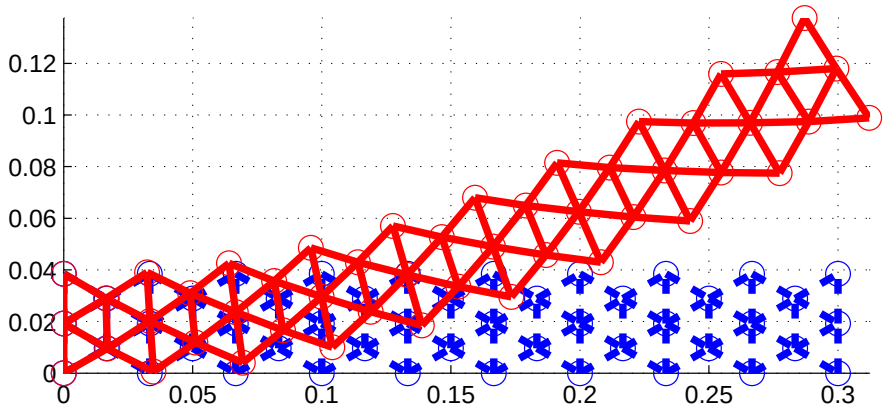

Figure 130: Chiral network actuated by double bending control strategy (scale factor 100): undeformed configuration (blue, dotted); actuated deformed configuration (red, solid)

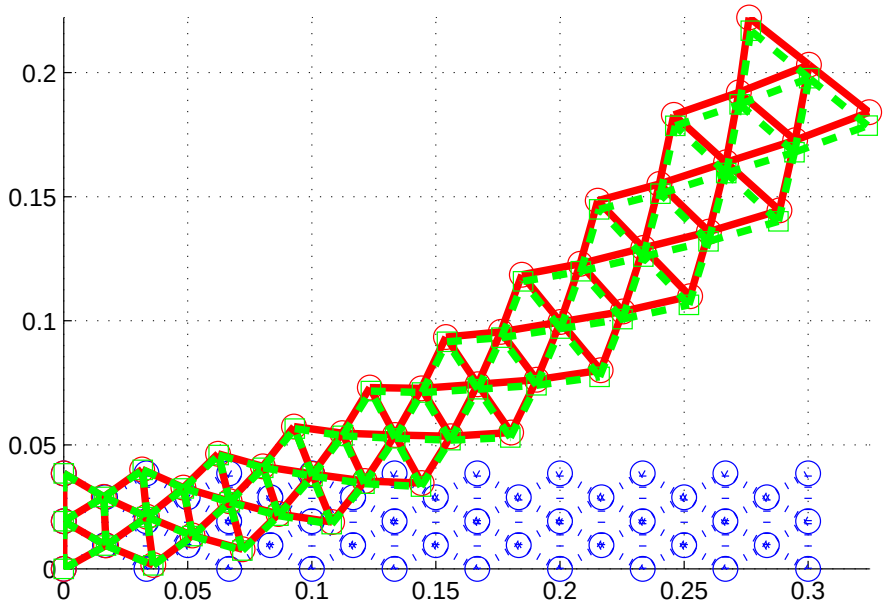

Figure 131: Chiral network actuated by control strategy approximately replicating the deformations of the passive system (scale factor 50): undeformed configuration (blue, dotted); passive deformed configuration (red, solid); actuated deformed configuration (green, dashed)

Figure 131 shows the results of actuating a chiral structure with a control strategy which attempts to replicate the curvature levels found in the corresponding passively deformed system. It is clear that this is feasible, although a major drawback exists. In this case, the induced tip displacement is ≈ 3.6 mm just as one would expect based on the passive response to a unit tip moment. However, the maximum applied voltage to achieve this is about 9 times larger than the allowable limit for a typical PZT-5A piezoelectric material. In other words, the physically realizable deflection would only be about 0.4 mm, which is not as efficient as simple or double bending. Since the curvature changes linearly over a ligament, certain parts may not be undergoing much stress. Likewise, certain ligaments are not stressed as much as others, and contribute only minimally to the global output.

7.3 Extension for 2D dynamic aeroelastic analysis

7.3.1 Structural dynamics equations

Similar to the previously derived static model, a dynamic model of the chiral network was derived and implemented. First, the ligaments are modeled as in the static case, but with time-dependent degrees-of-freedom instead, as well as time-varying loading (including actuation loading). Recall that in the static case, the displacement of a ligament was of the form

$$\underline{\mathcal{U}}^e(x_1) = \underline{\underline{N}}(x_1)\underline{\underline{T}}\,\underline{\underline{F}}\,\underline{\underline{R}}\,\underline{u}^i - \underline{\underline{N}}(x_1)\underline{\underline{T}}\,\underline{\mathcal{P}}^+ + \underline{\mathcal{P}}(x_1). \tag{227}$$

Now, the assumed displacement simply becomes

$$\underline{\mathcal{U}}^e(x_1,t) = \underline{\underline{N}}(x_1)\underline{\underline{T}}\,\underline{\underline{F}}\,\underline{\underline{R}}\,\underline{u}^i(t) - \underline{\underline{N}}(x_1)\underline{\underline{T}}\,\underline{\mathcal{P}}^+(t) + \underline{\mathcal{P}}(x_1,t). \tag{228}$$

With this expression, the equation for the strain energy of a ligament remains the same; the stiffness matrix is therefore unchanged.

The global static equation was augmented with a mass term to include inertial effects in the analysis. The equation is of the form

$$\underline{\underline{M}}^s\ddot{\underline{u}} + \underline{\underline{K}}^s\underline{u} = \underline{f}_{\text{load}} + \underline{f}_{\text{aero}}, \tag{229}$$

where $\dot{()}$ indicates a time derivative, $\underline{u}$ is the array of all structural degrees-of-freedom, which are the displacements and the rotation of all circular nodes in the chiral network, $\underline{\underline{K}}^s$ is the global stiffness matrix which was obtained in section 7.1, $\underline{\underline{M}}^s$ is a global mass matrix, yet to be defined, $\underline{f}_{\text{load}} = \underline{f}_{\text{ext}} + \underline{f}_{\text{act}}$ is the load vector associated with the externally applied loads and piezoelectric actuation loads, and $\underline{f}_{\text{aero}}$ is the load vector associated with applied unsteady aerodynamic forces. $\underline{f}_{\text{ext}}$ will be assumed not to depend on the deformation of the structure, while $\underline{f}_{\text{aero}}$ will depend on $\underline{u}$. If a feedback control law adapts the actuator voltages based on the structural configuration, $\underline{f}_{\text{act}}$ depends on the degrees-of-freedom; otherwise, the applied voltages would simply be prescribed as specific functions of time.

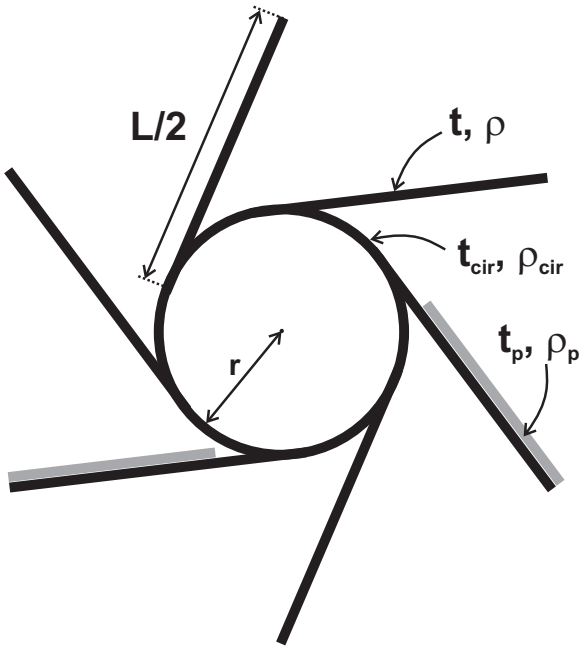

Figure 132: Geometry of an inertia element

The mass matrix is populated based on a simplifying assumption. The circles in the structure are modeled as inertia elements, representing the mass and inertia characteristics of the part shown in Fig. 132. It is composed of a rigid circle and the half-ligaments attached to it, and is assumed to be rigid as far as the inertial properties are concerned. It should be emphasized that each circle will have different associated mass properties depending on the number of ligaments it is connected to, as well as whether the ligaments have bonded piezoelectric benders or not. C denotes the center of the circle, while G refers to the center of mass of the entire element. $\underline{r}_{CG}$ is the position vector of G with respect to C. Its total mass is m and $\underline{\underline{I}}^C$ is its tensor of mass moments of inertia. The velocity of the center C is $\underline{v}_C = \dot{x}_c\bar{\imath}_1 + \dot{y}_c\bar{\imath}_2$ and the rigid body has angular velocity $\underline{\omega} = \dot{\theta}_c\bar{\imath}_3$, where x_c, y_c and θ_c represent the degrees-of-freedom associated with this circle. The kinetic energy of this rigid body is

$$K^{\text{cir}} = \frac{1}{2}m\underline{v}_C^T\underline{v}_C + m\underline{v}_C^T\tilde{r}_{CG}\underline{\omega} + \frac{1}{2}\underline{\omega}^T\underline{\underline{I}}^C\underline{\omega}, \tag{230}$$

where the tilde notation was introduced in Eq. (121) (see, for example, Ref. 7).

Introducing the expressions of $\underline{v}_C$ and $\underline{\omega}$, it can be written as

$$K^{\text{cir}} = \frac{1}{2}\underline{\dot{u}}_c^T \underline{\underline{M}}^{\text{cir}} \underline{\dot{u}}_c, \tag{231}$$

in which $\underline{u}_c^T = \{x_c\,,\, y_c\,,\, \theta_c\}$ and

$$\underline{\underline{M}}^{\text{cir}} = \begin{bmatrix} m & 0 & -my_{CG} \\ 0 & m & mx_{CG} \\ -my_{CG} & mx_{CG} & I_{zz}^C \end{bmatrix}. \tag{232}$$

Similar to the global stiffness matrix, the global mass matrix is simply assembled from these individual mass matrices. A block-diagonal matrix is formed in which the diagonal blocks are the individual mass matrices associated with the successive sets of three degrees-of-freedom belonging to each circle; the order of the diagonal blocks simply follows the ordering of circular nodes.

As before, the final structural equation is obtained by partitioning the original system of equations and retaining the set of equations whose unknowns are the unconstrained degrees-of-freedom. The first matrix equation of the partitioned system

$$\begin{bmatrix} \underline{\underline{M}}_{uu}^s & \underline{\underline{M}}_{uk}^s \\ \underline{\underline{M}}_{ku}^s & \underline{\underline{M}}_{kk}^s \end{bmatrix} \begin{Bmatrix} \underline{\ddot{u}}_u \\ \underline{\ddot{u}}_k \end{Bmatrix} + \begin{bmatrix} \underline{\underline{K}}_{uu}^s & \underline{\underline{K}}_{uk}^s \\ \underline{\underline{K}}_{ku}^s & \underline{\underline{K}}_{kk}^s \end{bmatrix} \begin{Bmatrix} \underline{u}_u \\ \underline{u}_k \end{Bmatrix} = \begin{Bmatrix} \underline{f}_{\text{k,load}} \\ \underline{f}_{\text{u,load}} \end{Bmatrix} + \begin{Bmatrix} \underline{f}_{\text{k,aero}} \\ \underline{f}_{\text{u,aero}} \end{Bmatrix}, \tag{233}$$

where $\underline{u}_u$ and $\underline{u}_k$ are the arrays of unconstrained (or unknown) and constrained (or prescribed) degrees-of-freedom, respectively, can be rearranged as

$$\underline{\underline{M}}_{uu}^s \underline{\ddot{u}}_u + \underline{\underline{K}}_{uu}^s \underline{u}_u = \underline{f}_{\text{k,load}} + \underline{f}_{\text{k,aero}} + \underline{f}_{\text{k,pdof}}, \tag{234}$$

where $\underline{f}_{\text{k,pdof}} = -\underline{\underline{M}}_{uk}^s \underline{\ddot{u}}_k - \underline{\underline{K}}_{uk}^s \underline{u}_k$ is an additional load vector enforcing prescribed degree-of-freedom values. If no time dependent constraints are allowed, the first term vanishes. The second term may be zero as well, if there are no prescribed degrees-of-freedom with non-zero value. $\underline{\underline{M}}_{uu}^s$ and $\underline{\underline{K}}_{uu}^s$ are the partitioned structural matrices, and $\underline{f}_{\text{k,load}}$ and $\underline{f}_{\text{k,aero}}$ are the partitioned load vectors of known forces (unknown

reactions at the constrained degrees-of-freedom are eliminated in the partitioning step).

In order to simplify notations somewhat, the structural equation will be written as

$$\underline{\underline{M}}^S \underline{\ddot{u}} + \underline{\underline{K}}^S \underline{u} = \underline{f}_{\text{load}} + \underline{f}_{\text{aero}} + \underline{f}_{\text{pdof}}, \tag{235}$$

where it should be understood that $\underline{u}$ represents the array of *unconstrained* degrees-of-freedom only, and the structural matrices and load vectors are partitions of the orginal matrices and vectors.

Note that with this general notation, one could easily represent other structures with the same formal equation. For example, this equation could model the dynamic behavior of a beam, $\underline{u}$ being the array of generalized coordinates associated with the free vibration mode shapes of the beam. The equation could be obtained by applying the Ritz method based on Lagrange's equations, using a finite number of mode shapes as the assumed functions (for example, see Ref. 48).

7.3.2 Aerodynamic model

Peters' unsteady airloads theory for deformable thin airfoils summarized in Appendix C will be adapted for implementation in a coupled chiral network analysis code. In addition, Peters' 2D inflow theory will also be used to determine the inflow needed to compute the aerodynamic loads, and this theory was also presented in Appendix C.

Based on Eq. (327), the Glauert components of the aerodynamic loads on the entire blade section can be written as

$$\underline{L}_{\text{aero}} = -\underline{\underline{M}}^A \underline{\ddot{h}} - \underline{\underline{C}}^A \underline{\dot{h}} - \underline{\underline{K}}^A \underline{h} + \underline{\Lambda}^A \lambda_0 + \underline{L}_{\text{aero}}^{\text{presc}}, \tag{236}$$

where $\underline{h}$ are the Glauert components of the lateral deflection $h(t)$, whose definition in terms of the structural degrees-of-freedom will be detailed below, λ_0 is the inflow

defined below as well, and

$$\underline{\underline{M}}^A = 2\pi\rho_a b b_a^2 \underline{\underline{M}}, \tag{237a}$$

$$\underline{\underline{C}}^A = 2\pi\rho_a b b_a u_0 \underline{\underline{C}}, \tag{237b}$$

$$\underline{\underline{G}}^A = 2\pi\rho_a b b_a u_0 \underline{\underline{G}}, \tag{237c}$$

$$\underline{\underline{K}}^A = 2\pi\rho_a b u_0^2 \underline{\underline{K}} + \dot{\underline{\underline{G}}}^A, \tag{237d}$$

$$\underline{\Lambda}^A = \mathrm{col}_1\left(\underline{\underline{C}}^A - \underline{\underline{G}}^A\right), \tag{237e}$$

$$\underline{L}_{\mathrm{aero}}^{\mathrm{presc}} = -\underline{\underline{M}}^A \dot{\underline{v}} - \left(\underline{\underline{C}}^A - \underline{\underline{G}}^A\right)\underline{v}, \tag{237f}$$

in which ρ_a is the air density, b the width of the section, b_a the semi-chord of the airfoil, $\underline{\underline{M}}$, $\underline{\underline{C}}$, $\underline{\underline{G}}$ and $\underline{\underline{K}}$ are defined in the appendix, $\mathrm{col}_1(\cdot)$ extracts the first column of the matrix argument, and finally, $u_0(t)$ and $\underline{v}(t) = \{v_0, v_1, 0, \ldots, 0\}^T$ are the velocity parameters defined in the appendix.

According to Peters' inflow equation, Eq. (332), the inflow parameter λ_0 is related to the inflow states $\underline{\lambda}$ through

$$\lambda_0 = \frac{1}{2}\underline{b}^T \underline{\lambda}, \tag{238}$$

where, based on Eq. (335), the inflow states satisfy the following differential equation

$$\underline{\underline{A}}\,\dot{\underline{\lambda}} + \underline{\underline{B}}\,\underline{\lambda} = \underline{\underline{E}}\,\ddot{\underline{h}} + \underline{\underline{F}}\,\dot{\underline{h}}, \tag{239}$$

in which $\underline{\underline{A}}$ is defined in the appendix, and

$$\underline{\underline{B}} = \frac{u_0}{b_a}\underline{\underline{I}}, \qquad \underline{\underline{E}} = \underline{c}\,\underline{e}^T, \qquad \underline{\underline{F}} = \frac{u_0}{b_a}\underline{c}\,\underline{f}^T. \tag{240}$$

All arrays $\underline{b}$, $\underline{c}$, $\underline{e}$ and $\underline{f}$ are defined in the appendix, and $\underline{\underline{I}}$ denotes the identity matrix.

In these equations, $\underline{h}$ is a finite (truncated) set of Glauert components associated with the continuously deformed thin airfoil. Clearly, such a continuous line is not easily available from the structural model. Rather, it is simpler to define the flexible airfoil as a set of discrete points along the length of the chiral structure. The transformation of structural degrees-of-freedom $\underline{u}$ into Glauert components $\underline{h}$, and

vice versa, then proceeds in two steps: a transformation between structural degrees-of-freedom and a discrete set of lateral deflection parameters $\underline{\eta}$ along a reference line of the structure; and a transformation between these parameters and the associated Glauert components. It will be shown that the relationship between $\underline{u}$ and $\underline{\eta}$ is of the matrix form

$$\underline{\eta} = \varsigma \underline{\underline{Z}}\, \underline{u}, \tag{241}$$

where ς is a parameter which can be set to $+1$ or -1 depending on the relative frame orientations between the structural degrees-of-freedom and the aerodynamic theory deflection h, while that between the discrete deflection values and $\underline{h}$ will be expressed as

$$\underline{h} = \underline{\underline{\mathcal{L}}}\, \underline{\eta}. \tag{242}$$

Since deflections are counted positively down in Peters' airloads theory, $\varsigma = -1$. Interestingly, whichever value ς takes, it will vanish almost completely from the final formulation, as detailed in the next section. Combining these equations and introducing $\underline{\underline{\Gamma}} = \underline{\underline{\mathcal{L}}}\, \underline{\underline{Z}}$, the full transformation is expressed as

$$\underline{h} = \varsigma \underline{\underline{\Gamma}}\, \underline{u} = \varsigma \underline{\underline{\mathcal{L}}}\, \underline{\underline{Z}}\, \underline{u}. \tag{243}$$

It should also be emphasized that this variable transformation relates the array of Glauert coefficients of aerodynamic forces to the generalized force representing the aerodynamics in the structural equations. Indeed, the virtual force associated with the aerodynamic forces may be written as

$$\overline{\delta W} = \delta \underline{u}^T \underline{f}_{\text{aero}}, \tag{244}$$

or

$$\overline{\delta W} = \delta \underline{h}^T \underline{L}_{\text{aero}} = \delta \underline{u}^T \left(\varsigma \underline{\underline{\Gamma}}\right)^T \underline{L}_{\text{aero}}, \tag{245}$$

and hence

$$\underline{f}_{\text{aero}} = \varsigma \underline{\underline{\Gamma}}^T \underline{L}_{\text{aero}}. \tag{246}$$

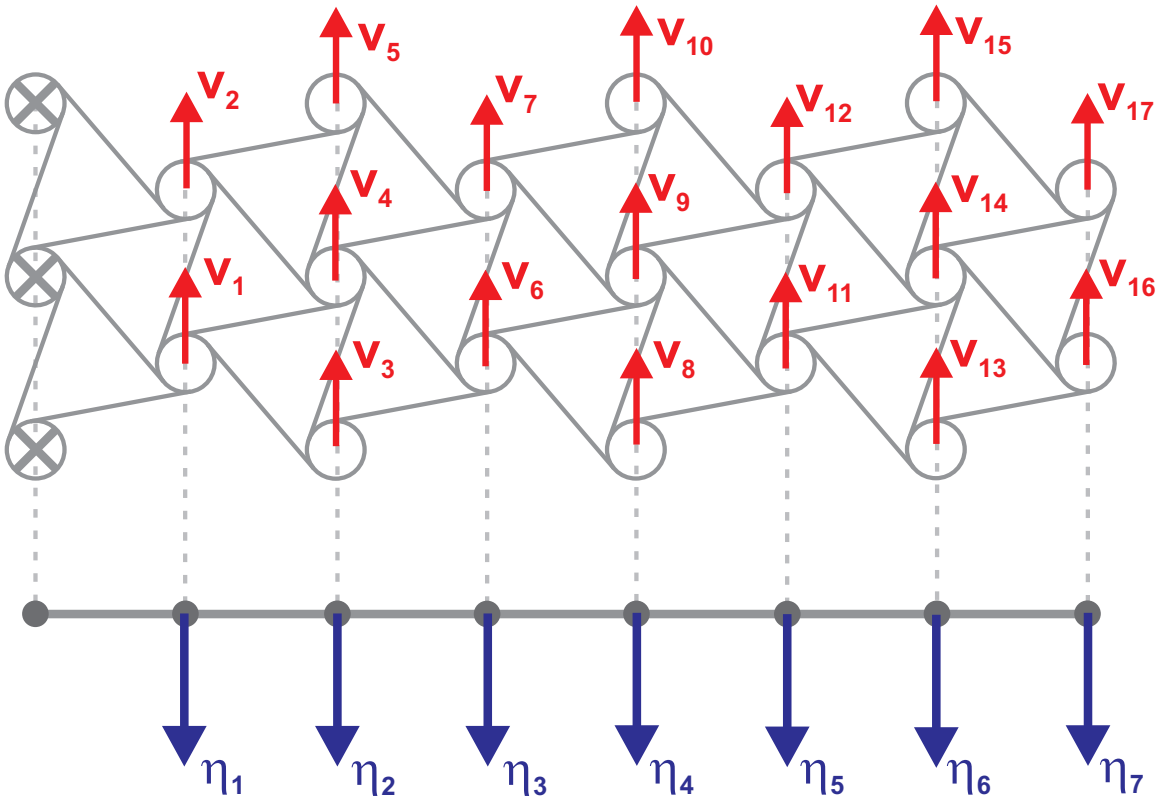

Figure 133: Correspondence between η_i values and v_j degrees-of-freedom

$\underline{\underline{Z}}$ simply relates the degrees-of-freedom on all circles of a given vertical row of the network to a single deflection value at the same horizontal location. At a given x_i, the corresponding η_i is computed as the average of the circle deflections in the $\bar{\imath}_2$ direction. For example, Fig. 133 shows the correspondence between a chiral structure with its associated vertical displacement degrees-of-freedom v_j, and an equivalent line with discrete points of vertical displacements η_i. The nodes on the left-hand side are assumed to be completely constrained, but in general that does not need be the case. In this example, η_2 would be computed as $\eta_2 = \varsigma\left(\frac{1}{3}v_3 + \frac{1}{3}v_4 + \frac{1}{3}v_5\right)$, and η_5 as $\eta_5 = \varsigma\left(\frac{1}{2}v_{11} + \frac{1}{2}v_{12}\right)$. These linear equations for the η_i can simply be cast in matrix form.

The derivation of the expression for $\underline{\underline{\mathcal{L}}}$ is somewhat more involved. Figure 134 graphically shows the representation of the airfoil's continuous deflection as a piece-wise linear deflection, where the discrete deflection values η_i fully define the latter

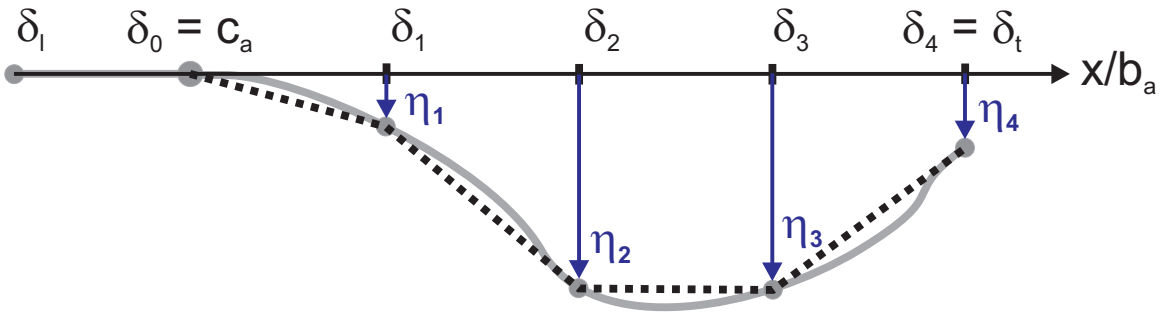

Figure 134: Discrete representation of continuously deforming airfoil

model. The profile deformation is assumed to vanish, $h(x,t) = 0$, on the rigid front D-spar, $-1 = \delta_l \leq \frac{x}{b_a} \leq \delta_0 = c_a$, where $\delta_l = -1$ corresponds to the non-dimensional location of the leading edge and c_a corresponds to the location of the left boundary of the chiral network, and on the flexible aft part, for $i = 1, \ldots, p$ and $\delta_{i-1} \leq \frac{x}{b_a} \leq \delta_i$, it is assumed to have the form

$$h(x,t) = \eta_{i-1} + \frac{\eta_i - \eta_{i-1}}{\delta_i - \delta_{i-1}} \left(\frac{x}{b_a} - \delta_{i-1} \right) = \frac{\eta_i}{l_i} \left(\frac{x}{b_a} - \delta_{i-1} \right) - \frac{\eta_{i-1}}{l_i} \left(\frac{x}{b_a} - \delta_i \right), \quad (247)$$

in which $l_i = \delta_i - \delta_{i-1}$. The associated Glauert terms, using the transformation $x = b_a \cos\varphi$, can be found as follows

$$h_0 = \frac{1}{\pi} \int_0^\pi h \, \mathrm{d}\varphi, \quad (248)$$

and for $n = 1, \ldots, N$

$$h_n = \frac{2}{\pi} \int_0^\pi h \cos(n\varphi) \, \mathrm{d}\varphi. \quad (249)$$

We introduce ϕ_i such that $\delta_i = \cos\phi_i$ for $i = 0, \ldots, p$ (noting that $\phi_p = 0$ since $\delta_p = +1$). Based on the assumed piecewise linear shape of the reference line, the Glauert expansion terms become

$$h_0 = \frac{1}{\pi} \sum_{i=1}^{p} \int_{\phi_i}^{\phi_{i-1}} \left[\frac{\eta_i}{l_i} (\cos\varphi - \delta_{i-1}) - \frac{\eta_{i-1}}{l_i} (\cos\varphi - \delta_i) \right] \mathrm{d}\varphi, \quad (250)$$

and for $n = 1, \ldots, N$

$$h_n = \frac{2}{\pi} \sum_{i=1}^{p} \int_{\phi_i}^{\phi_{i-1}} \left[\frac{\eta_i}{l_i} (\cos\varphi - \delta_{i-1}) - \frac{\eta_{i-1}}{l_i} (\cos\varphi - \delta_i) \right] \cos(n\varphi) \, \mathrm{d}\varphi. \quad (251)$$

These equations can be written in compact form as

$$h_0 = \sum_{i=1}^{p} I_{0,i}\,, \qquad h_n = \sum_{i=1}^{p} I_{n,i}, \tag{252}$$

in which the individual integrals are found to be, for $i = 1, \ldots, p$

$$I_{0,i} = \frac{1}{\pi l_i}\left[\eta_i\left(S_{1,i} - \delta_{i-1}\left(\phi_{i-1} - \phi_i\right)\right) - \eta_{i-1}\left(S_{1,i} - \delta_i\left(\phi_{i-1} - \phi_i\right)\right)\right], \tag{253}$$

$$I_{1,i} = \frac{1}{\pi l_i}\left[\eta_i\left(\left(\phi_{i-1} - \phi_i\right) + S_{2,i} - 2\delta_{i-1}S_{1,i}\right) - \eta_{i-1}\left(\left(\phi_{i-1} - \phi_i\right) + S_{2,i} - 2\delta_i S_{1,i}\right)\right], \tag{254}$$

and for $n = 2, \ldots, N$

$$I_{n,i} = \frac{1}{\pi l_i}\left[\eta_i\left(S_{n-1,i} + S_{n+1,i} - 2\delta_{i-1}S_{n,i}\right) - \eta_{i-1}\left(S_{n-1,i} + S_{n+1,i} - 2\delta_i S_{n,i}\right)\right], \tag{255}$$

where we have introduced for $n = 1, \ldots, N$ and $i = 1, \ldots, p$

$$S_{n,i} = \frac{\sin(n\phi_{i-1})}{n} - \frac{\sin(n\phi_i)}{n}. \tag{256}$$

If we extend the definition of $S_{n,i}$ to non-positive values of n as follows

$$S_{n,i} = \begin{cases} 0 & \text{if } n < 0 \\ \phi_{i-1} - \phi_i & \text{if } n = 0 \\ \frac{\sin(n\phi_{i-1})}{n} - \frac{\sin(n\phi_i)}{n} & \text{if } n > 0 \end{cases}, \tag{257}$$

and introducing

$$\nu_n = \begin{cases} 1 & \text{if } n = 0 \\ 2 & \text{if } n > 0 \end{cases}, \tag{258}$$

we can write $I_{n,i}$ for all $n = 0, \ldots, N$ in one compact form

$$I_{n,i} = J_{n,i}\,\eta_{i-1} + K_{n,i}\,\eta_i, \tag{259}$$

where

$$J_{n,i} = -\frac{1}{\pi l_i}\left(S_{n-1,i} + S_{n+1,i} - \nu_n \delta_i S_{n,i}\right), \tag{260a}$$

$$K_{n,i} = \frac{1}{\pi l_i}\left(S_{n-1,i} + S_{n+1,i} - \nu_n \delta_{i-1} S_{n,i}\right). \tag{260b}$$

Then, for $n = 0, \ldots, N$

$$h_n = \sum_{i=1}^{p} \left(J_{n,i}\eta_{i-1} + K_{n,i}\eta_i \right) = \sum_{i=1}^{p-1} \left(J_{n,i+1} + K_{n,i} \right) \eta_i + K_{n,p}\eta_p, \tag{261}$$

so that finally

$$h_n = \sum_{i=1}^{p} \mathcal{L}_{n,i}\eta_i \qquad \text{or in matrix form} \qquad \underline{h} = \underline{\underline{\mathcal{L}}}\,\underline{\eta}, \tag{262}$$

where for $i = 1, \ldots, p-1$, $\mathcal{L}_{n,i} = J_{n,i+1} + K_{n,i}$, and $\mathcal{L}_{n,p} = K_{n,p}$.

As an application, consider an airfoil with a single flap, $p = 1$, such that $\eta_0 = 0$ and $\eta_1 = \eta_t = \eta_p = l_1\, b_a\, \beta$. β represents the flap angle. Then

$$h_0 = \mathcal{L}_{0,p}\,\eta_p = \frac{\beta b_a}{\pi} \left(\sin\phi_0 - \phi_0 \cos\phi_0 \right), \tag{263}$$

$$h_1 = \mathcal{L}_{1,p}\,\eta_p = \frac{\beta b_a}{\pi} \left(\phi_0 - \cos\phi_0 \sin\phi_0 \right), \tag{264}$$

and for $n = 2, \ldots, N$, the results simplify to

$$h_n = \frac{\beta b_a}{\pi} \left(\frac{\sin((n-1)\phi_0)}{n-1} + \frac{\sin((n+1)\phi_0)}{n+1} - 2\cos\phi_0 \frac{\sin(n\phi_0)}{n} \right). \tag{265}$$

These results match the expressions provided in Ref. 67 for an airfoil with a flap.

As before, the general relationship $\underline{h} = \varsigma \underline{\underline{\Gamma}}\,\underline{u}$ could apply to other cases as well, albeit with a different expression of $\underline{\underline{\Gamma}}$. For example, for a simple beam, $\underline{\underline{Z}}$ is obtained by recognizing that $\underline{\eta}$ corresponds to discrete values of the lateral beam deflection $v(x,t) = \sum_{n=1}^{N_m} \Phi_n(x)\xi_n(t) = \underline{\Phi}^T(x)\underline{\xi}(t)$, where the $\Phi_n(x)$ are the free vibration mode shapes, and the $\xi_n(t)$ are the corresponding generalized coordinates. Hence,

$$\underline{\underline{Z}}^T = \left[\underline{\Phi}(x_1)\,,\, \underline{\Phi}(x_2)\,,\, \ldots\,,\, \underline{\Phi}(x_p) \right]. \tag{266}$$

7.3.3 Coupled formulation

These different models can be combined into one full, general formulation. Starting with the structural equation, Eq. (235), introducing the airloads equation, Eq. (236),

and the expression for the inflow, Eq. (238), using the transformation relationship between $\underline{h}$ and $\underline{u}$, Eq. (243), and rearranging the terms, one finds

$$\underline{\underline{\hat{M}}}\,\underline{\ddot{u}} + \underline{\underline{\hat{C}}}\,\underline{\dot{u}} + \underline{\underline{\hat{K}}}\,\underline{u} + \underline{\underline{\hat{\Lambda}}}\,\underline{\mu} = \underline{\hat{L}}_{\text{aero}}^{\text{presc}} + \underline{f}_{\text{load}} + \underline{f}_{\text{pdof}}, \tag{267}$$

where

$$\underline{\underline{\hat{M}}} = \underline{\underline{M}}^S\underline{\ddot{u}} + \underline{\underline{\Gamma}}^T\underline{\underline{M}}^A\underline{\underline{\Gamma}}, \tag{268a}$$

$$\underline{\underline{\hat{C}}} = \underline{\underline{C}}^S\underline{\ddot{u}} + \underline{\underline{\Gamma}}^T\underline{\underline{C}}^A\underline{\underline{\Gamma}}, \tag{268b}$$

$$\underline{\underline{\hat{K}}} = \underline{\underline{K}}^S\underline{\ddot{u}} + \underline{\underline{\Gamma}}^T\underline{\underline{K}}^A\underline{\underline{\Gamma}}, \tag{268c}$$

$$\underline{\underline{\hat{\Lambda}}} = -\frac{1}{2}\underline{\underline{\Gamma}}^T\underline{\Lambda}^A\underline{b}^T, \tag{268d}$$

$$\underline{\hat{L}}_{\text{aero}}^{\text{presc}} = \varsigma\underline{\underline{\Gamma}}^T\underline{L}_{\text{aero}}^{\text{presc}}. \tag{268e}$$

The new variable $\underline{\mu} = \varsigma\underline{\lambda}$ (and $\mu_0 = \varsigma\lambda_0$) was introduced, and note that an additional matrix $\underline{\underline{C}}^S$ could be introduced if structural damping should be included. The inflow equation, Eq. (239), is similarly rearranged into

$$\underline{\underline{\hat{E}}}\,\underline{\ddot{u}} + \underline{\underline{\hat{F}}}\,\underline{\dot{u}} + \underline{\underline{\hat{A}}}\,\underline{\dot{\mu}} + \underline{\underline{\hat{B}}}\,\underline{\mu} = \underline{0}, \tag{269}$$

where

$$\underline{\underline{\hat{A}}} = -\underline{\underline{A}}, \qquad \underline{\underline{\hat{B}}} = -\underline{\underline{B}}, \qquad \underline{\underline{\hat{E}}} = \underline{\underline{E}}\,\underline{\underline{\Gamma}}, \qquad \underline{\underline{\hat{F}}} = \underline{\underline{F}}\,\underline{\underline{\Gamma}}. \tag{270}$$

Defining the state vector $\underline{X}^T = \left[\underline{u}^T, \underline{\dot{u}}^T, \underline{\mu}^T\right]$, the equations can be combined into one matrix equation

$$\underline{\underline{\mathcal{M}}}\,\underline{\dot{X}} = \underline{\underline{\hat{\mathcal{A}}}}\,\underline{X} + \underline{\hat{\mathcal{Q}}}_{\text{load}} + \underline{\hat{\mathcal{Q}}}_{\text{pdof}} + \underline{\hat{\mathcal{Q}}}_{\text{aero}}^{\text{presc}}, \tag{271}$$

in which we have defined

$$\underline{\underline{\mathcal{M}}} = \begin{bmatrix} \underline{\underline{I}} & \underline{\underline{0}} & \underline{\underline{0}} \\ \underline{\underline{0}} & \underline{\underline{\hat{M}}} & \underline{\underline{0}} \\ \underline{\underline{0}} & \underline{\underline{\hat{E}}} & \underline{\underline{\hat{A}}} \end{bmatrix}, \tag{272}$$

$$\underline{\underline{\hat{\mathcal{A}}}} = \begin{bmatrix} \underline{\underline{0}} & \underline{\underline{I}} & \underline{\underline{0}} \\ -\underline{\underline{\hat{K}}} & -\underline{\underline{\hat{C}}} & -\underline{\underline{\hat{\Lambda}}} \\ \underline{\underline{0}} & -\underline{\underline{\hat{F}}} & -\underline{\underline{\hat{B}}} \end{bmatrix}, \tag{273}$$

$$\underline{\hat{\mathcal{Q}}}_{\text{load}} = \left\{ \underline{0}^T \quad \underline{f}_{\text{load}}^T \quad \underline{0}^T \right\}^T, \tag{274}$$

$$\underline{\hat{\mathcal{Q}}}_{\text{pdof}} = \left\{ \underline{0}^T \quad \underline{f}_{\text{pdof}}^T \quad \underline{0}^T \right\}^T, \tag{275}$$

$$\underline{\hat{\mathcal{Q}}}_{\text{aero}}^{\text{presc}} = \left\{ \underline{0}^T \quad (\underline{\hat{L}}_{\text{aero}}^{\text{presc}})^T \quad \underline{0}^T \right\}^T. \tag{276}$$

$\underline{\underline{\mathcal{M}}}$ is invertible if and only if $\underline{\underline{\hat{M}}}$ and $\underline{\underline{\hat{A}}}$ are non-singular. If this is the case, the system of differential equations may be rewritten in state-space form

$$\dot{\underline{X}} = \underline{\underline{\mathcal{A}}}\,\underline{X} + \underline{\mathcal{Q}}_{\text{load}} + \underline{\mathcal{Q}}_{\text{pdof}} + \underline{\mathcal{Q}}_{\text{aero}}^{\text{presc}}, \tag{277}$$

where

$$\underline{\underline{\mathcal{A}}} = \begin{Bmatrix} \underline{\underline{0}} & \underline{\underline{I}} & \underline{\underline{0}} \\ -\underline{\underline{\hat{M}}}^{-1}\underline{\underline{\hat{K}}} & -\underline{\underline{\hat{M}}}^{-1}\underline{\underline{\hat{C}}} & -\underline{\underline{\hat{M}}}^{-1}\underline{\underline{\hat{\Lambda}}} \\ \underline{\underline{\hat{A}}}^{-1}\underline{\underline{\hat{E}}}\,\underline{\underline{\hat{M}}}^{-1}\underline{\underline{\hat{K}}} & \underline{\underline{\hat{A}}}^{-1}\underline{\underline{\hat{E}}}\,\underline{\underline{\hat{M}}}^{-1}\underline{\underline{\hat{C}}} - \underline{\underline{\hat{A}}}^{-1}\underline{\underline{\hat{F}}} & \underline{\underline{\hat{A}}}^{-1}\underline{\underline{\hat{E}}}\,\underline{\underline{\hat{M}}}^{-1}\underline{\underline{\hat{\Lambda}}} - \underline{\underline{\hat{A}}}^{-1}\underline{\underline{\hat{B}}} \end{Bmatrix}, \tag{278}$$

$$\underline{\mathcal{Q}}_{\text{load}} = \begin{Bmatrix} \underline{0} \\ \underline{\underline{\hat{M}}}^{-1}\underline{f}_{\text{load}} \\ -\underline{\underline{\hat{A}}}^{-1}\underline{\underline{\hat{E}}}\,\underline{\underline{\hat{M}}}^{-1}\underline{f}_{\text{load}} \end{Bmatrix}, \tag{279}$$

$$\underline{\mathcal{Q}}_{\text{pdof}} = \begin{Bmatrix} \underline{0} \\ \underline{\underline{\hat{M}}}^{-1}\underline{f}_{\text{pdof}} \\ -\underline{\underline{\hat{A}}}^{-1}\underline{\underline{\hat{E}}}\,\underline{\underline{\hat{M}}}^{-1}\underline{f}_{\text{pdof}} \end{Bmatrix}, \tag{280}$$

$$\underline{\mathcal{Q}}_{\text{aero}}^{\text{presc}} = \begin{Bmatrix} \underline{0} \\ \underline{\underline{\hat{M}}}^{-1}\underline{\hat{L}}_{\text{aero}}^{\text{presc}} \\ -\underline{\underline{\hat{A}}}^{-1}\underline{\underline{\hat{E}}}\,\underline{\underline{\hat{M}}}^{-1}\underline{\hat{L}}_{\text{aero}}^{\text{presc}} \end{Bmatrix}. \tag{281}$$

It should be noted that $\underline{\underline{\mathcal{A}}}$ is constant if u_0 is constant; however, the problem is time-varying if $u_0(t)$. $\underline{\mathcal{Q}}_{\text{aero}}^{\text{presc}}$ is constant if u_0, v_0 and v_1 are all constant; otherwise it varies in time as well.

For a quasi-steady formulation in which there is no inflow, $\mu_0 = 0$, the inflow states can be neglected and the state-space formulation can be reduced to

$$\dot{\underline{X}}_{\text{qs}} = \underline{\underline{\mathcal{A}}}_{\text{qs}} \underline{X}_{\text{qs}} + \underline{\mathcal{Q}}_{\text{qs,load}} + \underline{\mathcal{Q}}_{\text{qs,pdof}} + \underline{\mathcal{Q}}^{\text{presc}}_{\text{qs,aero}}, \tag{282}$$

where

$$\underline{\underline{\mathcal{A}}}_{\text{qs}} = \begin{Bmatrix} \underline{\underline{0}} & \underline{\underline{I}} \\ -\underline{\underline{\hat{M}}}^{-1} \underline{\underline{\hat{K}}} & -\underline{\underline{\hat{M}}}^{-1} \underline{\underline{\hat{C}}} \end{Bmatrix}, \tag{283}$$

$$\underline{\mathcal{Q}}_{\text{qs,load}} = \begin{Bmatrix} \underline{\underline{0}} \\ \underline{\underline{\hat{M}}}^{-1} \underline{f}_{\text{load}} \end{Bmatrix}, \tag{284}$$

$$\underline{\mathcal{Q}}_{\text{qs,pdof}} = \begin{Bmatrix} \underline{\underline{0}} \\ \underline{\underline{\hat{M}}}^{-1} \underline{f}_{\text{pdof}} \end{Bmatrix}, \tag{285}$$

$$\underline{\mathcal{Q}}^{\text{presc}}_{\text{qs,aero}} = \begin{Bmatrix} \underline{\underline{0}} \\ \underline{\underline{\hat{M}}}^{-1} \underline{\hat{L}}^{\text{presc}}_{\text{aero}} \end{Bmatrix}. \tag{286}$$

7.4 Validation and results

7.4.1 Structural model validation

Dynamic eigenvalue simulations were run on the chiral structure shown in Fig. 135 to determine the natural frequencies of a chiral structure, as well as the associated free vibration mode shapes. They were compared in order to validate the new simplified structural model against an ANSYS model with rigid circles. Figure 136 shows a comparison of the natural frequencies associated with the first few modes of vibration. As could be expected, very good correlation is found for the lowest frequencies. Indeed, at low frequencies, the mode shapes would be expected to be characterized by global deformations (this will be verified below). On the contrary, for high frequencies, they would be characterized by more local deformations. In other words, one would expect that the impact of the assumptions made for obtaining the mass matrix is relatively small at low frequencies, and the error should increase with mode number. Figure 136

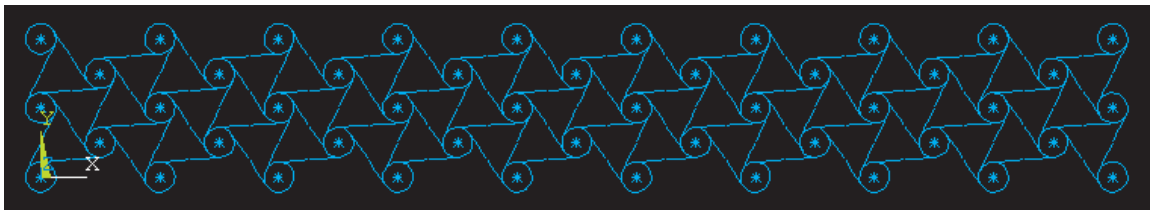

Figure 135: ANSYS model of chiral structure for modal analysis

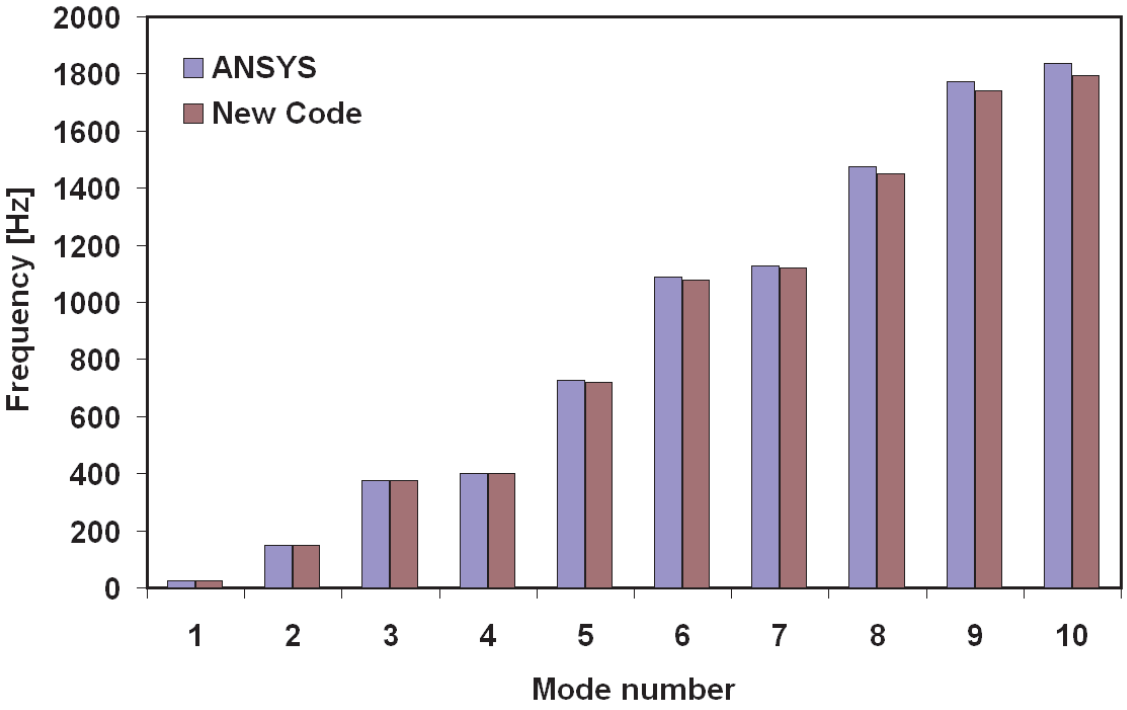

Figure 136: First few natural frequencies from modal analysis

confirms that small discrepancies appear as the frequency increases, but the results still show good agreement.

The mode shapes obtained in both cases were also compared. The results for the first three modes are presented in Figs. 137, 138 and 139. Extremely good correlation is found in terms of the degrees-of-freedom at the centers of the circular nodes. Good correlation would be found for further modes as well, although the level of agreement decreases with increasing frequency.

7.4.2 Eigenresponse tailoring

The possibility of tuning the natural frequencies of the chiral network structure to typical rotor frequencies was investigated. Designing the structure to match operational frequencies could allow for the use of dynamic resonances to amplify the actuator output. First, the evolution of the lowest natural frequencies of a chiral actuator sized to fit in the aft part of a UH-60 rotor blade airfoil was studied as a function of several geometric and material parameters, namely the ratio $\rho = L/R$ and the thickness of the ligaments t_{lig} (assuming constant properties throughout the structure). Figure 140 shows the value of the fundamental frequency for different combinations of the parameters, as well as the second and third natural frequencies. The fundamental frequency expectedly increases with t_{lig}, since this increases the stiffness of the structure. The variation is less straightforward with ρ. At fixed thickness, the fundamental frequency is minimum around $\rho = 0.8$, and increases on either side. This increase becomes steeper at values close to 1, where the nodes have smaller and smaller radius. Again, this is mostly related to an increase in stiffness, as was observed in section 6.3.3 for example. The loss of mass due to the decreasing size of the nodes also contributes. The other frequencies exhibit very similar trends, albeit at higher values.

Unfortunately, based on this figure, it is found that the fundamental frequency of

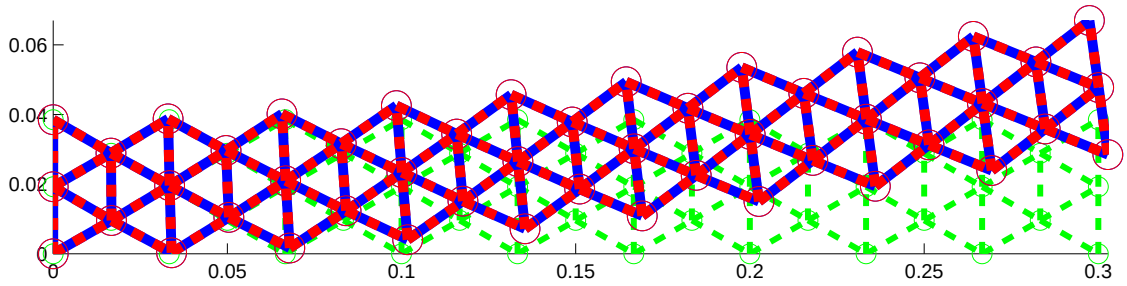

Figure 137: First mode shape: undeformed configuration (dashed, green), ANSYS result (dashed, blue), and result from simplified analysis (solid, red)

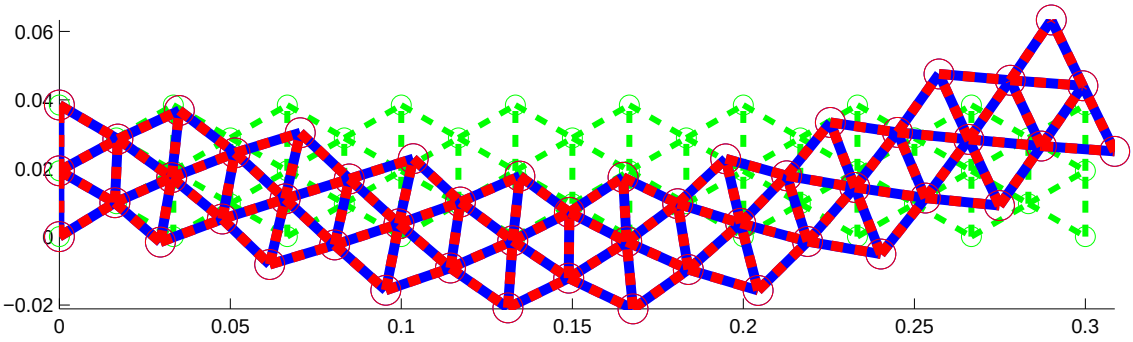

Figure 138: Second mode shape: undeformed configuration (dashed, green), ANSYS result (dashed, blue), and result from simplified analysis (solid, red)

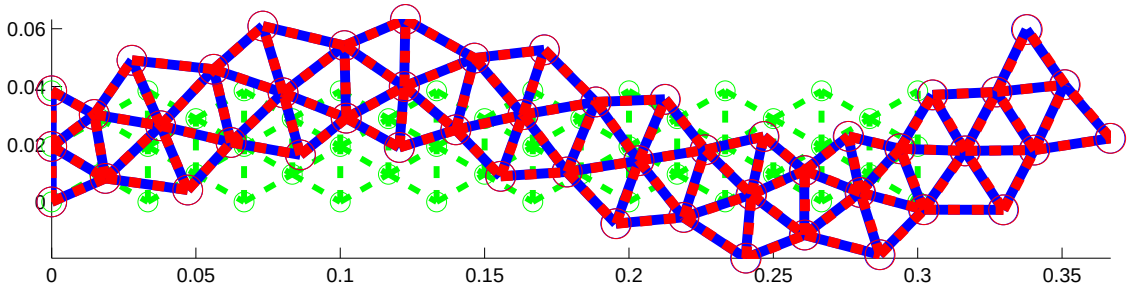

Figure 139: Third mode shape: undeformed configuration (dashed, green), ANSYS result (dashed, blue), and result from simplified analysis (solid, red)

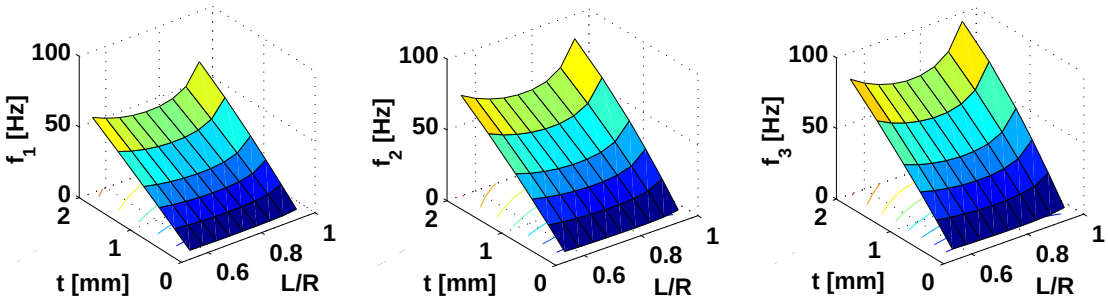

Figure 140: First three natural frequencies, from left to right, as they vary with ligament thickness and L/R ratio

the structure tends to be high compared to typical rotor frequencies. Specifically, the fundamental frequency of this chiral actuator, roughly the size of a UH-60 blade's aft section, was higher than the rotorcraft's 1/rev frequency of 4.3 Hz. The conducted sensitivity studies with respect to the main geometric and material parameters suggest that unreasonably extreme parameter values are required in order to decrease that frequency to appropriate levels. This is attributed to the fact that the amount of material in a chiral structure is distributed in a truss-like fashion, where the material is "spread out" over a large space relative to the amount of material, thus increasing the associated equivalent bending stiffness and increasing the modal frequencies.

As a result, other means of achieving lower natural frequencies were explored. In particular, the influence of geometric and material parameters on a chiral beam with piecewise constant properties was investigated. A manageable number of additional parameters were considered by defining three different sections, each having constant parameter values. The properties of the root section were chosen as the reference, and the values of corresponding properties in the other two sections were varied with respect to those.

The first step in this analysis was the determination of the evolution of the fundamental frequency of a regular beam with three sections of different bending stiffnesses and sectional masses. Figure 141 illustrates this situation and indicates how the stiffness and mass of each section is defined relative to the properties of the root section.

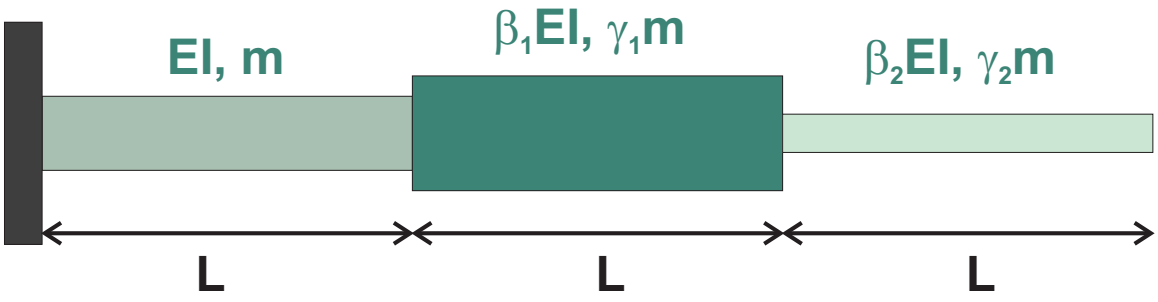

Figure 141: Regular beam with three different sections of constant properties

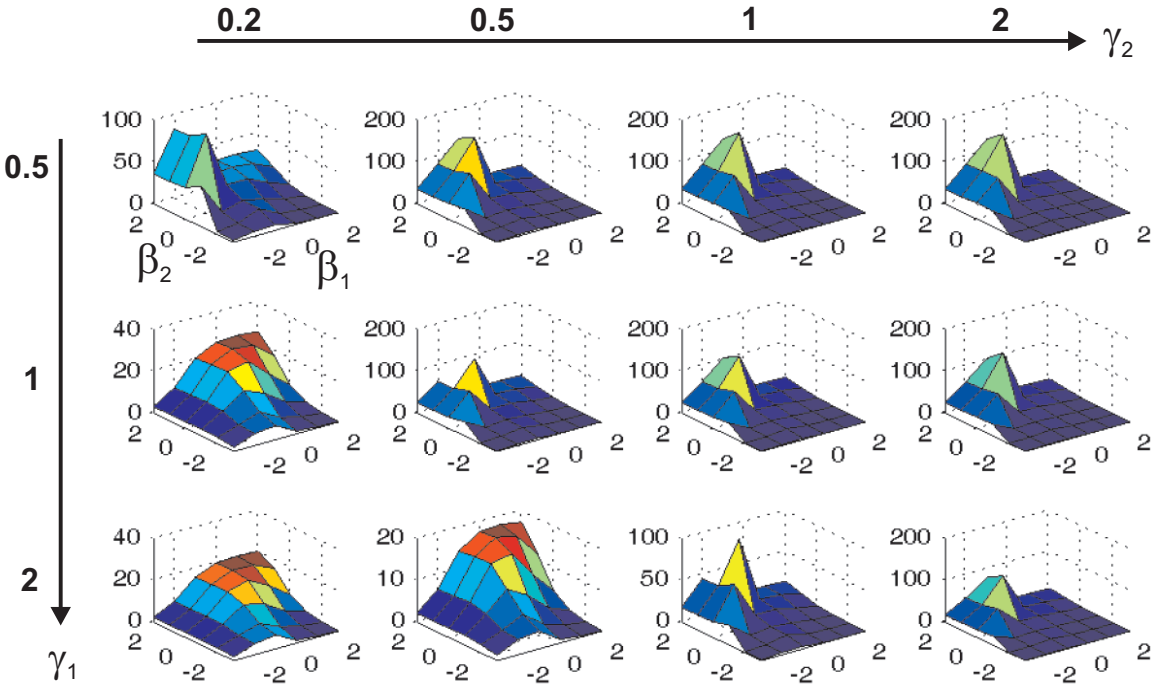

Figure 142: Fundamental frequency of regular beam with three sections

The lengths of all three sections are assumed to be identical, to limit the number of design parameters to a tractable number. The fundamental frequency is shown in Fig. 142 for various combinations of β_1, β_2, γ_1 and γ_2. This sensitivity study allows the identification of certain combinations of parameters that yield lower frequencies, without resorting to the extreme choices required in the previous paragraph.

For each of the sections, it is possible to use the equivalent mechanical properties of chiral lattices. A choice of geometric and material parameters can be determined which allows the equivalent bending stiffness to match the desired characteristics that drive the fundamental frequency down, as suggested by Fig. 142. Likewise, the mass distribution in each section of the chiral network can be adjusted to match the γ_1 and γ_2 values that yield lower frequencies. Once the properties of the structure have been selected, its fundamental frequency should be close to that predicted by the beam analysis, and the associated fundamental mode shape can be computed. Figure 143 schematically outlines the differences in ligament thickness needed to drive the fundamental frequency close to 1/rev. Figure 144 shows the mode shape associated with the fundamental frequency of 5 Hz. A flap-like behavior is observed, where most of the deformation is located in the last section. A second mode shape at 20.5 Hz is illustrated in Fig. 145, and similarly exhibits deformation patterns mainly towards the tip.

Despite improvements, it is questionable that such designs could withstand aerodynamic loads on the airfoil. Furthermore, the unsteady airflow generates damping which would impact the potential dynamic motion amplification. Additional aeroelastic effects are expected in the presence of unsteady aerodynamic conditions.

7.4.3 Aerodynamic model validation

In order to verify the implementation of Peters' airloads equation, Eq. (236), and the associated inflow state equation, Eqs. (238) and (239), a comparison was set up

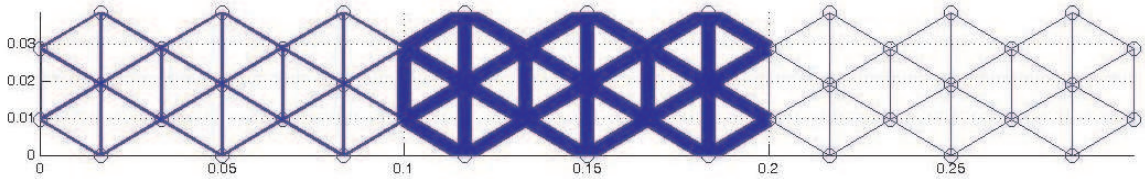

Figure 143: Undeformed configuration of chiral network with piecewise constant properties

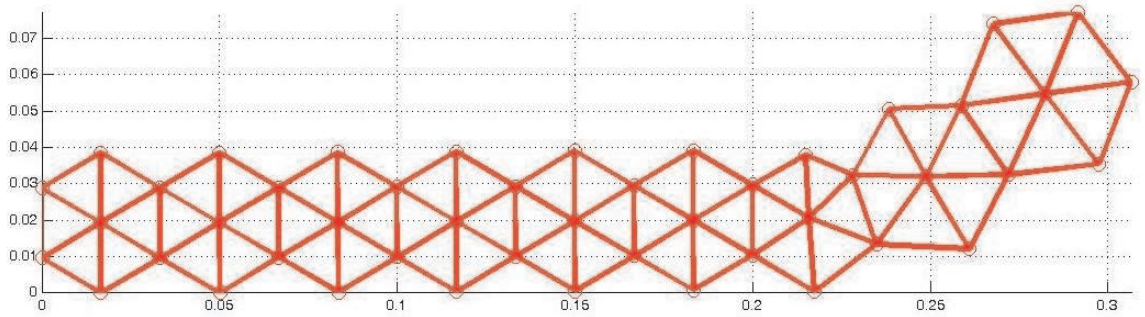

Figure 144: Fundamental mode shape at 5 Hz

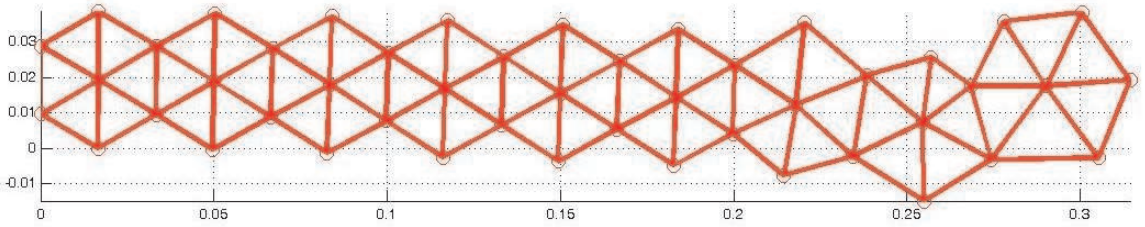

Figure 145: Second mode shape at 20.5 Hz

with Theodorsen's unsteady theory, which is detailed in Appendix C and was used in Chapter 4. A rigid thin airfoil with a flap was considered to undergo prescribed simple harmonic motion in the angle of attack α and the flap angle β, so as to satisfy the requirements of Theodorsen's theory. In the application of Peters' theory, there are two main parameters to choose, the number of Glauert terms and the number of inflow states. The airloads equations are derived for infinite Glauert expansions which are truncated for practical implementation. The finite-state representation of the wake requires that a number of states be selected; Ref. 67 suggests that 8 inflow states provide good results.

First, computations were carried out with a varying number of inflow states. For each case, the total lift P, the total moment about the quarter-chord M_α, and the moment of forces on the flap about the flap hinge M_β were determined, using both models, and with a large number of Glauert terms to identify the effects of each parameter independently. Fig. 146 shows the results obtained for the magnitude of the harmonically varying airload quantities as they change with the number of inflows. It is found that results are good up to about 10 states, and they degrade for more terms. Eight inflow states are indeed found to provide good correlation.

Next, the number of inflow states was fixed to be 8, and the number of included Glauert terms was increased instead, as shown in Fig. 147. Clearly, the results obtained with Peters' theory converge as the number of terms is increased. Overall, the correlation is good, with less than 1% difference in M_α and M_β, and 5% in P. It should be reminded that these results correspond to a particular choice for the number of inflow states. With a different choice, small variations are expected in the computed values, but for reasonable choices, the comparison holds satisfactorily.

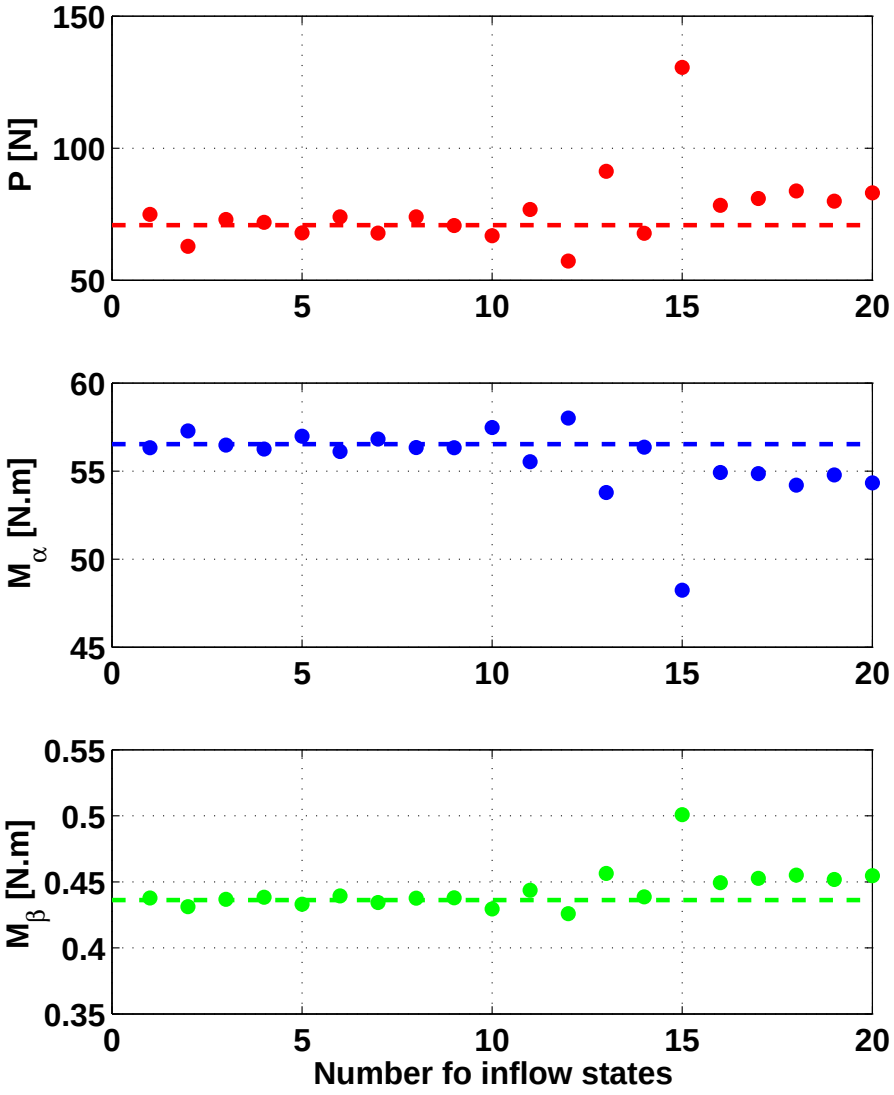

Figure 146: Amplitude of aerodynamic loads with increasing number of inflow states: Theodorsen's theory (−) and Peters' theory (•)

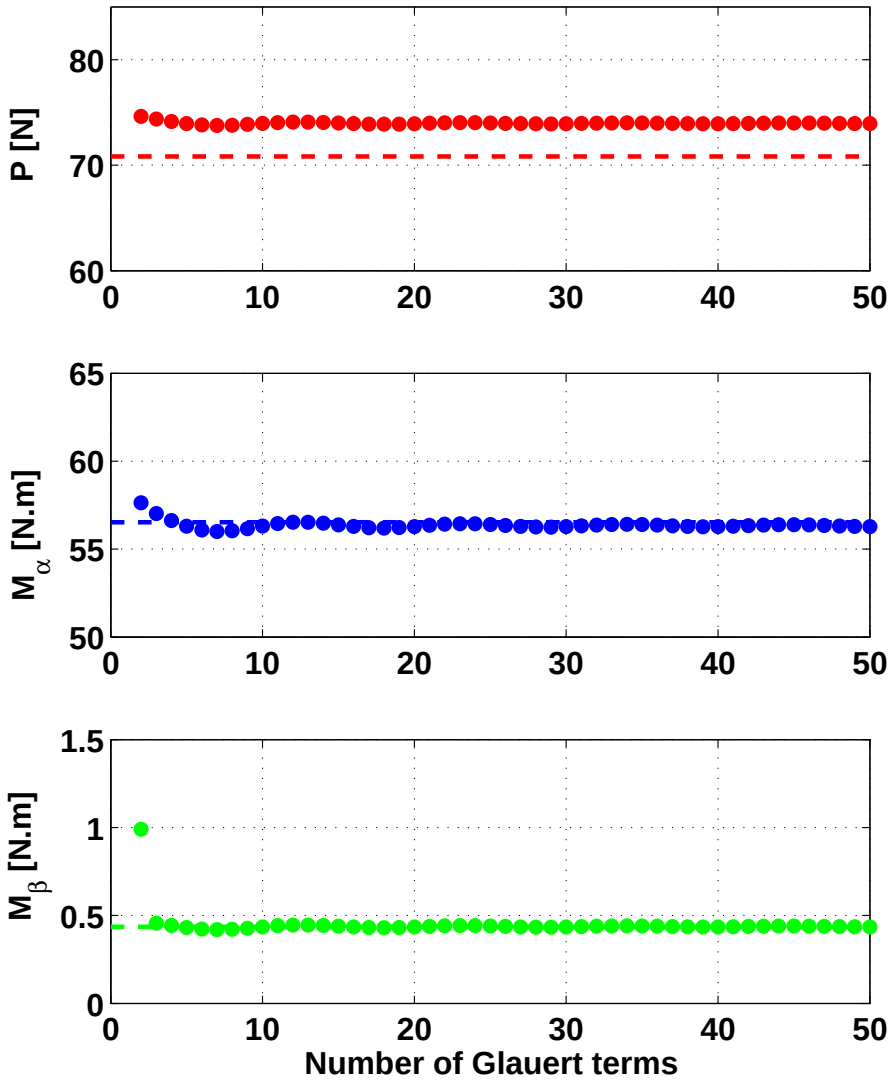

Figure 147: Amplitude of aerodynamic loads with increasing number of Glauert terms: Theodorsen's theory (−) and Peters' theory (•)

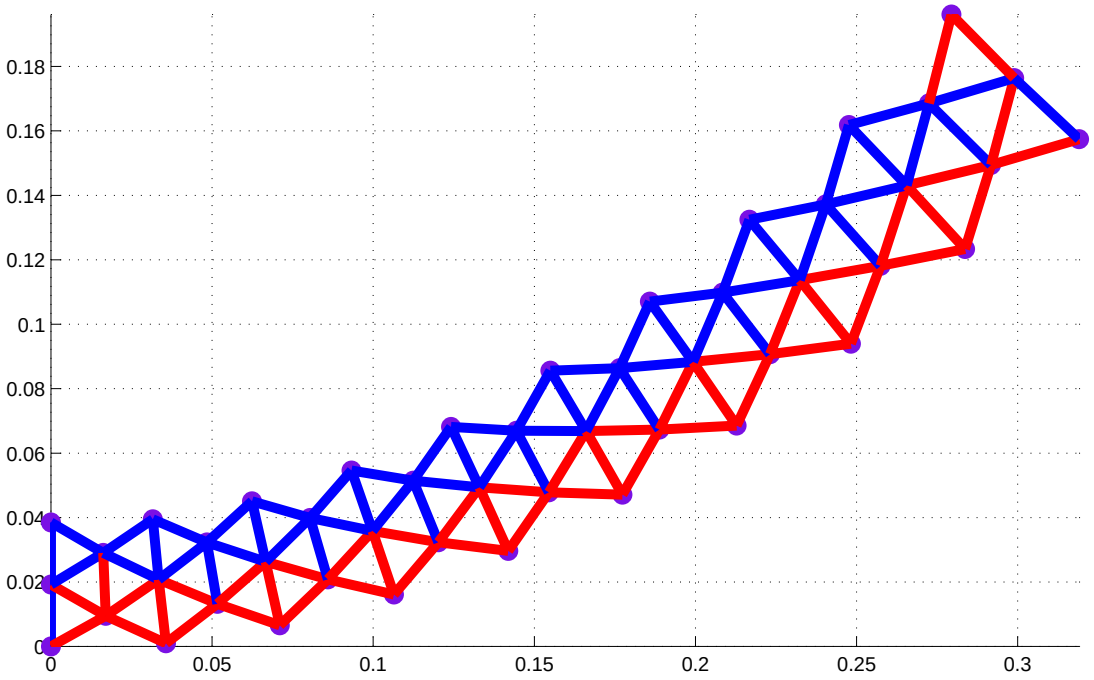

Figure 148: Deformed configuration of fully actuated chiral structure

7.4.4 Unsteady aeroelastic assessment

Finally, harmonic simulations were run in the presence of aerodynamic forces to investigate whether it is possible to improve the deflection amplitude of the chiral actuator considered before in the static case. Again, it was sized to roughly match the aft section of a UH-60 blade. At first, static runs were produced in which the voltages in each ligament were determined to maximize the output deflection at the tip. Based on previous studies, double bending was used for best results. In essence, if the voltage input to a particular ligament induces a positive tip displacement, it is kept as is; the sign of all other applied voltages are changed. By virtue of superposition, this ensures that the effects of all individual piezobenders add up. Hence, a fully actuated chiral structure is available for subsequent simulations. Figure 148 shows the deformed configuration of this structure. Ligaments indicated by identical colors have the same applied voltages; the two different colors correspond to opposite signs.

Harmonic simulations were then run in which the ligaments were actuated as

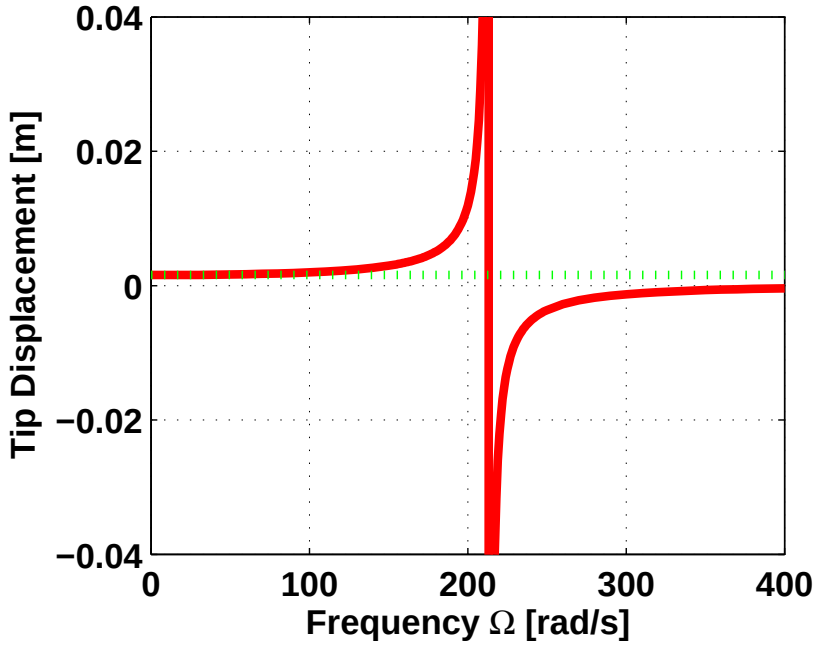

Figure 149: Tip deflection amplitude of fully actuated structure as a function of excitation frequency, without aerodynamics: static value (green, dotted) and harmonic amplitude (red, solid)

before, but with time-varying control input voltages. They were prescribed to follow harmonic variation with increasing frequency. First, the purely dynamic case was considered, without aerodynamic loading. Figure 149 shows the variation of the amplitude of motion as the excitation frequency is increased past the value of the fundamental frequency of the structure, at around 34 Hz. As one might expect, a resonance occurs at the fundamental frequency. Also as expected, for very low frequencies, the range of motion is essentially the same as in the static case, while at high frequencies, the deformation capability of the chiral actuator is essentially lost.

Finally, these results were refined by the addition of aerodynamic forces. The case of quasi-steady flow, in which certain sources of unsteadiness are neglected and the inflow parameter λ_0 is set to zero, is studied in Fig. 150. In quasi-steady flow, the motion of the airfoil is taken into account, including its dependence on time, while other sources of unsteadiness such as the shed vorticity at the trailing edge and

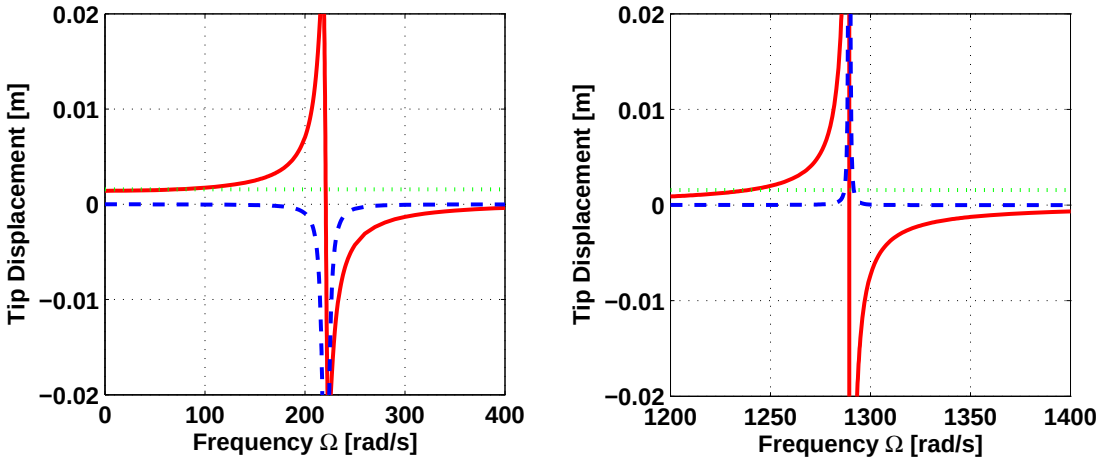

Figure 150: Tip deflection amplitude of fully actuated structure as a function of excitation frequency, with quasi-steady aerodynamics: static value (green, dotted), harmonic amplitude real part (red, solid) and imaginary part (blue, dashed)

additional effects due to the inertia of the air itself are not. The two plots correspond to the same set of results, but in different frequency ranges. The left plot contains the first frequency of the coupled aeroelastic system at about 35 Hz, while the right-hand side includes the second system frequency which is around 205 Hz. Amplification of the tip deflection is clearly possible at excitation frequencies close to the natural frequencies. The characteristics are found to be similar to the previous results, with the exception of the phase lag introduced by the aerodynamics, which is associated with the complex-valued amplitude, as well as the fact that aerodynamic damping from the airloads model limits the height of the resonance. The results in Fig. 151 are quite similar but include the additional influence of the inflow state dynamics. Even though the numbers may vary somewhat, the overall behavior remains qualitatively similar.

The outcome of these investigations seems to indicate that the concept could benefit greatly from dynamic actuation. However, this requires that the fundamental frequency of the chiral structure can be tailored to be close to the 1/rev rotor

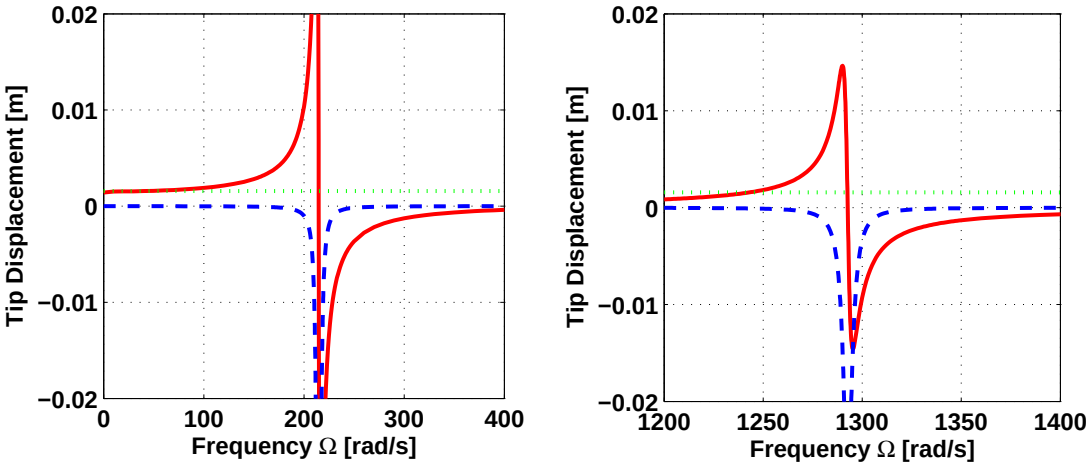

Figure 151: Tip deflection amplitude of fully actuated structure as a function of excitation frequency, with unsteady aerodynamics: static value (green, dotted), harmonic amplitude real part (red, solid) and imaginary part (blue, dashed)

frequency. This was not the case in these last simulations. Unfortunately, no satisfactory design was found in previous sections that would provide both low natural frequencies and sufficient stiffness to be able to withstand the external loading on the blade, in particular from the aerodynamic forces. The limited actuation capability of piezoelectric materials is not likely to provide enough reaction force to withstand such high forces. Nevertheless, further parametric studies could provide adequate performance for such a system.

7.5 Summary

In this chapter, a simplified analysis code was derived and implemented to perform static simulations of chiral structures under loading and piezoelectric actuation. The theory was presented in detail, and the assumptions clearly laid out. In particular, the circular nodes are assumed to be rigid, which was shown to be a good approximation. Moreover, specific forms of piezoelectric actuation were implemented, such as single and double bending actuation, axial actuation, and actuation varying along the length. This last situation is obtained with a linearly varying width electrode.

This analysis tool was validated, and used to investigate the benefits and drawbacks of an actuation scheme in which the widths and voltages in all ligaments are defined to replicate the curvatures observed in the passive case. It was found that such an approach does not improve on the much simpler double bending actuation scheme.

Next, this code was extended to include dynamic analysis capabilities, as well as an aerodynamic model. The dynamic equations are obtained with the approximation that circles and the half-ligaments attached to it constitute a rigid body as far as the inertial effects are concerned. The assumption was shown to still provide excellent results for the lowest modes of vibration; however, they degrade for higher mode numbers. The unsteady aerodynamic model is based on Peters' airloads theory for deformable airfoils, as well as Peters' inflow theory. Its implementation was also verified, by comparing the results obtained for a rigid wing with a flap to results computed using Theodorsen's theory. Finally, several studies attempted to improve the performance of chiral structures with piezoelectric actuators, but it was shown that a satisfactory design is difficult to attain with the current design constraints. However, further investigation of the parameter space could provide better results.

CHAPTER VIII

CONCLUDING REMARKS

8.1 Conclusions

8.1.1 Friction-based lead-lag dampers

Chapters 2 and 3 have focused on the analysis and performance evaluation of semi-active, Coulomb friction lead-lag dampers. Both adaptive and selective damping strategies were investigated. Simulations were run in both ground resonance and forward flight to assess the use of friction as an energy dissipation mechanism to control the ground resonance instability and provide adequate lead-lag damping levels. Through identification of modal decay rates, it was demonstrated that the energy dissipation capacity of the friction damper increases with increasing normal force levels. Furthermore, the concept is able to match or exceed the damping levels of the presently installed hydraulic dampers on the UH-60 aircraft. The ability to adapt the damping level of the device also enables the concept of damping on demand. For flight conditions requiring lower energy dissipation levels, it becomes possible to lower the damping forces in the damper, as well as those applied to the blade and hub, resulting in lower stress levels and potential weight savings.

The concept of selective damping was investigated next. Whereas many dampers are designed to absorb as much energy as possible, the purpose of rotorcraft lead-lag dampers is to control the rotor regressive lag mode. The concept of selective damping is to target energy dissipation to the regressive lag mode while minimally affecting the other modes. Selective algorithms were proposed and implemented within a simplified analytical framework. This exploratory study shows that selectivity can enhance the performance of lead-lag dampers. In fact, when using selectivity, it is

possible to stabilize a system that would be unstable when using a passive damper of identical dashpot constant. But while the potential of selective damping has been demonstrated, this concept faces numerous drawbacks that might prevent its practical implementation. Indeed, selectivity requires increased actuation and controller complexity; furthermore, fail safe operation considerations might drive the design to a configuration where selectivity provides little advantage over less complex designs. Clearly, further studies would be required to obtain fully satisfactory designs.

8.1.2 3D warping concept for rotor blade active twist

Chapters 4 and 5 have focused on the design of torsionally compliant open-section rotor blades actuated through out-of-plane warping. This concept enjoys great design flexibility. The study of an initial design led to some general design guidelines. Such a design was shown to be impractical due to the large aerodynamic moment. Since warping actuation is not inherent to a particular shape of the airfoil, a full-blade warping concept was proposed instead. This concept is based on the premise that a small relative axial displacement can induce large blade tip rotations. Vlasov beam theory was shown to properly model the system's behavior if proper constraints were included. The performance of distributed actuation was far superior to that of concentrated actuation, but a more practical approach involves several small actuators spread out along a potentially stiffened line of action. Dynamic effects such as resonances can improve the performance of the design. The sensitivity of the concept to external loads, in particular aerodynamic loads, was shown to be a primary concern for the design of such a system.

SECTIONBUILDER and DYMORE are finite-element-based codes for the analysis of arbitrary beam cross-sections and the analysis of flexible multibody dynamic systems, respectively. They were modified to provide additional capabilities for the analysis of warping-actuated beams. SECTIONBUILDER was extended to provide

additional sectional properties that are fundamental for the modeling of beams undergoing both twisting and warping. The theoretical foundation for these modifications was presented and its implementation was validated against both analytical and finite element results. DYMORE was modified to include the additional warping degree-of-freedom in multibody simulations. Details were provided on the derivation of the proper equations of motion, and interesting aspects of the numerical implementation were highlighted. The results for static cases obtained with DYMORE correlate extremely well with analytical solutions using the coefficients computed by SECTIONBUILDER, while the results for dynamic cases were found to be consistent with those from the static cases.

8.1.3 Active chiral networks for variable camber rotor blades

In Chapters 6 and 7, a novel concept for continuous camber deformation of rotor blades was proposed based on a particular type of cellular structure. Embedded actuation using piezoelectric materials can be distributed throughout the structure to deform it. The main focus has been on active chiral "beams" and their behavior. Static analyses of the actuation characteristics of conformable chiral structures were undertaken. Passive cases were studied to investigate the effects of the chiral lattice topology, and to determine the deformation mechanisms at work. In particular, symmetric and periodic deformation patterns could simplify the analysis. The response of a chiral structure can also be represented by beam equations with equivalent mechanical properties for the cellular designs. Next, simple actuation strategies were considered; those based on inducing curvature in the ligaments worked much better than those based on axial deformations. Active configurations were then considered, and several configurations were studied for their output deflections. Finally, the ability of active chiral networks to react typical rotorcraft airloads was investigated. The effects of chiral geometry properties, number of cells, and piezoelectric strip geometry

on the actuation capability were determined. It was shown that in a static environment, within specific ranges of given parameters, the piezo-benders do not provide the authority needed for a successful concept.

In order to eliminate certain limitations inherent to the analysis of the concept in ANSYS, a simplified code was implemented based on exact beam solutions for a single ligament. A process similar to that of the Finite Element Method was used to study the behavior of chiral structures. This tool provides more flexibility to model more complicated forms of piezoelectric actuation, at a lower computational cost. First, the theory was presented for static analyses of passive and active chiral networks. Its implementation allowed the investigation of a more refined actuation scheme. Although it was possible to approximately replicate the passive behavior, this strategy proved inefficient at generating enough deflection under the constraints imposed by the use of piezoelectric benders. Next, the code was extended to include the dynamic behavior of chiral networks in unsteady aerodynamic environments. The theory was presented and the implementation validated. Simulations showed the possibilities offered by tailoring the geometric and material properties of the chiral structure, as well as the limitations of using chiral networks and piezoelectric actuation. However, the paremeter space search was not exhausted and further improvement could be obtained by considering additional combinations of the design variables.

8.2 Recommendations for future work

The topic of adaptive friction lead-lag dampers would benefit from extended simulations. Their performance was mainly quantified in ground resonance and forward flight. The performance in other flight regimes could also be investigated to determine their behavior in all possible situations. But the most potential for improvement lies in the design of selective control laws for friction dampers. The current work is limited to a simple analytical model of a helicopter in ground resonance. Clearly, the

implementation of more realistic rotorcraft models in several flight conditions would be helpful in determining additional constraints for the control law design and to identify potential difficulties for practical implementation. While the proposed selective control law was shown to provide improved performance, it is still an imperfect strategy which can benefit from improvements to the regressive component identification, and possibly improvements to the selective strategy itself as well.

Warping-actuated variable-twist blades provide a fairly simple means of morphing a rotor blade while avoiding the mechanical complexity of some other methods. The provided design guidelines offer some insight, but should go into more detail for a true design beyond the preliminary stages. In particular, detailed plans for the actuation system and its integration in the blade's structure are required. More realistic dynamic rotorcraft models could be used, in more accurate aerodynamic environments. The analysis tools that were implemented could be leveraged to this effect. Finally, experimental investigations could validate the concept. In particular, practical issues could arise that are not considered in inevitably simplified numerical models.

Finally, chiral lattice networks with embedded piezoelectric benders were considered as another possible candidate to achieve controllable morphing of rotor blades. As before, since this preliminary design analysis was conceptual in nature, more detailed simulations could shed a light on practical implementation difficulties, but may also provide insight into a broader range of possible designs. In particular, incorporating these ideas in a multibody dynamics code such as DYMORE would provide an even clearer understanding of the particular obstacles and opportunities associated with them in rotorcraft applications. Experimental work would allow the validation of these computational tools. Nevertheless, this promising type of active compliant system has already been shown to enjoy great design flexibility. After exploring several options however, none were found to be fully satisfactory. Clearly, further work is

needed for a viable solution; the parameter space search should be extended. A major area of possible improvement is the choice of actuation. Indeed, while piezoelectric materials may not provide the best match to fulfill the requirements, other smart materials may have the needed capabilities. The inclusion of specifically tailored composite materials for the ligaments provides another possible area of improvement. Finally, other applications of chiral structures may be considered, such as fixed wing aircraft, UAVs and HALE aircraft.

APPENDIX A

GROUND RESONANCE EQUATIONS

In this appendix, the derivation of the ground resonance equations of motion of section 3.2.1 is summarized. The notations used are those from that section, and the derivation is an extension of that presented in Refs. 1, 32.

The coordinates of an arbitrary point P_i on the i^{th} blade are

$$x_i = q_x + e\cos\psi_i + r_i\cos\beta_i\cos(\psi_i + \zeta_i), \tag{287a}$$

$$y_i = q_y + e\sin\psi_i + r_i\cos\beta_i\sin(\psi_i + \zeta_i), \tag{287b}$$

$$z_i = r_i\sin\beta_i, \tag{287c}$$

where r_i is the radial position of point P_i on the blade. After differentiation in time, denoted by $\dot{()}$, its velocity is

$$\dot{x}_i = \dot{q}_x - e\Omega\sin\psi_i - r_i\dot{\beta}_i\sin\beta_i\cos(\psi_i + \zeta_i) - r_i(\Omega + \dot{\zeta}_i)\cos\beta_i\sin(\psi_i + \zeta_i), \tag{288a}$$

$$\dot{y}_i = \dot{q}_y + e\Omega\cos\psi_i - r_i\dot{\beta}_i\sin\beta_i\sin(\psi_i + \zeta_i) + r_i(\Omega + \dot{\zeta}_i)\cos\beta_i\cos(\psi_i + \zeta_i), \tag{288b}$$

$$\dot{z}_i = r_i\dot{\beta}_i\cos\beta_i. \tag{288c}$$

The total kinetic energy of the system includes that of the hub, K_{hub}, and that of each of the blades, $K_{\text{blade},j}$. The kinetic energy of the hub is simply

$$K_{\text{hub}} = \frac{1}{2}M_x\,\dot{q}_x^2 + \frac{1}{2}M_y\,\dot{q}_y^2, \tag{289}$$

while that of the j^{th} blade, which is modeled as a thin rod, is

$$K_{\text{blade},j} = \frac{1}{2}\int_0^L \left(\dot{x}_j^2 + \dot{y}_j^2 + \dot{z}_j^2\right)\lambda(r_j)\,\mathrm{d}r_j, \tag{290}$$

where $\lambda(r)$ is the mass per unit length of a blade. Upon substitution, one finds

$$\begin{aligned} K_{\text{blade},j} = &\frac{1}{2}m\dot{q}_x^2 + \frac{1}{2}m\dot{q}_y^2 + \frac{1}{2}me^2\Omega^2 \\ &- me\Omega\dot{q}_x \sin\psi_j + me\Omega\dot{q}_y \cos\psi_j \\ &- Se\Omega\dot{\beta}_j \sin\beta_j \sin\zeta_j \\ &+ Se\Omega\left(\Omega + \dot{\zeta}_j\right)\cos\beta_j \cos\zeta_j \\ &- S\dot{\beta}_j\dot{q}_x \sin\beta_j \cos(\psi_j + \zeta_j) \\ &- S\dot{\beta}_j\dot{q}_y \sin\beta_j \sin(\psi_j + \zeta_j) \\ &- S\left(\Omega + \dot{\zeta}_j\right)\dot{q}_x \cos\beta_j \sin(\psi_j + \zeta_j) \\ &+ S\left(\Omega + \dot{\zeta}_j\right)\dot{q}_y \cos\beta_j \cos(\psi_j + \zeta_j) \\ &+ \frac{1}{2}I\dot{\beta}_j^2 + \frac{1}{2}I\left(\Omega + \dot{\zeta}_j\right)^2 \cos^2\beta_j, \end{aligned} \tag{291}$$

where m, S and I are defined in section 3.2.1. The total kinetic energy is then

$$K = K_{\text{hub}} + \sum_{j=1}^{N} K_{\text{blade},j}. \tag{292}$$

After substituting the expressions for K_{hub} and $K_{\text{blade},j}$, the final expression of the kinetic energy can be simplified somewhat by applying the fact that, for all n (for example, see Ref. 51)

$$\sum_{j=1}^{N} \cos(n\psi_j) = N f_n \cos(n\Psi), \tag{293a}$$

$$\sum_{j=1}^{N} \sin(n\psi_j) = N f_n \sin(n\Psi), \tag{293b}$$

where the quantity f_n is defined by

$$f_n = \begin{cases} 1 & \text{if } n \text{ is a multiple of } N \\ 0 & \text{otherwise} \end{cases} \tag{294}$$

Assuming there are two blades or more on the rotor, 1 cannot be a multiple of N and

$$\sum_{j=1}^{N} \cos\psi_j = 0, \tag{295a}$$

$$\sum_{j=1}^{N} \sin\psi_j = 0. \tag{295b}$$

The total kinetic energy can finally be written as

$$\begin{aligned} K = {} & \frac{1}{2}\left(M_x + Nm\right)\dot{q}_x^2 + \frac{1}{2}\left(M_y + Nm\right)\dot{q}_y^2 + \frac{1}{2}Nme^2\Omega^2 \\ & + Se\Omega\sum_{j=1}^{N}\left(\left(\Omega + \dot{\zeta}_j\right)\cos\beta_j\cos\zeta_j - \dot{\beta}_j\sin\beta_j\sin\zeta_j\right) \\ & - S\dot{q}_x\sum_{j=1}^{N}\left(\left(\Omega + \dot{\zeta}_j\right)\cos\beta_j\sin(\psi_j + \zeta_j) + \dot{\beta}_j\sin\beta_j\cos(\psi_j + \zeta_j)\right) \\ & + S\dot{q}_y\sum_{j=1}^{N}\left(\left(\Omega + \dot{\zeta}_j\right)\cos\beta_j\cos(\psi_j + \zeta_j) - \dot{\beta}_j\sin\beta_j\sin(\psi_j + \zeta_j)\right) \\ & + \frac{1}{2}I\sum_{j=1}^{N}\left(\dot{\beta}_j^2 + \left(\Omega + \dot{\zeta}_j\right)^2\cos^2\beta_j\right). \end{aligned} \tag{296}$$

The total potential energy contains two terms from the equivalent springs in the x- and y-directions in the fuselage, N terms from the flap hinge rotational springs, and N terms from the lag hinge rotational springs

$$P = \frac{1}{2}k_x\,q_x^2 + \frac{1}{2}k_y\,q_y^2 + \sum_{j=1}^{N}\frac{1}{2}k_\beta\,\beta_j^2 + \sum_{j=1}^{N}\frac{1}{2}k_\zeta\,\zeta_j^2. \tag{297}$$

The total virtual work has two terms which stem from the equivalent viscous damper in the x- and y-directions in the fuselage and N terms coming from the lead-lag damper built into the lag hinge of each blade

$$\overline{\delta W} = -c_x\dot{q}_x\,\delta q_x - c_y\dot{q}_y\,\delta q_y + \sum_{j=1}^{N} Q_{\text{damper},j}\,\delta\zeta_j, \tag{298}$$

where the generalized force terms $Q_{\text{damper},j}$ depend on the damping mechanism chosen in the design of the lead-lag dampers

$$\text{Viscous damping:} \quad Q_{\text{damper},j} = -C(t)\,\dot{\zeta}_j, \tag{299a}$$

$$\text{Coulomb friction:} \quad Q_{\text{damper},j} = -\mu\,N(t)\,\text{sign}(\dot{\zeta}_j). \tag{299b}$$

Semi-active damping can be implemented through the time-dependent viscous damping coefficient $C(t)$ or the normal force $N(t)$. A control law using the state of the system would have to be defined.

The Lagrangian is defined as $L = K - P$ and Lagrange's equations can be applied for all $i = 1, \ldots, N$

$$\frac{\mathrm{d}}{\mathrm{d}t}\left(\frac{\partial L}{\partial \dot{q}_x}\right) - \frac{\partial L}{\partial q_x} = Q_{c,x}, \tag{300a}$$

$$\frac{\mathrm{d}}{\mathrm{d}t}\left(\frac{\partial L}{\partial \dot{q}_y}\right) - \frac{\partial L}{\partial q_y} = Q_{c,y}, \tag{300b}$$

$$\frac{\mathrm{d}}{\mathrm{d}t}\left(\frac{\partial L}{\partial \dot{\beta}_i}\right) - \frac{\partial L}{\partial \beta_i} = 0, \tag{300c}$$

$$\frac{\mathrm{d}}{\mathrm{d}t}\left(\frac{\partial L}{\partial \dot{\zeta}_i}\right) - \frac{\partial L}{\partial \zeta_i} = Q_{\mathrm{damper},i}. \tag{300d}$$

Note that if instead, β_i is assumed to be prescribed, all equations remain valid, and the N equations associated with β_i are simply dropped.

The flap angles β_i will be prescribed here. Hence, the remaining equations become

$$(M_x + Nm)\ddot{q}_x + c_x\dot{q}_x + k_x q_x + S\sum_{j=1}^{N}\frac{\mathrm{d}^2}{\mathrm{d}t^2}\left[\cos\beta_j\cos(\psi_j + \zeta_j)\right] = 0, \tag{301a}$$

$$(M_y + Nm)\ddot{q}_y + c_y\dot{q}_y + k_y q_y + S\sum_{j=1}^{N}\frac{\mathrm{d}^2}{\mathrm{d}t^2}\left[\cos\beta_j\sin(\psi_j + \zeta_j)\right] = 0, \tag{301b}$$

$$\begin{aligned} I\ddot{\zeta}_i\cos^2\beta_i - S\ddot{q}_x\cos\beta_i\sin(\psi_i + \zeta_i) + S\ddot{q}_y\cos\beta_i\cos(\psi_i + \zeta_i) \\ + Se\Omega^2\cos\beta_i\sin\zeta_i - I(\Omega + \dot{\zeta}_i)\dot{\beta}_i\sin 2\beta_i + k_\zeta\zeta_i = Q_{\mathrm{damper},i}. \end{aligned} \tag{301c}$$

Next, a number of assumptions are made. ζ_i is considered to be a small angle, so that $\cos\zeta_i \approx 1$ and $\sin\zeta_i \approx \zeta_i$. The flap angle is written as $\beta_i = \beta_0 + \beta_{1,i}$, and $\beta_{1,i}$ is regarded as a small angle as well. All higher-order terms in q_x, q_y, ζ_i and $\beta_{1,i}$ and their derivatives are neglected. And finally, the effect of the springs of stiffness k_ζ is neglected. With these assumptions, the equations become

$$\bar{q}_x^{**} + \bar{c}_x\bar{q}_x^{*} + \bar{\omega}_x^2\bar{q}_x - \bar{S}_x C_0\sum_{i=1}^{N}(\zeta_i\sin\psi_i)^{**} = \bar{S}_x S_0\sum_{i=1}^{N}(\beta_{1,i}\cos\psi_i)^{**}, \tag{302}$$

$$\bar{q}_y^{**} + \bar{c}_y \bar{q}_y^{*} + \bar{\omega}_y^2 \bar{q}_y + \bar{S}_y C_0 \sum_{i=1}^{N} (\zeta_i \cos\psi_i)^{**} = \bar{S}_y S_0 \sum_{i=1}^{N} (\beta_{1,i} \sin\psi_i)^{**}, \tag{303}$$

and for $i = 1, \ldots, N$

$$C_0^2 \zeta_i^{**} + \bar{\nu}_\zeta^2 C_0 \zeta_i - \bar{S} C_0 \bar{q}_x^{**} \sin\psi_i + \bar{S} C_0 \bar{q}_y^{**} \cos\psi_i = 2 S_0 C_0 \beta_{1,i}^{*} + \bar{Q}_i, \tag{304}$$

where $C_0 = \cos\beta_0$ and $S_0 = \sin\beta_0$, and all nondimensionalized quantities were defined in section 3.2.1. If, to simplify the equations further, β_0 is assumed to be a small angle as well, one finally obtains Eqs. (6), (7) and (8). Setting $C_0 \approx 1$ in the equations does not significantly impact the study of selective damping.

APPENDIX B

SECTIONAL PROPERTIES FOR OUT-OF-PLANE WARPING ANALYSIS

In this appendix, the warping functions and warping-related sectional properties, both with unconstrained and constrained center of rotation, will be summarized for the open triangular section. This type of cross-section is relevant for the analysis of the original warping-actuated rotor blade design in Chapter 4. The differences between the two sets of results will be highlighted. Figure 152 shows the geometry of this particular thin-walled cross-section. $\bar{\imath}_2$ and $\bar{\imath}_3$ are principal axes of bending due to the symmetry of the section. O represents the centroid of the section, at a distance d to the right of the cut

$$d = \frac{1}{1+\sin\alpha}\frac{b}{2}, \tag{305}$$

and K the shear center, located at a distance e to the right of the tip of the triangle (which corresponds to the trailing edge)

$$e = \frac{\sin\alpha}{1+\sin\alpha}\frac{b}{2}. \tag{306}$$

Finally, R will be the constrained point of rotation at the cut for the second set of results. Note that the torsional stiffness H_{11} is identical in both cases, and is given by

$$H_{11} = \frac{1}{3}Gt^3h\,\frac{1+\sin\alpha}{\sin\alpha}. \tag{307}$$

B.1 Open triangular section with unconstrained center of rotation

When the section is able to rotate freely, the center of twist, whose coordinates are computed with Eq. (24), coincides with the shear center K, and the warping function

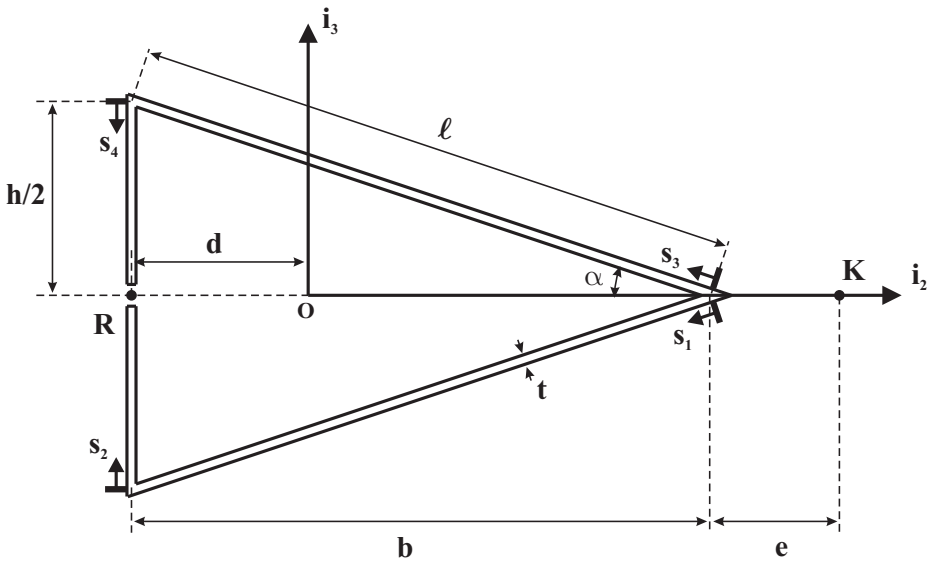

Figure 152: Thin-walled open triangular section

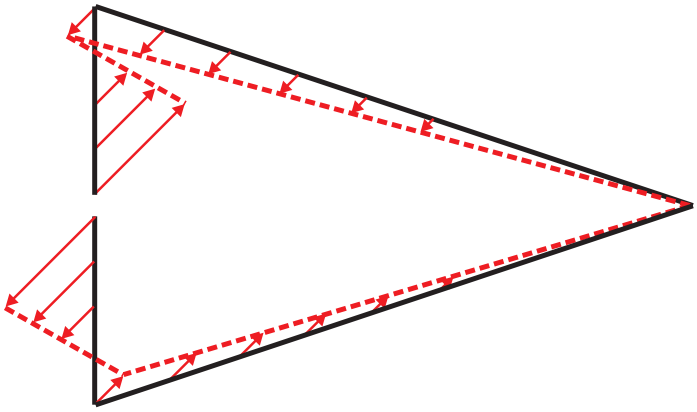

Figure 153: Classical warping function for open triangular section

can be obtained using Eq. (23)

$$\Psi_1(s_1) = -\frac{\sin\alpha}{1+\sin\alpha}\frac{bh}{4}\frac{s_1}{l}, \tag{308a}$$

$$\Psi_2(s_2) = -\frac{\sin\alpha}{1+\sin\alpha}\frac{bh}{4}\left[1-\frac{2+3\sin\alpha}{\sin\alpha}\frac{2s_2}{h}\right], \tag{308b}$$

$$\Psi_3(s_3) = -\Psi_1(s_3), \tag{308c}$$

$$\Psi_4(s_4) = -\Psi_2(s_4), \tag{308d}$$

where the curvilinear coordinate s is defined in Fig. 152. Figure 153 illustrates this function along the entire contour $\mathcal{C}$.

Based on this expression, H_{11w} and I_p can be computed according to Eqs. (40) and (41)

$$H_{11w} = \frac{1}{48}\frac{4+3\sin\alpha}{1+\sin\alpha}\,Etb^2h^3, \tag{309}$$

$$I_p = \frac{1}{4}\frac{\sin^2\alpha+8\sin\alpha+4}{1+\sin\alpha}\,Gthb^2, \tag{310}$$

and finally the parameter k is obtained by applying Eq. (64c)

$$k_w^2 = 16\frac{G}{E}\left(\frac{t}{b}\right)^2\left(\frac{L}{h}\right)^2\frac{(1+\sin\alpha)^2}{\sin\alpha(4+3\sin\alpha)}, \tag{311}$$

$$k_p^2 = 3\frac{(\sin^2\alpha+8\sin\alpha+4)\sin\alpha}{3(\sin^2\alpha+8\sin\alpha+4)\sin\alpha+4(t/b)^2(1+\sin\alpha)^2}, \tag{312}$$

$$k^2 = k_w^2\;k_p^2. \tag{313}$$

B.2 Open triangular section with constrained center of rotation at the cut

In this case, the coordinates of the center of twist R are given and do not coincide with those of the shear center K. The warping function is still obtained with Eq. (23), but the integration constant is now determined by Eq. (29)

$$\Psi_1(s_1) = \frac{bh}{2}\frac{s_1}{l}, \tag{314a}$$

$$\Psi_2(s_2) = \frac{bh}{2}, \tag{314b}$$

$$\Psi_3(s_3) = -\Psi_1(s_3), \tag{314c}$$

$$\Psi_4(s_4) = -\Psi_2(s_4). \tag{314d}$$

Figure 154 illustrates this function along the entire contour $\mathcal{C}$. Clearly, it is quite different from the classical function shown in Fig. 153. For example, the two functions have opposite signs on most of the contour. Furthermore, the warping function is constant on the vertical part for the modified theory, while it is linear and changes signs on those parts in the classical case.

Again, H_{11w} and I_p may be determined based on this warping function

$$H_{11w} = \frac{1}{12}\frac{1+3\sin\alpha}{\sin\alpha}\,Etb^2h^3, \tag{315}$$

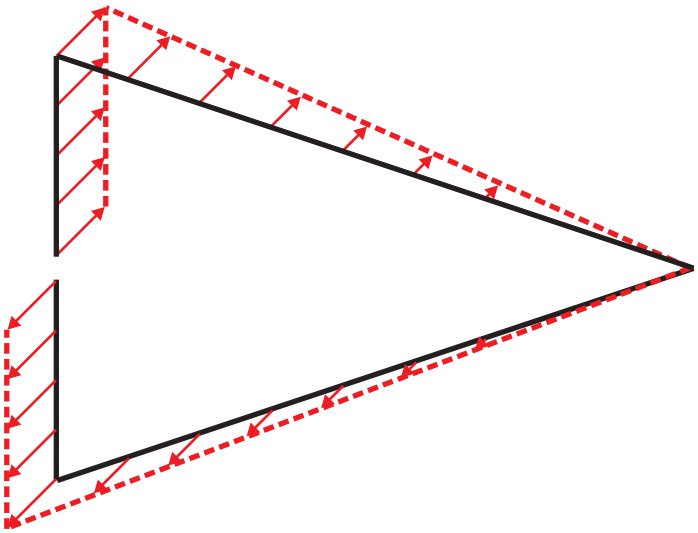

Figure 154: Modified warping function for open triangular section with constrained center of rotation

$$I_p = Gthb^2 \sin\alpha, \tag{316}$$

and k is then found as

$$k_w^2 = 4\frac{G}{E}\left(\frac{L}{h}\right)^2\left(\frac{t}{b}\right)^2\frac{1+\sin\alpha}{1+3\sin\alpha}, \tag{317}$$

$$k_p^2 = \frac{\sin^2\alpha}{\sin^2\alpha + \frac{1}{3}(t/b)^2(1+\sin\alpha)}, \tag{318}$$

$$k^2 = 4\frac{G}{E}\left(\frac{L}{h}\right)^2\left(\frac{t}{b}\right)^2\frac{1+\sin\alpha}{1+3\sin\alpha}\frac{3\sin^2\alpha}{3\sin^2\alpha + (t/b)^2(1+\sin\alpha)}. \tag{319}$$

Clearly, they have different values compared to the preceding case. This demonstrates the importance of using the right coefficients in a given analysis.

APPENDIX C

UNSTEADY AERODYNAMIC THEORIES

C.1 Theodorsen's unsteady aerodynamic theory

Reference 84 provides sectional aerodynamic load expressions for a thin airfoil of chord $2b$ in simple harmonic motion, with a flap whose hinge is located at a distance $c\,b$ from the center of the airfoil toward the trailing edge. The airfoil, which extends from the leading edge of coordinate $-b$ to the trailing adge at $+b$, rotates about a point a distance $a\,b$ away from the center toward the trailing edge. Clearly, $-1 \leq a \leq +1$ and $-1 \leq c \leq +1$. The degrees-of-freedom under consideration are: the vertical displacement h of the axis of rotation, measured positive downward with respect to a fixed reference frame; the angle of attack α of the airfoil, measured positive in the clockwise direction from the horizontal; and the angle β of the aileron with respect to the undeflected position relative to the airfoil, defined to be positive in the clockwise direction as well. The air of density ρ has a wind velocity v along the horizontal.

The total (downward) lift on the entire airfoil, P, the (positive clockwise) moment of aerodynamic forces on the flap around the hinge, M_β, and the moment on the entire

airfoil around the axis of rotation, M_α, are

$$\begin{aligned}
P &= -\rho b^2\left(v\pi\dot{\alpha}+\pi\ddot{h}-\pi ba\ddot{\alpha}-vT_4\dot{\beta}-T_1b\ddot{\beta}\right)\\
&\quad -2\pi\rho vbC\left(v\alpha+\dot{h}+b\left(\frac{1}{2}-a\right)\dot{\alpha}+\frac{1}{\pi}T_{10}v\beta+b\frac{1}{2\pi}T_{11}\dot{\beta}\right), \qquad (320a)\\
M_\beta &= -\rho b^2\left[\left\{-2T_9-T_1+T_4(a-\frac{1}{2})\right\}vb\dot{\alpha}+2T_{13}b^2\ddot{\alpha}\right.\\
&\quad \left.+\frac{1}{\pi}v^2\beta\left(T_5-T_4T_{10}\right)-\frac{1}{2\pi}vb\dot{\beta}T_4T_{11}-\frac{1}{\pi}T_3b^2\ddot{\beta}-T_1b\ddot{h}\right]\\
&\quad -\rho b^2vT_{12}C\left\{v\alpha+\dot{h}+b\left(\frac{1}{2}-a\right)\dot{\alpha}+\frac{1}{\pi}T_{10}v\beta+b\frac{1}{2\pi}T_{11}\dot{\beta}\right\}, \qquad (320b)\\
M_\alpha &= -\rho b^2\left[\pi\left(\frac{1}{2}-a\right)vb\dot{\alpha}+\pi b^2\left(\frac{1}{8}+a^2\right)\ddot{\alpha}+\left(T_4+T_{10}\right)v^2\beta\right.\\
&\quad \left.+\left(T_1-T_8-\left(c-a\right)T_4+\frac{T_{11}}{2}\right)vb\dot{\beta}-\left(T_7+\left(c-a\right)T_1\right)b^2\ddot{\beta}-a\pi b\ddot{h}\right]\\
&\quad +2\rho vb^2\pi\left(a+\frac{1}{2}\right)C\left\{v\alpha+\dot{h}+b\left(\frac{1}{2}-a\right)\dot{\alpha}+\frac{T_{10}}{\pi}v\beta+b\frac{T_{11}}{2\pi}\dot{\beta}\right\}. \qquad (320c)
\end{aligned}$$

The Theodorsen function $C = C(k)$, where $k = \frac{b\omega}{v}$ and v is the constant velocity of the fluid relative to the airfoil at infinity, can be expressed in terms of Hankel functions of the second kind as

$$C(k) = F(k) + iG(k) = \frac{H_1^{(2)}(k)}{H_1^{(2)}(k) + iH_0^{(2)}(k)}, \qquad (321)$$

and the constants appearing in these equations are

$$T_1 = -\frac{1}{3}\sigma\left(2+c^2\right)+c\tau, \tag{322a}$$

$$T_2 = c\sigma^2-\sigma\left(1+c^2\right)\tau+c\tau^2, \tag{322b}$$

$$T_3 = -\left(\frac{1}{8}+c^2\right)\tau^2+\frac{1}{4}c\sigma\tau\left(7+2c^2\right)-\frac{1}{8}\sigma^2\left(5c^2+4\right), \tag{322c}$$

$$T_4 = -\tau+c\sigma, \tag{322d}$$

$$T_5 = -\sigma^2-\tau^2+2c\sigma\tau, \tag{322e}$$

$$T_6 = T_2, \tag{322f}$$

$$T_7 = -\left(\frac{1}{8}+c^2\right)\tau+\frac{1}{8}c\sigma\left(7+2c^2\right), \tag{322g}$$

$$T_8 = -\frac{1}{3}\sigma\left(2c^2+1\right)+c\tau, \tag{322h}$$

$$T_9 = \frac{1}{2}\left(\frac{1}{3}\sigma^3+aT_4\right), \tag{322i}$$

$$T_{10} = \sigma+\tau, \tag{322j}$$

$$T_{11} = \tau\left(1-2c\right)+\sigma\left(2-c\right), \tag{322k}$$

$$T_{12} = \sigma\left(2+c\right)-\tau\left(2c+1\right), \tag{322l}$$

$$T_{13} = \frac{1}{2}\left(-T_7-\left(c-a\right)T_1\right), \tag{322m}$$

$$T_{14} = \frac{1}{16}+\frac{1}{2}ac, \tag{322n}$$

where $\sigma=\sqrt{1-c^2}$ and $\tau=\cos^{-1}(c)$.

If there is no flap, one may set $c=1$, so that $\sigma=\tau=0$ and

$$T_1=T_2=T_3=T_4=T_5=T_6=T_7=T_8=T_9=T_{10}=T_{11}=T_{12}=T_{13}=0. \tag{323}$$

The only non-vanishing constant in this case is

$$T_{14} = \frac{1}{2}\left(\frac{1}{8}+a\right). \tag{324}$$

The expressions for the aerodynamic forces and moments acting on such a thin rigid

airfoil simplify greatly to

$$\begin{aligned} P &= -\rho b^2 \left(v\pi\dot{\alpha} + \pi\ddot{h} - \pi b a\ddot{\alpha} \right) \\ &\quad - 2\pi\rho v b C \left(v\alpha + \dot{h} + b\left(\frac{1}{2} - a\right)\dot{\alpha} \right), \end{aligned} \tag{325a}$$

$$M_\beta = 0, \tag{325b}$$

$$\begin{aligned} M_\alpha &= -\rho b^2 \left[\pi\left(\frac{1}{2} - a\right) v b\dot{\alpha} + \pi b^2 \left(\frac{1}{8} + a^2\right)\ddot{\alpha} - a\pi b\ddot{h} \right] \\ &\quad + 2\rho v b^2 \pi \left(a + \frac{1}{2}\right) C \left\{ v\alpha + \dot{h} + b\left(\frac{1}{2} - a\right)\dot{\alpha} \right\}. \end{aligned} \tag{325c}$$

Unsurprisingly, the moment of aerodynamic forces on the flap, M_β, vanishes in the limit when the flap's length tends to zero.

C.2 Peters' unsteady aerodynamic theory

References 2, 65, 67 provide a finite-state airloads theory for deformable airfoils. The origin is set at the mid-chord location. The airfoil spans from $x = -b$ (leading edge) to $x = +b$ (trailing edge), where b is the semi-chord. The velocity of the air of density ρ (as seen in the moving coordinate system associated with the airfoil) is u_0 in the positive x direction, v_0 in the positive y direction (positive down), and having a velocity gradient v_1 positive for an angular variation in the clockwise direction. The total positive vertical air velocity is given by $v_0 + v_1 x/b$. The deformations of the airfoil within the x-y frame are denoted by $h(x,t)$ and are assumed to be small. This generalized airfoil motion is measured positive down as well. Glauert expansions are used to represent all variables. The change of variable $x = b\cos\varphi$ leads to an expansion of the airfoil deflection in Glauert terms

$$h(x,t) = \sum_{n=0}^{\infty} h_n(t)\cos(n\varphi). \tag{326}$$

Then, keeping only up to the n^{th} Glauert term ($n+1$ terms in total including the

zeroth term), the generalized forces associated with the defined generalized displacements are given in the following matrix form

$$\frac{\underline{L}}{2\pi\rho} = -b^2 M\{\ddot{\underline{h}} + \dot{\underline{v}}\} - bu_0 C\{\dot{\underline{h}} + \underline{v} - \underline{\lambda}_0\} - u_0^2 K\underline{h} - bG\{\dot{u}_0\underline{h} - u_0\underline{v} + u_0\underline{\lambda}_0\}, \quad (327)$$

where the $(n+1)$-by-1 vectors $\underline{L} = \{L_0, L_1, L_2, \ldots, L_n\}^T$, $\underline{h} = \{h_0, h_1, h_2, \ldots, h_n\}^T$, $\underline{v} = \{v_0, v_1, 0, \ldots, 0\}^T$ and $\underline{\lambda}_0 = \{\lambda_0, 0, 0, \ldots, 0\}^T$ were introduced, as well as the following $(n+1)$-by-$(n+1)$ matrices

$$M = \begin{bmatrix} 1/2 & 0 & -1/4 & 0 & 0 & \ldots \\ 0 & 1/16 & 0 & -1/16 & 0 & \ldots \\ -1/4 & 0 & 2/12 & 0 & -1/24 & \ldots \\ 0 & -1/16 & 0 & 3/32 & 0 & \ldots \\ 0 & 0 & -1/24 & 0 & 4/60 & \ldots \\ \vdots & \vdots & \vdots & \vdots & \vdots & \ddots \end{bmatrix}, \quad (328)$$

where the diagonal elements $M_{i+1,i+1}$ with $i \geq 2$ are generated with $M_{i+1,i+1} = i/4(i^2-1)$ and the off-diagonal terms $M_{i,i+2} = M_{i+2,i}$ where $i \geq 2$ are obtained using $M_{i,i+2} = M_{i+2,i} = -1/(8i)$,

$$C = \begin{bmatrix} f & 1 & 0 & 0 & 0 & \ldots \\ -1/2 & 0 & 1/2 & 0 & 0 & \ldots \\ 0 & -1/2 & 0 & 1/2 & 0 & \ldots \\ 0 & 0 & -1/2 & 0 & 1/2 & \ldots \\ 0 & 0 & 0 & -1/2 & 0 & \ldots \\ \vdots & \vdots & \vdots & \vdots & \vdots & \ddots \end{bmatrix}, \quad (329)$$

$$K = \begin{bmatrix} 0 & 1f & 2 & 3f & 4 & \dots \\ 0 & -1/2 & 0 & 0 & 0 & \dots \\ 0 & 0 & -2/2 & 0 & 0 & \dots \\ 0 & 0 & 0 & -3/2 & 0 & \dots \\ 0 & 0 & 0 & 0 & -4/2 & \dots \\ \vdots & \vdots & \vdots & \vdots & \vdots & \ddots \end{bmatrix}, \tag{330}$$

$$G = \begin{bmatrix} 0 & 1/2 & 0 & 0 & 0 & \dots \\ 0 & 0 & 1/4 & 0 & 0 & \dots \\ 0 & -1/4 & 0 & 1/4 & 0 & \dots \\ 0 & 0 & -1/4 & 0 & 1/4 & \dots \\ 0 & 0 & 0 & -1/4 & 0 & \dots \\ \vdots & \vdots & \vdots & \vdots & \vdots & \ddots \end{bmatrix}. \tag{331}$$

Parameter f is a reversed flow factor. When reversed flow is neglected, $f = 1$. If reversed flow is expected, the expression of f depends on the sign of u_0. The inflow λ_0 is given in terms of N inflow states $\underline{\lambda}$ by

$$\lambda_0 \approx \frac{1}{2}\sum_{n=1}^{N} b_n \lambda_n = \frac{1}{2}\underline{b}^T \underline{\lambda}, \tag{332}$$

in which $\underline{\lambda} = \{\lambda_1, \lambda_2, \dots, \lambda_N\}^T$ and $\underline{b} = \{b_1, b_2, \dots, b_N\}^T$ are N-by-1 vectors. The coefficients are obtained using

$$b_n = (-1)^{n-1} \frac{(N+n-1)!}{(N-n-1)!} \frac{1}{(n!)^2} \quad \text{if} \quad 1 \le n \le N-1, \tag{333}$$

and

$$b_N = (-1)^{N+1}. \tag{334}$$

The evolution of the inflow states $\underline{\lambda}$ for two-dimensional flow is modeled by the set of ordinary differential equations presented in Refs. 2, 68

$$\frac{b}{u_0} A \dot{\underline{\lambda}} + \underline{\lambda} = \frac{b}{u_0} \underline{c}\, \underline{e}^T \left\{ \dot{\underline{v}} + \ddot{\underline{h}} \right\} + \underline{c}\, \underline{f}^T \dot{\underline{h}}, \tag{335}$$

in which the following N-by-1 arrays are defined as

$$\underline{c}^T = \left\{ \frac{2}{1}, \frac{2}{2}, \frac{2}{3}, \ldots, \frac{2}{N} \right\}, \tag{336a}$$

$$\underline{d}^T = \left\{ \frac{1}{2}, 0, 0, \ldots, 0 \right\}, \tag{336b}$$

the following $(M+1)$-by-1 arrays as

$$\underline{e}^T = \left\{ 1, \frac{1}{2}, 0, \ldots, 0 \right\}, \tag{337a}$$

$$\underline{f}^T = \{0, 1, 2, \ldots, M\}, \tag{337b}$$

and finally the N-by-N matrix A is given by

$$A = D + \underline{d}\,\underline{b}^T + \underline{c}\,\underline{d}^T + \frac{1}{2}\underline{c}\,\underline{b}^T, \tag{338}$$

where matrix D has components $D_{i+1,i} = \frac{1}{2(i+1)}$, $D_{i,i+1} = -\frac{1}{2i}$, and 0 otherwise.

REFERENCES

[1] Agarwal, S., *Aeromechanical Stability Augmentation Using Semi-Active Friction-Based Lead-Lag Dampers*. PhD thesis, Georgia Institute of Technology, School of Aerospace Engineering, Atlanta, GA, USA, 2005.

[2] Ahaus, L. and Peters, D., "Unified airloads model for morphing airfoils in dynamic stall," in *American Helicopter Society Specialist's Conference on Aeromechanics*, (San Francisco, CA), pp. 1–24, January 20-22 2010.

[3] Banerjee, A. and Kane, T., "Modeling and simulation of rotor bearing friction," *Journal of Guidance, Control and Dynamics*, vol. 17, no. 5, pp. 1137–1151, 1994.

[4] Barlas, T. and VanKuik, G., "State of the art and prospectives of smart rotor control for wind turbines," *Journal of Physics: Conference Series*, vol. 75, pp. 1–20, 2007.

[5] Bauchau, O., *DYMORE User Manual*. Georgia Institute of Technology, Atlanta, GA, USA.

[6] Bauchau, O., "On the modeling of friction and rolling in flexible multi-body systems," *Multibody System Dynamics*, vol. 3, no. 1, pp. 209–239, 1999.

[7] Bauchau, O., *Flexible Multibody Dynamics*. Dordrecht: Springer, 2011.

[8] Bauchau, O., Bottasso, C., and Nikishkov, Y., "Modeling rotorcraft dynamics with finite element multibody procedures," *Mathematical and Computer Modeling*, vol. 33, no. 10-11, pp. 1113–1137, 2001.

[9] Bauchau, O. and Craig, J., *Structural Analysis: With Applications to Aerospace Structures*. Dordrecht: Springer, 2009.

[10] Bauchau, O. and Ju, C., "Modeling friction phenomena in flexible multibody dynamics," *Computer Methods in Applied Mechanics and Engineering*, vol. 195, pp. 6909–6924, October 2006.

[11] Bauchau, O. and Liu, H., "On the modeling of hydraulic components in rotorcraft systems," *Journal of the American Helicopter Society*, vol. 51, pp. 175–184, April 2006.

[12] Bauchau, O. and Rodriguez, J., "Modeling of joints with clearance in flexible multibody systems," *International Journal of Solids and Structures*, vol. 39, no. 1, pp. 41–63, 2002.

[13] Bauchau, O., Rodriguez, J., and Bottasso, C., "Modeling of unilateral contact conditions with application to aerospace systems involving backlash, freeplay and friction," *Mechanics Research Communications*, vol. 28, no. 5, pp. 571–599, 2001.

[14] Bauchau, O., Van Weddingen, Y., and Agarwal, S., "Semiactive coulomb friction lead-lag dampers," *Journal of the American Helicopter Society*, vol. 55, pp. 012005/1–12, January 2010.

[15] Bauchau, O. and Wang, J., "Stability analysis of complex multibody systems," *Journal of Computational and Nonlinear Dynamics*, vol. 1, pp. 71–80, January 2006.

[16] Bauchau, O. and Wang, J., "Stability evaluation and system identification of flexible multibody systems," *Multibody System Dynamics*, vol. 18, pp. 95–106, October 2007.

[17] Bauchau, O. and Wang, J., "Efficient and robust approaches to the stability analysis of large multibody systems," *Journal of Computational and Nonlinear Dynamics*, vol. 3, pp. 1–12, January 2008.

[18] Bernhard, A. and Chopra, I., "Trailing edge flap activated by a piezo-induced bending-torsion coupled beam," *Journal of the American Helicopter Society*, vol. 44, pp. 3–15, January 1999.

[19] Bernhard, A. and Chopra, I., "Hover test of a mach-scale rotor model with active blade tips," *Journal of the American Helicopter Society*, vol. 47, pp. 273–284, October 2002.

[20] Bettini, P., Airoldi, A., Sala, G., Di Landro, L., Ruzzene, M., and Spadoni, A., "Composite chiral structures for morphing airfoils: Numerical analyses and development of a manufacturing process," *Composites - Part B: Engineering*, vol. 41, pp. 133–147, 2010.

[21] Bharti, S. and Frecker, M., "Compliant mechanical amplifier design using multiple optimally placed actuators," *Journal of Intelligent Material Systems and Structures*, vol. 18, pp. 209–217, March 2007.

[22] Bornengo, D., Scarpa, F., and Remillat, C., "Evaluation of hexagonal chiral structure for morphing airfoil concept," *Proceedings of the Institution of Mechanical Engineers - Part G: Journal of Aerospace Engineering*, vol. 219, no. 3, pp. 185–192, 2005.

[23] Bousman, W. and Maier, T., "An investigation of helicopter rotor blade flap vibratory loads," in *American Helicopter Society 48th Annual Forum Proceedings*, (Washington, D.C.), pp. 977–999, June 3-5 1992.

[24] Campanile, L. and Sachau, D., "The belt-rib concept: A structronic approach to variable camber," *Journal of Intelligent Material Systems and Structures*, vol. 11, pp. 215–224, March 2000.

[25] Canudas de Wit, C., Olsson, H., Astrom, K., and Lischinsky, P., "A new model for control of systems with friction," *IEEE Transactions on Automatic Control*, vol. 40, no. 2, pp. 419–425, 1995.

[26] Cardona, A. and Géradin, M., "Kinematic and dynamic analysis of mechanisms with cams," *Computer Methods in Applied Mechanics and Engineering*, vol. 103, pp. 115–134, 1993.

[27] Cesnik, C. and Hodges, D., "Vabs: A new concept for composite rotor blade cross-sectional modeling," *Journal of the American Helicopter Society*, vol. 42, pp. 27–38, January 1997.

[28] Cesnik, C. and Shin, S., "On the modeling of integrally actuated helicopter blades," *International Journal of Solids and Structures*, vol. 38, pp. 1765–1789, March 2001.

[29] Chakravarty, U., *Section Builder: A Finite Element Tool for Analysis and Design of Composite Beam Cross-Sections*. PhD thesis, Georgia Institute of Technology, School of Aerospace Engineering, Atlanta, GA, USA, 2008.

[30] Chen, P. and Chopra, I., "Induced strain actuation of composite beams and rotor blades with embedded piezoceramic elements," *Smart Materials and Structures*, vol. 5, pp. 35–48, February 1996.

[31] Chen, P. and Chopra, I., "Wind tunnel test of a smart rotor with individual blade twist control," in *Proceedings of the SPIE - The International Society for Optical Engineering*, vol. 3041, pp. 217–230, June 1997.

[32] Coleman, R. and Feingold, A., "Theory of self-excited mechanical oscillations of helicopter rotors with hinged blades," Tech. Rep. 1351, NACA Report, 1956.

[33] Dahl, P., "Solid friction damping of mechanical vibrations," *AIAA Journal*, vol. 14, no. 12, pp. 1675–1682, 1976.

[34] dos Santos e Lucato, S. and Evans, A., "The load capacity of a kagome based high authority shape morphing structure," *Transactions of the ASME - Journal of Applied Mechanics*, vol. 73, pp. 128–133, January 2006.

[35] dos Santos e Lucato, S., McMeeking, R., and Evans, A., "Actuator placement optimization in a kagome based high authority shape morphing structure," *Smart Materials and Structures*, vol. 14, no. 4, pp. 869–875, 2005.

[36] Dupont, P., Kasturi, P., and Stokes, A., "Semi-active control of friction dampers," *Journal of Sound and Vibration*, vol. 202, no. 2, pp. 203–218, 1997.

[37] Ferri, A. and Heck, B., "Analytical investigation of damping enhancement using active and passive structural joints," *Journal of Guidance, Control, and Dynamics*, vol. 15, no. 1, pp. 1258–1264, 1992.

[38] Fulton, M. and Ormiston, R., "Hover testing of a small-scale rotor with on-blade elevons," *Journal of the American Helicopter Society*, vol. 46, pp. 96–106, April 2001.

[39] Gandhi, F., Wang, K. W., and Xia, L., "Magnetorheological fluid damper feedback linearization control for helicopter rotor application," *Smart Materials and Structures*, vol. 10, no. 1, pp. 96–103, 2001.

[40] Gaul, L., Albrecht, H., and Wirnitzer, J., "Semi-active damping of large space truss structures using friction joints," in *Proceedings of the SPIE - The International Society for Optical Engineering*, vol. 4935, pp. 232–243, 2002.

[41] Gaul, L., Albrecht, H., and Wirnitzer, J., "Semi-active friction damping of large space truss structures," *Shock and Vibration*, vol. 11, no. 4, pp. 173–186, 2004.

[42] Gaul, L. and Lenz, J., "Active damping of space structures by contact pressure control in joints," *Mechanics of Structures and Machines*, vol. 26, no. 1, pp. 81–100, 1998.

[43] Gaul, L. and Nitsche, R., "Friction control for vibration suppression," *Mechanical Systems and Signal Processing*, vol. 14, no. 2, pp. 139–150, 2000.

[44] Gaul, L. and Nitsche, R., "The role of friction in mechanical joints," *Applied Mechanics Reviews*, vol. 54, no. 2, pp. 93–105, 2001.

[45] Haessig, D. and Friedland, B., "On the modeling and simulation of friction," *ASME Journal of Dynamic Systems, Measurement and Control*, vol. 113, no. 1, pp. 354–362, 1991.

[46] Hall, S., Tzianetopoulou, T., Straub, F., and Ngo, H., "Design and testing of a double x-frame piezoelectric actuator," in *Proceedings of the SPIE - The International Society for Optical Engineering*, vol. 3985, pp. 26–37, June 2000.

[47] Hodges, D., *Nonlinear Composite Beam Theory*. Virginia: American Institute of Aeronautics and Astronautics, 2006.

[48] Hodges, D. and Pierce, G., *Introduction to Structural Dynamics and Aeroelasticity*. Cambridge: Cambridge University Press, 2002.

[49] Hsu, T.-K. and Peters, D., "A simple dynamic model for simulating draft-gear behavior in rail-car impacts," *ASME Journal of Engineering for Industry*, vol. 100, pp. 492–496, November 1978.

[50] Hu, W. and Wereley, N., "Magnetorheological fluid and elastomeric lag damper for helicopter stability augmentation," *International Journal of Modern Physics B*, vol. 19, no. 7, 8 & 9, pp. 1471–1477, 2005.

[51] Johnson, W., *Helicopter Theory*. Mineola: Dover, 1994.

[52] Ju, C., *Modeling Friction Phenomena and Elastomeric Dampers in Multibody Dynamics Analysis*. PhD thesis, Georgia Institute of Technology, School of Aerospace Engineering, Atlanta, GA, USA, 2009.

[53] Koratkar, N. and Chopra, I., "Wind tunnel testing of a smart rotor model with trailing-edge flaps," *Journal of the American Helicopter Society*, vol. 47, pp. 263–272, October 2002.

[54] Kudva, J., Sanders, B., Pinkerton-Florance, J., and Garcia, E., "Overview of the darpa/afrl/nasa smart wing phase 2 program," in *Proceedings of the SPIE - The International Society for Optical Engineering*, vol. 4332, pp. 383–389, March 2001.

[55] Kudva, J., Sanders, B., Pinkerton-Florance, J., and Garcia, E., "The darpa/afrl/nasa smart wing program - final overview," in *Proceedings of the SPIE - The International Society for Optical Engineering*, vol. 4698, pp. 37–43, 2002.

[56] Lampaert, V., Swevers, J., and Al-Bender, F., "Modification of the leuven integrated friction model structure," *IEEE Transactions on Automatic Control*, vol. 47, no. 4, pp. 683–687, 2002.

[57] Lee, T. and Chopra, I., "Design issues of a high-stroke, on-blade piezostack actuator for a helicopter rotor with trailing-edge flaps," *Journal of Intelligent Material Systems and Structures*, vol. 11, pp. 328–342, May 2000.

[58] Lee, T. and Chopra, I., "Design of a bidirectional piezoelectric actuator for blade trailing-edge flap," in *Proceedings of the SPIE - The International Society for Optical Engineering*, vol. 4327, pp. 36–45, August 2001.

[59] Marathe, S., Gandhi, F., and Wang, K. W., "Helicopter blade response and aeromechanical stability with a magnetorheological fluid based lag damper," *Journal of Intelligent Material Systems and Structures*, vol. 9, no. 4, pp. 272–282, 1998.

[60] McGowan, A., Cox, D., Lazos, B., Waszak, M., Raney, D., Siochi, E., and Pao, P., "Biologically-inspired technologies in nasa's morphing project," in *Proceedings of the SPIE - The International Society for Optical Engineering*, vol. 5051, pp. 1–13, March 2003.

[61] Milgram, J., Chopra, I., and Straub, F., "Rotors with trailing edge flaps: Analysis and comparison with experimental data," *Journal of the American Helicopter Society*, vol. 43, pp. 319–332, October 1998.

[62] Moored, K. and Bart-Smith, H., "The analysis of tensegrity structures for the design of a morphing wing," *Transactions of the ASME - Journal of Applied Mechanics*, vol. 74, pp. 668–676, July 2007.

[63] Nissly, A., Anusonti-Inthra, P., Gandhi, F., and Frecker, M., "Design optimization of a controllable camber rotor airfoil," in *American Helicopter Society 61st Annual Forum Proceedings*, (Grapevine, TX), pp. 707–716, June 1-3 2005.

[64] Oden, J. and Martins, J., "Models and computational methods for dynamic friction phenomena," *Computer Methods in Applied Mechanics and Engineering*, vol. 52, pp. 527–634, 1985.

[65] Peters, D. and Johnson, M., "Finite-state airloads for deformable airfoils on fixed and rotating wings," in *Symposium on Aeroelasticity and Fluid/Structure Interaction, American Society of Mechanical Engineers Winter Annual Meeting*, (Chicago, IL), November 6-11 1994.

[66] Peters, D. and He, C., "Finite state induced flow models, part ii: Three-dimensional rotor disk," *Journal of Aircraft*, vol. 32, no. 2, pp. 323–333, 1995.

[67] Peters, D., Hsieh, M., and Torrero, A., "A state-space airloads theory for flexible airfoils," *Journal of the American Helicopter Society*, vol. 52, pp. 329–342, October 2007.

[68] Peters, D., Karunamoorthy, S., and Cao, W., "Finite state induced flow models, part i: Two-dimensional thin airfoil," *Journal of Aircraft*, vol. 32, no. 2, pp. 313–322, 1995.

[69] Prahlad, H. and Chopra, I., "Design of a variable twist tiltrotor blade using shape memory alloy (sma) actuators," in *Proceedings of the SPIE - The International Society for Optical Engineering*, vol. 4327, pp. 46–59, August 2001.

[70] Prall, D. and Lakes, R., "Properties of a chiral honeycomb with a poisson's ratio of -1," *International Journal of Mechanical Sciences*, vol. 39, no. 3, pp. 305–314, 1996.

[71] Prechtl, E. and Hall, S., "An x-frame actuator servo-flap actuation system for rotor control," in *Proceedings of the SPIE - The International Society for Optical Engineering*, vol. 3329, pp. 309–320, July 1998.

[72] Preumont, A., *Vibration Control of Active Structures*. Dordrecht: Springer, 2nd ed., 2002.

[73] Rodgers, J. and Hagood, N., "Preliminary mach-scale hover testing of an integral twist-actuated rotor blade," in *Proceedings of the SPIE - The International Society for Optical Engineering*, vol. 3329, pp. 291–308, July 1998.

[74] Shaner, M. and Chopra, I., "Design and testing of a piezostack actuated leading-edge flap," in *Proceedings of the SPIE - The International Society for Optical Engineering*, vol. 3668, pp. 50–59, June 1999.

[75] Shigley, J. and Mischke, C., *Mechanical Engineering Design*, ch. 6. New York: McGraw-Hill Book Company, 1989.

[76] Shin, S., Cesnik, C., and Hall, S., "Closed-loop control test of the nasa/army/mit active twist rotor for vibration reduction," *Journal of the American Helicopter Society*, vol. 50, pp. 178–194, April 2005.

[77] Shin, S., Cesnik, C., and Hall, S., "Design and simulation of integral twist control for helicopter vibration reduction," *International Journal of Control, Automation, and Systems*, vol. 5, pp. 24–34, February 2007.

[78] Spadoni, A., *Application of Chiral Cellular Materials for the Design of Innovative Components*. PhD thesis, Georgia Institute of Technology, School of Aerospace Engineering, Atlanta, GA, USA, 2008.

[79] Spadoni, A. and Ruzzene, M., "Numerical and experimental analysis of the static compliance of chiral truss-core airfoils," *Journal of Mechanics of Materials and Structures*, vol. 2, pp. 965–975, May 2007.

[80] Spadoni, A. and Ruzzene, M., "Static aeroelastic response of chiral-core airfoils," *Journal of Intelligent Material Systems and Structures*, vol. 18, pp. 1067–1075, October 2007.

[81] Straub, F., Ngo, H., Anand, V., and Domzalski, D., "Development of a piezoelectric actuator for trailing edge flap control of full scale rotor blades," *Smart Materials and Structures*, vol. 10, pp. 25–34, February 2001.

[82] Straub, F. and King, R., "Application of smart materials to control a helicopter rotor," in *Proceedings of the SPIE - The International Society for Optical Engineering*, vol. 2721, pp. 66–77, February 1996.

[83] Swevers, J., Al-Bender, F., Ganseman, C., and Prajogo, T., "An integrated friction model structure with improved presliding behavior for accurate friction compensation," *IEEE Transactions on Automatic Control*, vol. 45, no. 4, pp. 675–686, 2000.

[84] Theodorsen, T., "General theory of aerodynamic instability and the mechanism of flutter," Tech. Rep. 496, NACA, 1935.

[85] Trease, B. and Kota, S., "Synthesis of adaptive and controllable compliant systems with embedded actuators and sensors," in *Proceedings of the ASME Design Engineering Technical Conference*, September 2006.

[86] Trease, B. and Kota, S., "Adaptive and controllable compliant systems with embedded actuators and sensors," in *Proceedings of the SPIE - The International Society for Optical Engineering*, vol. 6525, pp. 1R1–1R13, 2007.

[87] Valanis, K., "A theory of viscoplasticity without a yield surface," *Archives of Mechanics*, vol. 23, no. 4, pp. 171–191, 1971.

[88] Van Weddingen, Y., Bauchau, O., Kottapalli, S., Ozbay, S., and Mehrotra, Y., "Application of out-of-plane warping to control rotor blade twist," in *American Helicopter Society Specialist's Conference on Aeromechanics*, (San Francisco, CA), pp. 1–14, January 20-22 2010.

[89] Vasilescu, R. and Dancila, S., "Modeling and analysis of active flap using coiled bender piezoelectric actuators," *Journal of Intelligent Material Systems and Structures*, vol. 15, pp. 783–792, September/October 2004.

[90] Wang, D., Bartley-Cho, J., Martin, C., and Hallam, B., "Development of high-rate, large deflection, hingeless trailing edge control surface for the smart wing wind tunnel model," in *Proceedings of the SPIE - The International Society for Optical Engineering*, vol. 4332, pp. 407–418, June 2001.

[91] Welsh, W., "Simulation and correlation of a helicopter air-oil strut dynamic response," in *American Helicopter Society 43rd Annual Forum Proceedings*, (St. Louis, Missouri), May 18-20 1987.

[92] Welsh, W., "Dynamic modeling of a helicopter lubrication system," in *American Helicopter Society 44th Annual Forum Proceedings*, (Washington, DC), June 16-18 1988.

[93] Wlezien, R., Horner, G., McGowan, A., Padula, S., Scott, M., Silcox, R., and Simpson, J., "The aircraft morphing project," in *Proceedings of the SPIE - The International Society for Optical Engineering*, vol. 3326, pp. 176–187, 1998.

[94] Yang, B. and Menq, C., "Characterization of contact kinematics and application to the design of wedge dampers in turbomachinery blading: Part I - stick-slip contact kinematics," *ASME Journal of Engineering for Gas Turbines and Power*, vol. 120, no. 3, pp. 410–417, 1999.

[95] Yang, B. and Menq, C., "Characterization of contact kinematics and application to the design of wedge dampers in turbomachinery blading: Part II - prediction of forced response and experimental verification," *ASME Journal of Engineering for Gas Turbines and Power*, vol. 120, no. 3, pp. 418–423, 1999.

[96] Yu, W., *Variational Asymptotic Modeling of Composite Dimensionally Reducible Structures*. PhD thesis, Georgia Institute of Technology, School of Aerospace Engineering, Atlanta, GA, USA, 2002.

[97] Yu, W., Volovoi, V., Hodges, D., and Hong, X., "Validation of the variational asymptotic beam sectional analysis," *AIAA Journal*, vol. 40, no. 10, pp. 2105–2112, 2002.

[98] Zhao, Y., Choi, Y., and Wereley, N., "Semi-active damping of ground resonance in helicopters using magnetorheological dampers," *Journal of the American Helicopter Society*, vol. 49, pp. 468–482, October 2004.